Heat Transfer Analysis of a 50% Scale Formula 1 Wheel Assembly

KRYSTINA EMMANOUILIDES

Heat Transfer Analysis of a 50% Scale Formula 1 Wheel Assembly

by

Krystina Emmanouilides

Supervised by
Dr D. B. Sims-Williams,
Dr R. G. Dominy

A Thesis submitted for the degree of
Master of Science by Research

School of Engineering and Computing Sciences
Durham University
England

March 2015

Abstract

The heat transfer of a 50% scale model F1 wheel assembly has been analysed experimentally with hot films, using a brake cooling test rig for internal analyses, and the Durham University wind tunnel for combined internal and external analyses. Computational analysis using the Exa PowerFlow CFD software was undertaken as both a correlation exercise, and to complement the experimental results, providing insight into the flow characteristics within the wheel assembly.

The systematic error within the system was evaluated by determining the level of heat transfer at zero-flow conditions, which led to the conclusion that varying flow application method does not affect the disc heat transfer coefficient. Experimental and computational results were used to derive the Nusselt number equation, with the wind tunnel disc revealing a Reynolds number exponent of 0.87, a figure closely correlating to literature. Results for the sidewall presented a range of heat transfer values, to which a combined model fit was applied.

Investigations into unmatched tyre surface velocity and flow velocity determined that 77% of the convective heat transfer experienced at the sidewall was due solely to the tyre's rotation. The level of applied air-flow, did however, affect the rate of heat transfer. Internal of the upright, comparison of results for a blocked and open Inlet scoop found the Inlet scoop to be the predominant source of cooling to the disc.

Wind tunnel heat transfer coefficient results for the tyre sidewall displayed a relationship to radial position, with HTC increasing from the central position of the sidewall both toward the internal diameter and external diameter. The capability of the CFD software to extract heat transfer coefficients was assessed using two rotational simulation methods; Sliding mesh (physical rotation) and moving reference frame (imposed rotation through the application of rotational fluid forces), neither of which was able to reproduce the patterns of heat transfer outlined in the wind tunnel results.

Declaration

The material contained within this thesis has not previously been submitted elsewhere for any other degree or qualification. The research reported has been conducted by the author unless referenced to the contrary in the text.

Acknowledgements

My sincerest thanks to my supervisors, Dr D. B. Sims-Williams and Dr R. G. Dominy, for their continued support and opinion throughout the undertaking of this thesis. Your knowledge and assistance proved invaluable, and your friendly and welcoming nature made for an enjoyable time within the department.

Further thanks to the Engineering Workshop staff, who worked on the components necessary to, quite literally, support the experimental work, and who always stopped to see how things were going. To the staff at the Durham University Engineering Café, without whom my daily consumption of caffeine would have consisted of overpriced tea in paper cups, and to the ever-smiling staff at Trevelyan College, who never failed to make me laugh at the end of a tough day, and knew when seconds were an absolute necessity.

To my friends and team-mates of DUWAFC, who pretended to listen to me talk about my work throughout the year, but who also enriched my experience at Durham University and became family.
Lastly, but most importantly, to my family for supporting me through the last 5 years of my further education, and enduring the pain of listening to me talk about tyres for a good portion of that time. Thank you for giving me the opportunity to pursue my dreams.

Contents

List of Figures

List of Tables

List of Abbreviations

Abbreviation	Definition
3D	3-Dimensional
BDC	Bottom Dead Centre
CAD	Computer Aided Design
CCW	Counter Clockwise
CFD	Computational Fluid Dynamics
CTA	Constant Temperature Anemometer
CTS	CTA-to-Short
HFN	Hub Flow Number
HTC	heat transfer coefficient
ID	Internal Diameter
LHS	Left Hand Side
MRF	Moving Reference Frame
OD	Outside Diameter
PIV	Particle Image Velocimetry
RHS	right Hand Side
SM	Sliding Mesh
SP	Stagnation Point
STS	Short-to-Sensor
TDC	Top Dead Centre
VB	Velocity Boundary
VLES	Very Large Eddy Simulation
WT	wind tunnel

List of Symbols

Symbol	Definition
a	Temperature coefficient of resistance
A, $A_{effective}$, A_s	Area
C	Coefficient in the Nusselt number equation
D, d, Ø	Diameter
h	Heat transfer coefficient (referred to as HTC in text)
k	Thermal conductivity
m	Exponent of Reynolds number in the Nusselt number equation
n	Exponent of Prandtl number in the Nusselt number equation
Nu	Nusselt number
P	Electrical power
Pr	Prandtl number
Q	Heat transfer/The amount of thermal energy transferred to air (W)
R	Resistance
Re	Reynolds number
T, T_{amb}, T_{hot}, T_s	Temperature
U, U_s, U_∞	Velocity
v	Kinematic viscosity
V, V_{dial}, $V_{probe,}$ V_{sensor}	Voltage
$\dot{Q}$	Rate of heat transfer
α	Coefficient of heat transfer split (Yavari et al., 1993)
δ	Boundary layer thickness
ΔT	Difference in temperature
θ	Angular position
μ	Dynamic viscosity

1.0. Introduction

1.1. Aim

The aim of this work is to experimentally determine the convective heat transfer coefficient at various locations on a 50% scale F1 wheel assembly through the use of hot film sensors, and to generate a computational fluid dynamics simulation using Exa PowerFlow, to evaluate the computational ability of predicting the convective heat transfer coefficient.

1.2. Objectives

To identify the effects of rotation on tyre aerodynamics.

The exploration of the effect of rotating components on the convective heat transfer, including the resulting advancement of flow separation, and the identification of the internal flow effect of rotation on recirculation and heat transfer.

The application of heat transfer knowledge to the identification of heat generation and cooling mechanisms of the wheel assembly, including the creation of a heat transfer diagram.

The outline and mapping of heat transfer, considering internal and external flow and the interaction between components, in order to understand system heat transfer.

The generation of upright geometry CAD models.

The geometry to be used in experimental testing is to be modelled using CAD software in a format compatible with the PowerFlow CFD software for creation of the computational simulation. Geometry is also required for the setup of the wind tunnel test, including the design of rig fixtures to support/mount the geometry.

Undertaking of brake cooling test rig experiments in order to determine the internal convective heat transfer coefficient.

A rolling tyre rig test will be used to collect internal heat transfer data using a hot film sensor positioned in a disc Vane. The collected data will then be used to determine the convective heat transfer coefficient for each of the given test configurations.

To undertake wind tunnel tests in order to determine the external convective heat transfer coefficient.

The collection of external convective heat transfer coefficient data through the development of a wind tunnel test, recording internal values alongside external, so as to validate results recorded from the rig test.

The creation of a tyre sidewall heat transfer map for experimental tyre sidewall results.

Visual positional development tool for analysis of heat transfer levels on a local and global scale. This will aid in the depth of analysis possible with respect to computational comparison.

The generation of computational fluid dynamics (CFD) simulations; understanding the correlation between experimental and simulated results including the capabilities of a scaled computational model.

The CFD simulation will utilise the wheel assembly CAD geometry in order to predict the convective heat transfer coefficient; supported by flow analysis. Various setup parameters will be explored in order to determine best practice based on experimental comparisons, including the capability of scaled simulations with respect to heat transfer results.

1.3. Industrial Relevance

As a result of speed and aerodynamic loading, Formula 1 vehicles experience high vertical loads on their tyres, increasing heat generation due to frictional effects with the road, and extreme braking temperatures, making temperature control an imperative aspect for performance optimisation. Vehicle setup parameters, such as camber/toe and the use of aerodynamic components forward of the front axle can be used to redirect airflow so as to optimise heat transfer.

Before interactions between the wheel assembly and other components can be considered, it remains important to understand airflow and heat transfer in isolation as they may influence the design of components upstream of the wheel in order to optimise cooling requirements.

A major aspect of this investigation is to evaluate the correlation and best practice of both experimental and computational processes for determining convective heat transfer coefficients (HTC). Correlation can be evaluated so long as setup parameters remain consistent throughout the experimental and computational procedures. Regardless of whether or not correlation is achieved, changes of setup may show variations in correlation, however, it is assumed that the most basic of scenarios (the stand-alone configuration) should provide the best correlation, with increased setup complexity resulting in correlation discrepancies.

2.0. Literature Review

The following sections explore literature relevant to the subject of this thesis, including fundamental aerodynamic principles of rotating wheels, mechanisms of heat transfer, including their presence within wheel assemblies, and an outline of hot film anemometry.

2.1. Rotating Wheel Aerodynamics

Though several existing studies compare the aerodynamic parameters of rotating cylinders with their stationary equivalents, few explore the impact of rotation on heat transfer. The disparity between aerodynamic characteristics of a stationary and rotating wheel is fundamental to understanding the resulting variation between heat transfer capabilities.

2.1.1. Boundary Layer

Principles of fluid flow dictate that a boundary layer will occur over a body due to the no-slip condition, whereby the fluid incurs a zero-velocity relative to the body upon contact, the formation of which, Browne and Wickliffe (1980) found to cause a lower level of heat transfer toward the rear of a cylinder than the front given its increasing thickness.

2.1.2. Flow Structures

Cylindrical rotation is found to advance separation (Knowles, 2005), and supress rearward vortex shedding in the turbulent wake (Stojkovic, et al., 2002). The introduction of a ground plane in contact with the cylinder (rather than the study of a free-floating cylinder), results in the blockage of flow, however, for a rotating 3-Dimensional (3D) tyre of finite span, partial circulation due to the presence of interstices and the no-slip condition of the ground, where zero-flow velocity remains on the surface of the tyre as it circulates through its rotation, may cause jetting effects. Mears (2004) used particle image velocimetry (PIV) to describe the downwash of air over/past a rotating tyre, with majority of separated flow, the portion of fluid flow detached from the tyre's surface after reaching a point of zero-velocity, following the tread, while sidewalls experienced a predominantly free-stream flow. Conversely, the stationary tyre displayed majority of air-flow directed around the sidewalls. The effect of ground contact brings tyre simulation and experimentation a level above generic cylindrical flow investigations, with ground contact eliminating vortex shedding for both low and high aspect ratios as a result of supressing the separation of the boundary layer (Lei, et al., 1999).

Fackrell (1974) determined the separation point of a stationary wheel to occur at 210deg counter clockwise (CCW) from the stagnation point (SP). Furthermore, both Fackrell and Mears found that the separation point for rotating wheels was approximately 280deg CCW from the SP. This was confirmed though the studies of Nemati et al. (2011), who concluded that the rotation of 3D cylinders of finite span advances the point of flow separation. Similarly, for a rotating tyre, Hinson (1999) experienced experimental separation at 270deg, while computational separation occurred at 295deg CCW from the SP. Mears found a similar trend between computational and experimental results, with separation of his rotating wheel using CFD occurring at 245deg.

Further research into the wake structures of stationary and rotating wheels by Bearman et al. (1988) showed that at a distance of 2.5D downstream, the wake for a stationary tyre was dominated by a contra-rotating vortex pair near the ground, while that of the rotating wheel was centred approximately 0.25D above the ground and of a much lower intensity; tyre rotation resulting in the aforementioned suppression of vortex development.

2.2. Heat Transfer Mechanisms

Heat transfer is the determination of the rate of heat travel; energy that is transferred from a high to low temperature by means of one/more of three transfer processes; convection, conduction and/or radiation. The fundamentals of convection and the effect of fluid-flow over a surface upon convection are decribed in detail in many texts (Cengel et al., 2008; Massey, 1989), from which the following section summarises the flow features that are of direct relevance to the flow about a rotating wheel, and those that influence the capacity of convective heat transfer in the wheel assembly.

2.2.1. Convection

Convective heat transfer is the study of heat transport processes affected by fluid flow (Bejan, 2013), and is governed by Newton's Law of cooling [1], which outlines that the rate of heat transfer is proportional to the temperature differential between the surface of an object and ambient conditions.

$$\frac{dQ}{dt} = hA(T_s - T_{amb}) \quad [1]$$

Convective heat transfer is a cumulative result of two main characteristic phenomena; molecular motion and macroscopic motion (Bergman & Lavine, 2011). The molecular motion is the basis of the effect, with particles colliding in a random manner within the flow, causing a constant heat exchange, influenced and carried by the macroscopic motion of the fluid. Convective heat transfer is characterised by one of two flow types; natural or forced. The work in this thesis will focus on forced convection rather than convection due to natural buoyancy-driven flow.

When a free-stream flow undergoes contact with a solid surface, a boundary layer is generated, throughout which there exists a varying velocity; resulting in a velocity distribution in the y-direction.
Flat plate theory can be used to describe the two variations of boundary layer; velocity and thermal.
A velocity boundary layer occurs due to the retardation of flow upon contact with a solid (Figure 1). The boundary layer causes a chain of fluid particle retardation in consecutively adjoined fluid layers due to the shear stress parallel to the fluid velocity, until, at distance y = δ, the effect becomes negligible, reaching the free-stream value.

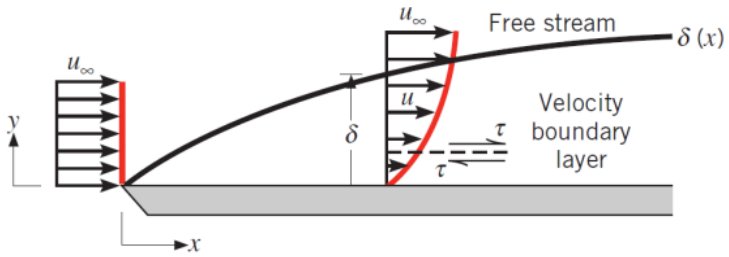

Figure 1: Representation of a boundary layer velocity distribution (Image source: Cengel et al., 2008).

A thermal boundary layer develops when the free-stream flow and surface temperature differ. Figure 2 shows the flow over an isothermal plate beginning with a uniform temperature gradient at x = 0. When the fluid comes into contact with the surface, fluid particles achieve thermal equilibrium, resulting in a n energy exchange between consecutively adjoined fluid layers; introducing a thermal boundary layer. In the case of a rolling tyre, there exists both a velocity and thermal boundary layer; thermal boundary layers exist in either fluid-solid contact or solid-solid contact.

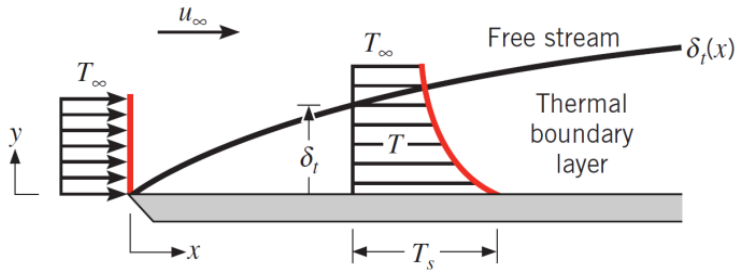

Figure 2: Representation of a thermal boundary layer's temperature distribution (Image source: Cengel et al., 2008).

The characteristic curve of a velocity boundary layer is dependent on the flow type, which can be categorised as either laminar or turbulent, and affects the degree of convective heat transfer. Flat plate theory demonstrates that both flow conditions can occur, with laminar flow preceding turbulent. Each flow type is characterised by the nature of the fluid coordinate components of velocity.

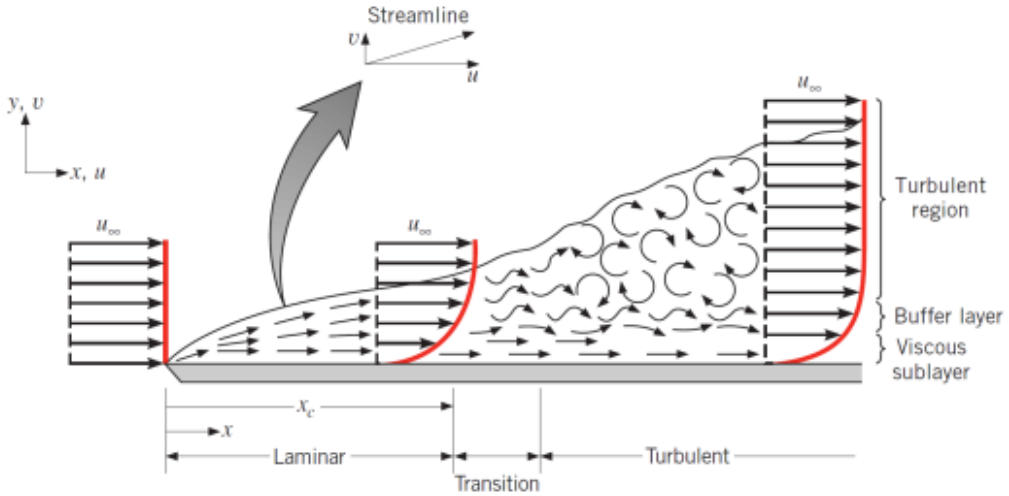

Figure 3: Representation of the velocity boundary layer development (Image source: Cengel et al., 2008).

Laminar flow is characterised by its highly fluid, undisturbed flow, while turbulent flow is highly unstable and irregular, consisting of random 3-Dimensional flow structures; high-speed flow is drawn toward the surface, while low-speed flow is directed further into the flow-stream.
The transition between these two flow types is due to mechanisms related to flow disturbance; natural or un-natural disturbances. Natural disturbances are associated with flow fluctuations, whereas un-natural disturbances are dependent on the flow situation, such as the solid component's surface roughness. It is important to understand the behaviour of the various flow types given the variation that occurs in heat transfer coefficient between laminar and turbulent flow.

Boundary layer transition is dependent upon Reynolds number (Re) [2], a dimensionless quantity describing the ratio of inertial and viscous forces. Flat-plate theory can be extended to circular flows, such as that of the flow around a tyre, whereby a $Re \leq 2x10^5$ is representative of a laminar boundary layer, with theoretical separation occurring at θ=280deg CCW of the SP (where θ=angular position), and an $Re \geq 2x10^5$ representative of a turbulent boundary layer transition, with separation delayed to θ=220deg CCW of SP.

$$Re_D = \frac{\rho V D}{\mu} = \frac{V D}{v} \quad [2]$$

Free-stream flow is stagnated upon contact of a cylinder, resulting in an increased pressure, accelerating the flow and forcing it around the cylinder. The pressure gradient continues to decrease until it equals zero, termed the separation point; the point at which fluid momentum is not great enough to overcome the pressure gradient, resulting in boundary layer separation and inducing a wake.

Section 2.1 explored the variation between static and rotating wheel aerodynamics, describing the effect rotation has on aspects such as the separation point. In much the same way, cylindrical theory is limited in its accuracy to describe flow characteristics, as tyres do not rotate in a free domain, but in proximal contact with a wall/ground plane (the road). Cylindrical theory assumes that the flow bifurcates at the stagnation point and travels over the cylinder until the separation point. Vortex shedding is found to decrease, or even become obsolete, for cylinders where wall proximity is less than e/D=0.3, which in the case of this study, was a gap of 93mm (Sumer & Fredsoe, 2006); where e=gap between cylinder and wall and D=cylinder diameter.

2.2.2. Conduction

Conduction is the transfer of energy from the more energetic particles of a substance to the adjacent, less energetic ones as a result of interactions between the two. In gasses and liquids, this motion is a result of the collision and diffusion of molecules during their random motion. In solids it is due to the combination of molecular vibrations in the lattice structure, and the energy transported by free moving electrons. In conduction processes, energy transfer occurs in the direction of decreasing temperature (Bergman & Lavine, 2011). The rate of heat transfer is dependent on the geometry of the medium through which it is travelling, as

well as the material and temperature difference through its structure (Cengel et al., 2008). The rate of conductive heat transfer can be described mathematically by Fourier's law [3].

$$\dot{Q}_{cond} = kA\frac{T_1 - T_2}{\Delta x} = -kA\frac{\Delta T}{\Delta x} \quad (W) \qquad [3]$$

Equation 1: Rate of heat conduction.

The material property describing the ability to conduct heat is termed thermal conductivity (k). In the case of vehicle brakes, the heat generated is both beneficial and detrimental to performance. Brake generated heat provides performance benefits with respect to achieving optimum temperature for disc-pad interaction and heat transfer to tyre rubber for increased grip. Achieving appropriate levels of convective heat transfer is required to maintain a balance between performance optimisation and component durability.

2.3. Heat Transfer in Wheel Assemblies

Heat transfer is of particular importance for performance optimisation of vehicle braking systems, given the heat energy dissipated by the disc-pad contact can generate rises in temperature between 300-800degC in the disc (Belhocine & Bouchetara, 2012). Heat generation occurs from an energy conversion, mechanical to heat energy, by means of the friction between the brake pad and disc surfaces (Ratamero & Ferreira, 2010). The frictional heat generated does not remain within the brake assembly, but is dissipated by means of conduction to parts within the brake assembly, by radiation and convection. Further detail on the heat transfer of the braking system will be discussed in 2.3.3.

A particular intricacy of cooling in braking systems is that of radial cooling within the disc vanes – the channels that run from the outer to inner diameter of the disc to channel air and induce cooling.
disc ventilation design was investigated by Lopez & Tirovic (2012) through the variation in disc vane design to maximise convective heat transfer characteristics; 90% of the heat produced is absorbed by the disc (Ratamero & Ferreira, 2010), a result of the typical brake disc's thermal conductivity being higher than that of the brake pad's (Belhocine & Bouchetara, 2012).
Results from a study by Jancirani et al. (2003) involving the analysis of a heat transfer simulation of a vehicle braking system and experimentally collected heat transfer data, were found to be comparable. Heat transfer analysis of thermally influential systems, such as that of the braking system by Jancirani et al., can provide time sensitive thermal data useful in the design of efficient thermal management systems.
With respect to the importance of heat transfer in braking systems, brake disc performance is dependent on its sustained capability of withstanding thermal stresses during braking, with heat conduction occurring between the brake disc and pad due to friction; causing heat to be dissipated by means of convection (Jancirani et al., 2003).

The braking system also plays an influential role in the temperature experienced by the tyre, with heat transferred from the brakes into the rubber.

Kato et al. (2009) conducted investigations into the numerical prediction and experimental complement of the determination of tyre surface HTC, resulting in a modified tyre sidewall design to increase convective heat transfer, a useful tool given that excessive increase in temperature increases the degradation of the tyre. It was found that an optimal rib design on a tyre sidewall would create a turbulent flow along the sidewall boundary, increasing the convective HTC. This led to a decrease in temperature of 16degC, consequently increasing the life of the tyre by 50% after only 600seconds.

The effect of modified sidewall geometry on the heat transfer by Kato et al. (2009) identifies the sidewall as a region of interest, particularly given the variation in geometry as a result of deflection from loading. The experiments conducted in this study, however, used a non-deformable 50% scale F1 tyre, as such, no loading was placed on the tyre; zero loading results in the absence of sidewall bulge and circumferential deformation, particularly at the contact patch, therefore providing a slightly different flow to that which would be experienced with a pneumatic tyre. Deformation within a tyre introduces jetting and through-hub flow variations, rendering its inclusion as beneficial to intricate flow detail. The effect, however, is most severely implicated on the downstream wake of the tyre (Sprot et al., 2011) rather than around the sidewall – the area of measurement in this study.

2.3.1. Factors Affecting the Level of Heat Transfer between Components

The study and design of ribbed tyre sidewalls by Kato et al. (2009) is an indication of the effect of aerodynamics on the level of heat transfer within a system. Oncoming flow will vary depending on aerodynamic component design forward of the tyre, and the presence of flow disturbances upstream of the vehicle; in racing this is generally exhibited by turbulent flow from a leading vehicle. Any flow variation toward the wheel will also affect the flow onto the braking system; the key system of heat generation within the wheel assembly.

The effect of internal flow on the heat transfer experienced by the braking system is emphasised through the findings of Sakamoto (2004), who performed studies on the effect of flow on railway brake discs as a means of evaluating the heat convection. The work, primarily focusing on the basic equations for heat convection, concluded that the exponential cooling term was the most influential factor of heat transfer within disc design considerations, with respect to convective area and the HTC. Furthermore, investigations by Palmer et al. (2009) into the variation of disc vane designs, such as the use of pin/diamond shaped features to increase the rate of convective heat transfer, indicated that in a three-tiered pin-feature design (Figure 4), the first row has the most significant effect on the flow field, given it directs the flow through the remainder of the ‘vane’. This has a cumulative effect, carrying through to the mass flow rate and heat transfer rate. Overall, the pin-vented disc showed an increased HTC due to the increase in turbulent flow (Palmer et al., 2009); the same reasoning behind the increase in HTC found by Kato et al. (2009) in the ribbed tyre sidewall design.

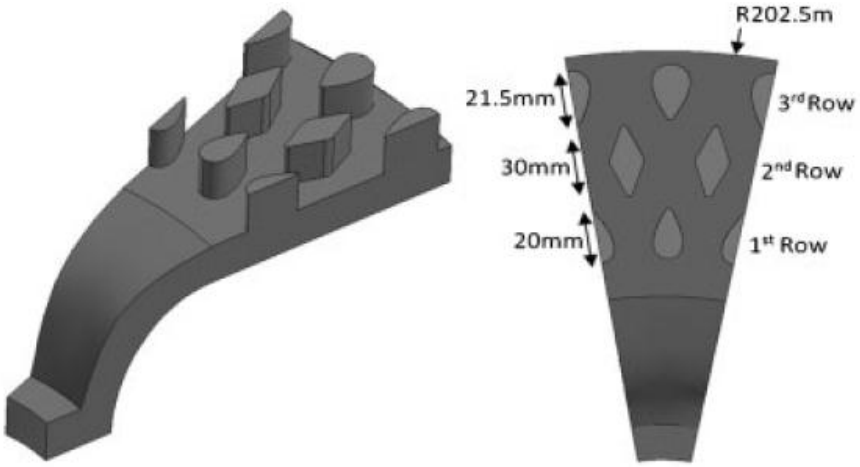

Figure 4: Geometric outline of three-tiered pin-feature design (Palmer et al., 2009).

2.3.2. Heat Generation

Before being able to create an accurate computer generated simulation, the components of heat generation within the wheel assembly must be identified. The understanding of temperature is necessary given the negative effects on performance that are incurred by any material operating at temperatures higher than their optimum.

When considering tyre heat generation, there are four key factors that must be measured, the heat generated by the tyre through friction and rolling resistance, the heat being generated from the braking system, the heat lost through convection and the heat transferred by conduction. Tyres generate heat internally throughout their layers, but are also influenced by environmental factors such as cooling by oncoming air, therefore resulting in a continuous heat exchange - the thermal origins of tyres are outlined in Figure 5.

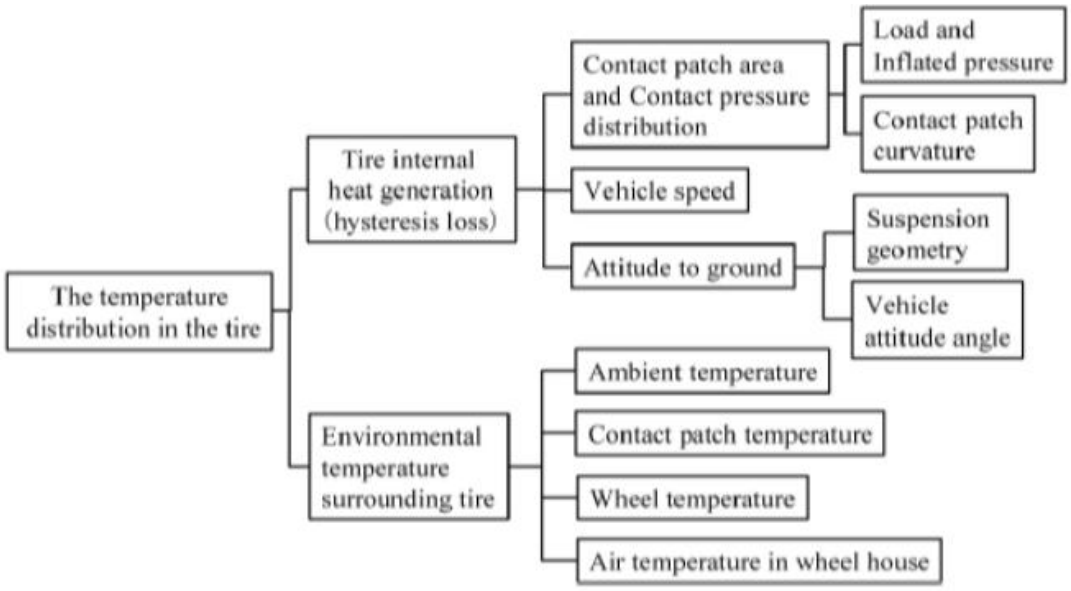

Figure 5: Thermal origins in tyres (Yokota et al., 2012).

Though influenced by inflation pressure, the thermal behaviour of a tyre is dominated by external effects as a result of the inner surface of the tyre being solely in contact with the zero-velocity inflation air, hence, the heat transfer on the external surfaces of the tyre is more significant (Clark, 1976). Heat transfer on the external surface is a result of both temperature generation, and temperature reduction; generation through friction and hysteresis, and cooling due to convection to air. Vehicle handling is influenced by tyre temperature, which is also affected by the heat generated as a result of the material viscosity (Kato et al., 2009), the subsequent hysteresis causing rolling resistance, and by the heat transfer to ambient air.

A typical schematic of the viscoelasticity of a tyre (Figure 6) shows that, during a rolling tyres life, cyclic loading (Figure 7) generates heat due to the hysteresis in the material, and, without the occurrence of convective cooling, would continue increasing until a point of failure. The rolling resistance of a tyre is therefore a key component of heat generation, and an important characteristic defining the longevity of optimal performance windows.

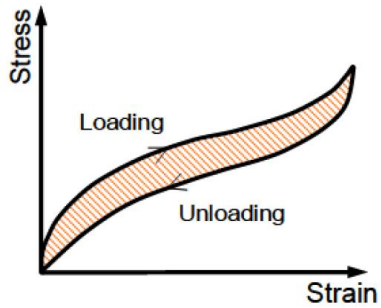

Figure 6: Graphical representation of the viscoelastic nature of rubber (Yamaguchi et al., 2008).

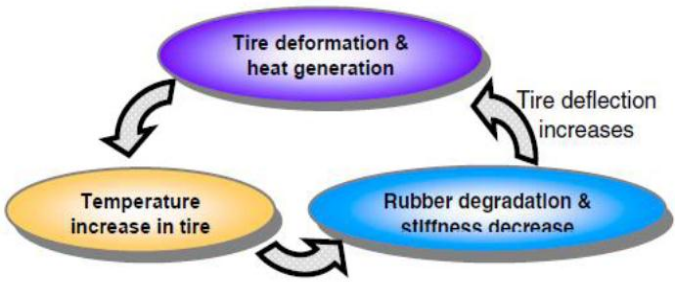

Figure 7: Cyclic interaction between tyre deformation and temperature (Yamaguchi et al., 2008).

Rolling resistance is a measure of the energy lost as the tyre temperature increases due to the hysteresis of its rubber and chord (Song et al., 1998). The cyclic deformation in Figure 6 introduces stresses into the system, with the tyre constituents acting as springs, producing energy through movement, resulting in energy losses in the form of heat (Clark, 1976). Assad et al. (2008) investigated the dependency of the HTC on temperature by varying load; increasing load increases the rolling resistance, a product of the dimensionless rolling resistance coefficient and normal force (load). The cyclic loading of the tyre, given the elastic nature of rubber, is present under zero loading conditions, however, loading will induce change to the strain energy, therefore varying the heat energy. The tests, however, were not long enough to reach steady state conditions, behaviour indicative of the HTC's temperature dependency. Experiments conducted for this thesis used a un-loaded rigid tyre,

avoiding effects of non-uniform deformation of the sidewall in order to establish the baseline heat transfer across the sidewall.

The heat generation, however, is not just a function of the rolling resistance, but also of the frictional interaction with the road (Beringer et al., 1987).
Frictional heat is generated in applications where sliding occurs between two surfaces, however, in the case of highly deformable materials, such as rubber in tyres, there involves a factor of wear which becomes detrimental to performance (grip); thus highlighting the importance of understanding heat transfer within a wheel assembly. During braking, energy is converted to heat through the braking system due to frictional interaction, whereby c90% of the energy is absorbed by the disc, and the remaining 10% by the pad (Ratermo & Ricardo, 2010). The convective cooling of brake discs is an important phenomenon which influences the long term durability of the disc, much the same as the tyre's rate of wear and optimum performance window (Nutwell & Ramsay, 2009). In order to construct an accurate formulation which reflects the split of heat absorption between road and tyre, a coefficient is utilised. Such an approach was implemented by Yavari et al. (1993), who produced [4].

$$Q = \alpha . \mu . v . P \quad [4]$$

Where, 'α' is the coefficient used to describe the split of heat transfer between the two components.

The disc also undergoes convective cooling and internal conduction with other components, particularly those in close proximity such as the mounting bell – used to mount the disc onto the hub. This can be assimilated to the contact between road and tyre, whereby the tyre will absorb most of the energy, and the remainder by the road. The wheel will then dissipate the energy through convection and conduction internally, heating the air inside the tyre. The road left behind will cool naturally reaching almost ambient conditions. For continued braking time, the surface temperature of the disc increases proportionately with time (Jancirani et al., 2003), making it difficult to maintain heat between braking events; highlighting the importance of heat transfer.

A study by Belhocine & Bouchetara (2012) using two modes of braking (Figure 8), one with repeated braking, and one with idle time between braking instances, was undertaken to determine the effect on disc temperature through repeated cycles, and the ability of the disc to return to ambient temperature.
Results (Figure 9) indicate that in both cases, the temperature rises with the number of braking instances, each resulting in an increase upon brake application, and an exponential decay upon release. The initial state of the disc changes after each braking cycle, where maximum temperature continues to increase given the brake release period only allows partial cooling.

Drive cycle 1, with no extra idling period, shows the disc's cooling capacity due to free rotation is insufficient to lower the surface temperature to near initial temperature, causing an accumulation of energy and therefore a higher surface temperature (Belhocine & Bouchetara, 2012). The transient thermal behaviour of a disc

therefore depends on the braking cycle imposed; tyre temperature generation due to friction follows much the same pattern. The higher the rotational velocity of the tyre, the less time a singular tread element has to cool (i.e. the time when a certain point is not in contact with the ground, is decreased). This would continue to increase until the ultimate maximum temperature was reached, however, in the case of tyres, where the material deforms plastically, temperature gradients are more complex with wear rates. Temperature will not increase/drop constantly, but will be dependent on tread thickness, road surface roughness etc.

Belhocine & Bouchetara (2012) saw a reduction of brake temperature of approximately 45.9% in drive cycle 2 compared to drive cycle 1. Given a tyre will always be in contact with the road, it would not have the same sort of effect as there will always be frictional heat generation. In fact, under braking, more heat will be transferred into the tyre from the braking system and there will be increased frictional heat generation between tyre and road given the increased loading on the tyres. The level of cooling capability will further decrease as the velocity of oncoming air decreases under braking. The complexity of the situation is testament to the benefits of computer simulated heat transfer, as drive cycle simulations may benefit developmentally from such resources.

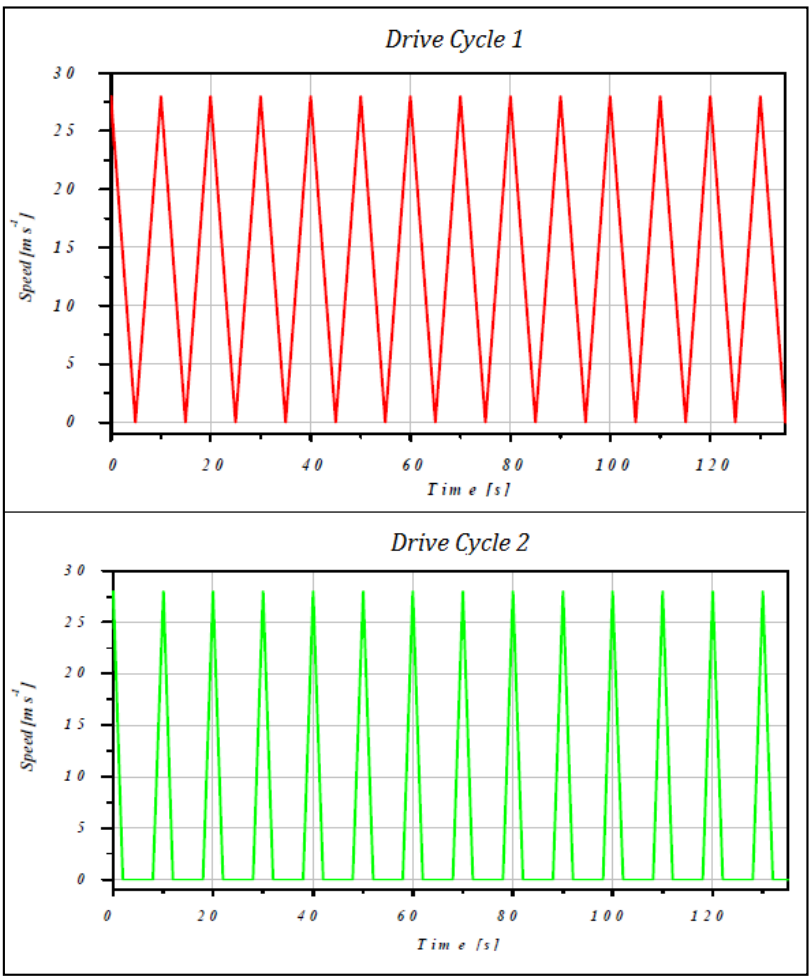

Figure 8: Drive cycle 1 – 14 repeated braking instances & drive cycle 2 – 14 braking and idle instances (Belhocine & Bouchetara, 2012).

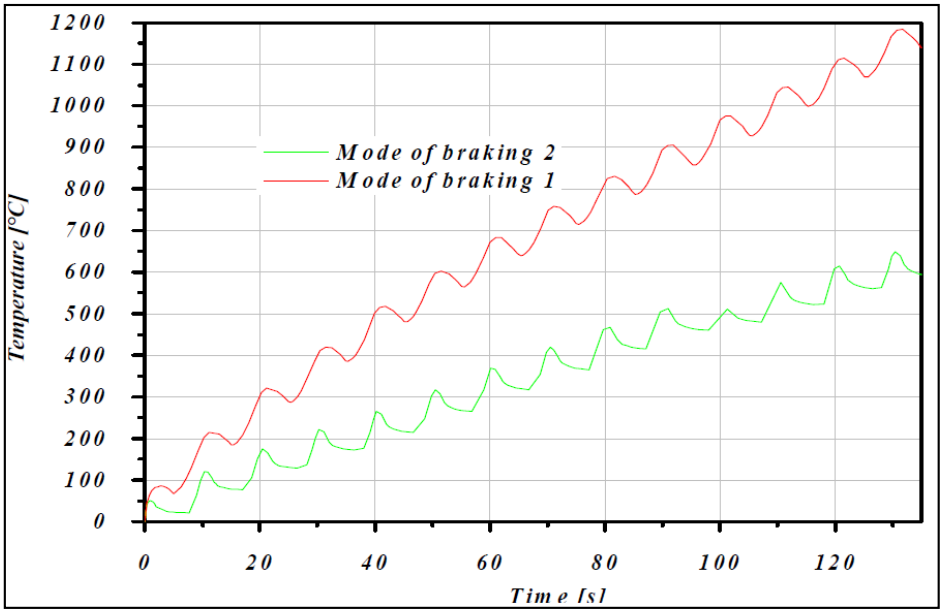

Figure 9: Temperature generation curve during braking cycles (Belhocine & Bouchetara, 2012).

2.3.3. Heat Transfer Analysis

The importance of temperature management can be visualised through a heat transfer diagram, where it is possible to understand how temperature generation/rejection from one sub-system in a wheel assembly can affect another. Figure 10 was created to outline the heat transfer for three simplified steady-state scenarios; stationary tyre, rolling tyre (constant velocity) and tyre under braking. The analysis considers only main components within the wheel assembly given that this investigation is concerned with the brake disc and tyre sidewall only, where case 1 and case 2 refer to the scenarios investigated in this study.

Case 1 relates to a stationary tyre experiencing oncoming flow, a test that will be conducted to determine the relative influence of tyre rotation and oncoming flow to the HTC. In this case, the tyre is undergoing one form of heat transfer, convection (neglecting atmospheric effects such as radiation from the sun).

Case 2, in which the tyre is undergoing a constant velocity rotation, shows how the mechanical properties of the tyre are influential to its heat development and transfer. The hysteretic nature of the tyre will cause temperature generation and radiation through from the carcass to the internal air. The mechanical properties will also have an effect on the level of heat transferred by conduction between the road and tread. In this case, there exist two mechanisms of heat generation, while convection remains the sole means of heat extraction from the system. In the case where the internal air, inflation pressure, is affected, it must be considered that this will cause a cyclic effect with the amount of heat generated at the contact patch given the contact patch area will transform; this same effect is seen under braking, however, loading under braking will outweigh the effect of internal air pressure differentiation due to heat transfer.

Case 3 represents the occurrence of braking, where a high degree of radiation occurs from the braking system to internal components such as the wheel rim. Further radiation and conduction occur as in the rolling tyre

case. A key consideration is that the convection will be reduced given the retardation of flow under braking, however, the degree of heat transfer may change with increasing temperature differential; this is, however, beyond the scope of the project.

Given the experimental configurations will utilise an unloaded rigid tyre, therefore eliminating frictional heat generation between tyre and road (heat from tyre and wind tunnel belt contact is considered to be negligible), this analysis is solely concerned with the convective heat transfer. Jancirani et al. (2003) found that convection accounts for over 90% of total heat dissipation under braking, the understanding of convective behaviour is therefore essential to maximise heat management. The assumption of solely convective heat transfer within the experimental system is supported by Jancirani et al., whose studies made apparent that radiative heat transfer does not occur at low temperatures.

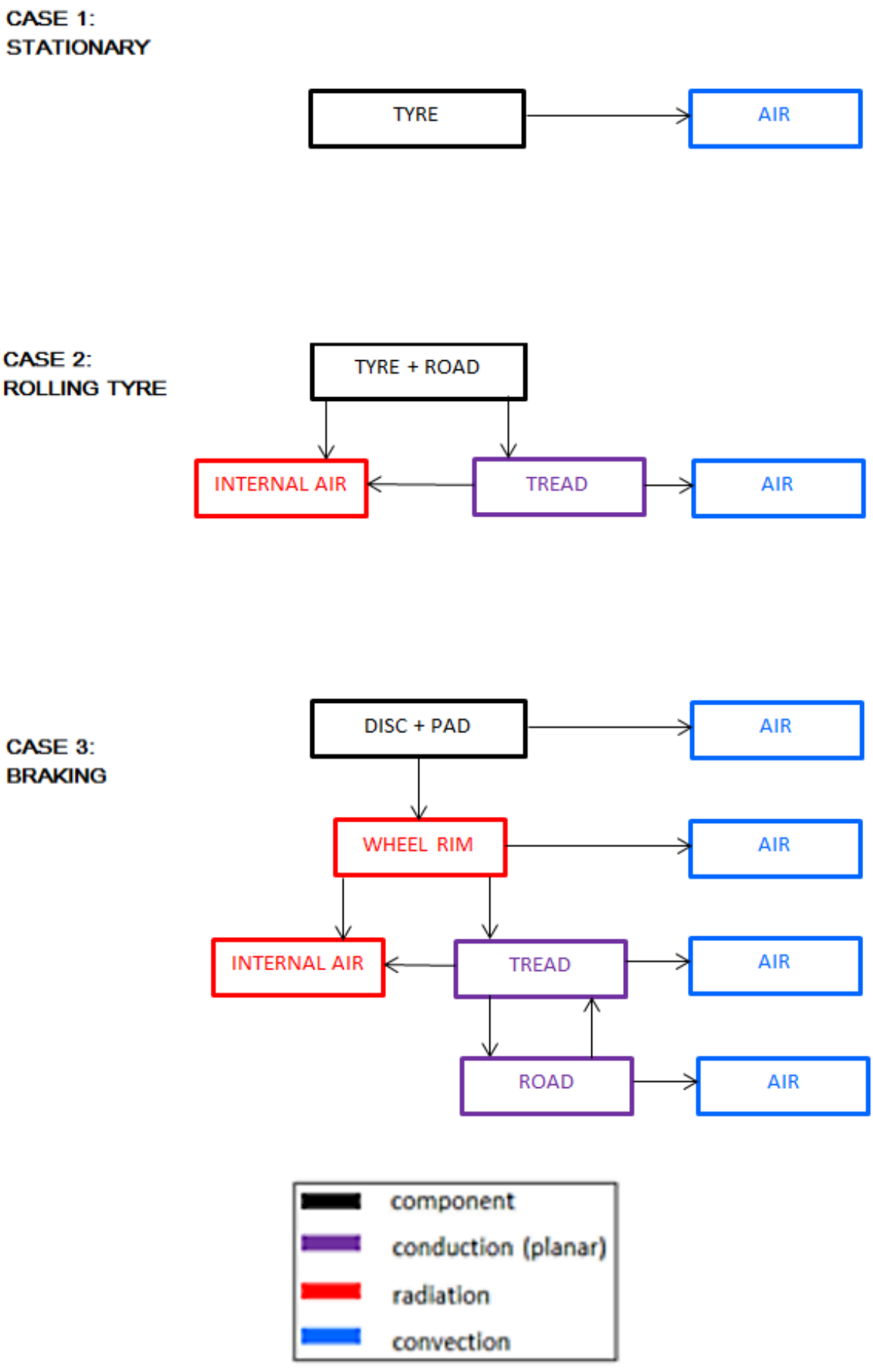

Figure 10: Heat transfer flow diagram for 3 steady state scenarios.

2.3.4. Measuring Heat Transfer

The deformable nature of a tyre renders its cyclic temperature distribution highly variable; depending on running time, braking conditions, ambient conditions etc. For accurate results, it is therefore necessary to make transient measurements. Experimental techniques for the measurement of heat transfer can be flow-invasive, leading to the development of simulated measurement techniques.

Experimental collection of heat transfer data can be split into two main subcategories; sensors and imagery. Temperature sensors are a readily available and inexpensive method for measuring temperature; mountable probes/sensors/cameras introduce a degree of flow disturbance, influencing results in a non-realistic manner (Siqueira & Fragoso, 2003).

Figure 11 shows the typical capture regions of a real-time F1 mounted Infrared sensor and Infrared camera. Configurations of this type are minimally invasive when compared to the use of sensor booms (Figure 12 & Figure 13), but are limited to data collection when the tyre is in a straight-ahead position. The use of booms, though flow-invasive, allows for data collection for a wider range of steering-angles, a beneficial collection method given the temperature variation induced on tyres under cornering/loading. Unlike its sensor counterpart, the infrared camera has a wider capture area, allowing collection across the entire front surface.

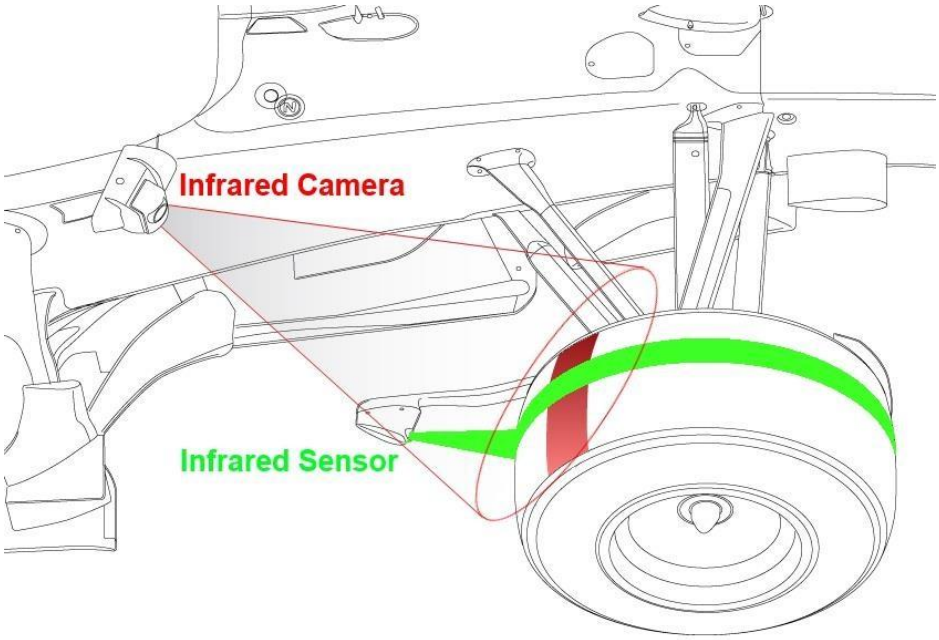

Figure 11: Typical F1 infrared sensor and camera mountings (Scarborough, 2010)[1].

[1] Separate images combined from same source.

Figure 12: 2002 Jaguar F1 infrared sensor boom (Scarborough, 2010).

Figure 13: Williams F1 external measurement boom (Scarborough, 2010).

Experimentally, infrared technology has been used in a variety of wheel related applications such as the investigation by Kato et al. (2009), who used topographical infrared thermography to measure the temperature variation of a film heater in varying flow conditions (Figure 14), with which they were able to calculate the HTC. A similar approach was taken by Siroux et al. (2001), whereby temperature measurements were taken for a heated disc (electrical resistance simulating frictional heat dissipation) by an infrared camera, and were then used to numerically solve for HTC's.

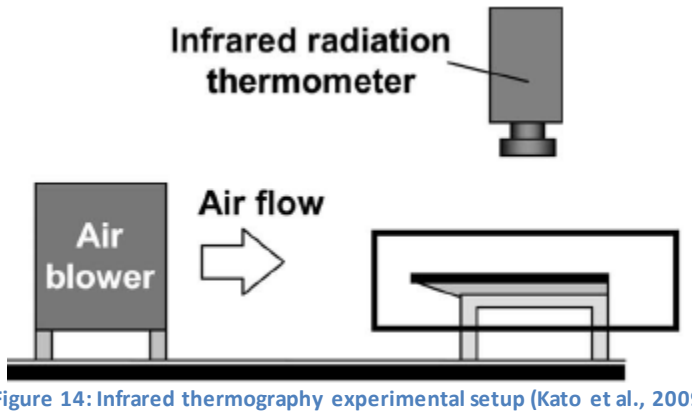

Figure 14: Infrared thermography experimental setup (Kato et al., 2009).

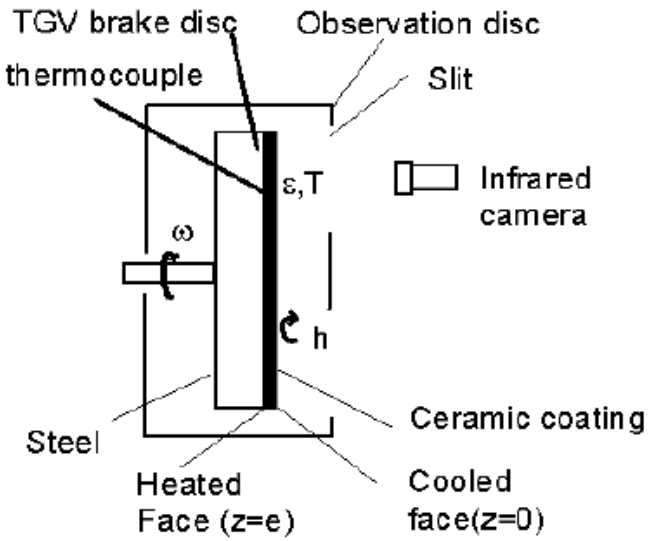

Figure 15: TGV Infrared Thermography Experimental Setup (Siroux et al., 2001).

Both approaches used infrared thermography as a means of obtaining temperature data to determine the HTC as the heat input was known. A different measurement technique was undertaken by Rae & Skinner when measuring the velocity distribution inside a rolling tyre, whereby numerical modelling of the flow field was used to relate heat transfer to the velocity distributions (Rae & Skinner, 1984). This approach, however, utilised hot film anemometry as a measurement technique, with a three-wire probe mounted in a bushing in the rim of the tyre.

While much of the reviewed literature has concerned measurement of temperature, there is little reflecting the measurement of convective heat transfer. As such, a combination of the presented methods were utilised for this study, with the use of constant temperature hot film anemometers to measure resistance variations with applied air-flow, combined with numerical post-processing to determine the convective HTC's; a useful addition to the existing body of work concerning temperature. Much like Rae & Skinner (1984), the hot film sensors were mounted within the wheel assembly, inside a disc vane in a rapid prototyped disc, or on the tyre sidewall; given the disc is the internal component most likely to experience the most heat flux. The use of hot film anemometry allows the flux to be understood, rather than just the temperature; a more accurate analysis tool with respect to heat transfer. Further details regarding hot film anemometry will be discussed in 2.4.

Despite the limitation with regard to flow-field disturbance, realistic environmental data acquisition provides an accurate representation for temperature/heat transfer analysis, given the rest of the vehicle is providing its natural influence over the area of interest (i.e. aerodynamic flow variation from upstream components). Experimental testing and numerical analysis are also imperative for validation of simulated models (Siqueira & Fragoso, 2003).

Simulation is an important development tool in disciplines where experimental testing is inefficient; time and cost. Simulated data recording does not impose flow disturbance, and simplifies the measurement of varying heat transfer, allowing for transient analysis in locations that would otherwise be inaccessible in experimental

testing (Jancirani et al., 2003). In motorsport, simulation of wheel assemblies is favoured given the limitation to the availability of tyres and their plastically deforming nature. This thesis combines the use of computer simulation as a means of developing a rolling tyre heat transfer distribution, an otherwise expensive and timely test configuration when testing design variations of aerodynamic components which affect the flow fields on and around a wheel assembly. Validation of the simulation will be done through the experimental collection of convective heat transfer coefficients.

Heat Transfer Coefficient

When looking to evaluate a heat transfer scenario, the convective heat transfer coefficient provides a quantitative overview of the heat transferred between a given surface and fluid; proportionality of heat flux (q), and surface-fluid temperature differential (ΔT) (Kurganov, 2011).

General consensus over the function of the convective heat transfer coefficient is of its dependency on wheel rotational speed (Beringer et al., 1987), and the consequential air-flow circulation (Belhocine & Bouchetara, 2012). Wheel assembly geometries, such as that of the braking system, will thus affect the HTC.

An investigation by Browne and Wickliffe (1980) outlined the effect of several experimental variations on the convective HTC. The dependence on velocity is supported by their findings, which show that the magnitude of the convective HTC is primarily influenced by the thickness of the thermal boundary layer and the nature of the flow. The apparent association with HTC measurements and wind speed velocity gives reason to conduct tests within this thesis at various wind speeds.

Figure 16 shows the transition from laminar to turbulent boundary layer flow occurs at the low end of the speed range, with the transition from trailing measurements beginning at a lower velocity than those from the leading ones (Browne & Wickliffe, 1980). The lower HTC values toward the rear of the tyre, as for any object, are a cause of the increasing thickness of both hydrodynamic and thermal boundary layers; inhibiting heat loss, thus decreasing the HTC (Browne & Wickliffe, 1980). Given the dynamic nature of the two experiments within this study, the cyclic positioning of the sensor allows for a more comprehensive analysis of HTC in varying flow windows.

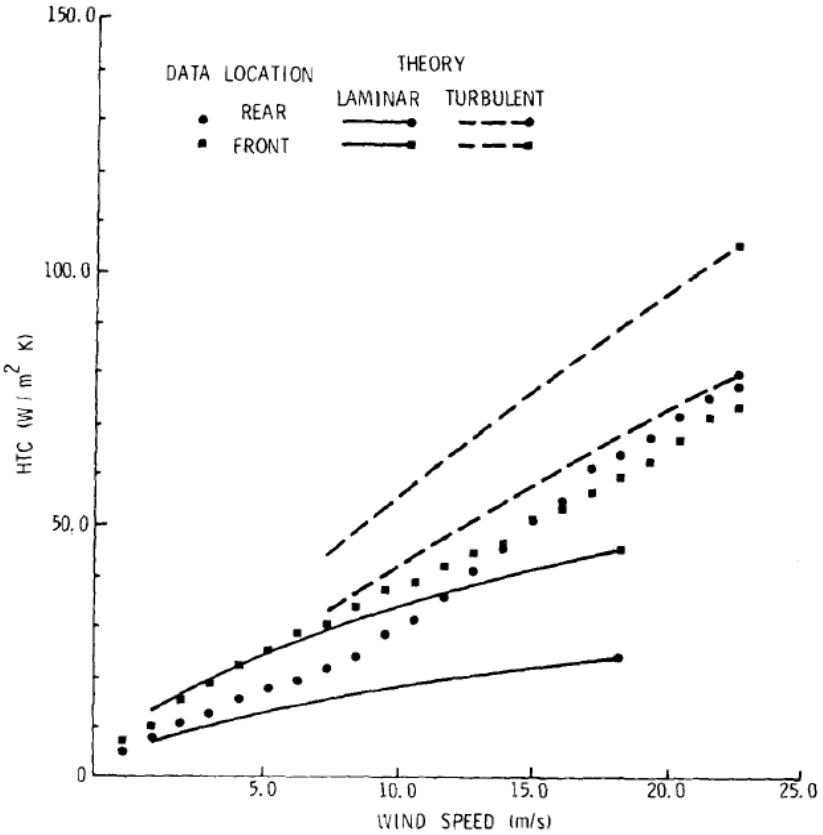

Figure 16: Dependence of HTC on velocity and position (Browne & Wickliffe, 1980).

2.4. Hot film Anemometry

Hot film/wire anemometry is a measurement technique based on forced convective heat transfer from a thin heated film/wire, made of a material with temperature dependent resistivity (Laurantzon et al., 2010). An applied electric current heats the film/wire to a temperature above the fluid in which it is immersed, in this case, air, and the heat transfer is measured based on the variation in resistance occurring as a result of change in heat transfer. This heating cycle is typified as Joule heating, whereby the heat released is proportional to the square of the current (Laurantzon et al., 2010). Thermal anemometers are operated under various heat excitation principles; with constant temperature being used within this study. Constant temperature anemometry maintains the temperature of the hot film/wire through management of the resistance by a feedback loop, with the forced convective heat transfer balanced by Joule heating (Laurantzon et al., 2010).

For the experimental configurations in this study, constant temperature anemometry was utilised as it allowed for the measure of heat transfer through relationships of power and velocity (further exploration in 2.4.1), and is known to have a much quicker response time than constant power anemometry (Lundstrom et al., 2007), making it suitable for the application where air flow or tyre rotational speed variations can affect the level of heat transfer.

For constant temperature anemometry, a constant temperature anemometer (CTA) is needed to provide the resistance to the hot film/wire. As with any measurement tool, accurate measurements are achieved through initial calibrations, which, for a CTA, are done against known air velocities (Lundstrom et al., 2007). A CTA provides output data in the form of voltages, which are related to the power lost across the Wheatstone bridge in the sensor (Lundstrom et al., 2007).

2.4.1. Hot Films

Hot film sensors are made of a material with a high temperature coefficient of resistance; usually tungsten or platinum (Shekhter, 2011). The sensor is connected to an arm of the Wheatstone bridge and the other to the variable resistor, balancing the bridge (See 'R2' in Figure 17) under zero-flow conditions. When a flow is applied, the resistance becomes unbalanced, regaining balance through the use of a differential amplifier (Webster, 2000).

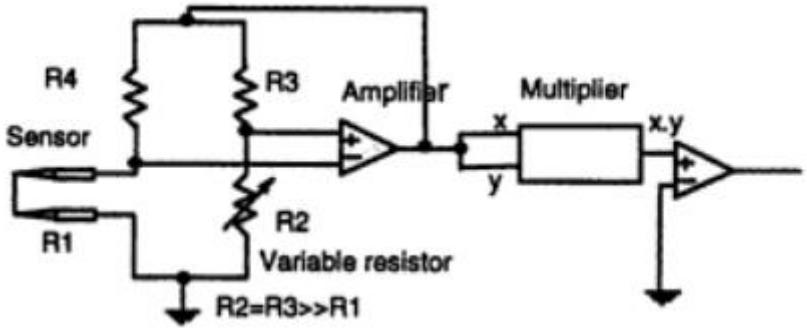

Figure 17: Constant temperature anemometer Wheatstone bridge (Webster, 2000).

Newton's law of cooling [5] outlines the behaviour of heat flux within the hot film sensor with relation to the convective heat transfer coefficient, h.

$$Q = hA\Delta T \quad (\frac{W}{m^2}) \qquad [5]$$

Where, $\Delta T = T_s - T_{amb}$

In an anemometry situation, the heat transferred, Q, is related to $Q_{convection}$, and is equal to the electrical power, P, delivered to the wire (Lundstrom et al., 2007). By rearranging [5] and substituting for P, the heat transfer coefficient can be determined [6] (Lundstrom et al., 2007). The same mathematical formulations are presented by Laurantzon et al. (2010), however, power is expressed as voltage squared over wire resistance (Laurantzon et al., 2010).

$$h = \frac{P}{A\Delta T} = \frac{P}{A(T_S - T_{amb})} \qquad [6]$$

2.4.2. Similar Applications

The application of hot film/wire anemometry extends from motorsport applications to cardiovascular flow studies, and there exists a reassuring foundation of knowledge to the application of hot films for studies similar to that in this thesis.

One of the most resourceful pieces of literature is that of Assaad et al. (2008), who designed a small, flexible sensor that is able to bend with the tyre as it rolls; effectively a hot film sensor that is marginally deformable. The sensor is dual sided, making it capable of measuring temperature and heat flux at both the inner and outer surfaces of the tyre using the same principles of variable resistance measurement as a hot film/wire.

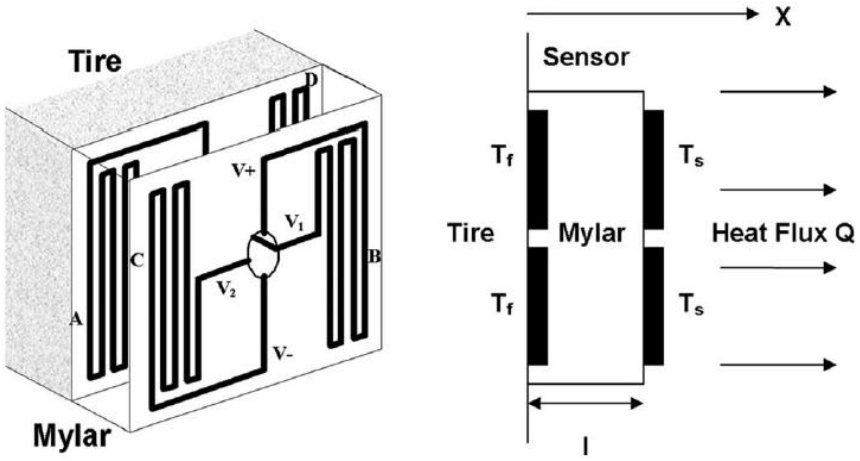

Figure 18: Double Sided Heat Flux Sensor (Assaad et al., 2008).

The use of hot film sensors by a prominent tyre manufacturer (Assaad worked in conjunction with Goodyear) is a strong indication of their accuracy for use as measurement tools. Despite not having access to a double sided sensor, the use of a single layer hot film was employed in the same manner, as it allowed more flexibility to apply to a curved surface, particularly as the tyre used was unloaded. This ensured no damage occurred to the hot film when collecting data for the external HTC. The use of a rigid carbon fibre tyre removes the difficulty associated with collecting HTC data on flexible surfaces undergoing deformation (Rae & Skinner, 1984). As with the experimental testing in this thesis, Assaad et al. (2008) employed slip rings on the motor shaft to pass the sensor wires through the rotating objects to the CTA and data logging equipment. Data acquisition equipment recorded the voltage and current across the bridge, so as to manipulate into useful information, such as HTC's and flow velocities. Lundstrom et al. (2007) followed the same principle of applying a forced convective flow to a tyre and passing an electrical current through the sensor (Hot Wire), with data logging equipment measuring voltages across the wire.

Browne & Wickliffe (1980) investigated the effect of variation of flow speed, boundary layer turbulence (positioning), humidity, surface contamination, surface roughness and wetness. Results showed that recorded HTC varied as follows:

- Rapid increase with increasing air speed
- Rapid decrease with increased downstream distance
- No variation due to humidity for an un-wetted surface

- Decrease due to presence of a smooth surface contamination
- Increase due to presence of rough-textured surface contaminants or sidewall scuffing
- Increased by up to 8x due to surface wetting
- Increase due to raised regions such as sidewall lettering

The increase due to raised regions was also validated through further experimentation, where a test surface mounted flush to the base of a wind tunnel carried a single stack of thermocouples, and 3 stacks on another. Results showed the stacked thermocouples returning higher HTC (Browne & Wickliffe, 1980). In light of the findings, it was noted that testing should be done at various air flow velocities. With respect to the varying air flow velocities, similar tests have found that voltage and current measurements can take up to twenty minutes before stabilising (Assaad et al., 2008). In this study, air flow was provided by an externally applied fan, as was undertaken by Kato et al. (2009). To overcome the possibility of any damage to the hot film, Kato et al. applied the hot film to the sidewall of the tyre (Figure 19). This, however, does not provide an accurate representation of the varying flow during the tyres rotation, as positionally it would encounter varying flow across the span of the sidewall. For this reason, experimental data for this thesis was collected across various sidewall mounting positions in order to capture the complete heat transfer map.

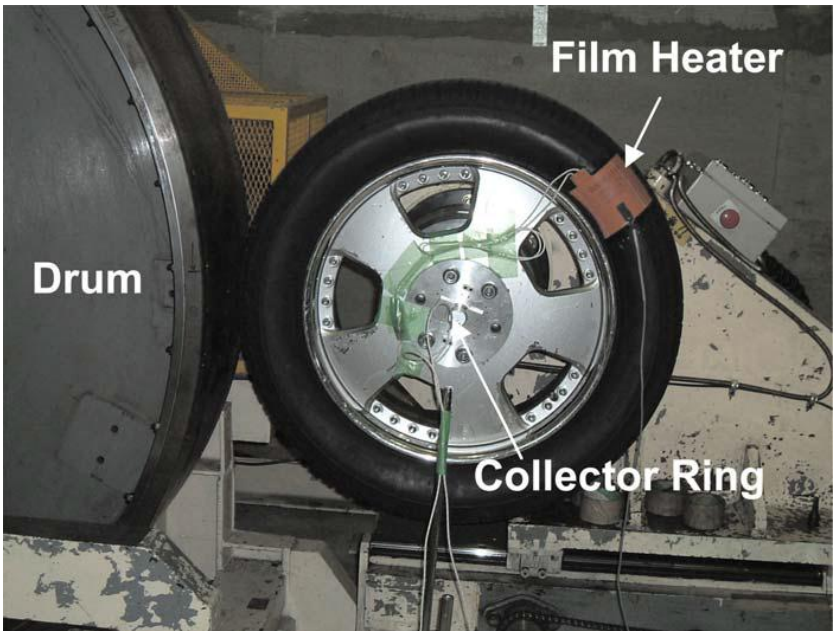

Figure 19: Sidewall placement of hot film (Kato et al., 2009).

However wide the application of hot film sensors and thermal anemometry in the automotive and motorsport industry is, much research has been done, particularly with braking systems, using other measurement apparatus such as thermocouples, infrared thermometers and infrared thermographs.

Ratamero & Ferreira (2010) undertook experimental work heating brake discs using electrical thermal sources, measuring localised temperature using thermocouples. This is similar to the work done by Kato et al. (2009) on the tyre sidewall. Thermocouples were also applied to the brake disc and wheel cover, however, the use of thermocouples provides only localised temperature analysis, neglecting the heat transfer process that occurs

within a complex system such as that of a wheel assembly (Refer to Section 2.3.3). Using hot films to determine the heat transfer provides a better understanding of its behaviour within the system, and, combined with understanding of heat generation mechanisms such as friction, can be used to create simulations that provide a rolling analysis of a dynamic tyre; a more useful tool in the automotive and motorsport industry.

2.5. Wheel CFD

Recent computational investigations used the most up-to-date methods of rotation that were available at the time, however, since the introduction of the sliding mesh (SM) method, involving physical rotation of components, there has been scarce use of any previous methodologies, with leading automotive and motorsport manufacturers utilising the SM methodology where available. Other methods include the velocity boundary (VB), a theoretical velocity applied at the boundary, and moving reference frame (MRF), which applies rotational forces, centrifugal and Coriolis, to the fluid within a bounded region.

SM has shown better correlation to wind tunnel results for aerodynamic force measurements; capable of predicting within 2% of experimental results, while MRF methodologies have been proven to achieve correlation within 5% for aerodynamic force measurements (Kandasamy et al., 2012). The SM's capability of capturing local changes in transient flow (Gaylard et al., 2010), allows for a more precise and iterative calculation dependant on rotational position and velocity. Gaylard et al. were able to capture the variations of the three rotating methodologies through the use of surface flow (Figure 20), surface static pressure (Figure 21), flow velocity (Figure 22) and streamlines (Figure 23).

The surface flow provides a good outline of the distinct variation between the VB rotational methodology, which appears to lack the ability to compute the radial velocity gradient, compared to the more realistic MRF and SM methodologies, which incorporate small-scale flow structures to generate a more accurate result (Gaylard, et al., 2010). Static pressure plots emphasise the observations made surrounding the variation between VB, MRF and SM.

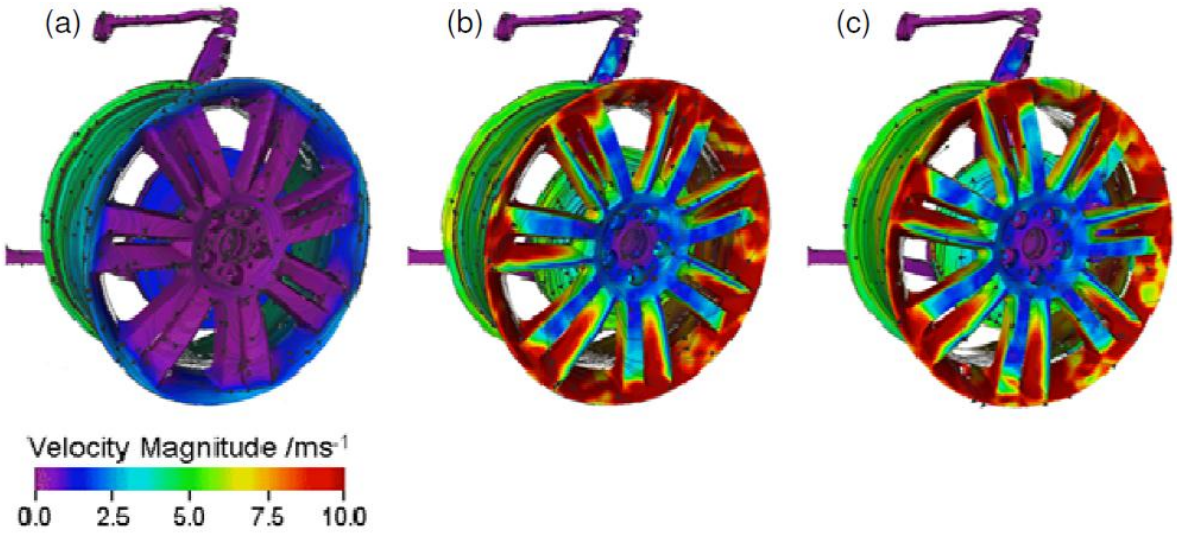

Figure 20: Instantaneous surface flow (a) VBC (b) MRF (c) SM (Gaylard, et al., 2010).

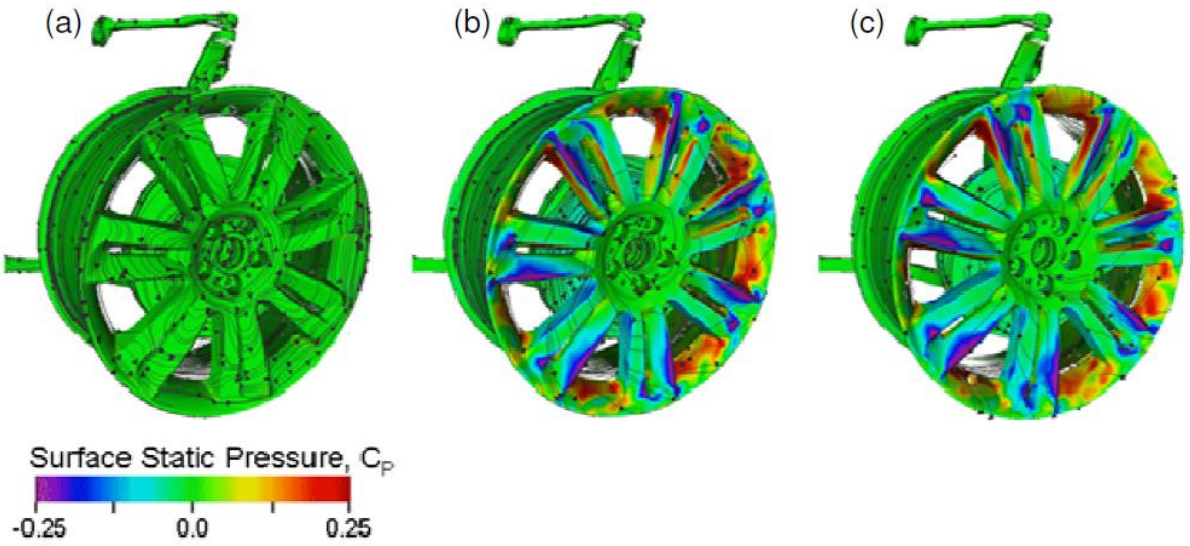

Figure 21: Surface static pressure distribution (a) VBC (b) MRF (c) SM (Gaylard, et al., 2010).

The flow velocity of the VB indicates its inability to accurately describe boundary layer development, with the boundary layer generated solely over the external surface of the rim, while there is evidence of radial flow for both MRF and SM methodologies (Gaylard, et al., 2010). Flow in the SM case is more disturbed, indicating the physical rotation varies the flow by possible induced mixing from the forward rotation of the wheel.

The suction on the outboard face/spokes is evident in the static pressure diagrams, where there exists a high pressure differential. Forced through flow inside the hub is evident on the streamline visualisations for the MRF (b) and SM (c) methodologies; an important consideration with respect to disc heat transfer values.

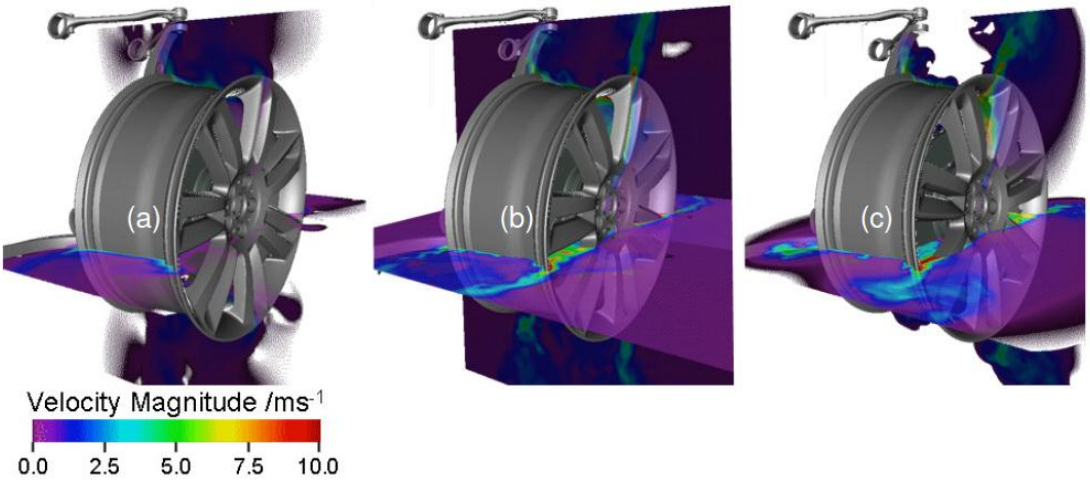

Figure 22: Flow velocity (a) VBC (b) MRF (c) SM (Gaylard, et al., 2010).

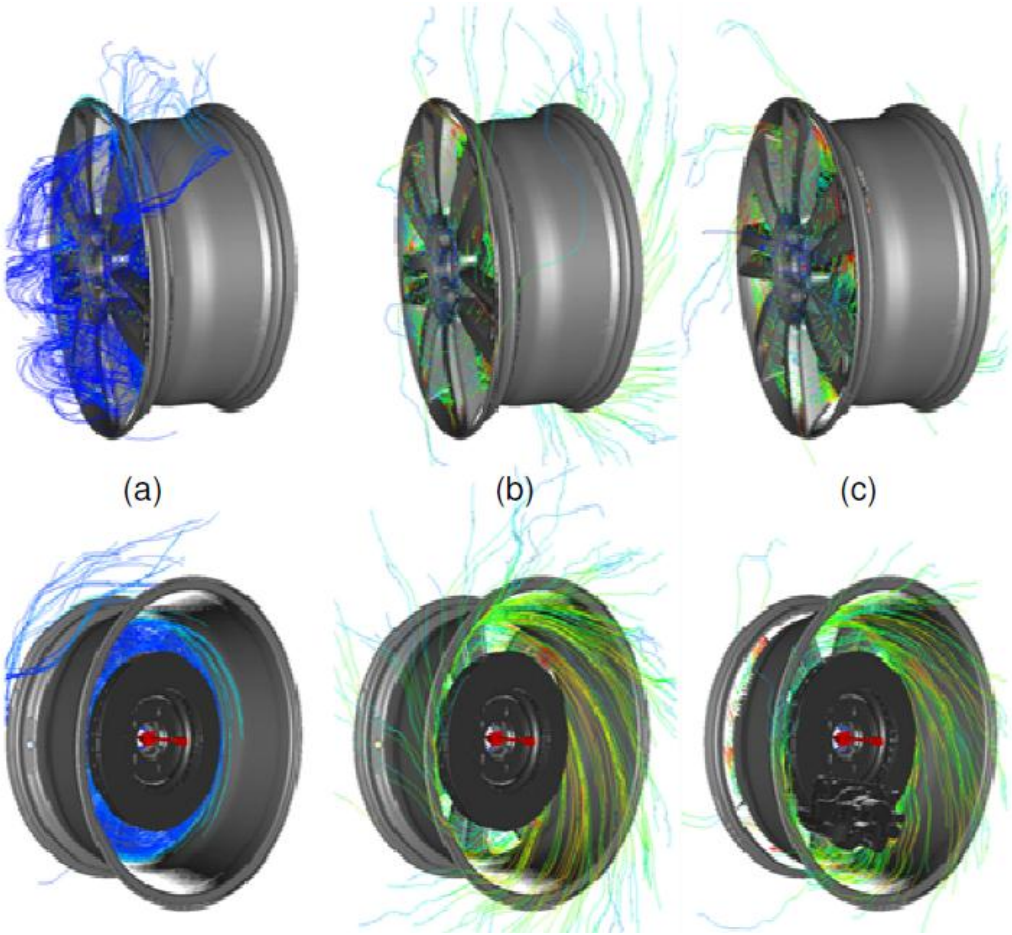

Figure 23: Flow structure (a) VBC (b) MRF (c) SM (Gaylard, et al., 2010).

2.6. Summary

The analysis of rotating wheels has identified that rotation affects aerodynamic characteristics at and surrounding the wheel compared to a stationary wheel, such as the advancement of separation and the suppression of rearward vortex shedding. Convective heat transfer is linked to the aerodynamics of the wheel, however there exists little literature encompassing the heat transfer within aerodynamic investigations, rendering the directed investigation of this thesis useful in complementing the existing body of work. While there have been several previous investigations of temperature distribution within wheel assemblies, the underlying convective heat transfer has seen much less investigation. The heat transfer within a wheel assembly must be well understood in order to achieve optimal efficiency from components such as the tyre, whose viscoelastic nature results in hysteretic behaviour resulting in energy/heat transfer, and the disc, which utilises both conductive and convective heat transfer and reaches extremely high temperature.

The range of rotational methods available within computational simulations has been found to increase in correlation with updated methods, but rotational methods have only been validated in aerodynamic cases. The implementation of the CFD within this study will provide a supplementary evaluation of the capability of the software with regard to determining heat transfer.

3.0. Methodology

The following chapter outlines the three key methodologies used to determine the convective heat transfer; two experimental programs and a CFD analysis.

Both experimental setups utilised hot films as means of determining HTC. A brake cooling rig test with a rotating wheel and an applied flow was used to determine the HTC at the disc, while the wind tunnel utilised a moving ground and a full external flow, and included capabilities to determine the external HTC of the wheel. Experimentally collected data was processed to remove the recorded datum to account for conduction to the substrate. A periodic averaging technique was also used, combining results from multiple rotations to produce cleaner traces. CFD studies using Exa PowerFlow were conducted to supplement the understanding of experimentally determined HTC's by analysing flow characteristics, and utilised to evaluate the ability of the CFD to accurately predict HTC's.

3.1. Geometry

The geometry used the three programmes of investigation—brake cooling test rig, wind tunnel and CFD—utilised the same geometry; a 50% Scale model wheel assembly of a 2005 F1 race-car.

In order to design the necessary components for experimental configuration, and to undertake CFD simulations, the geometry was modelled in the Solidworks CAD package (Figure 24). The main components analysed in this thesis were the tyre, wheel rim, disc and upright (Figure 25).

Figure 24: 50% Scale model CAD geometry (Translucent tyre for visualisation purposes only).

Figure 25: Upright CAD geometry (Translucent sidewall for visualisation purposes only).

The upright consisted of complex internal curvature (Figure 26) that could not be entirely measured. The internals of the scoop are important features as the air entering the scoop will follow the path of the internal geometry, which will affect the flow speed. As much detail as possible was collected for the model, however, any irregularities within the CFD may be attributed to the difference of internal geometry between the physical and CAD models. The degree to which this will affect results, however, should not be concerning as the resulting flow rate through the upright will be consistent for each simulation, providing comparable trends.

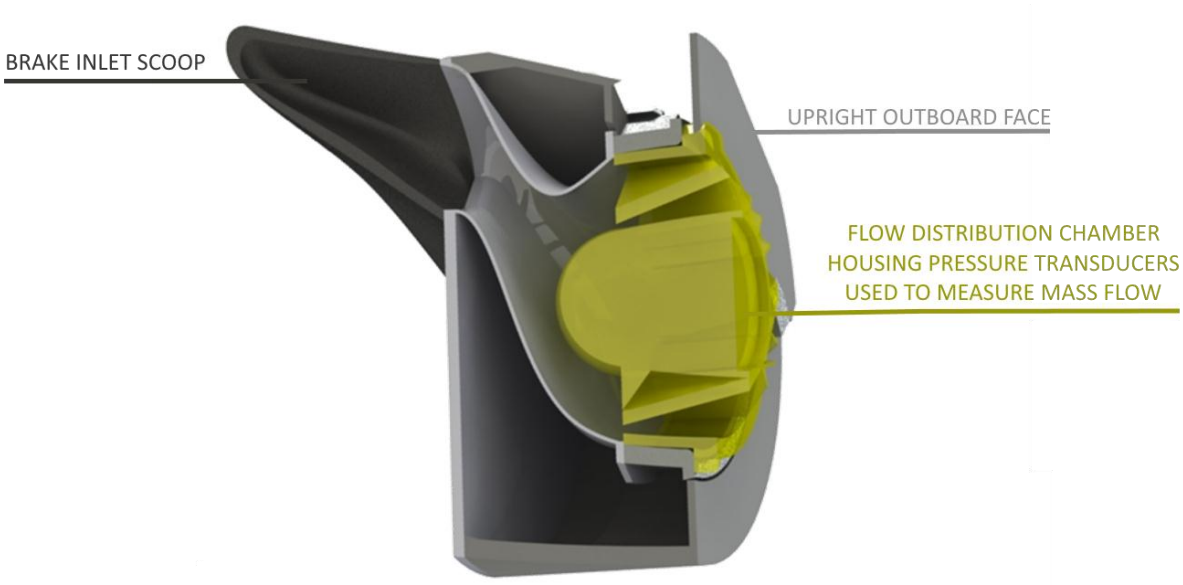

Figure 26: Upright CAD geometry cross sectional view of scoop inlet.

3.2. Motorised rig Test

3.2.1. Test Configuration and Specification

The rig used was comprised of a base frame and variable speed motor (Marelli Motori MA100LA6). The outboard face of the wheel was mounted on the motor shaft, leaving the inboard face of the wheel and upright exposed, allowing for attachment of a fan to provide forced convection from the rear of the upright hub where brake cooling scoops are usually fitted.

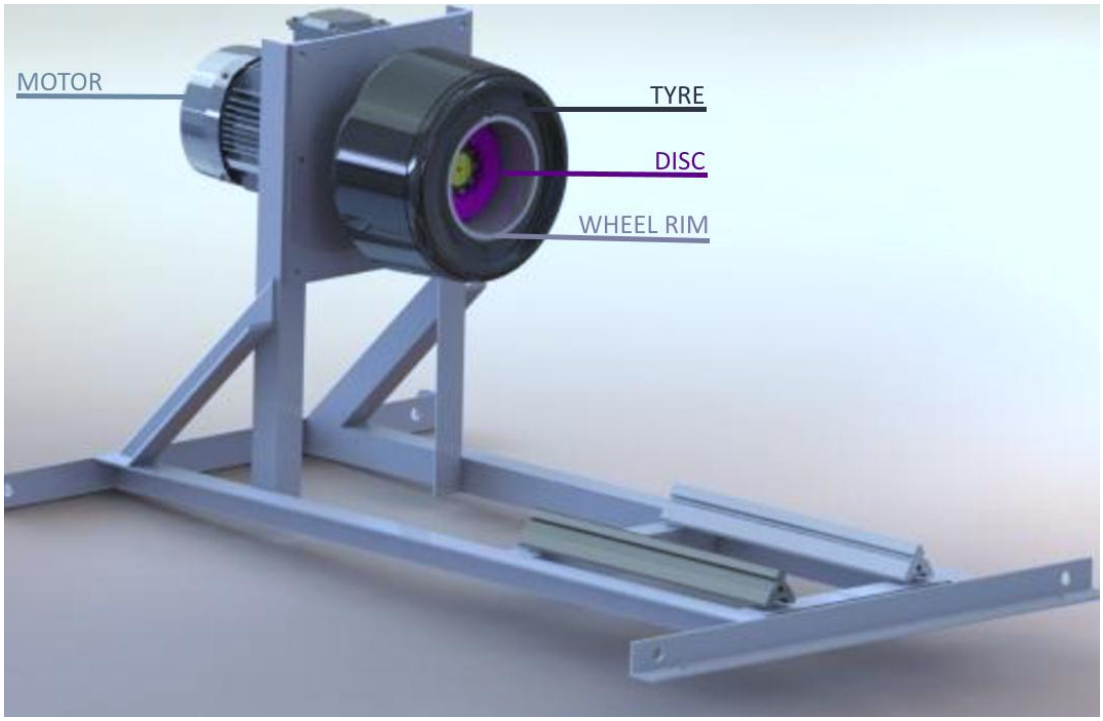

Figure 27: Schematic of rig test and the 50% scale tyre, rim and disc (Image and existing rig from Ng (2013)).

As part of the complete vehicle scale model, the upright relied on the suspension being attached to the model spine, a rigid mount through the centreline of the model) (Figure 28). A method of mounting was therefore developed to hold the upright inside the wheel rim and attach to the existing rig.

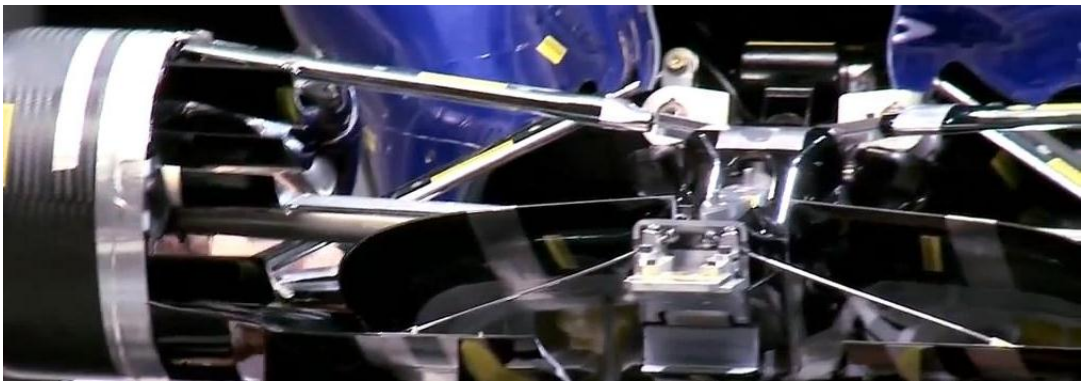

Figure 28: Example of F1 scale model suspension mounting points on the model spine (Screenshot taken from referenced video) (Williams in 60 seconds: Wind Tunnel, 2012).

The mounting frame was designed with the capability to:

- Suspend the geometry at a height within the wheel assembly
- Withstand the vibrational movement from the motor
- Allow for upright positional adjustability and ease of removal from the wheel assembly

The initial proposed layout of the upright mount can be seen in Figure 29, comprised of four main components; a retaining face plate, two extruded Aluminium struts and two mounting ledges (brackets). The Aluminium struts were connected to the optical rails with a 10mm diameter rod passing through an existing central diameter cut in the strut, and tightened in the optical rail carrier/post-holder. The purpose of the retaining face plate was to ensure that the two struts remain parallel, and to counter-balance any torque created from the mounting of the upright to the opposite side and length of the strut.

Optical rail carriers with level tops were sourced, eliminating the need for stabilising rods. The configuration was then built with a single horizontal aluminium strut as a base to join two vertical struts using Rexroth Angle Joints. Individual brackets were mounted on the vertical struts to allow adjustability in height for all three suspension arms (Figure 30). Contrary to the on-vehicle configuration, the pushrod was mounted below the upper wishbones as it was a more rigid method than if the pushrod were holding the weight of the upright.

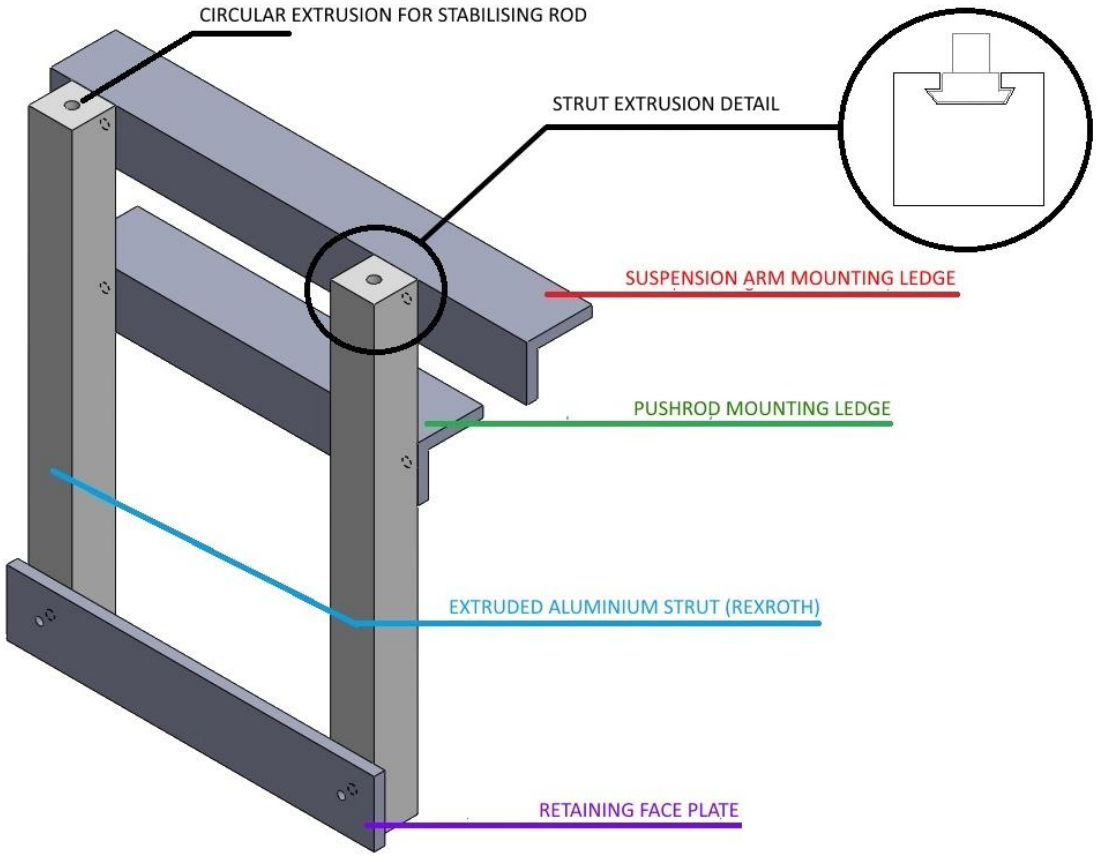

Figure 29: Proposed upright mounting method.

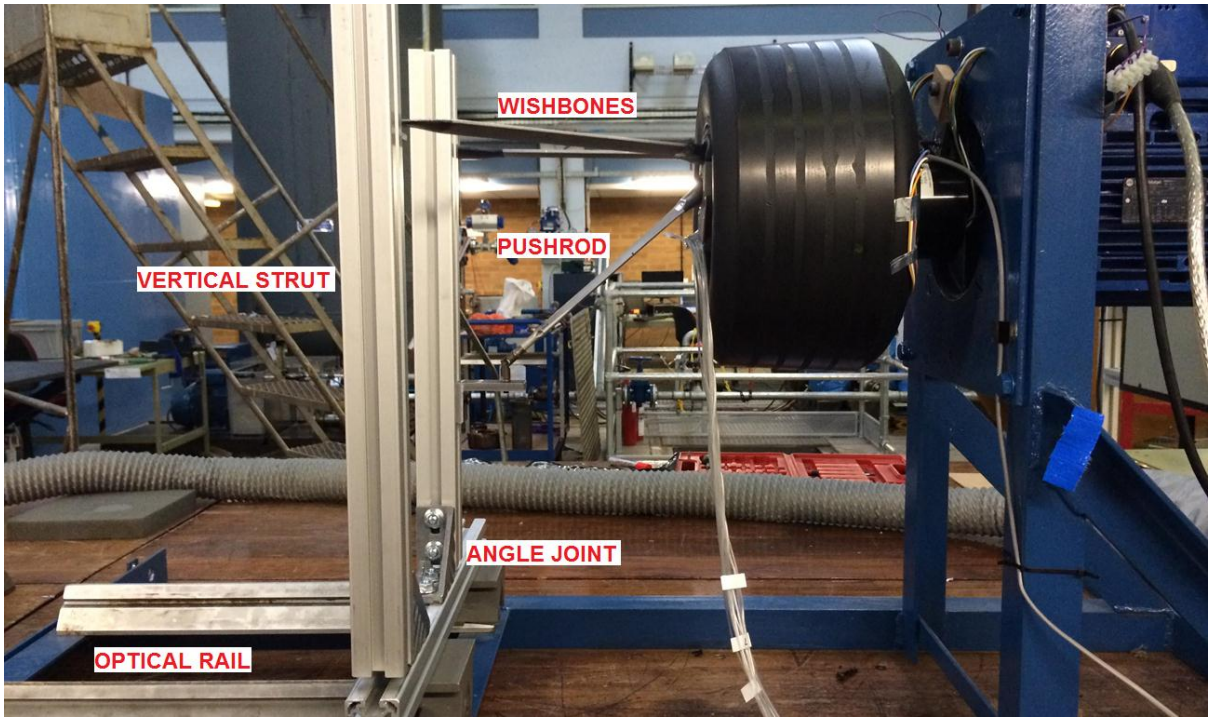

Figure 30: Brake cooling test rig final configuration – Rexroth angle joints supporting vertical struts used to mount the upper wishbones (upper mounts) and pushrod (lower mount).

3.2.2. Orifice Plate Calibration

The following section outlines the standards followed for the calibration of the orifice plate within the fan used in the rig tests. British Standard BS EN ISO 5167-2:2003 outlines the dimensional requirements for an orifice plate (Figure 31), in order to accurately calculate the mass flow rate, q_m [7] (British Standards, 2003).

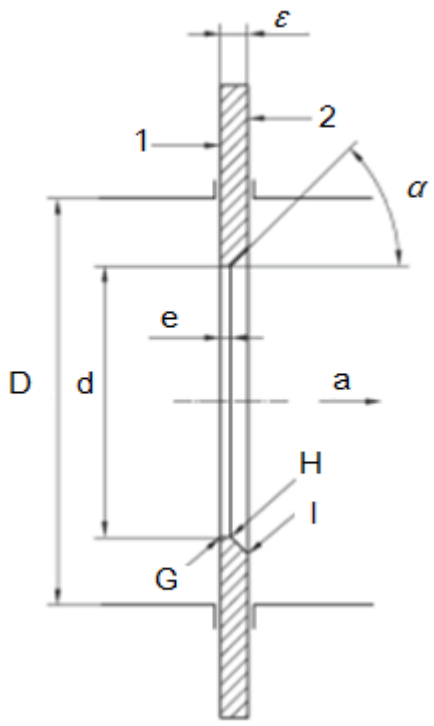

Figure 31: Standard orifice plate schematic (British Standards, 2003).

$$q_m = \frac{C}{\sqrt{1-\beta^4}} . \varepsilon . \frac{\pi}{4} . d^2 . \sqrt{2\Delta P \rho} \quad [7]$$

The orifice plate used in this study satisfied the following requirements, as stated in the British Standard:

- Downstream (2) face is parallel to Upstream face (1)
- Chamfer angle, α = 45 ± 15
- d is concentric with D
- d ≥ 12.5mm
- e < E < 0.05D
- 0.005D < e < 0.02D
- 0.10 ≤ β ≤ 0.75 (where β = d/D)

Given the orifice plate satisfied the dimensional requirements of BS EN ISO 5167-2:2003, the equations and tables within the standard were used in order to calculate the necessary variables required to create the calibration file for the pipe (nozzle); allowing the correct recording of dynamic pressure and air flow velocity. The orifice plate used employed a D and D/2 tapping arrangement (Appendix 4), whereby the upstream pressure tap must be at a distance D ± 0.1D, while the downstream pressure tap must be at distance 0.5D ± 0.002D, given that β < 0.6 in this case (Appendix 5).

Within the BS EN 5167-2 are lookup tables for the discharge coefficient, with respect to diameter ratio, β, and Reynolds number, Re, and also for the expansibility factor (Appendix 6), with respect to dynamic pressure and diameter ratio. The use of lookup tables, however, produced a characteristic curve which did not take into account realistic expansion. It was therefore decided to extract values of the Reynolds number and discharge Coefficient from the tables at the known β value (Figure 32).

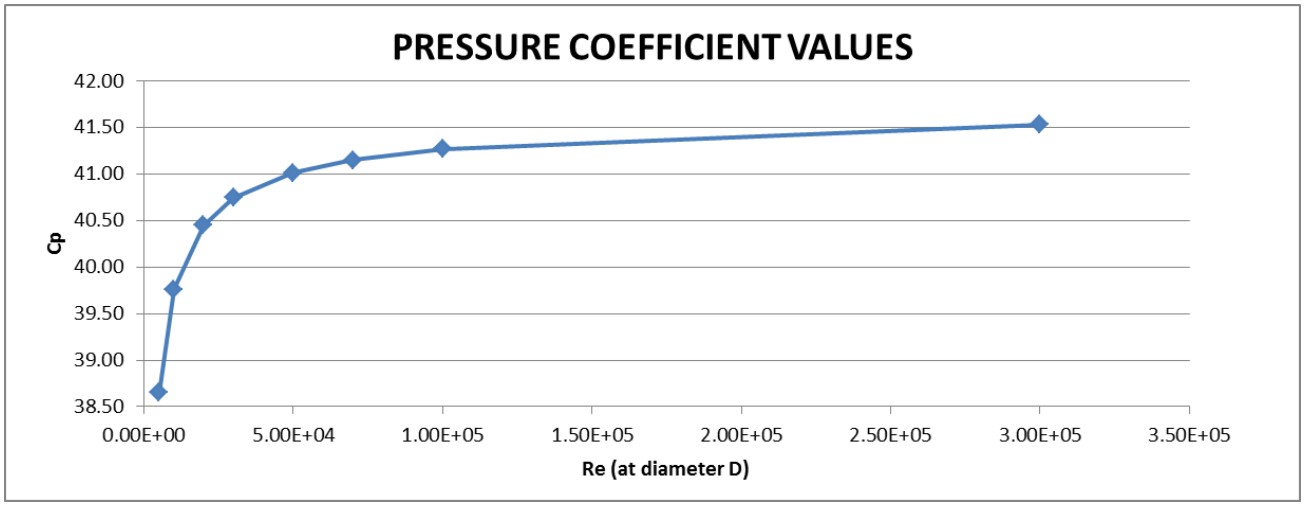

Figure 32: Cp values determined from British Standards tabular data.

The fan pipe consisted of a large pipe of diameter 'D' connecting the fan to the orifice, however, the diameter of the pipe leaving the orifice (D) was half the diameter (d) of the original pipe (D). Calculations were made based upon the larger diameter (D), therefore flow at the smaller diameter fan pipe exit was calculated as a factor of A_D/A_d. Given the small pipe diameter further contracts at the opening of the upright inlet duct scoop, calculations were based upon the area of the upright; the final orifice the flow passed before entering the upright. Given the non-uniform diameter of the opening, it was calculated by compiling a profile trace of on a 1cm^2 grid, with the area calculated at 0.0022m^2. As a result, the recorded velocity at orifice of diameter D = 0.014m, was transformed from a range of 0.2m/s-2.8m/s to 1.6m/s to 20m/s.

3.2.3. Fan Velocity Validation using Hub Flow Number Theory

Further processing was required to evaluate the true velocity as would be experienced by the scoop inlet of the upright where the fan was applied. Despite the previous assumptions that the flow velocity could be assumed to be that of the ratio of pipe diameter to upright area, further investigation revealed that the scoop geometry further accelerated the flow, and should therefore be considered as the final area at which the flow velocity is determined.

Minto et al. (2011) defined the volumetric flux ratio between the scoop and the free-stream velocity as the hub flow number (HFN), which is represented by [8].

$$HFN = \frac{A_S U_S}{A_f U_\infty} \quad [8]$$

$$where; A_s = area\ of\ the\ Inlet\ Scoop\ cross\ sectional\ plane$$

$$A_f = frontal\ area\ of\ the\ model\ taken\ as\ cross\ sectional\ area$$

The HFN was also implemented by Sprot (2013) to evaluate various aerodynamic performance characteristics for an array of wheel fairing designs that varied the hub flow. Minto's equation was applied to the geometry in this study to determine the ratio of equivalent velocity at the scoop to that of the free-stream. Using the calculated values for the frontal area of the tyre, 0.0592m^2, and scoop inlet area, 0.0017m^2, and the relationship devised by Minto et al. [8], calculations showed that the equivalent velocity at the scoop inlet plane was approximately equal to that of the free-stream velocity; indicated by the resulting velocity ratio of 1.0029 (Table 1).

VARIABLE	RESULT	FORMULA
A_S	0.0017m^2	
A_F	0.0592 m^2	=diameter*width
HFN_{OPEN}	0.0288	
U_S/U_{FS}	1.002917647	=HFN_{OPEN}*(A_F/A_S)

Table 1: Speed ratio determination.

3.2.4. Velocity Selection for Analysis

As a result of the fan velocity validation with relation to the findings from Minto's HFN, the velocity range of the fan from the rig test experiment was calculated based on the area ratio of the calibrated fan diameter and the scoop inlet area (Table 2).

Given the results from the relationship by Minto et al. (2011), a velocity range from the rig Test Results was selected that agreed with that of the wind tunnel test range; 0-25m/s. As Reynolds numbers below 2.00E+05 are in the laminar flow range (Cengel et al., 2008), analyses in this study were focused more toward the higher end of the velocity range, with 25m/s selected as the comparison velocity for all tests.

RIG TEST SPEEDS			
	V_{FAN} (m/s) (@ scoop inlet)		V_{TYRE} (m/s)
0	2.1	**0**	2.1
1	22.6	**1**	6.8
2	25.2	**2**	11.4
3	25.4	**3**	16.7
4	25.5	**4**	22.1
		5	24.1

Table 2: Rig test Fan settings.

The two upper tyre velocities tested on the rig were 22.1m/s (Setting 4-Orange) and 24.1m/s (Setting 5-Blue). This agreed well with the wind tunnel tests, where, although the selected velocity was set, underwent slight fluctuations as the tunnel controls aimed to maintain the flow velocity. An average was taken of the fan and tyre velocities across 6 tests in the wind tunnel, results of which (Table 3) showed a good correlation to the rig test velocity (Fan Setting 2, tyre Setting 5), confirming the match between data sets.

	V_{TYRE_AV} (m/s)	V_{FAN_AV} (m/s)
WT	23.9	24.4
RIG	24.1	24.8

Table 3: Comparison of average tyre and fan velocities for WT and rig tests.

3.3. Wind Tunnel Test

3.3.1. Durham University Wind Tunnel

The Durham University wind tunnel was used for all wind tunnel tests for this thesis. The tunnel is comprised of a $2m^2$ open jet configuration with a 3.0 x 1.4m moving ground belt capable of speeds up to 30m/s.

3.3.2. Pre-Process

Configuration

Similar to the rig tests, those undertaken in the wind tunnel also required a method for mounting the wheel to allow for rotation, and a method for suspending the upright into the wheel. The wheel assembly was mounted from the outboard side floor using an existing sting arm, while the upright was suspended inside the wheel rim using a custom designed mount, consisting of a back-plate and brackets designed to fit the suspension arm ends (Figure 33). The lengths of the upright arms (upper and lower wishbones, track-rod and push-rod) varied in length, making any perpendicular mount complex, but suitable given the similarity to the upright's original

vehicle mounting on the model's spine. It was decided to design a vertical backplate mount, utilising various attachments to overcome the differing suspension arm lengths (Appendix 8).

On the wheel side, as with the existing bench test, a rotary shaft was utilised, with attachment to an existing sting-arm using pillow-block bearings mounted to a base plate. Other considerations included the wiring arrangement, slip ring, and connection to the wheel face by the shaft in order to have consistent rotation as there already exists a cylindrical bearing in the wheel nut housing.

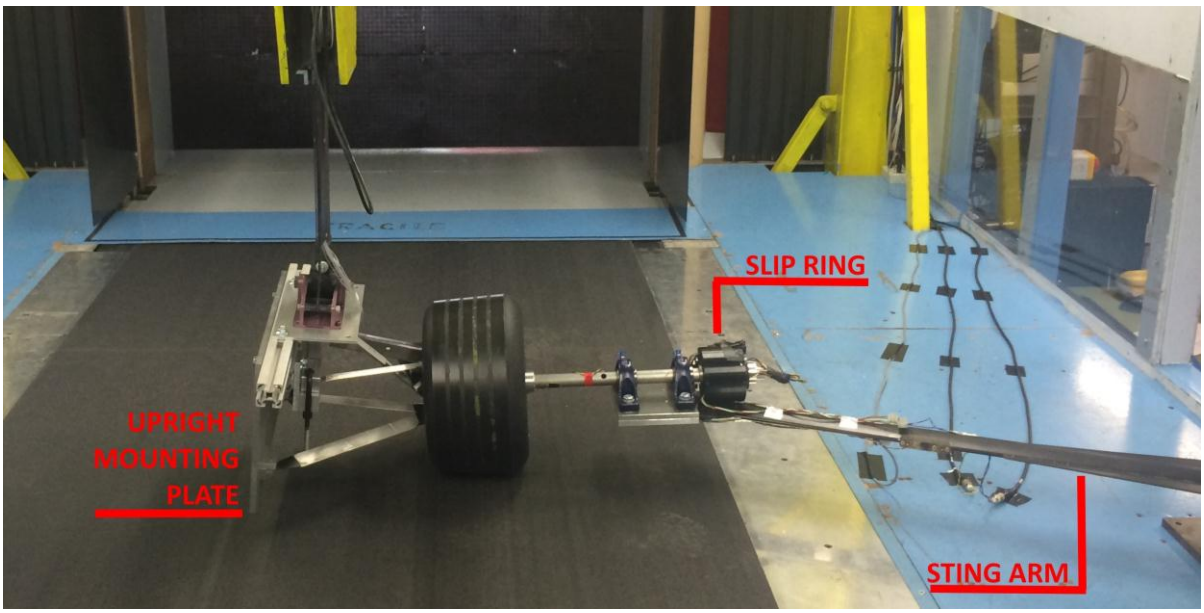

Figure 33: Wind tunnel test configuration using existing sting arm mount and custom upright mounting plate.

The use of hot films in this experiment required wiring to the slip ring from both the disc and tyre sidewall locations. Though the slip ring provided a safe rotational path for the wires, the nature and design of the test required wire routing along the length of the shaft. To solve this problem for the majority of the shaft length, a hole was drilled along the centre of the shaft to a length of 280mm, allowing the non-rotating wires to pass from the sensor to the slip ring with minimal interference with the rotating components. The slip ring used in the rig tests was carried across to the wind tunnel test in order to maintain consistency within results. In order to minimise costs, a smaller diameter than the rig mounting shaft was chosen for the shaft design, resulting in the requirement of a cylindrical adaptor to allow for use of the original slip ring. A similar design was utilised to ensure contact of the shaft to the outboard face of the wheel rim. This was essential to ensure rotational conformity of the shaft and wheel, as the wheel nut housing contained a bearing that would otherwise have disrupted rotation.

Data Collection

The data range collected throughout the experimental wind tunnel procedure covered two sub-categories; experimental data and wind tunnel data.

After calibration, hot film voltage for both sensors was recorded to determine the HTC, alongside with the voltage of the optical sensor, which was used to track hot film positioning throughout the tyre's rotation. The

transducers internal of the upright were used for correlation against bench test results, where fan velocity variation due to upright opening (scoop inlet) area required correlation to confirm internal velocity.

3.3.3. Post-Processing

3D Analysis

After the post processing from recorded data into HTC, the data was then transferred into a visual analytic by means of a 3D map of heat transfer across the tyre sidewall.

The process involved:

1. Measuring the profile position of each sensor location across the sidewall
2. Correlating measurements to Solidworks model co-ordinates
3. Creating a data grid file
4. Importing the Wheel Assembly model file into Tecplot (graphical data management software)
5. Importing the grid file of data into Tecplot

Sensor positions were marked out on the tyre sidewall and measured using a height gauge. Grid files contained the HTC's for each sidewall position at a single speed; sidewall sensor positions located by a radial and profile height measurement. The grid files were then overlaid in a 3D Cartesian plot with the wheel assembly model offset 1mm from the map surface so as to avoid merging surfaces.

3.4. Heat Transfer Coefficient Analysis

3.4.1. HTC Calculations

The heat transfer coefficient (HTC) is derived from the basic equation of heat transfer as in [5], yielding [9]. In the case of the sensors used in this thesis, the sensor temperature, T_{HOT}, is unknown, but can be solved using resistance [10][11] (Assaad, 2008).

$$Q = h.A.\Delta T \quad (W)$$

$$h = \frac{Q}{A.\Delta T} \quad \left(\frac{W}{m^2 K}\right)$$

$$= \frac{Q_{conv}}{A_{eff}.(T_{hot} - T_{air})} \quad \left(\frac{W}{m^2 K}\right) \qquad [9]$$

$$where; T_{hot} = sensor\ hot\ temperature$$

$$R_{hot} = R_{cold}(1 + \alpha(T_{hot} - T_{cold})) \quad (\Omega) \qquad [10]$$

$$T_{hot} = T_{cold} + \left(\frac{(\frac{R_{hot}}{R_{cold}})}{\alpha}\right) \quad (K) \qquad [11]$$

$$where;\ \alpha = temperature\ coefficient\ of\ resistance\ for\ conductor\ metal\ at\ T_{cold}$$

The temperature coefficient of resistance is stated in the sensor's data sheet as 0.40%/degC (Appendix 3), while the effective area is known to be 1.47E-06m^2.The resistances can best be described through a bridge diagram (Figure 34), where the location of the short, introduced when measuring resistance in the circuit using a multimeter, is marked so as to identify the resistance locations (e.g. R_{STS} = R_{Sensor} to R_{short}).

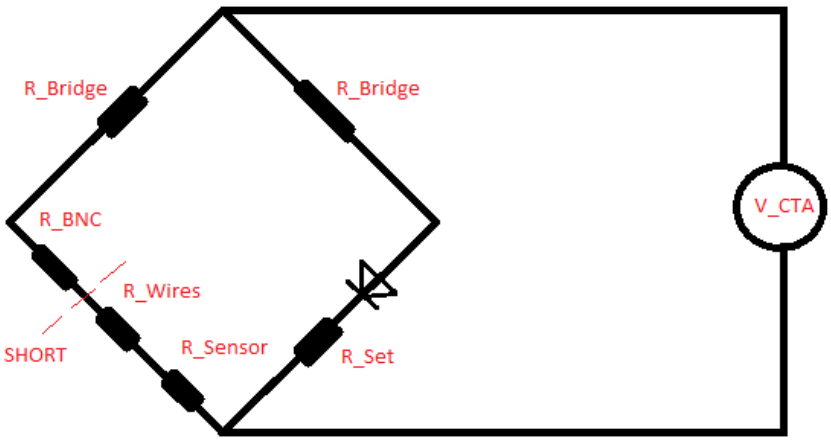

Figure 34: Hot film sensor bridge diagram.

Despite having used different CTA's, the two experiments (rig and wind tunnel) may still be compared with respect to HTC as the calculations are relative to the recorded datum set in each test run. The bridge resistance for each CTA was also calculated and considered in calculations of HTC (Appendix 1).

The required unknown variables to calculate HTC can be solved by working backwards from the heat transfer equation as follows:

From the heat transfer equation: $$h = \frac{Q_{sensor\_convective}}{A_{effective}\cdot(T_{sensor\_hot}-T_{amb})} \quad (\frac{W}{m^2K})$$ [9]

Where: $A_{effective}$ = 1.4777E-06m^2 and,

T_{ATM} was recorded for each test run

$$T_{sensor_{hot}} = T_{sensor_{cold}} + \left(\frac{\left(\frac{R_{hot}}{R_{cold}}\right)-1}{\alpha}\right) \quad (K)$$ [11]

Where: α = temperature coefficient of resistance at 20degC

Since: $$Q_{sensor} = Q_{sensor\_convective} + Q_{sensor\_conductive} \quad (W)$$

$$Q_{sensor\_convective} = Q_{sensor} - Q_{sensor_{conductive}} \quad (W)$$ [12]

$$Q_{sensor} = \frac{V_{sensor}^{\ 2}}{R_{sensor}} \quad (W)$$ [13]

Where: $$V_{sensor} = \frac{V_{CTA}\cdot(R_{sensor\_hot}+R_{sts}+R_{cts})}{R_{bridge}+R_{sensor\_hot}+R_{sts}+R_{cts}} \quad (V)$$ [14]

$$Q_{sensor\_conductive} = \frac{V_{datum}}{Gain} * Offset \quad (W)$$

$$= \frac{V_{sensor}\cdot(R_{sensor\_hot}*R_{sts}*R_{cts})}{R_{bridge}+R_{sensor}+R_{sts}+R_{cts}} \quad (V)$$ [15]

3.4.2. Hot Film Positioning

The rig tests, consisting of the wheel mounted on a motor driven shaft, were run under two geometry conditions; with (shielded) and without (open); the disc shield covered the outer diameter of the disc for 135deg of rotation. Integration of an optical sensor in the assembly, which produced a stepped-signal after each full rotation of the wheel, allowed the position of the hot film to be traced. At the instance of the leading edge At the instance of the leading edge, the hot film was located at the point of exit of the shielded region, the hot film was located at the point of exit of the shielded region. Measurements taken in the shielded region therefore begin 135deg before the leading edge of the optical signal. The leading edge can be distinguished in a data set as At the instance of the leading edge, the hot film was located at the point of exit of the shielded region (θ=0deg).

As the wind tunnel test did not utilise the shield, the hot film was aligned bottom dead centre (BDC) of the tyre; approximately 10deg advanced of the rig results to allow for tractability. The rig results have therefore been rotated 10deg CCW for viewing so as to directly compare the trace characteristics of both experimental tests.

3.5. CFD Methodology

3.5.1. PowerFlow

The Computational Fluid Dynamics (CFD) software adopted for this project was Exa PowerFlow 5.0, a code solving for velocity and temperature (Mukutmoni, et al., 2010), with capabilities of rotational meshing, and the ability to extract convective heat transfer data.

PowerFlow utilises the Lattice Boltzmann method, a solver that aims to track the motion of macromolecules of gases/liquids (Lietz, et al., 2002). Its designated turbulence model is that of the Very Large Eddy Simulation (VLES), a time dependent variation of the k-ε turbulence model, configured using 'law of the wall' boundary treatments so as to minimise the required mesh refinement for accurate return (Sprot, 2013), taking into account stream wise pressure gradients, and as a result, has the capability to predict boundary layer growth and separation to a high degree of accuracy (Albukrek, et al., 2006). The accuracy of boundary layer growth and separation is key to modelling the convective heat transfer, with previous literature having found the thickness of the boundary layer affects the level of heat transfer (Browne & Wickliffe, 1980).

The Lattice-Boltzmann (LBM) equations are used by PowerFlow to conduct initial formulations of the case in terms of the distribution function f(x, v, t), the number density of molecules at position 'x', speed 'v' and time 't' (Mukutmoni, et al., 2010). The LBM equations have been used to recover the Navier Stokes equations, tracking particle collisions with density representations; conserving mass, momentum and energy for compressible flow (Albukrek, et al., 2006).

Given the influence the wheel's rotation has upon the airflow path and interaction with its components, it is essential that the rotation, particularly the rotational boundary, be modelled accurately to best represent a realistic flow scenario.

PowerFlow offers various levels of rotational capabilities; velocity boundary condition (VBC), moving reference frame (MRF) and sliding mesh (SM). Each of the rotations was defined by Gaylard et al. (2012) in their computational simulation of brake dust deposition using PowerFlow as follows:

- VBC is the application of a constant velocity as the boundary condition for a solid wall with no physical rotation
- MRF applies rotational forces, centrifugal and Coriolis, to the fluid within a bounded region, but has no physical rotation
- SM implies a physical rotation on components within the rotating frame

3.5.2. Test Configurations

The simulation flow domain consisted of nine variable resolution regions of decreasing mesh refinement. The finest mesh region was located within the hub and was used as the measurement region for residuals; the wheel hub area was chosen for residual management due to the complex nature of the flow structure from the spokes. This was followed by a 30mm offset region around the entire CAD geometry of the experimental setup, and seven rectangular regions increasing in size throughout the domain up until the wind tunnel main enclosure. The main enclosure of the wind tunnel was sized to ensure an appropriate blockage ratio below 5% (Katz, 1947); the blockage ratio of the CFD domain was measured at 1.5%.

The experimental configuration was replicated in the CFD by reverse engineering the models into CAD geometries. The limitation of computational accuracy stems from the approximated curved surface measurements on the CAD geometry, particularly the scoop inlet. Sub-assemblies were imported into PowerFlow to ensure rotating components were separated; this allowed rotational reference frames to be created without interfering static parts (Figure 35). In order to create rotational reference frames between rotating and static components (e.g. wheel rim and shaft).

Parallel to the analysis of computational correlation to experimental data, the computational capability was evaluated through the undertaking of various simulation methods as described in Table 4 in order to determine which provided the highest degree of correlation to experimental data, as well as further exploring the variation between static and rotational tyre simulations.

SETUP #	TYRE	RIM	DISC
1	Stationary	Stationary	Stationary
2	SM	SM	SM
3	MRF	MRF	MRF

Table 4: Rotational simulation setups.

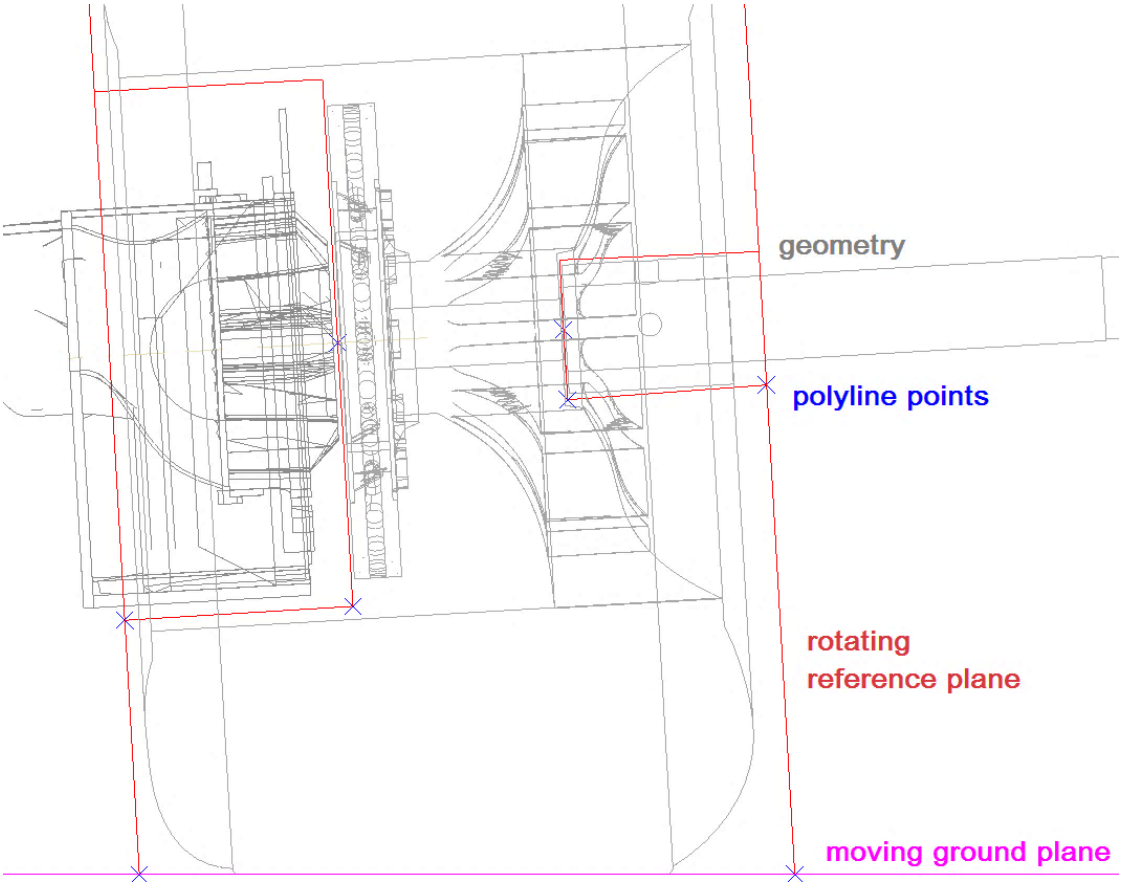

Figure 35: Rotating mesh reference frame polylines.

3.6. Errors and Limitations

Experimental setups and computational limitations are potential factors of error within collected data, the management of which must be considered.

Results across experiments and simulations were based on a 50% scale model wheel assembly. Scaling factors can be adopted in an aerodynamic setting, however the behaviour of scaling factors for heat transfer is not well understood. Results from this study aim to take the first step with regard to understanding correlation/variation between each method. In order to determine the potential variations between a scaled and full size model; a 100% model was run under the same computational simulation conditions.

Experimentally, sources of error and sensitivity stem from three key areas—sensor capability, noise and setup variation.

Hot film sensors are prone to circuit damage when incorrectly handled; damaging the integrity of data. In order to manage stability of the sensor during movement across the tyre sidewall, various mounting techniques were tested to avoid circuit damage. It was found that a stronger polyamide tape provided a more structurally supportive base, with less flex than generic, commercial adhesive tape. Further precautions involved the recording of resistance across the circuit after each hot film movement, so as to ensure no variation between experimental tests.

Sensitivity of the sensor could also lead to non-flow voltage signals. An error band test was designed to log sensor voltages at a theoretical no-flow condition by sealing all potential airflow entry and exit points on the disc. Signal traces can be used to determine any characteristic signatures within the data which may infer an induced positional error from a rotating component. The rotational nature of the experiments could give rise to noise within traces; noise from rotating slip rings, electrical components within the test, or local air movement. Results of the error band test were used to explore the degree of noise.

Experiments were logged using two channels; one for each hot film, positioned in the disc and sidewall. In an ideal situation, all positional movements of the sensor would be logged using separate sensors, therefore eliminating the possibility of circuit damage, however, in order to minimise costs of the experimentation, this was not a feasible approach. The disc hot film, however, was used as a reference point in order to ensure the behaviour of the CTA was constant throughout experiments in the wind tunnel. Though this could not ensure stability of the other sensor, it allowed a certain level of insight into the stability of both sensors in the circuit, given the dual-channel CTA shared resistance across both sensors; a change/error in one would assume a change/error in the other.
The CTA used in the rig experiment (DISA55M10) required manual calibration using dials, while the dual-channel FlowPoint CTA used for the wind tunnel tests was a more advanced system with computationally managed calibration. In order to overcome any variation between the two, the bridge resistance for each was calculated and included in the calibration files (Appendix 1), ensuring that recorded voltage was captured correctly for the comparison of both experiments.

Computationally, CFD Software has many inherent limitations within its calculation methods. Best practice for simulations is to ensure that any residuals are converged, ensuring stability of results, though further instability may occur at some period after the point of convergence. For this reason, despite residuals showing convergence, the effect of unsettled flow must be considered given that the duration extended only one full tyre revolution. A longer simulation of five revolutions was analysed (Appendix 2), results of which exhibited residuals with an on-going characteristic curve as in the initial, shorter, simulation. The purpose of the simulation was to determine whether residuals remained constant, or reached a point of revisited inconsistency.

Geometry accuracy is an area of high fidelity within simulations and may have introduced error to the computational results in this thesis. The limited accuracy of the upright Inlet scoop, consisting of curved surfaces, may have introduced variation to the heat transfer results in the disc as a result of variation between simulated and experimental internal air flow patterns. In order to determine the degree of significance the scoop inlet has on the heat transfer of the disc, stationary tests were conducted outlining the degree of heat transfer due solely to the air flow.

4.0. Results

All results have been presented in a Front Left configuration; airflow from left to right and rotation in an anti-clockwise direction. In practise, the wind tunnel used a Front right configuration and so these results have been mirrored to present findings in a comparable manner (Figure 36). Results for the sidewall refer to positions numbered 0 to 5; numbering based on test runs – an even distribution of results was required in case of hot film sensor failure, the numbering therefore reflects the central position recorded first, with radial positions recorded alternately between ID and OD. Figure 37 outlines the positions referred to within the results and discussion.

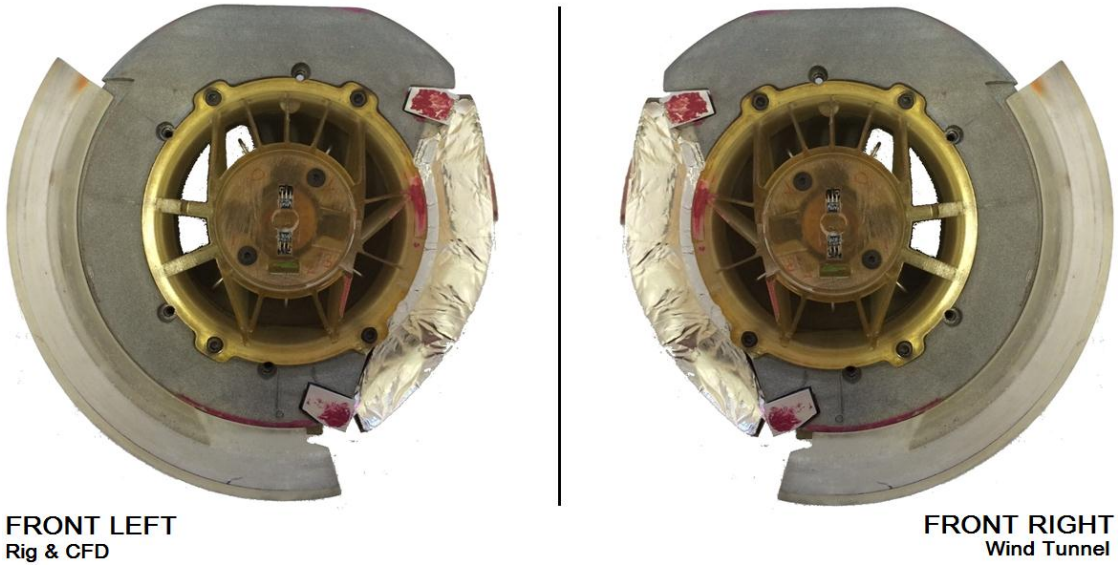

Figure 36: Front right and front left configurations (Shielded).

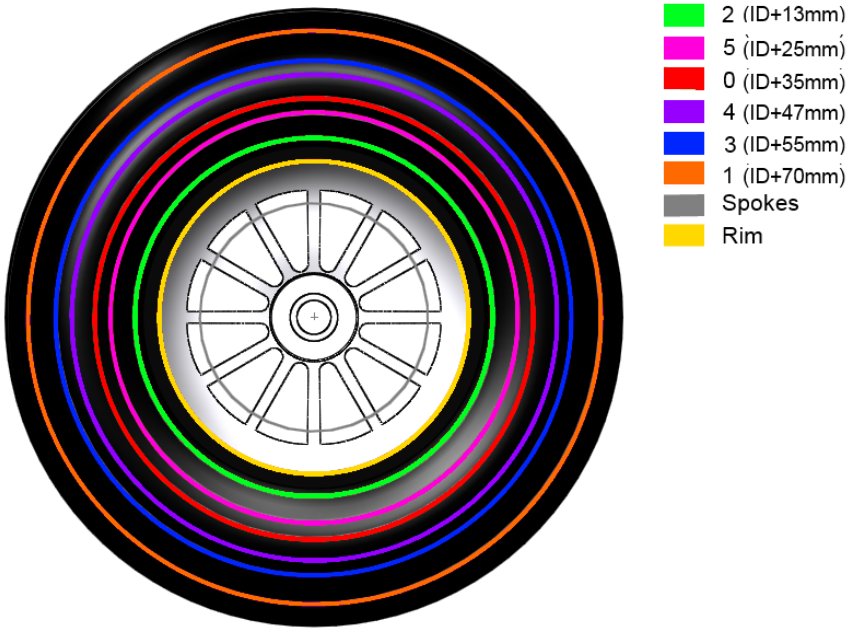

Figure 37: Sidewall position reference map.

Reynolds number has been quoted at various stages throughout the following analyses and discussions. It should be noted that Reynolds number has been defined separately for tyre and disc, each using their own diameter within calculations; 0.31m for the tyre and 0.14m for the disc (for the 50% scale model).

4.1. Motorised Rig

As previously stated, The wind tunnel test ran with the hot film datum location aligned to bottom dead centre (BDC) of the tyre. The rig results, for which the datum was located at 10deg CCW from BDC, have therefore been rotated for presentation to directly compare the measurements from both experimental tests.

4.1.1. Error Band Test

Section 2.4.1 explored the functionality of hot film sensors in that, when a flow is applied the resistance becomes unbalanced, regaining balance through the use of a differential amplifier within the film's bridge (Webster, 2000). A datum voltage at wind off and stationary tyre conditions was recorded for every test in order to quantify the size of conduction occurring from the hot film to the disc. The use of a slip ring was employed so as to allow rotation of the hot film wires. On the rotating side of the slip ring, the wires were arranged to minimise any out of balance introduced, and were secured to minimise their movement during wheel rotation.

CTA's are sensitive to change in resistance, both in the sensor itself, and in external components within the system such as the cables. As such, slip ring resistance variation throughout a wheel rotation would introduce measurement errors. The occurrence of slip ring noise would present itself as a signature within the trace; a facet of the data which cannot be established. Further exploration into the possibility of slip ring noise is revisited in the Section 4.2.2. In order to determine any error within the system a test was developed whereby both the inner and outer diameter openings to the disc vanes were sealed with tape (Figure 38); blocking the only possible air flow entry points so as to ensure any fluctuation in recorded sensor voltage was not attributed to through flow. Resistance variations in the slip ring could be speed dependent, and so a simple static evaluation of slip ring resistance was not considered a sufficiently robust test.

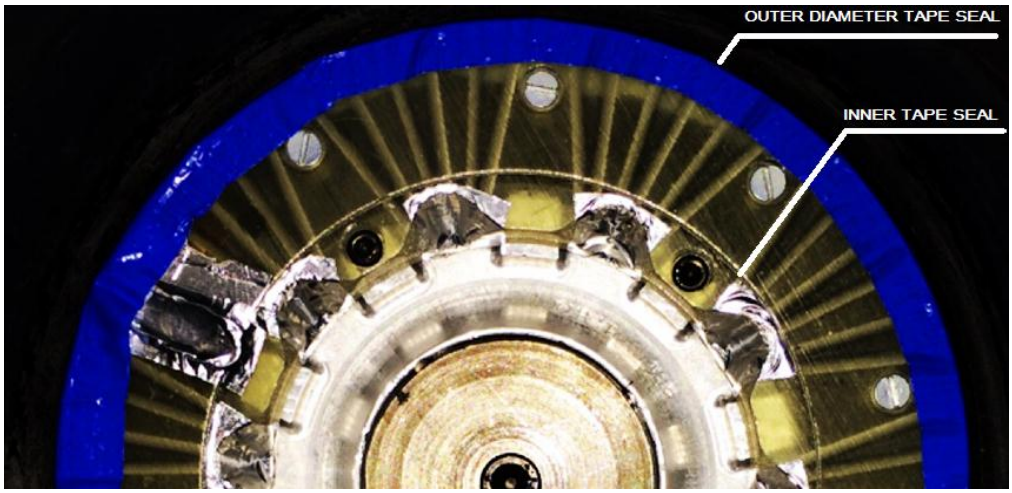

Figure 38: Schematic of disc vane sealing for error band test.

From the results in Figure 39, it is evident that the signal trace becomes sharper at the higher end of the velocity range. In order to capture the angular position of both the hot film and slip ring, the results have been presented with respect to rotational position, theta; capturing an entire rotation for each speed.

By plotting the average HTC of the sealed disc at each speed (Figure 40), it was determined that the average HTC of the sealed disc followed an almost linear relationship. Presence of HTC up to 14W/m^{2}K in the sealed disc suggests either noise within the system, or a localised flow.

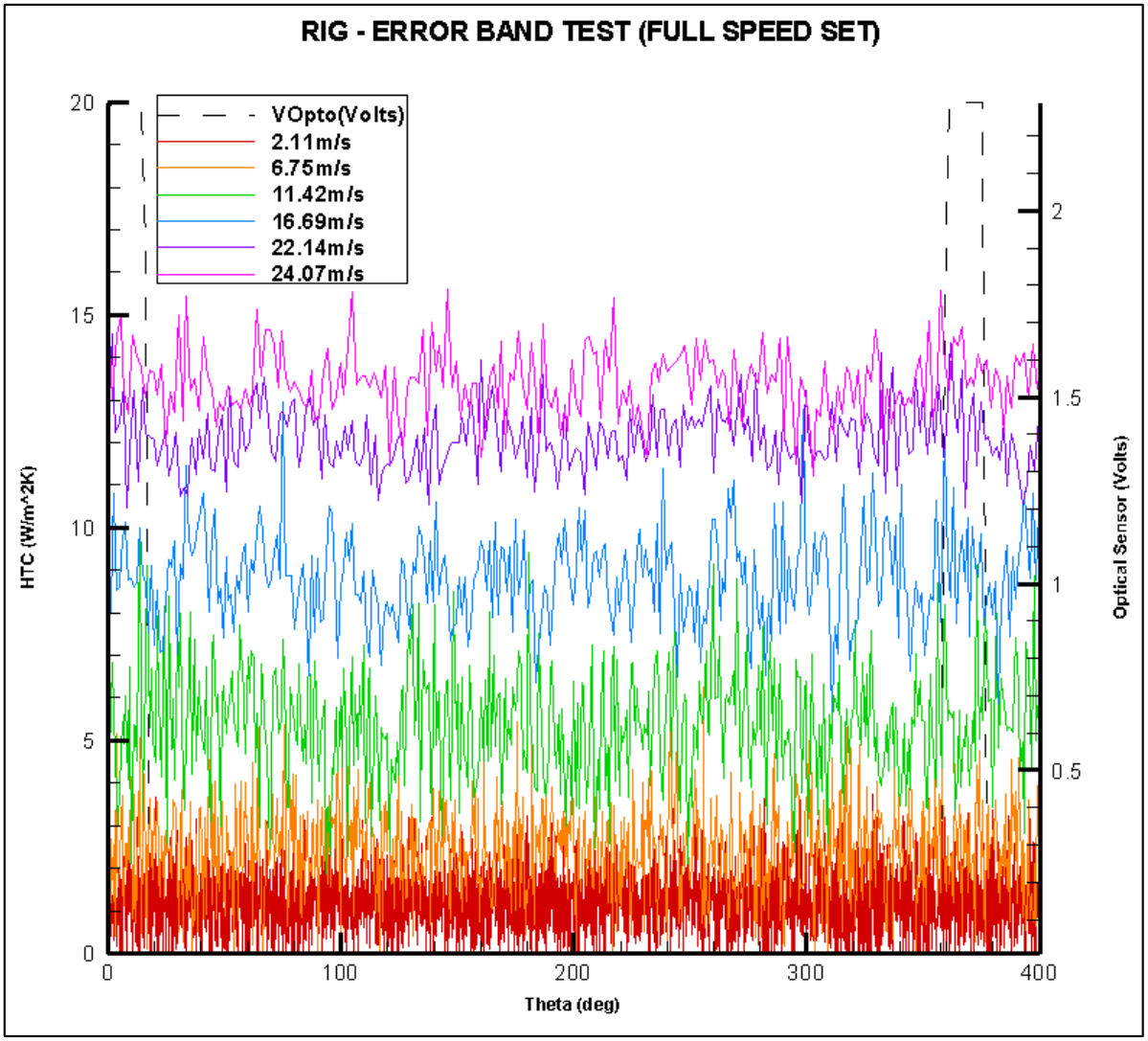

Figure 39: Brake cooling test rig error band test results.

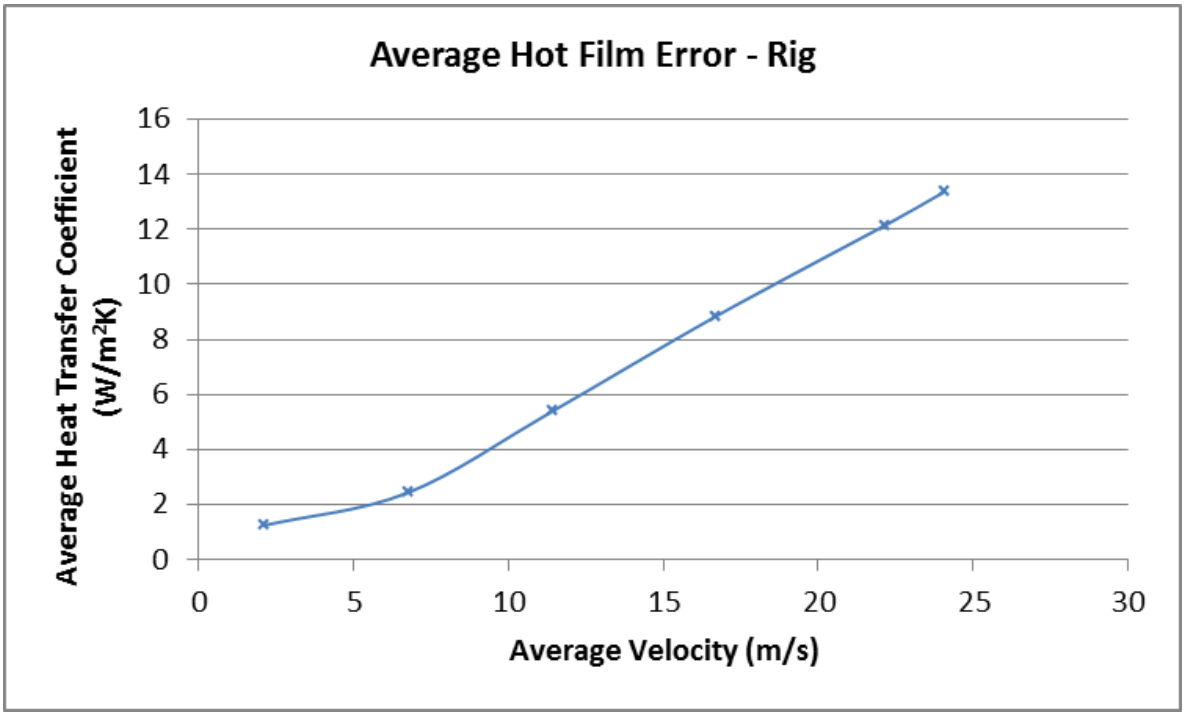

Figure 40: Average hot film error for rig test.

4.1.2. Heat Transfer Coefficient and Speed Relationship

The heat transfer coefficient's dependency on temperature differential infers a relation to the degree of cooling; governed by the imposed airflow and tyre rotational velocity. Results at the higher flow speeds tested were compared as both they lay in a Reynolds number past the transitional range (Figure 41); the Reynolds number for the flow at 20 and 25m/s at the disc diameter was 2.02E05 and 2.25E05 respectively.

Both speeds incurred the highest level of cooling at the region of the scoop inlet area (180-250deg), with the opening allowing for a direct flow. Increased heat transfer is a result of the increased voltage at the sensor given the intensification of applied flow on its surface, which in [15] is shown to affect the HTC. The internal geometry may have caused flow blockage/retardation, which would have affected the heat transfer capabilities; this analysis may therefore prove useful for design optimisation. The margin between the two data sets is consistent throughout the cycle of rotation at an approximate value of 5W/m^{2}K. Such a result suggests that there is no significant variation between airflow structure at 20 and 25m/s.

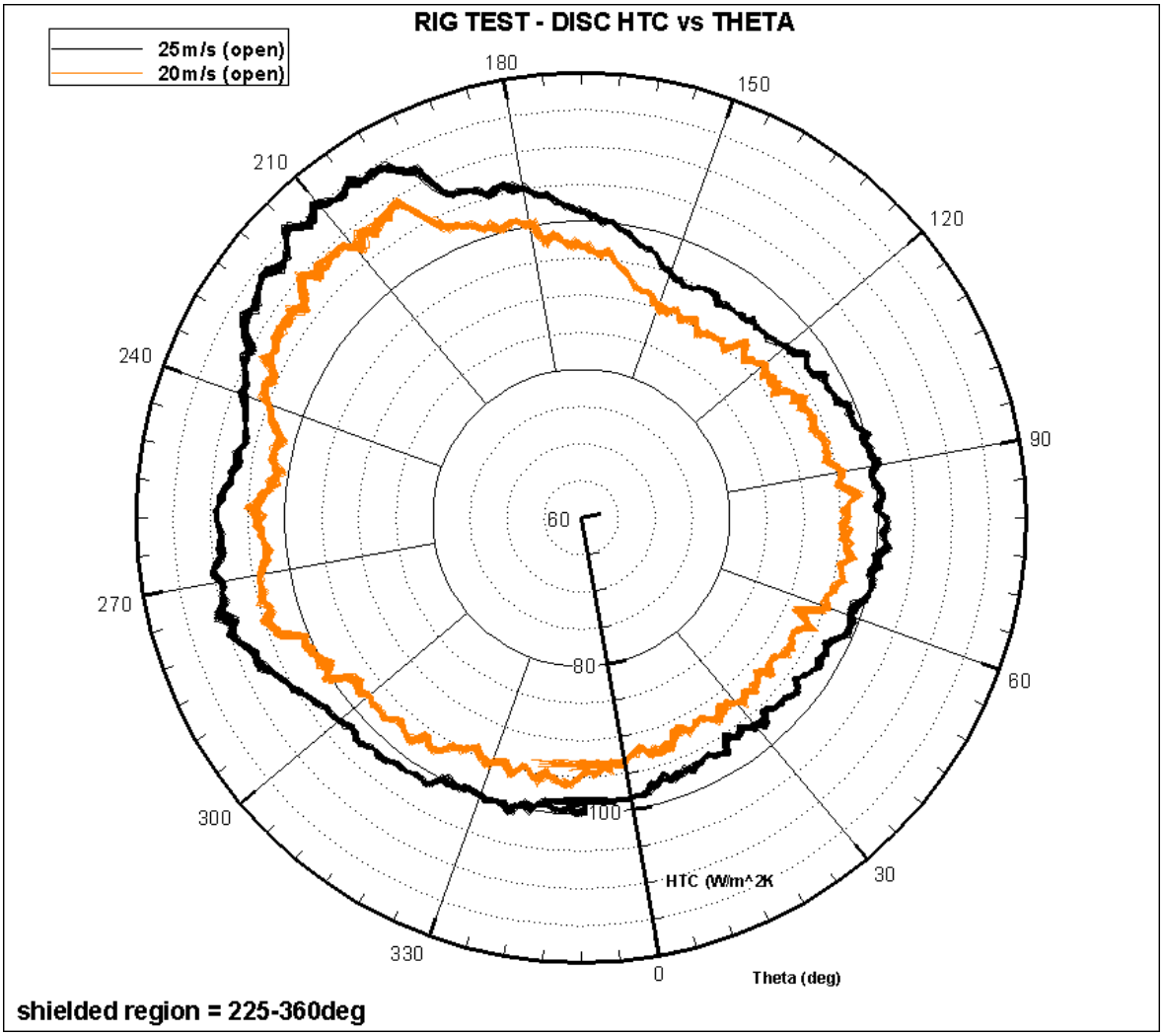

Figure 41: Disc heat transfer coefficient for 20m/s & 25m/s rig test.

4.1.3. Upright Shield Effect

Figure 42 outlines the heat transfer variation between the shielded and unshielded geometries, establishing that both geometries have equal HTC until entering the shielded region, the shielded configuration shows a lower HTC by approximately 3W/m^{2}K for 20 and 25m/s. Despite the use of the shield introducing a reduction in HTC for both speeds, the magnitude of the difference between shielded and unshielded is not high enough to be certain of its effect on results.

The frontal positioning of the shield suggests that it was employed to retain/recirculate airflow within the area as pushed forward by the momentum of the disc, thus increasing the cooling; however, results imply that the shield reduced heat transfer capabilities measured in the disc vane. The flow redirection induced by the shield may be affecting the disc vane's capability of collecting air, therefore reducing the HTC at the location of the hot film sensor.

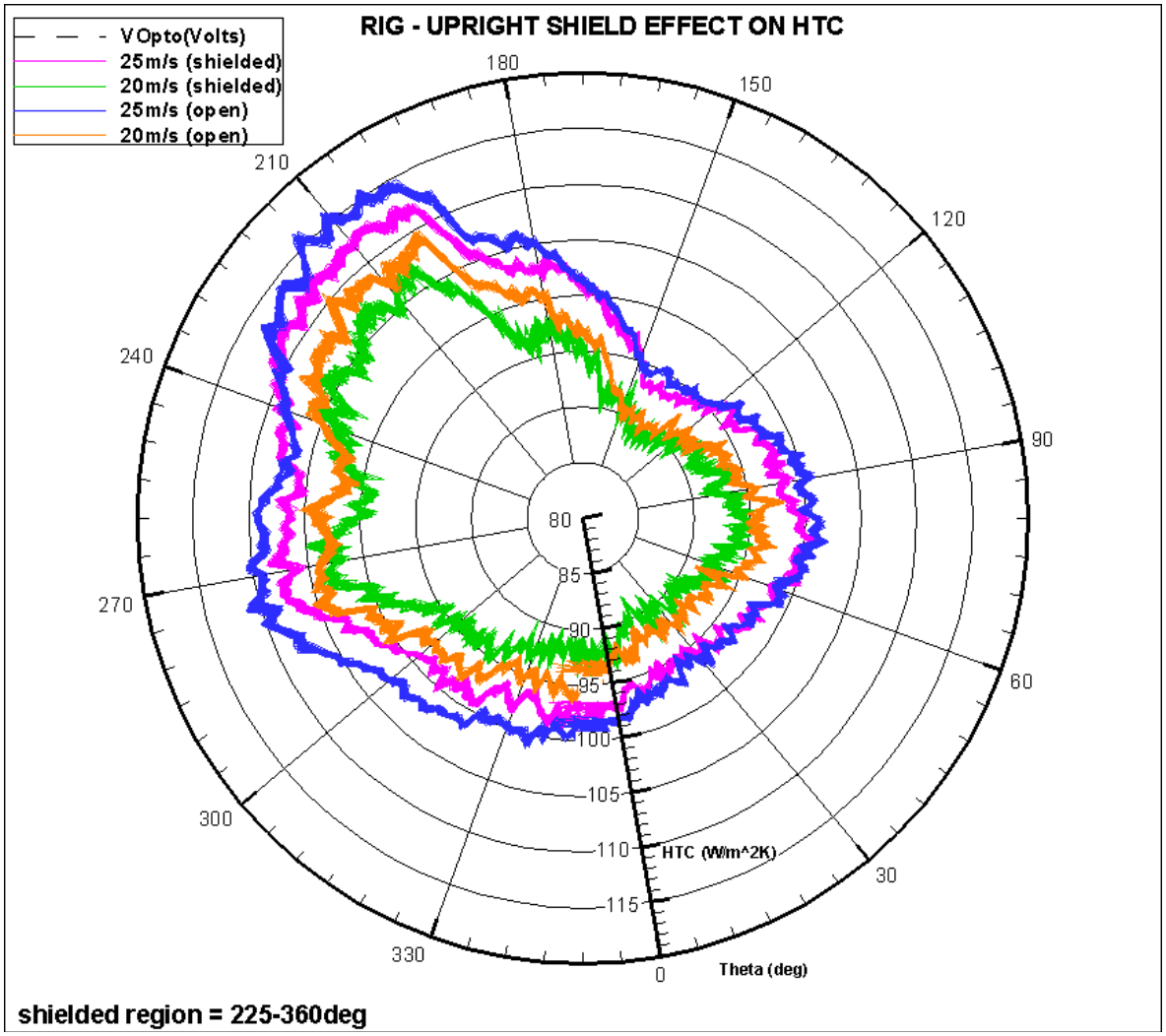

Figure 42: Effect of upright shield on disc heat transfer as measured on the rig.

4.2. Wind Tunnel

Wind tunnel testing was conducted to determine the HTC at different locations on the wheel assembly, and to validate the ability of CFD software to predict HTC. This section will outline the various tests conducted in the tunnel which involved validation of the system and determination of HTC values.

Validation of the system will be extended from the original error band test to the determination of the Nusselt number equation. The level of heat transfer as a result of the Inlet scoop flow will be determined through comparison of HTC results for the blocked and open scoop configurations, and the sidewall HTC will be discussed and presented using 3-Dimensional plots to aid in assessment of HTC trends.

Results presented at 0m/s correspond to zero flow velocity with a 1m/s moving ground velocity input as means of providing wheel rotation in order for the optical sensor to scan through all angular positions and identify the hot film position.

4.2.1. Error Band Test

The same approach used for the rig error band test (Section 4.1.1) was carried out in the wind tunnel, sealing the disc to determine the level of 'error' within the system. The level of HTC error in the wind tunnel results

was consistently below 3W/m^{2}K, significantly lower than results seen in the rig experiment (max HTC error of 14W/m^{2}K).

Traces of HTC for the error band test show a larger error in the high speed traces, with values reaching a limit in maximum error — evident by the traces for 15, 20 and 25m/s being similar in magnitude throughout a cycle. Presenting results as a function of theta (rotational angle) allows for identification of positional error, as values/traces match across the span of the trace. Positional error would suggest relation to a function of the rotation in the system, such as that of the slip ring.

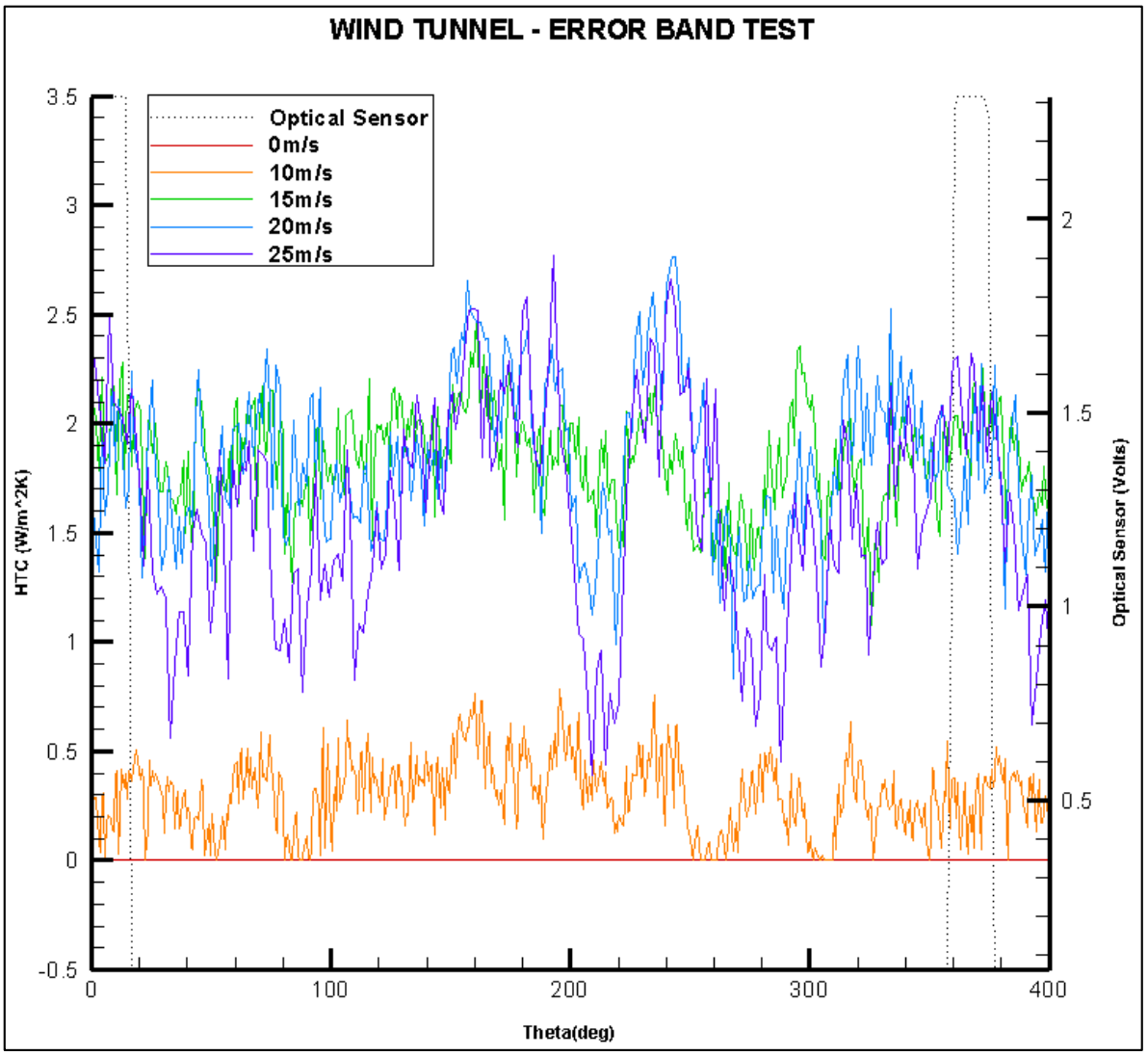

Figure 43: Error band test HTC values for wind tunnel disc.

The relationship of speed to HTC error (Figure 44) is shown to be one of significance, with speed increasing the range of HTC error experienced throughout a cycle of the sealed test. The increased range, however, results in a cubic relation between velocity and average HTC. The decline after the maximum error on the cubic trace may be representative of high speed stability within the system; with the increased speed, the system has reached a more stable state, eliminating harsh vibrations, however, this cannot be confirmed with the data set recorded.

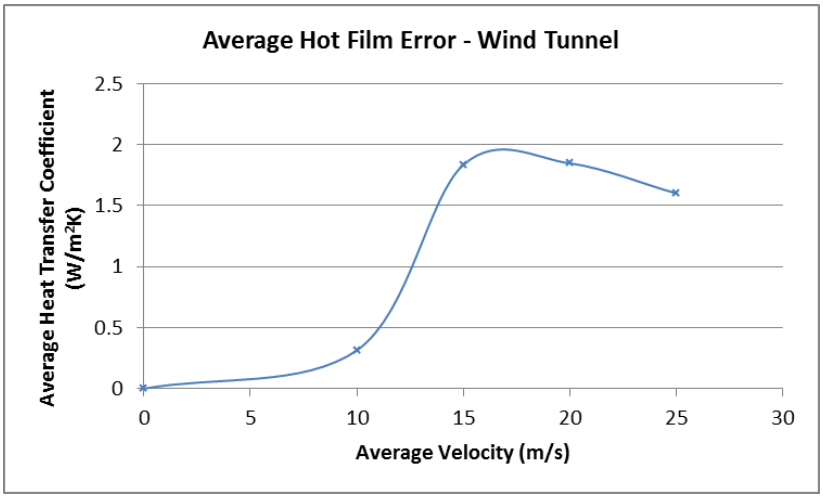

Figure 44: Wind tunnel average hot film error for 0-25m/s speed range.

4.2.2. Slip Ring Error Investigation

Investigation of the error band test from the wind tunnel prompted the question as to whether the curve peaks were characteristics of slip ring error, given they appear in a repeatable manner for each speed trace. Considering voltage increased with speed due to the intensification of applied flow, there was cause for concern that this was due to an element of the circuitry such as the slip ring; any variation in voltage could not be due to increase in cooling from flow velocity as there was no applied flow.

With the following formulations ([16] to [28]) and consideration of Figure 45, the degree of error for a hot film in a non-sealed disc was determined. When the CTA is operating at a higher current due to cooling at the sensor, the error associated with the cable path resistance change is increased. The calculations followed therefore predict error due to the presumed slip ring resistance change during rotation under applied-flow conditions; contrasting the error calculated in the error band test under zero-flow conditions. The error can be described as in Figure 46, where the trace for each speed takes a similar characteristic shape, but with a varying magnitude. The lower speeds (0-10m/s) showed a smaller delta between open and sealed error than the higher speed range (15-25m/s).

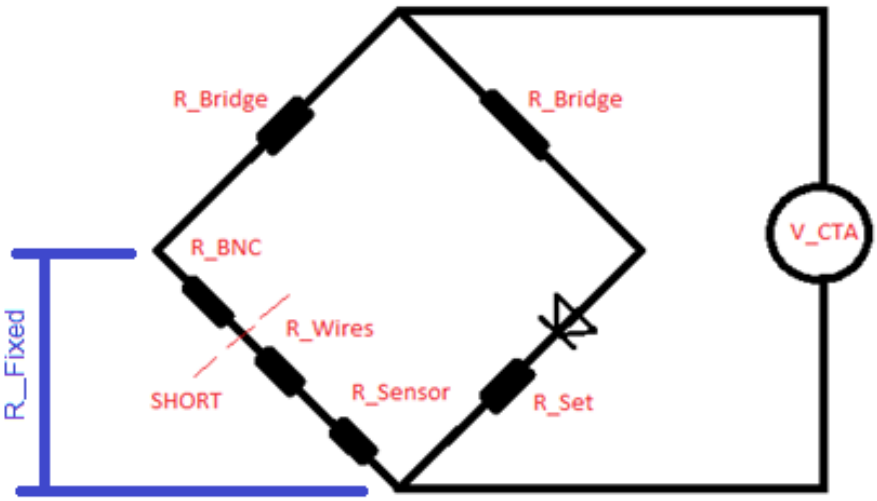

Figure 45: Representation of hot film and CTA circuit.

From Ohm's Law:

$$I = \frac{V}{R}$$

$$I = \frac{V_{bridge}}{R_{fixed}} \quad (A) \tag{16}$$

$$R_{fixed} = R_{cable} + R_{slip\_ring} + R_{hot} \tag{17}$$

$$\therefore R_{hot} = R_{fixed} - R_{cable} - R_{slip_{ring}} \quad (\Omega) \tag{18}$$

Where:

$(R_{fixed} - R_{cable})$ is fixed

And:

$$R_{slip\_ring} = \overline{R_{slip\_ring}} + R'_{\ slip\_ring} \quad (\Omega) \tag{19}$$

Given that the slip ring effect will vary based on its position in time.

$$\therefore \mathrm{R_{hot\_calc}} = \mathrm{R_{fixed}} - \mathrm{R_{cable}} - \overline{R_{slip\_ring}} - R'_{slip\_ring} \quad (\Omega) \tag{20}$$

From Joule's 1st Law:

$$Q = I^2.R$$

$$Q_{calc} = I^2.R_{hot}$$

$$= I^2.\left(R_{fixed} - R_{cable} - \overline{R_{slip\_ring}}\right) \quad \mathrm{(W)} \tag{21}$$

$$Q_{actual} = I^2.R_{hot\_calc}$$

$$= I^2.\left(R_{fixed} - R_{cable} - \overline{R_{slip_{ring}}} - R'_{slip_{ring}}\right)$$

$$= I^2.R'_{sr} \quad (W) \tag{22}$$

Since:

$$I = \frac{V}{R}$$

$$I^2 = \frac{V^2_{probe}}{R^2_{fixed}}$$

$$= \frac{Q_{total}}{R_{hot}} \quad (A^2) \tag{23}$$

$$\therefore \mathrm{Q_{calc}} - \mathrm{Q_{actual}} = \frac{\mathrm{Q_{total}}}{\mathrm{R_{hot}}}.\mathrm{R'_{sr}} \quad \mathrm{(W)} \tag{24}$$

Since:

$$h = \frac{A}{\Delta T}$$

$$\frac{Q_{calc} - Q_{actual}}{A_{effective}.(T_{hot} - T_{amb})} = \frac{Q_{total}}{A_{effective}.(T_{hot} - T_{amb})}.\frac{R'_{sr}}{R_{hot}} \tag{25}$$

$$h'_{error} = h_{total} - \frac{R'_{sr}}{R_{hot}} \quad (\frac{W}{m^2K}) \qquad [26]$$

Where:

h'_{error} is the HTC of the sealed disc and R_{hot} is known

$\overline{h_{total}}$ can be found by setting the datum's in the sealed test to zero

$$\frac{R'_{sr}}{R_{hot}} = \frac{h'_{error\_sealed\_disc\_actual\_datum}}{\overline{h_{sealed\_zeroed\_datum}}} \qquad [27]$$

Since:

$$h'_{error\_unsealed} = \frac{R'_{sr}}{R_{hot}} \cdot \left(h_{convective} + h_{sealed_{zeroed_{datum}}}\right)$$

$$h'_{error\_unsealed} = \frac{h'_{error\_sealed\_disc\_actual\_datum} \cdot (h_{convective} + \overline{h_{sealed\_zeroed\_datum}})}{\overline{h_{sealed\_zeroed\_datum}}} \quad (\frac{W}{m^2K}) \qquad [28]$$

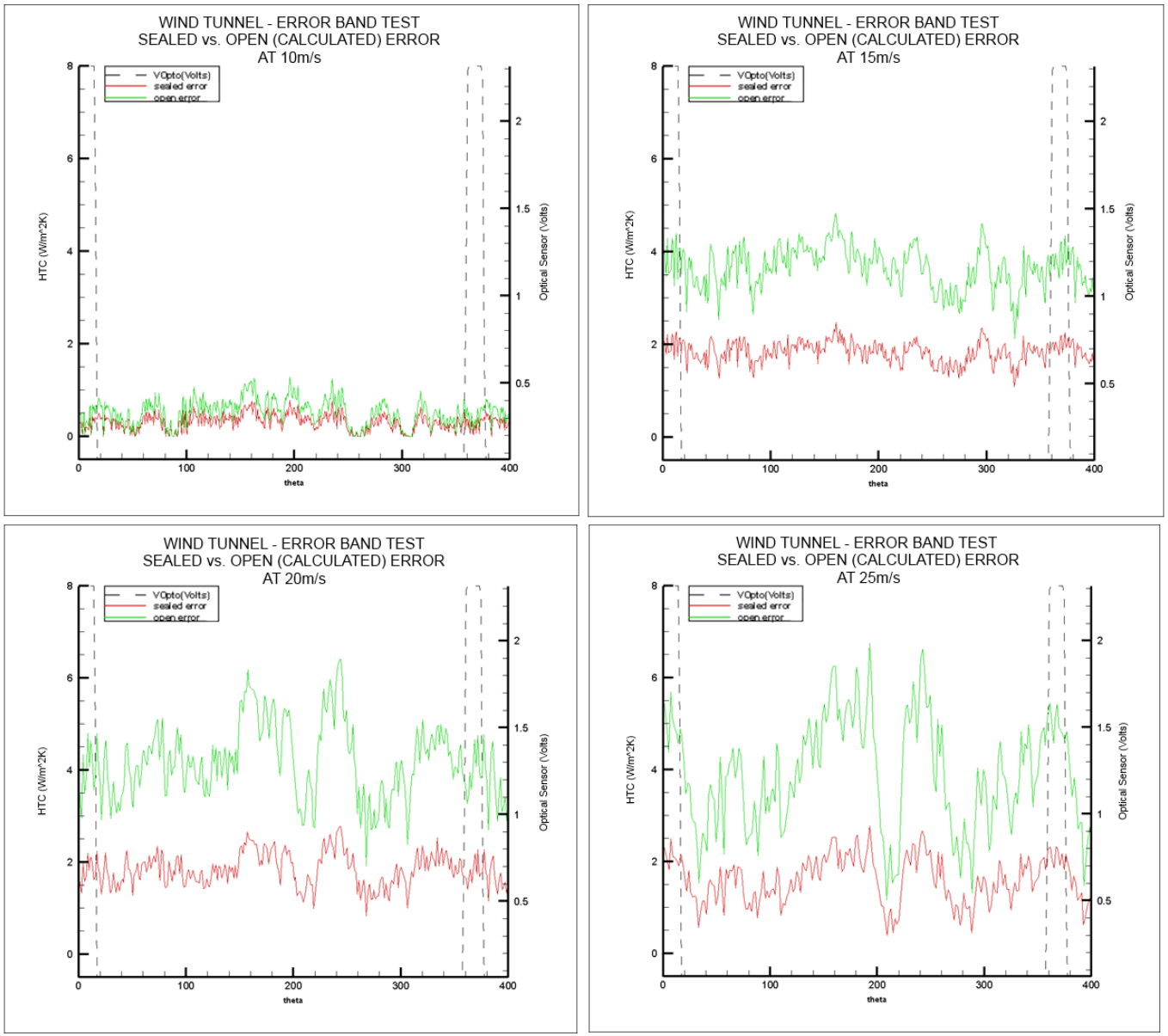

Figure 46: Comparison of open and sealed error for wind tunnel test (10-25m/s).

The average error for each speed (Figure 47) was derived in the same manner as Figure 40, and shows that the error was analogous up to 10m/s, after which the degree of error increased to approximately double. The difference between original to corrected HTC of calculated error on an open disc run, changes the magnitude of results rather than the shape of the trace. The delta between original and corrected values increases with increasing speed, but to a point of diminishing return; such a relation is likened to the square root function velocity calibration curve of a typical hot film wire/sensor. The lack of variation in trace shape suggests that the error is not slip ring related, and perhaps there may be internal cooling within the disc despite its sealing. It is therefore appropriate to quantify the error using the detailed calculated approach, but not impose any data correction, as this would require making assumptions that are not accurate, and could potentially damage the integrity of the data.

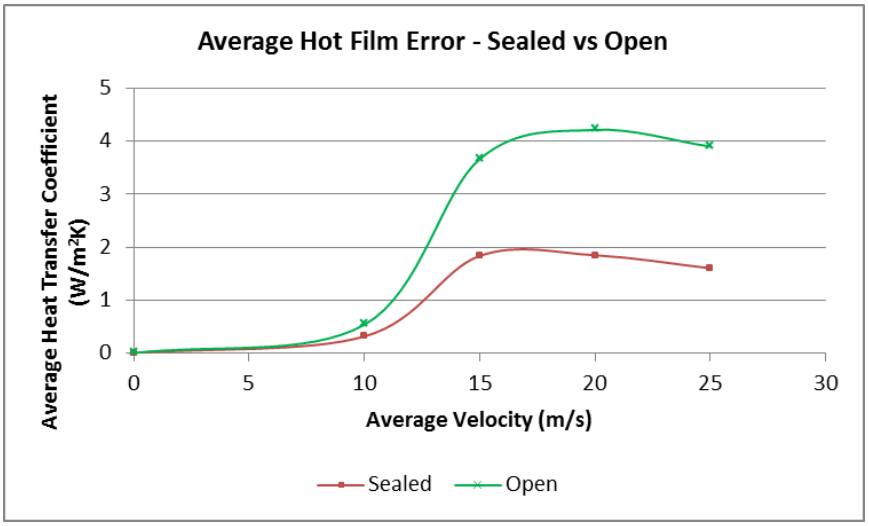

Figure 47: Average heat transfer coefficient error at the disc for sealed and open configurations.

4.2.3. Blocked scoop

A wind tunnel test configuration was run with a blocked scoop, utilising multiple layering of heavy duty tape, to block the scoop at the Inlet plane. By blocking the inlet scoop of the upright (scoop opening internal of the upright position at 190-250deg), the degree of heat transfer occurring as a result of the scoop flow was determined; the main source of flow velocity within the upright. The open scoop produced average HTC results at least ten times larger than the blocked scoop case (Figure 48), inferring that cooling due to the scoop inlet flow is the predominant cooling source. Assessment of the results for each speed, and the consideration that the maximum error in the wind tunnel disc results was found to be approximately 2W/m^{2}K, suggesting that heat transfer within the disc while employing a blocked scoop, is only apparent for the higher flow speeds.

The XY plot demonstrates the distinct variation around the scoop area, where a sudden drop in heat transfer occurs only in the blocked scoop configuration (marked as drop initiation point). Figure 49 describes the spread of heat transfer around the disc's rotation. Results suggest that although the scoop is responsible for the majority of cooling, the positional heat transfer is only affected at the region of direct airflow entry near the scoop.

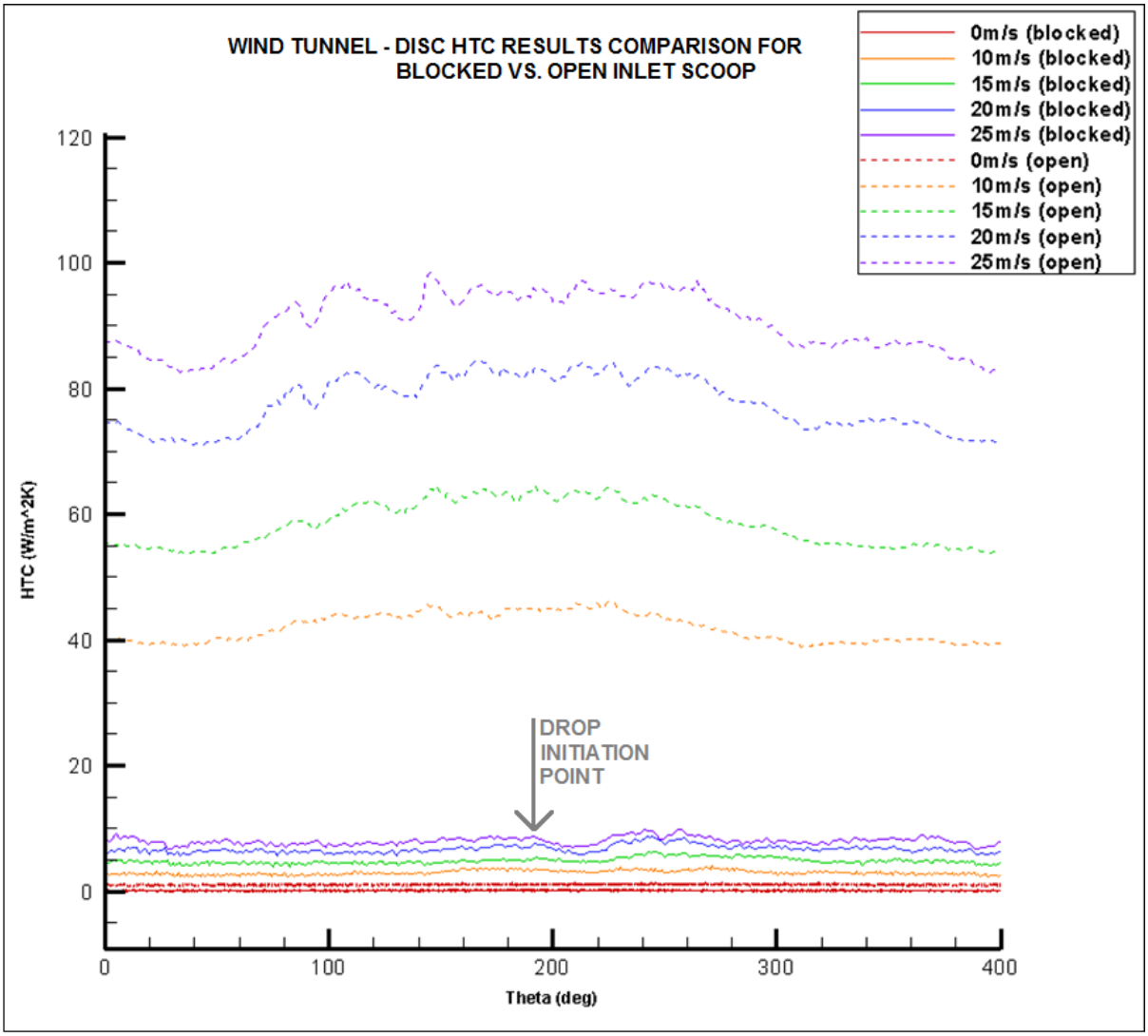

Figure 48: Resulting disc heat transfer for blocked vs. open brake inlet scoop geometries recorded in the wind tunnel.

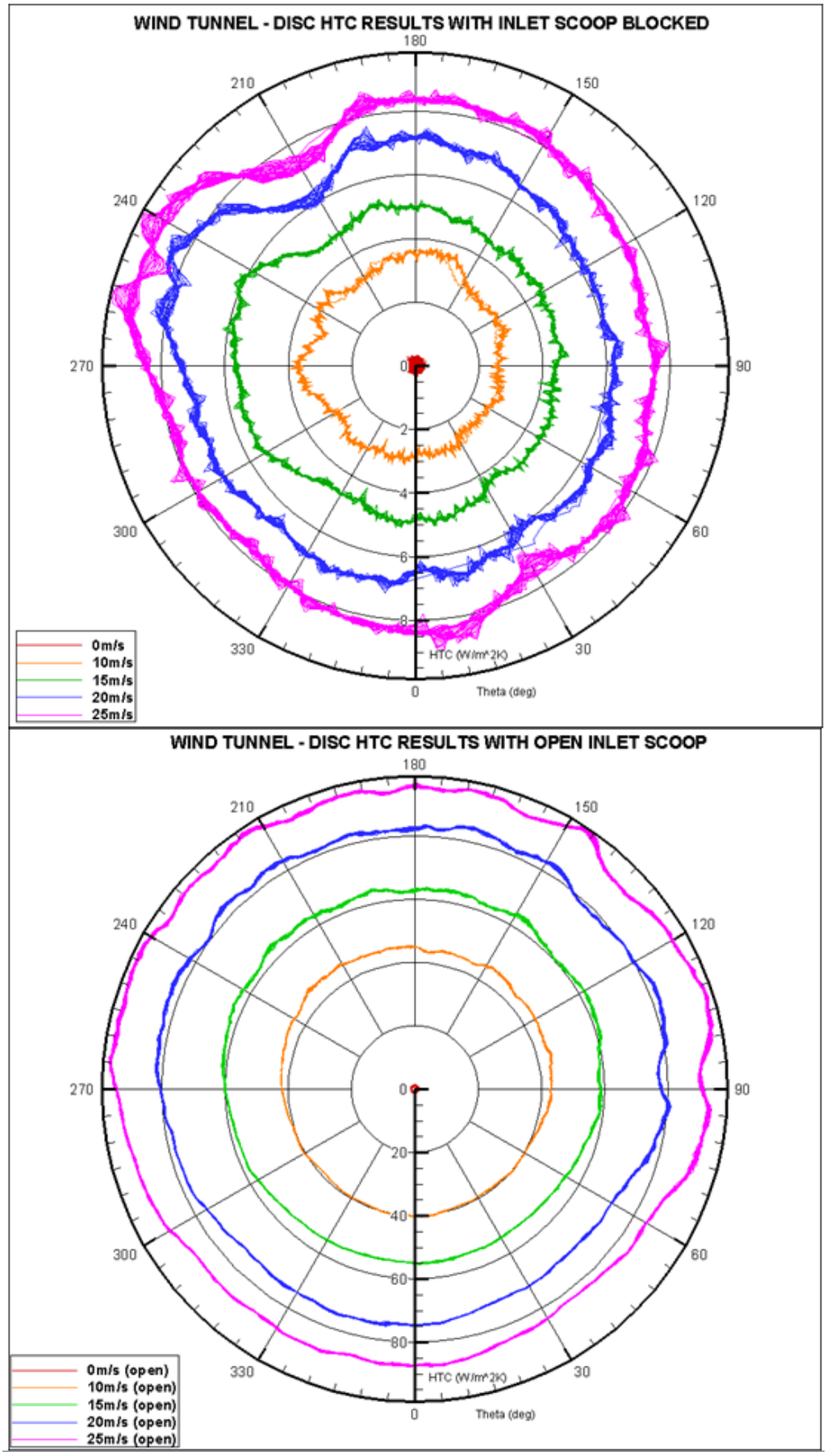

Figure 49: Blocked vs. open scoop - Disc HTC results recorded in the wind tunnel.

The non-dimensional heat transfer, Nusselt number (Nu), is plotted against Reynolds number for both configurations in Figure 50. The average Nu for flow across cylinders can be expressed by [29]. The plots allowed for a linear regression analysis to determine the exponents of the equation.

$$Nu = \frac{hD}{k} = CRe^{m}Pr^{n} \quad [29]$$

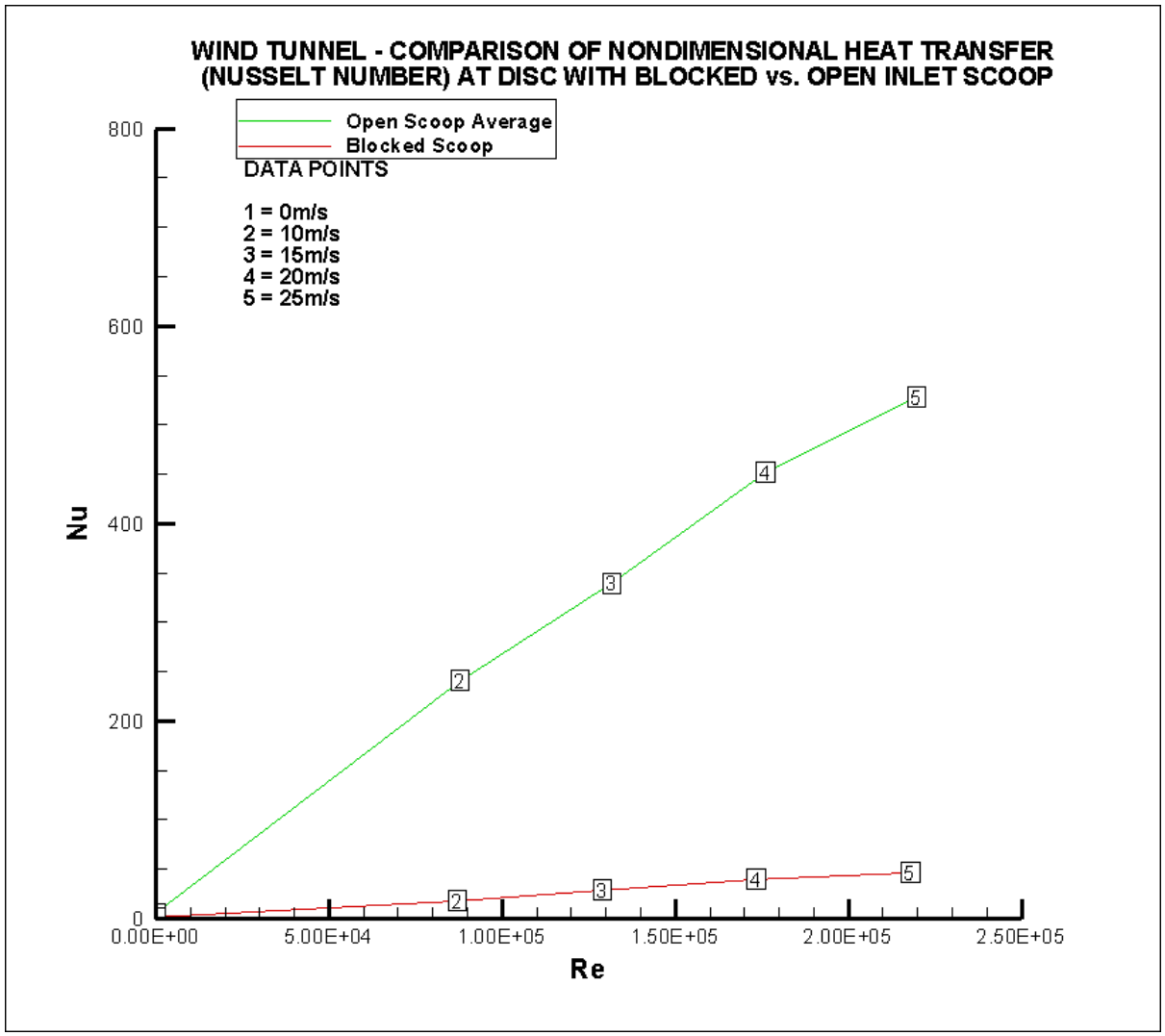

Figure 50: Non-dimensional heat transfer (Nu) and flow (Re) for open and sealed disc configurations.

4.2.4. Nusselt Number Calculation

The exponent of the Prandtl number – the ratio of momentum to thermal diffusivities – has been widely accepted to take the value of 1/3, while coefficient 'C' and Reynolds number exponent 'm' are dependent on flow conditions. Cengel et al. (2008) designed a table of experimentally determined values for the constants that make up the Nusselt number formulation (Table 5), which was used as a reference for the validation of constants in the wind tunnel experiments. Jancirani et al. (2003) experimentally derived Nusselt number relationships for various components within the brake assembly. Equations constructed from their experimentally collected data are outlined in Table 6.

EXPERIMENTALLY DETERMINED NU RELATIONSHIPS BY CENGEL ET AL.	
Range of Re	**Nu Relationship**
0.4-4	$Nu=0.989Re^{0.330}Pr^{1/3}$
4-40	$Nu=0.911Re^{0.385}Pr^{1/3}$
40-4000	$Nu=0.683Re^{0.466}Pr^{1/3}$
4000-40,000	$Nu=0.193Re^{0.618}Pr^{1/3}$
40,000-400,000	$Nu=0.027Re^{0.805}Pr^{1/3}$

Table 5: Nu relationships for a range of Re values (Data source : Cengel et al., 2008).

EXPERIMENTALLY FITTED COMPONENT NU EQUATIONS BY JANCIRANI ET AL.	
Components	**Nu Relationship**
Disc Faces Inboard Wheel Face Outboard Wheel Face Wheel Hub	$Nu = 0.0435(Re^{0.8})(Re_T/Re_O)$ Where; Re_T = Transverse Re Re_O = Rotational Re
Inboard Flange Outboard Wheel Face Disc Hat Disc OD Disc ID Hub	$Nu = 0.0195(Re_O)^{0.8}$
Brake Pads Brake Caliper	$Nu = 0.174(Re_T)^{0.618}$

Table 6: Component Nu relationships derived for brake system components (Data source: Jancirani et al., 2003).

The values of 'C' and 'm' were derived in this study from the experimental wind tunnel data; where 'C' was solved for using the Nusselt number equation [29], and m was determined as the gradient of the curve defined by the natural log of Nu versus Re. Data were processed separately for the disc and tyre sidewall (Table 7), each using their own diameter within calculations; 0.31m for the tyre and 0.14m for the disc.

NU RELATIONSHIPS	
Disc	$Nu = 0.013Re^{0.87}Pr^{1/3}$
Sidewall	$Nu = 2.80Re^{0.46}Pr^{1/3}$

Table 7: Nusselt number validation of 'C' and 'm' from experimentally collected data.

The disc HTC values collected in the wind tunnel showed good correlation to HTC values determined in other experimental setups explored in the literature, with Jancirani et al. (2003) quoting the Reynolds number exponent, m, as 0.8 for the disc surfaces, and the coefficient, C, to be comparable to the results in this study (0.0195 compared to 0.013 in this thesis). The Reynolds numbers experienced in the wind tunnel were all within the range of 40,000-400,000, which Cengel et al. (2008) quoted to present a Reynolds number exponent of m=0.805. Results from the wind tunnel correlated well to the model fit equations derived (Figure 51).

Contrarily, the expression for the average Nu along the tyre sidewall did not agree as well to the referenced literature for neither m, nor C; outlining the fact that HTC varies for different regions within the wheel assembly. The wind tunnel results, however, maintained a good fit to the derived expression for Nusselt number (Figure 52). The degree of correlation between wind tunnel and CFD Nusselt number results will be explored in Section 5.5.

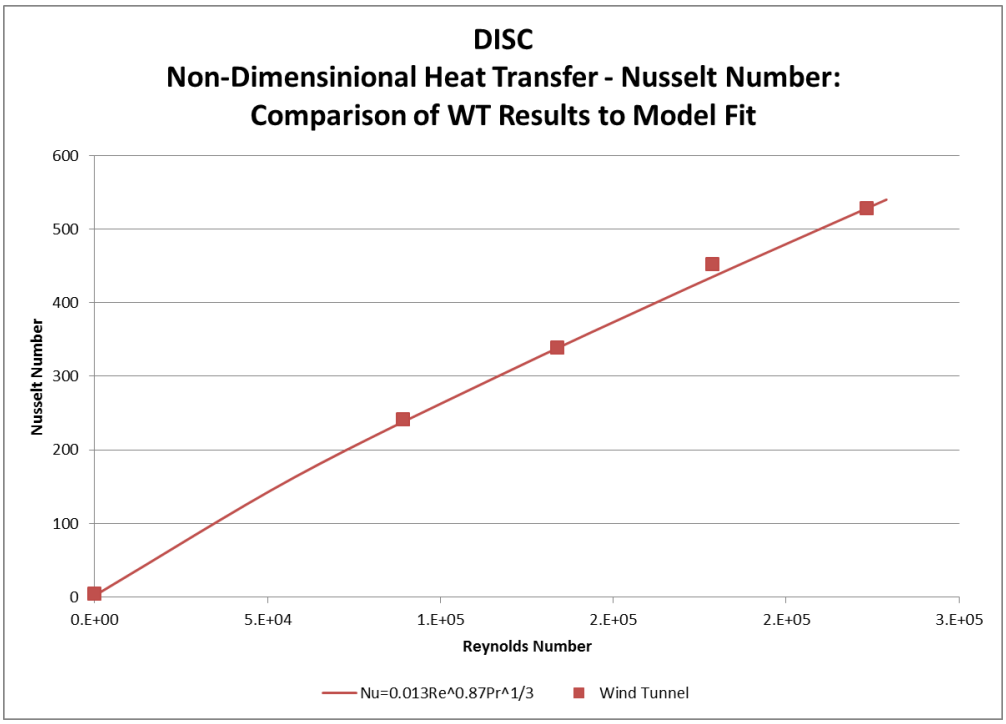

Figure 51: Wind tunnel data points for disc Nusselt number fit well to derived Nusselt number equation.

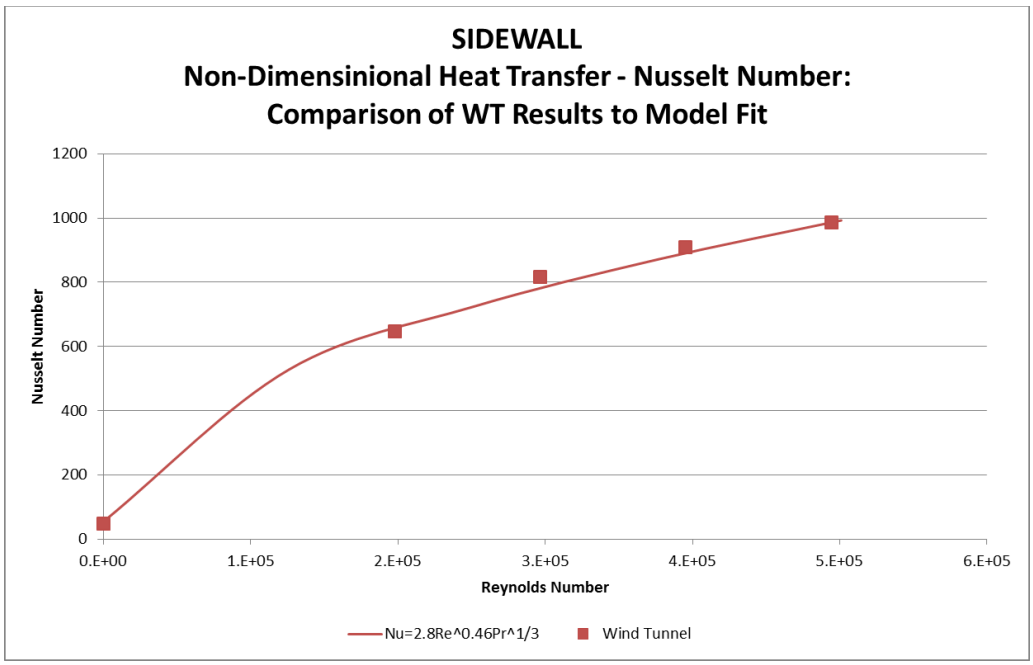

Figure 52: Wind tunnel data for the tyre sidewall and the model fit derived Nusselt number equation.

4.2.5. Disc

The disc hot film was logged for each test run, acting as a reference to identify any large variations signifying error. Results for the disc showed minimal variation of HTC, with variation between runs approximately 4W/m^{2}K for 10-20m/s (Figure 53 to Figure 55), while results at 25m/s (Figure 56) showed a slightly larger increase in variation, approximately 7W/m^{2}K. The run for sidewall position 5, the last of the sensor position moves, showed consistently lower results. There does not exist a trend between HTC and hot film positional movement (i.e. induced error after each increment of movement), suggesting that the hot film did not incur any circuit damage during its movement. Results lay within the approximate error of ±2W/m^{2}K.

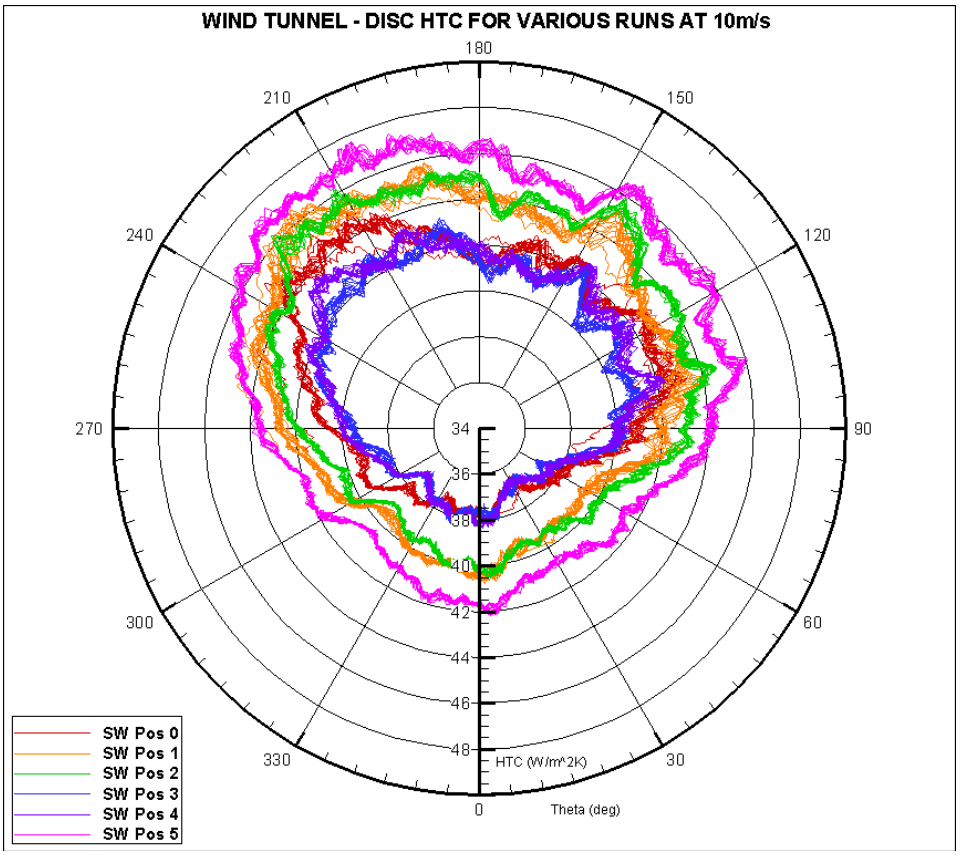

Figure 53: Disc heat transfer coefficient comparison over various runs during sidewall measurements (10m/s).

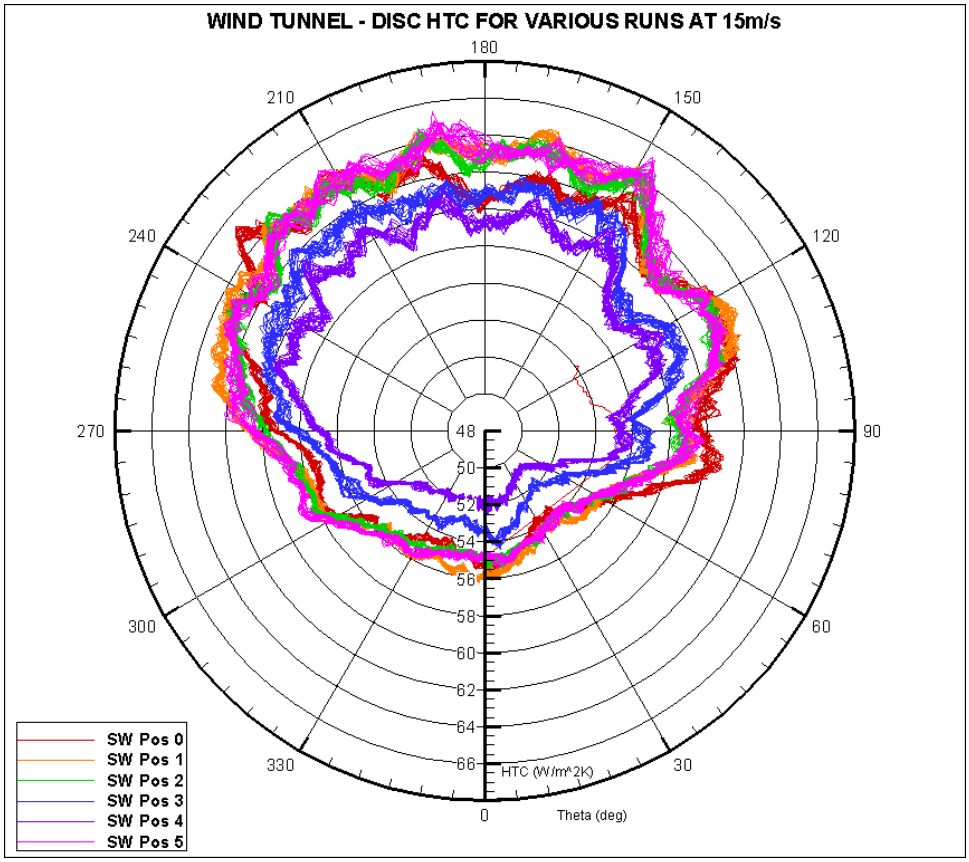

Figure 54: Disc heat transfer coefficient comparison over various runs during sidewall measurements (15m/s).

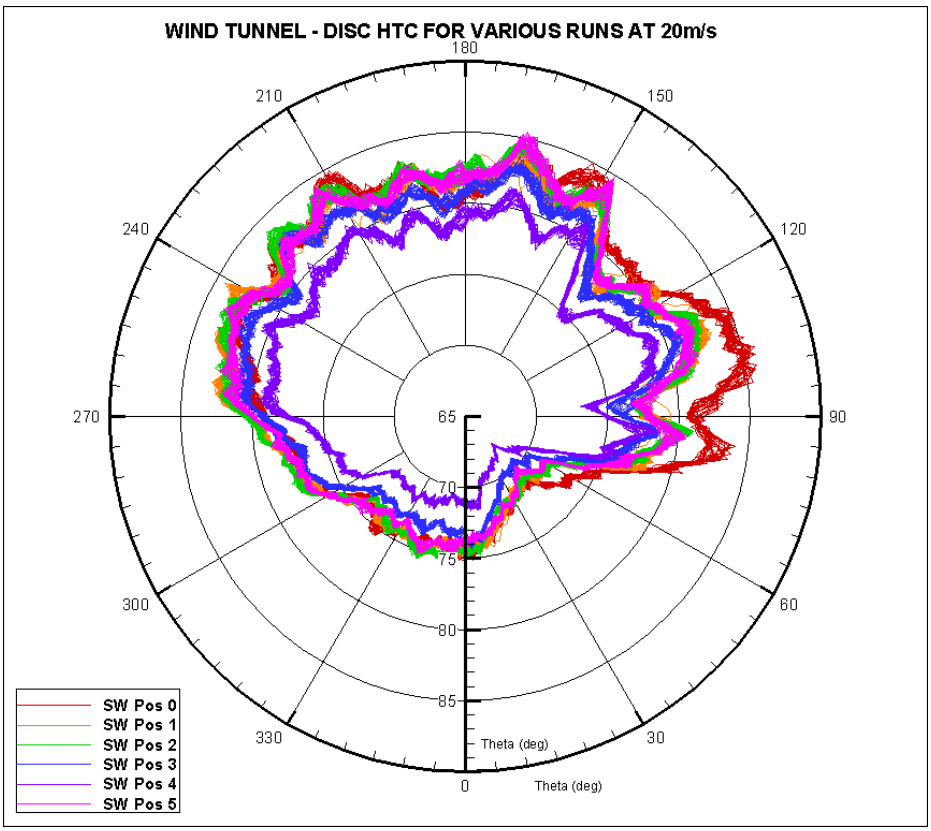

Figure 55: Disc heat transfer coefficient comparison over various runs during sidewall measurements (20m/s).

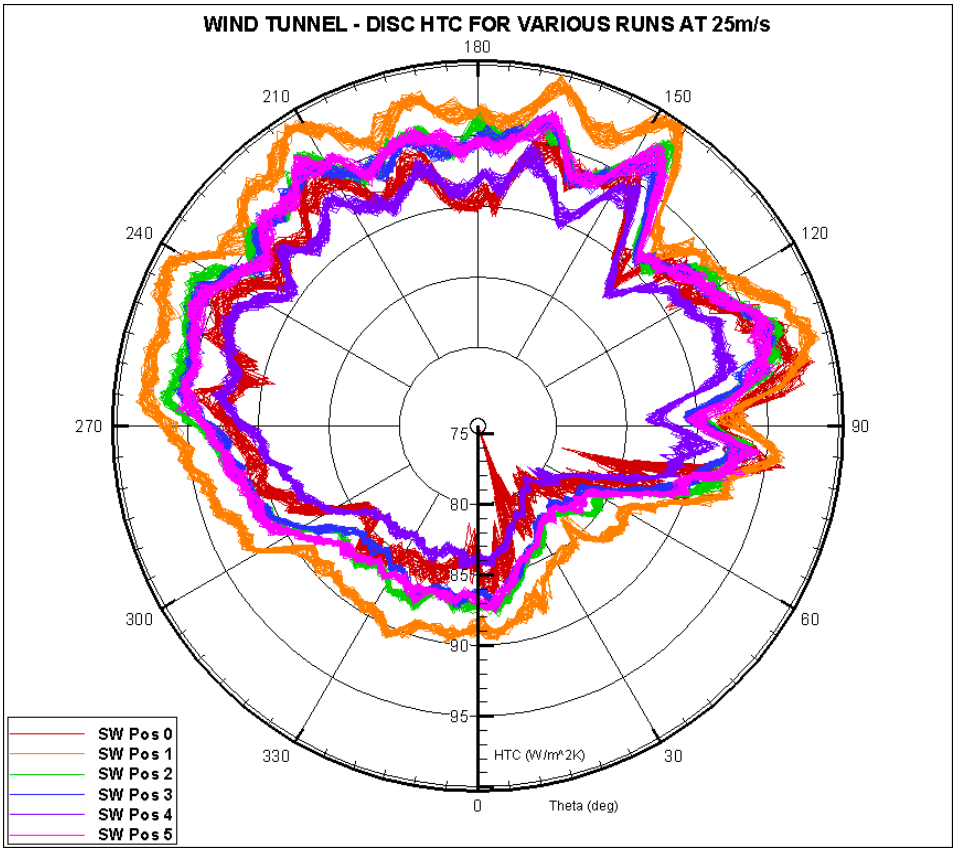

Figure 56: Disc heat transfer coefficient comparison over various runs during sidewall measurements (25m/s).

4.2.6. Sidewall

HTC's at various positions were recorded across the sidewall profile (Figure 37), where it was expected that the variation in sidewall profile, combined with the tyre's rotation, would create a complex heat transfer situation dependant on position. The average HTC at the sidewall (Figure 57) shows similarity between all positions when averaged around a 360degree cycle, however, given the complexity of the flow structures due to the tyre's rotation, non-averaged positional analysis was required in order to capture and compare the positional variation in heat transfer at different speeds for each hot film radial position. The general trends in the cyclically averaged results can be summarised as follows:

- Position 2 (ID+13mm) incurred the highest degree of heat transfer
- Position 3 (ID+55mm) incurred the lowest degree of heat transfer
- Position 5 (ID+25mm) deviated from a trend based on positioning and exposure to air, where positions showed the pattern 2 > 5 > 0 > 4 < 3 < 1
- Positions 0 (ID+35mm) and 3 (ID+55mm) were very similar despite a position separating them (4)
- Positions 3 (ID+55mm) and 5 (ID+25mm) were the most over generalised in the averaged results

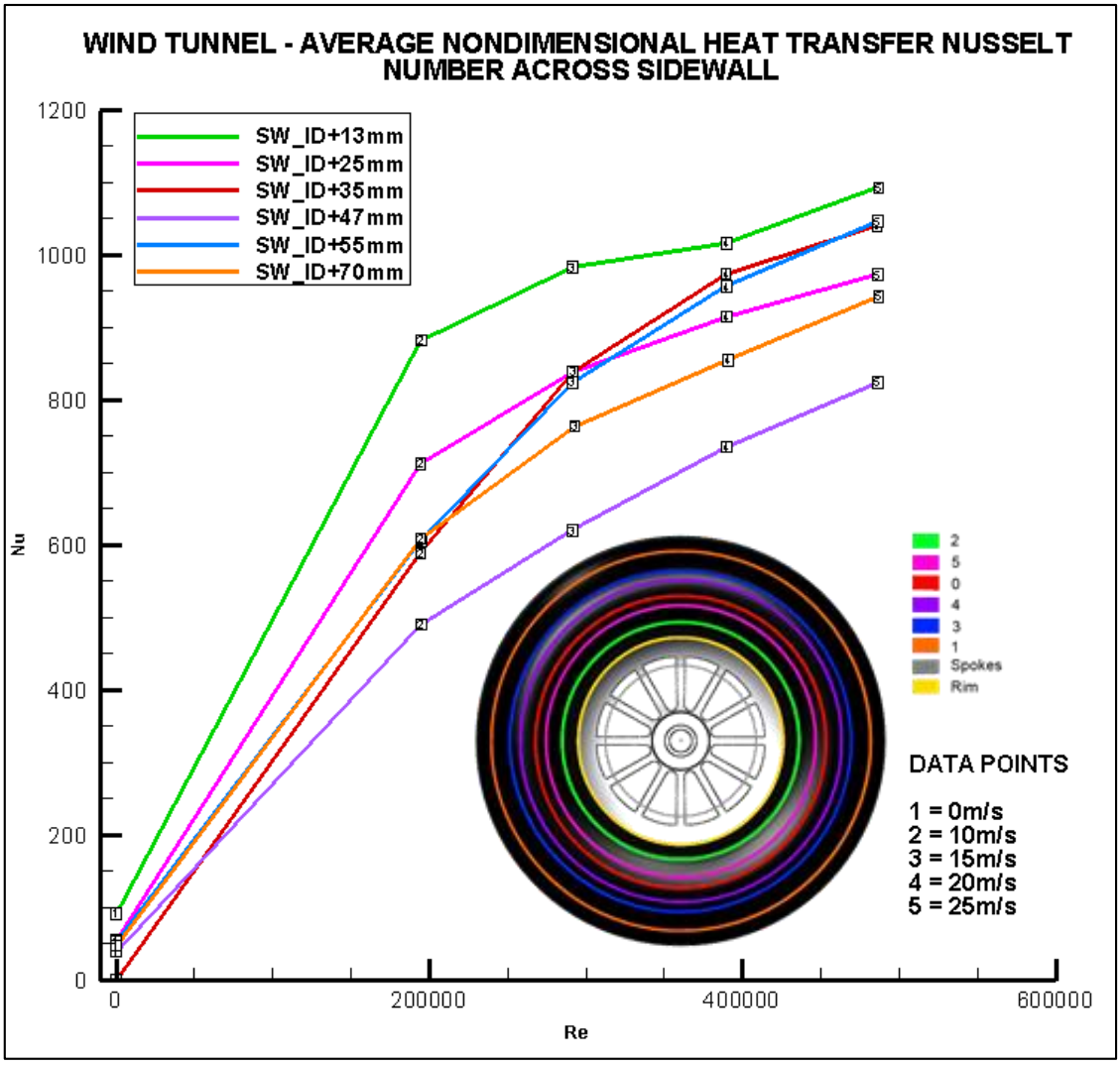

Figure 57: Average heat transfer coefficient across tyre sidewall measurement positions.

Speed Variation Analysis

For each flow velocity, key data points were retrieved from the result set, including highest and lowest HTC positions across the tyre sidewall, while also determining trends in the global result set for each velocity. The trends discovered in the 0-15m/s speed range were prevalent within the higher speed range of 20-25m/s, as such, analysis was considered for 20m/s and 25m/s only (Results for 0-15m/s can be found in Appendix 9).

It was proven that the tyre sidewall profile geometry affects the level of heat transfer, with consistent location of minimum and maximum HTC. Position 4 (ID+47mm) displayed the lowest level of HTC, while position 2 (ID+13mm) experienced the highest on average throughout the tyre's rotation, suggesting that the turbulence introduced due to the proximity of the spokes may have exacerbated results.

Earlier it was discussed how boundary layer thickness increases toward the rear of the tyre, which was found by Browne and Wickliffe (1980) to cause a lower level of HTC than at the front. The constant occurrence of minimum (Position 2 – ID+13mm) and maximum (Position 4 – ID+47mm) HTC indicates that the boundary layer is more complex than a simple continuous motion, but that the positions upstream and downstream of the

highest point of the curved tyre sidewall profile (z-direction in Figure 58) experienced different boundary layer characteristics. Such a phenomena is supplemented by the XY plot (Figure 59 and Figure 60), where Position 4 (ID+47mm) (purple) and the positions outside it (toward tyre OD), 1 (orange) and 3 (blue), followed similar HTC trends throughout the rotation, while 0 (red), 2 (green) and 5 (pink), inside of position 4 (toward tyre ID), followed a trend of their own; a clear variation of HTC for positions upstream and downstream of the highest point of the tyre's sidewall profile .

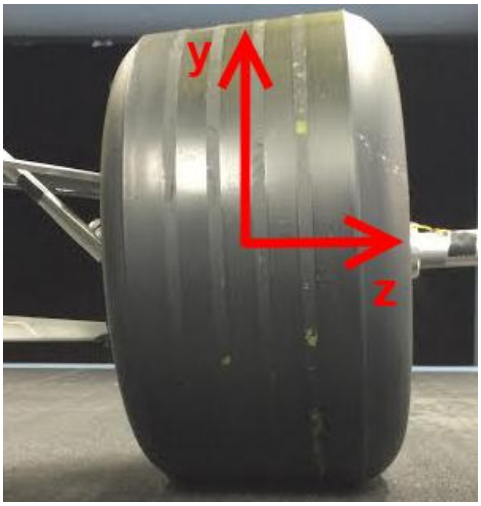

Figure 58: Tyre sidewall profile high point located in positive z-direction.

Moving away from the central point (Position 4 – ID+47mm) in either direction increases the HTC, rendering position 4 as the inflection point. The exception occurs at Position 0 (ID+35mm), which displayed characteristics of the inner positions when in rearward flow, and outer positions when in free-stream flow. The peaks of the positions closest to the rim (Positions 1, 3 and 4) occurred at approximately 275deg (bifurcation point/stagnation point); the area of most exposure to the free-stream flow. Before the peaks in HTC, the outer three positions showed lower HTC values than the inner three positions (i.e. the heat transfer from the ID to the high point of the profile was greater than that after the high point to the OD); a result of the rearward flow contacting the inner positions upstream of the sidewall high point, before those downstream.

Such an arrangement reflects the sidewall positional layout, where the highest heat transfer occurs near the rim, where turbulent flow is particularly evident, while the lowest occurs at the highest point on the tyre sidewall profile. This agrees with the findings of Kato et al. (2009), whereby turbulence is found to increase the level of heat transfer.

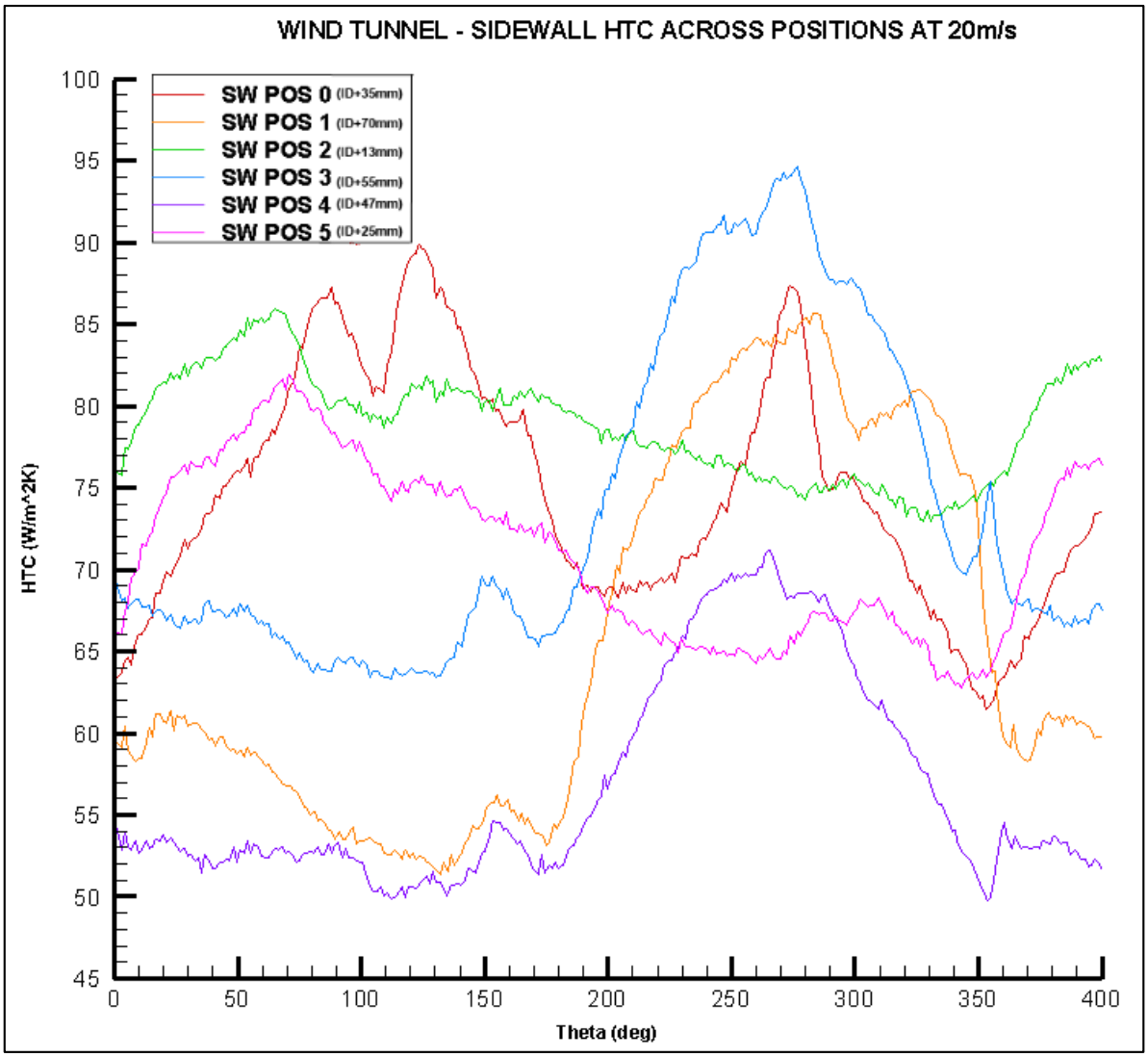

Figure 59: sidewall HTC for 20m/s wind tunnel tests.

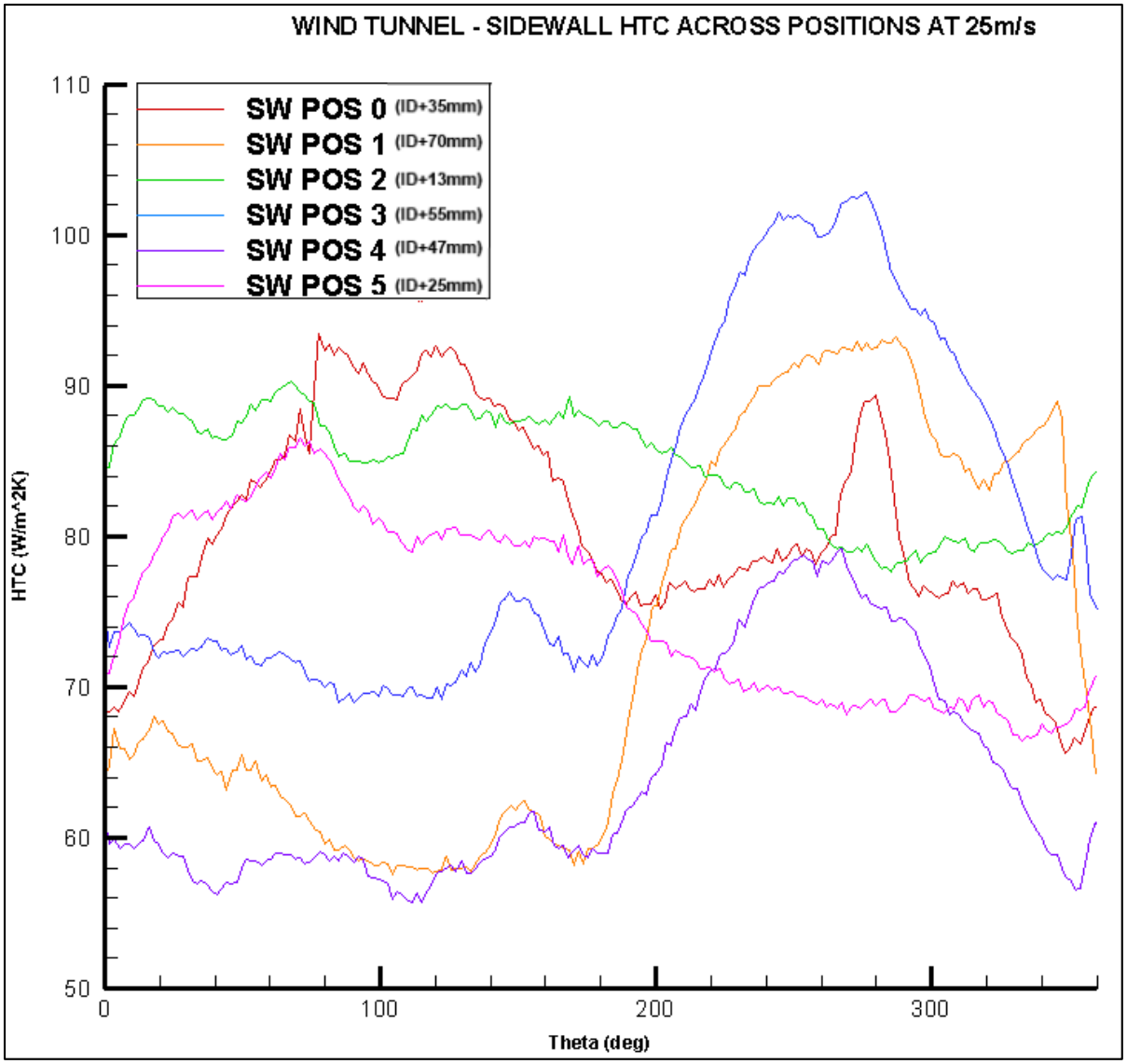

Figure 60: Sidewall HTC for 25m/s wind tunnel tests.

Positional Analysis

Representing the HTC experienced at each position for the 0-25m/s speed range allowed for the visualisation of heat transfer characteristics around the radial profile of the tyre (Figure 61 & Figure 62).

Positions 1 (ID+70mm), 3 (ID+55mm) and 4 (ID+47mm) showed distinct traces at every speed, with almost constant heat transfer up to 180deg where the HTC increased until, (1) 290deg, (3) 280deg and (4) 270deg, after which the curve decreased until 360deg. The start and end points of the increased heat transfer area were the same for all three positions, however there was a noticeable advancement of 10deg between positions 1, 3 and 4.

The range of heat transfer between 10-25m/s increased for positions moving outward toward the tyre OD, this was probably due to the fact that there is more turbulence in the spoke region, which is known to increase heat transfer. Positions 2 (ID+13mm) and 5 (ID+25mm) were steadier throughout the rotation, while position 0 showed peaks at both ends of the rotation across the centreline of the tyre (along 270 to 90deg in the x-

direction). In the previous investigation the position adjacent to 4 (ID+47mm), position 0 (ID+35mm), showed characteristics of the outer and inner positions in terms of HTC trace shape at each speed. Despite the slight variation, the positional investigation compliments that of the velocity investigation, whereby it was found that central area around the tyre sidewall profile peak is highly influenced by the free-stream flow and the development of the boundary layer.

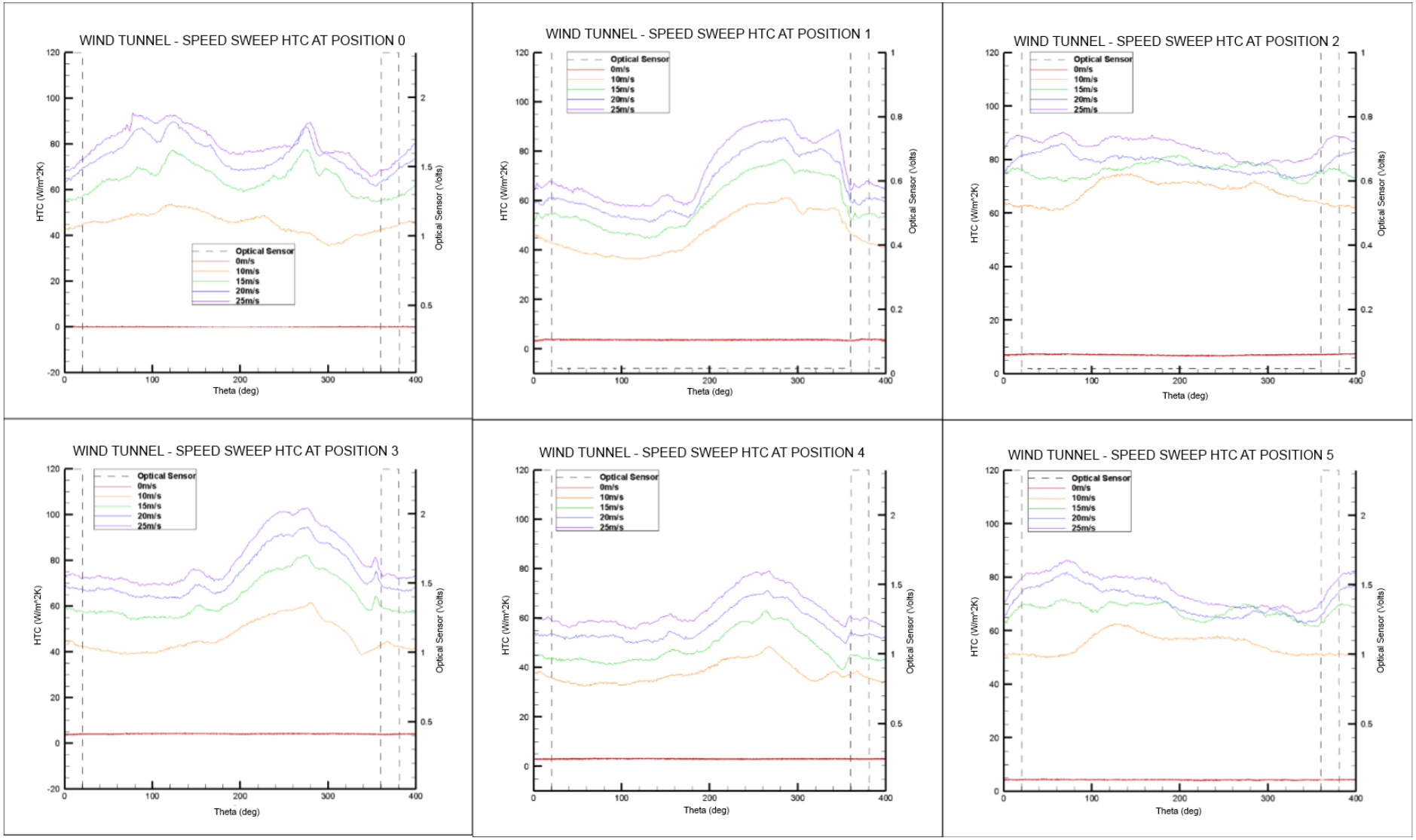

Figure 61: Sidewall positional graphs of heat transfer coefficient through 0-25m/s speed range.

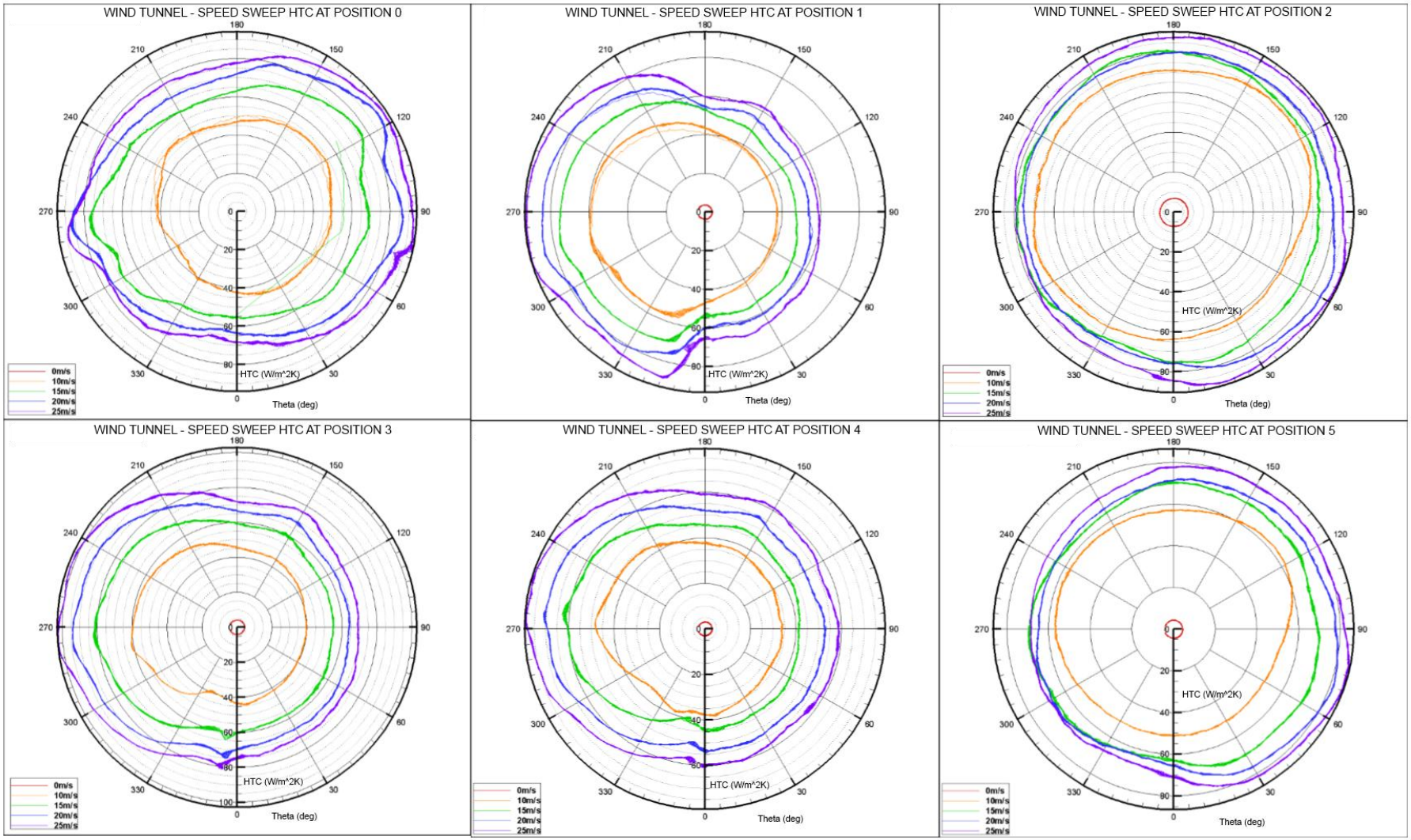

Figure 62: Sidewall positional polar graphs of heat transfer coefficient through 0-25m/s speed range.

4.2.7. 3D Analysis

Data recorded in the wind tunnel was transferred into 3-Dimensional (3D) visualisations as described in Section 3.3.3, with the results summarised in Figure 64 and Figure 65. The 3D visualisation utilised a coloured surface contour across the tyre sidewall, spanning the areas recorded by the sensor. In order to view the entire surface of results, the 3D plots have been orientated to a frontal view, but can be freely rotated within the Tecplot software.

The global scale, showing the surface contour plot for a fixed range of HTC, identifies two key elements. The first relates to a key principle of heat transfer, whereby the average HTC increased with speed; relative velocity between the wheel's surface and the air flow. The global scale also provides good visualisation for the previous analysis, where it was found that the highest levels of heat transfer on the upstream side (LHS) of the tyre occurred toward the outer diameter (Point 1 in Figure 63) where the flow is partially stagnated, while on the trailing side, right-hand side, they occurred toward the inner diameter (Point 3 in Figure 63), where flow disturbances from the Spoke area affected the degree of HTC. Point 2 in Figure 63 corresponds to Position 4 of the hot film locations, where the highest level of HTC was experienced given its location on the sidewall high point where free-stream flow dominates.

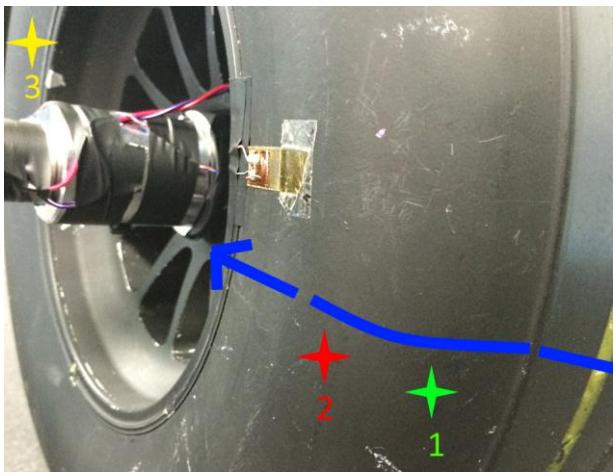

Figure 63: Identification of the key areas of sidewall HTC (1) Highest level of heat transfer on tyre sidewall (upstream side) (2) tyre sidewall high-point (3) Highest level of heat transfer on tyre sidewall (downstream side).

On the local scale, showing a custom range of HTC for each speed, the HTC from the ID to the high point of sidewall profile was greater than that downstream of the high point to the OD; a much more user friendly methodology for presenting results where pattern occurs across the radius and circumference of the sidewall. Earlier, it was discovered that position 4 (ID+47mm) experiences the lowest average heat transfer throughout the speed range. The use of 3D plots eliminates the ambiguity when reading polar plot traces by employing a coloured surface contour. The results showed a blue band for 0-20m/s indicating low HTC according to the scale, while 25m/s showed a green-yellow moderate HTC comparably smaller to the rest of the surface at that speed.

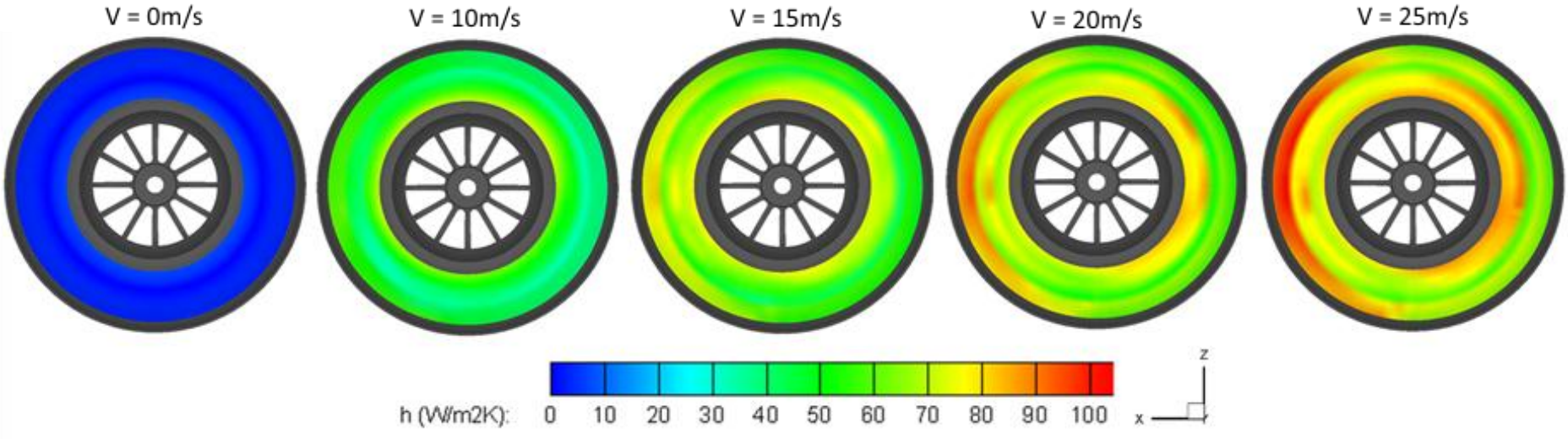

Figure 64: Visual data plot of wind tunnel results for velocity (V) = 0-25m/s within a global scale.

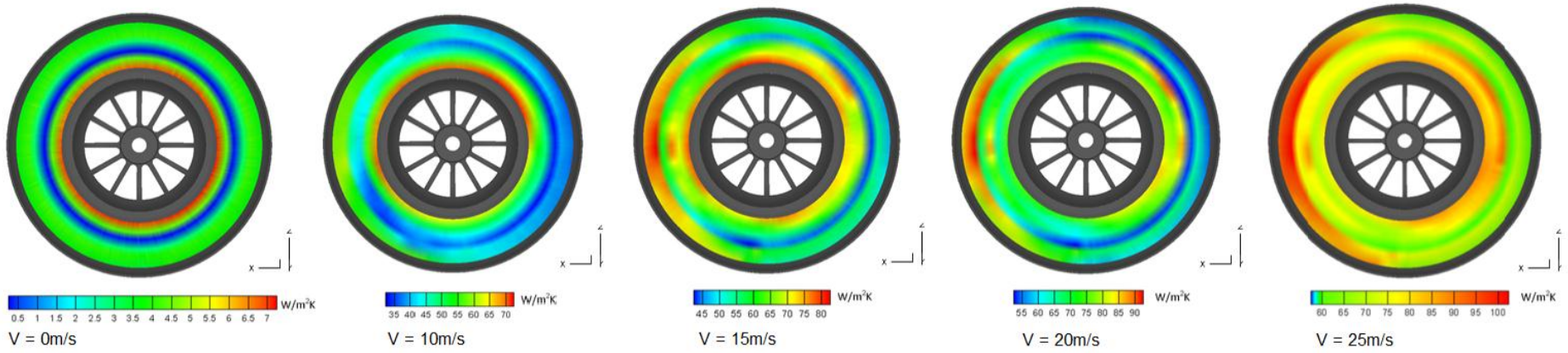

Figure 65: Visual data plot of wind tunnel results for velocity (V) = 0-25m/s with local scales.

4.2.8. Spokes

The non-dimensional heat transfer, Nusselt number (Nu), can be used to provide an overview of heat transfer within the system, averaged across an entire rotation. Figure 66 outlines the results for the spoke region (including wheel rim) on both the leading, and trailing surfaces.

The trailing surface shows lower average heat transfer compared to that of the leading, which experienced a higher degree of heat transfer as a result of its more direct pathway through the air; the leading spoke experiencing stagnated flow. The leading spoke surface was also in the path of the turbulent air from the spoke directly preceding it, resulting in greater heat transfer capability.

Both surfaces of the spoke follow the same trend, where at a Reynolds number (based on tyre velocity and diameter, 0.31m) of approximately 200,000 (10m/s) there occurred a transitional period between flow velocities of 10-15m/s.

The wheel rim shows similar characteristics in non-dimensional heat transfer as the two spoke positions, with magnitude akin to that of the leading spoke surface, however, after the transitional period, distinguishes the variation in heat transfer at different positions, with heat transfer of the rim increasing at a different rate compared to that experienced by the spoke surfaces.

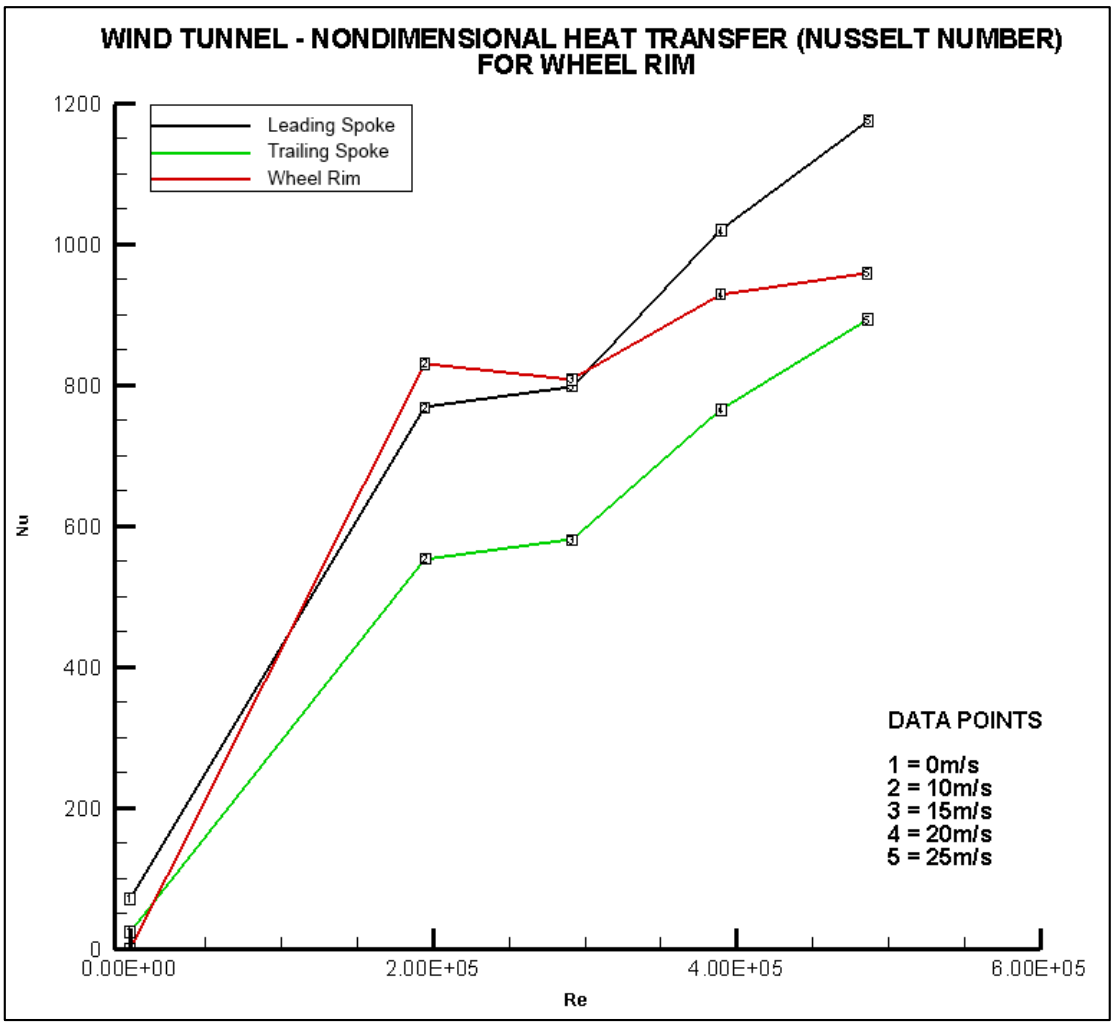

Figure 66: Non-dimensional heat transfer (Nu) of spokes and rim from wind tunnel test speed sweep.

Given the evident transitional period occurring between 10-15m/s, a more focused analysis was restricted to 20-25m/s (Figure 67), so as to ensure a clear analysis without the effect of transitional airflow on the heat transfer. The leading and trailing spoke surfaces varied by approximately 10W/m^{2}K at both speeds; given the variations seen at 10-15m/s, this is a good indication that the flow structure became steady in this speed range.

The leading spoke showed the least variation between 20 and 25m/s, located between 150-200deg in the rear top quadrant of the wheel. Both leading and trailing spokes exhibited the same characteristic as the sidewall whereby the HTC increased from TDC to BDC for the leading LHS of the tyre, and decreased from BDC to TDC on the trailing RHS. The leading spoke, however, experienced a period of HTC increase for a range approximately 50deg greater than that of the trailing spoke.

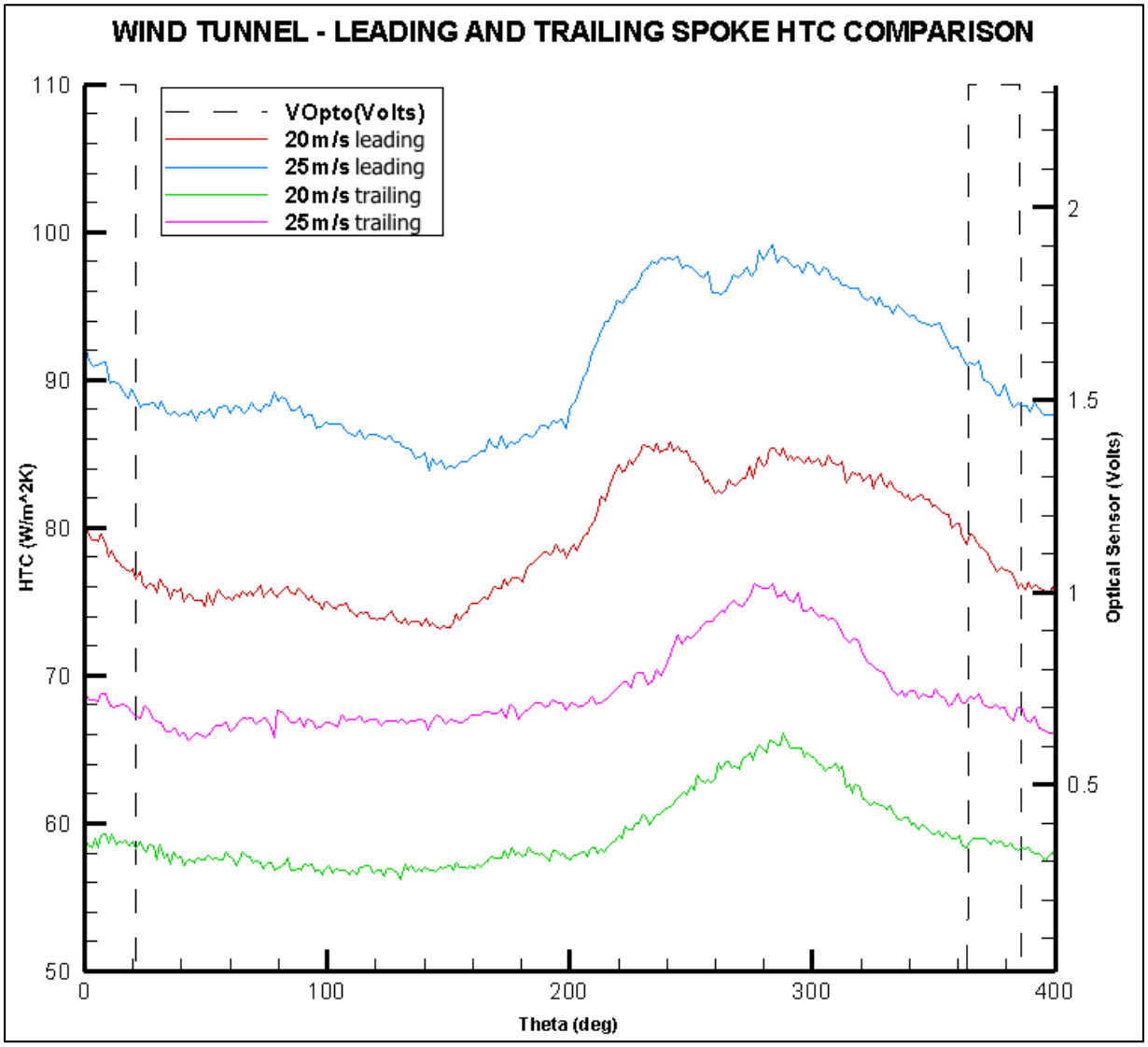

Figure 67: Spoke heat transfer data for 20-25m/s in the wind tunnel.

4.2.9. Tyre Surface Velocity and Air Speed Mismatch

Tests were conducted under various velocity configurations to determine the influence on sidewall HTC as a result of external flow application and tyre rotation. The effect of misaligned tyre surface velocity and external flow velocity was also analysed.

Sidewall

Point 5 in Figure 68, corresponding to 25m/s, shows that at a Reynolds number (at tyre diameter of 0.31m) of approximately 480,000, the effect of tyre rotation becomes negligible with respect to the averaged dimensionless heat transfer, Nu_{av}. Instead, it was characterised by the speed of the airflow; the stationary tyre showed very similar results (See sub-plot A) to the speed matched tyre (25m/s tyre and air). The results below 25m/s, however, showed the effect of over and under-speed tyre rotation to vary the rate of heat transfer at a given flow velocity.

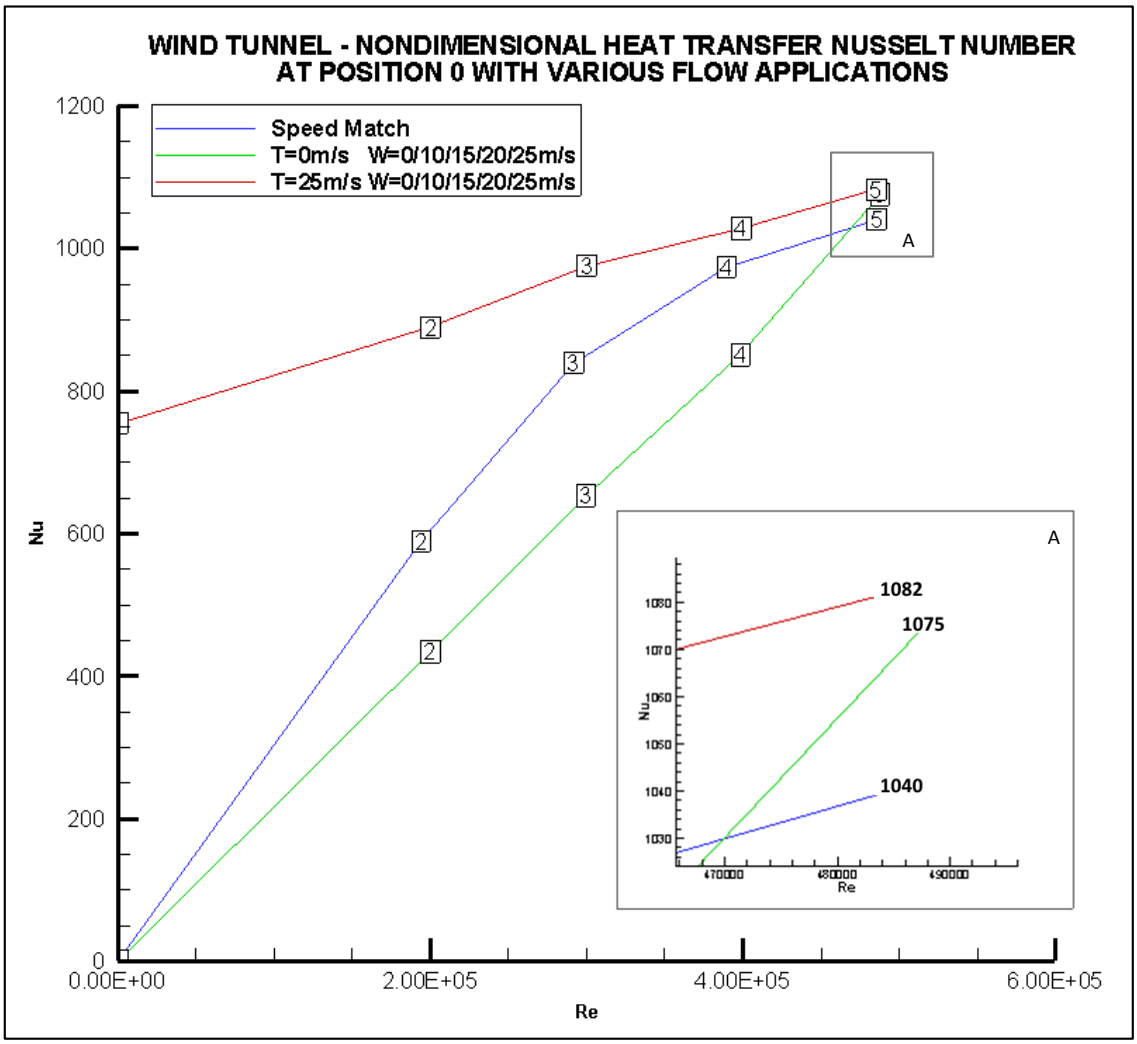

Figure 68: Sidewall HTC for various speed configurations (T = tyre surface speed, W = wind tunnel flow velocity) under-speed when $V_{TYRE} < V_{WIND}$, over-speed when $V_{TYRE} > V_{WIND}$.

The over-speed tyre—where tyre surface velocity was higher than that of the air flow velocity applied—rotating at 25m/s throughout an airflow sweep from 0-25m/s, showed consistently higher HTC values compared to the speed matched case—where tyre surface and air flow velocities were equal; the delta between the two decreased as the air flow increased. The initial HTC at point 1 (0m/s) for the over-speed trace outlines the degree of heat transfer due solely to the tyre's rotation. This accounts for approximately 77% of the overall heat transfer, with heat transfer showing an almost linear trend with increasing air flow. This linear trend stems from the stationary tyre results, whereby it becomes evident that increasing airflow had an increasing linear effect on the HTC, however, comparing the two data sets, it is evident that the constant tyre speed affected the rate of increase; with 25m/s showing a much shallower gradient compared to that of the stationary tyre. This is related to the fact that the initial data point for the heat transfer was non-zero given the induced flow that the tyre's rotation causes, corresponding to findings by Knowles (2005), that a cylinder rotating at a speed equal to that of the air flow is less sensitive to the effects of Reynolds number than when stationary. Despite the concordance in results at 25m/s, it is evident that flow structures still vary for stationary and rotating wheels at speeds below 25m/s. Perhaps at Re=480,000 a highly turbulent flow field has been reached, resulting in a standardised HTC across each of the speed variations.

4.3. Computational Results

In the following section the computational results are presented and explored in order to gain insight into the characteristics of the flow and heat transfer associated with the wheel assembly used in the wind tunnel tests—stationary and rotating configurations. Comparisons of two rotational meshing methodologies within the Exa PowerFlow CFD suite are compared to determine the most accurate methodology, and the effect of geometry scaling is investigated. CFD measurements utilise a surface integration, which involves every surface of the selected component. Though probes can be used to identify a point measurement, they cannot follow a surface point throughout its rotation.

4.3.1. Stationary Wheel Assembly

The original simulation was conducted without measurement time boundaries, in order to determine the time required for convergence. Residuals were found to converge at approximately timeframe 50. All further simulations were then set to record from timeframe 70, to ensure that measurements were initiated after the point of convergence (timeframe 50). Data recording commenced from timeframe 70 and ended at timeframe 110, averaging results every 1 timeframe (approximately every 9deg of rotation). Simulation properties were set to ensure that a full tyre rotation was captured within the given simulation time (Appendix 2). Integrated results on PowerFlow allow the user to capture the average HTC over the entire surface of the component (herein separated as tyre and disc).

Separation point location will affect the heat transfer given its effect on wake structure, and therefore recirculated flow due to tyre rotation; the earlier the separation, the earlier the development of the turbulent

wake. Despite the rearward turbulence, the low speed nature of the vortices results in less efficient cooling than undisturbed flow, particularly given that the tyre's rotation induces flow recirculation.
Simulated results for this thesis (Figure 69) correlate well to findings within the literature, with separation for the stationary tyre occurring at approximately 235deg CCW from the SP. Note that results in Figure 69 and other CFD result figures show the instantaneous flow rather than a time-average, and hence contain various unsteady structures. Fackrell (1974) determined from stationary wheel experiments, that the separation point of a stationary wheel occurs at approximately 210deg CCW from the stagnation point. Mears (2004) found stationary separation to occur at 210deg experimentally, while that of the rotating case occurred at approximately 280deg CCW from the SP, with CFD simulations showing separation to occur at 245deg CCW.

The effect of cylindrical proximity to a wall was discussed by Sumer & Fredsoe (2006), whereby the angular position of the stagnation point was found to move to a lower angular position as the tyre's rotation forced the flow in a downward direction (Sumer & Fredsoe, 2006). Simulated results show the stagnation point seems to be slightly lower than the central point on the tyre, following the findings of Sumer.

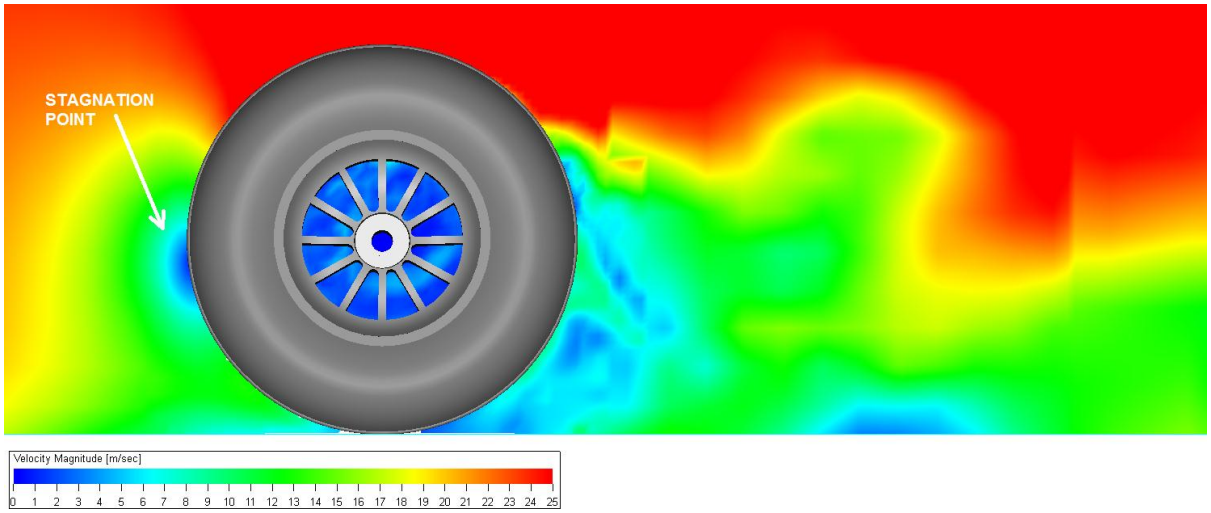

Figure 69: Velocity magnitude cross-sectional image plane for stationary tyre.

Though results through integration cannot be compared to single surface results from the wind tunnel, they allow for comparison of the overall heat transfer capability of the component in each separate test case; providing insight into the variation of flow interaction through the use of realistic and theoretical moving wall boundaries. Integrated results for the stationary configuration (Figure 70) indicate the tyre sidewall HTC averaged 78W/m^{2}K. Marginal variation from the wind tunnel result, 83W/m^{2}K, can be attributed to the integration considering both sidewalls (inboard and outboard), the tread, and the internal surface of the tyre, whereas the wind tunnel results are determined for the outboard sidewall only. Investigation of the simulation revealed low HTC at the front and rear of the tyre (stagnation points), while maintaining magnitude similarity on both sidewalls. A second integration box was generated to contain only the outboard sidewall, with results attesting to this assumption, showing an average HTC of 89W/m^{2}K. The CFD prediction is approximately 7% higher than the wind tunnel measurement.

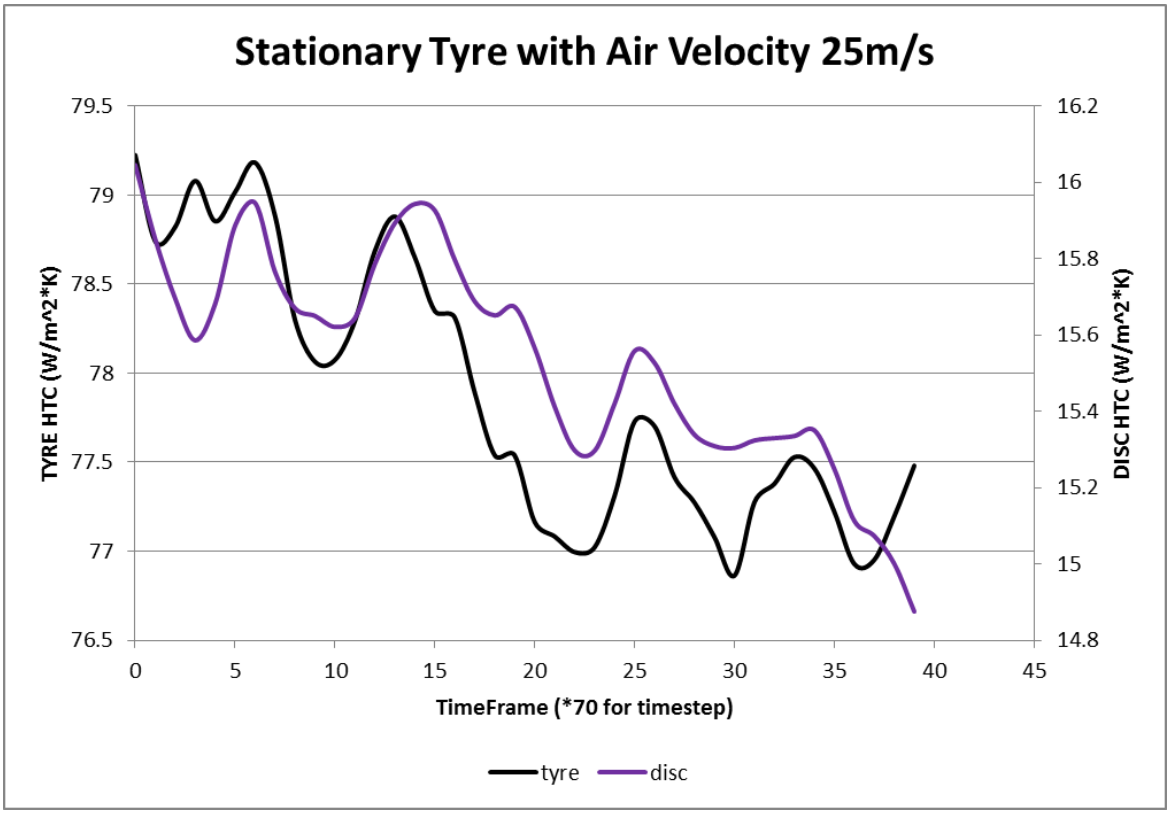

Figure 70: Integrated heat transfer coefficient for tyre and disc component surfaces.

Throughout the simulation, the results for both tyre and disc show good consistency, with minor fluctuations of HTC within a range 3W/m^{2}K. Tyre and disc fluctuations followed a similar trend despite their varying magnitudes; HTC of the tyre was approximately five times higher than that of the disc. This would suggest that they were experiencing similar flow structures relative to their size despite the external/internal variation. When considering the Reynolds number experienced at 25m/s by the tyre (using tyre diameter of 0.31m) , 4.94x10^5, and disc (using disc diameter 0.14m), 2.23x10^5, it is understandable that the magnitude of the tyre HTC was much larger than that of the disc given its higher degree of turbulence, however, consideration of the geometrical variation between disc and tyre, diameters 0.14m and 0.31m respectively, the two are experiencing similar flows relative to their diameters (Re ÷ Ø = 1x10^5 for both disc and tyre).

The rear bottom quadrant of the tyre sidewall has comparatively low HTC to the rest of the surface (Figure 71) as a result of the stagnant airflow behind the tyre. Flow rearward of the tyre will tend to be recirculated from the vortical structures, which were evident in the streamline traces. The highest level of heat transfer is evident rearward of the wheel rim, a result of the turbulent flow induced by through hub flow from the Inlet scoop.

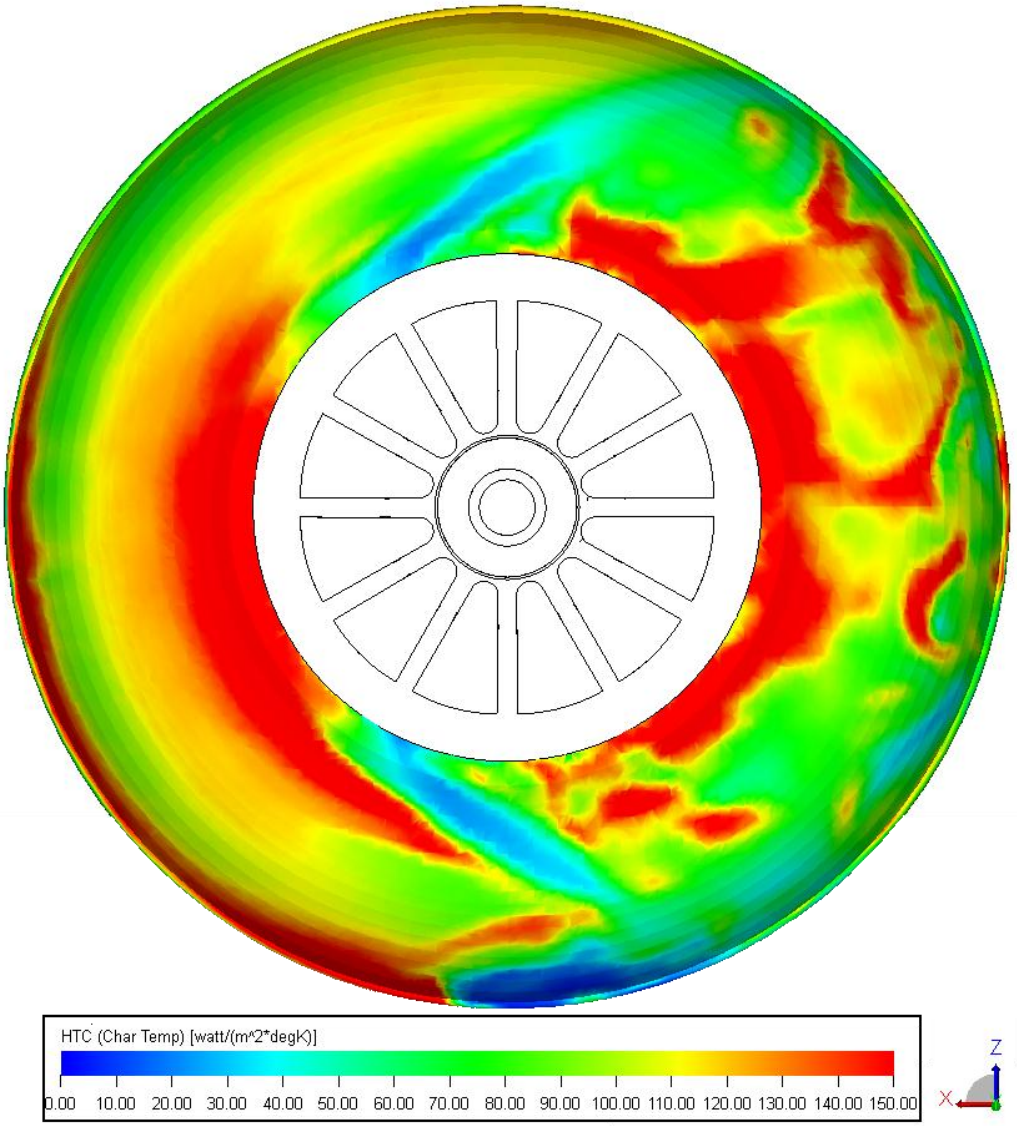

Figure 71: Sidewall HTC for stationary Wheel in 25m/s flow.

Figure 72 outlines the HTC experienced on the surface of the disc in all directions; flow in negative x-direction. The inboard face experienced a much greater level of heat transfer given the scoop flow is directed onto the inboard side; this is supported by Figure 73 where the inboard flow is higher than the outboard side. The contrast between the level of flow on the inboard side to the outboard is the reason behind the disc inboard face curved extrusions, however, flow around the front of the disc was more prominent in the streamline representation than flow through the disc vanes. Both upper and lower surfaces showed similar trends in HTC, contrary to the upper and lower areas of the tyre sidewall; this is most likely related to the fact the disc is near a wall, however, at an equal distance around its circumference, therefore not incurring the effects the tyre is exposed to due to the ground plane contact.

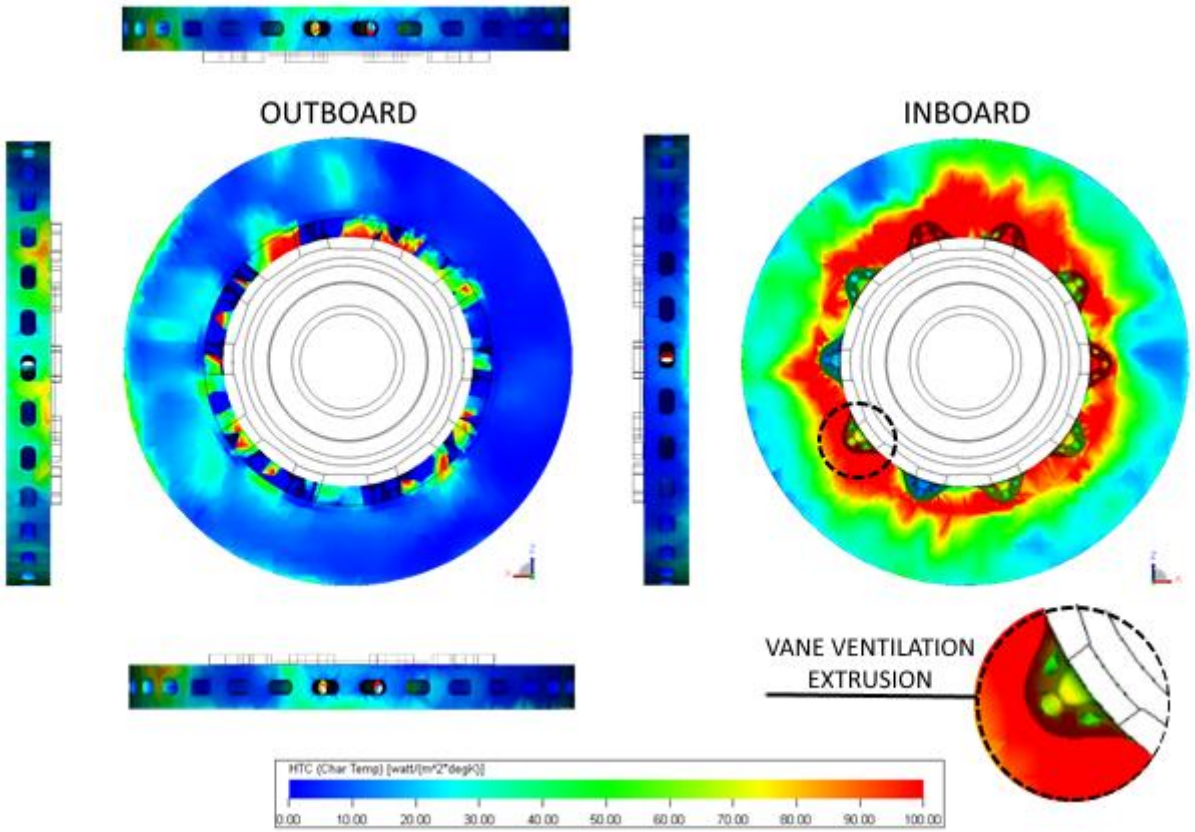

Figure 72: Disc HTC surface image for the stationary assembly with V_{AIR} =25m/s (tyre, upright and wheel rim hidden).

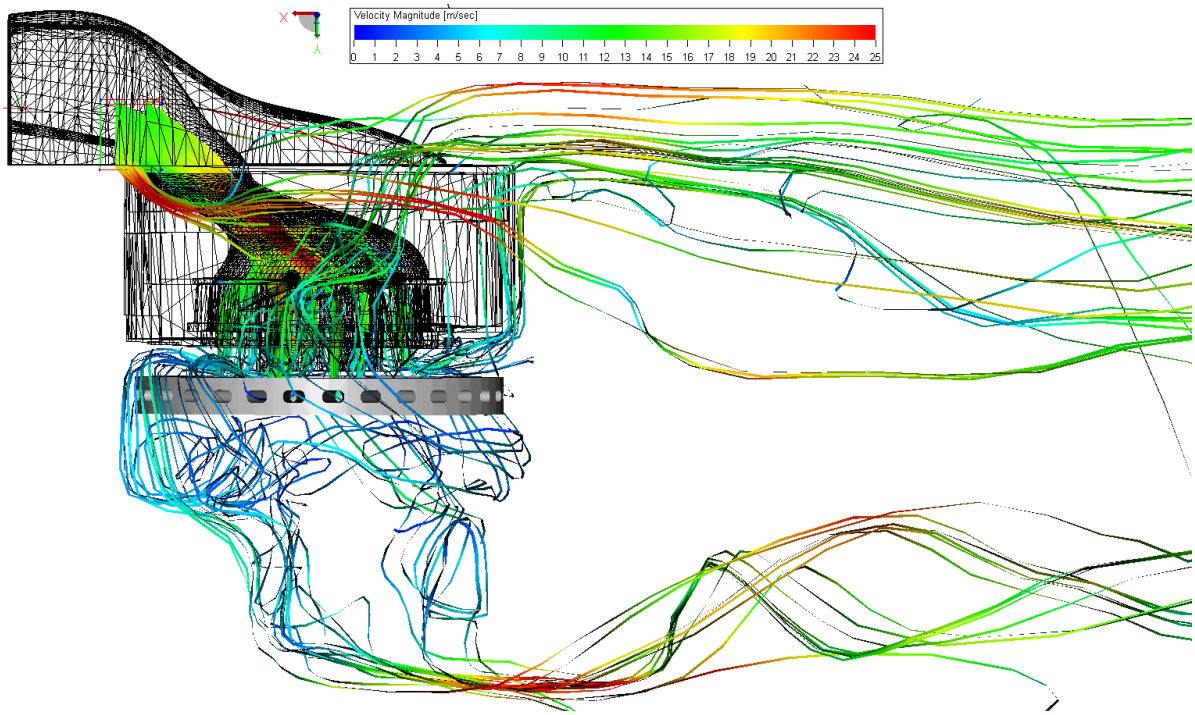

Figure 73: Through Hub flow from scoop inlet of stationary wheel assembly with V_{AIR}=25m/s (tyre and wheel rim hidden).

Despite the significant level of flow evident on the outboard side of the disc, Figure 74 displays that the inner sidewall surface of the rim, between spokes, experienced the lowest levels of heat transfer of the component. The stationary position of the tyre allows the free-stream flow to travel past the sidewall and wheel rim, picking up the flow spillage from the wheel rim, carrying it further downstream—this is a potential cause of higher HTC toward the inner diameter of the sidewall downstream of the rim.

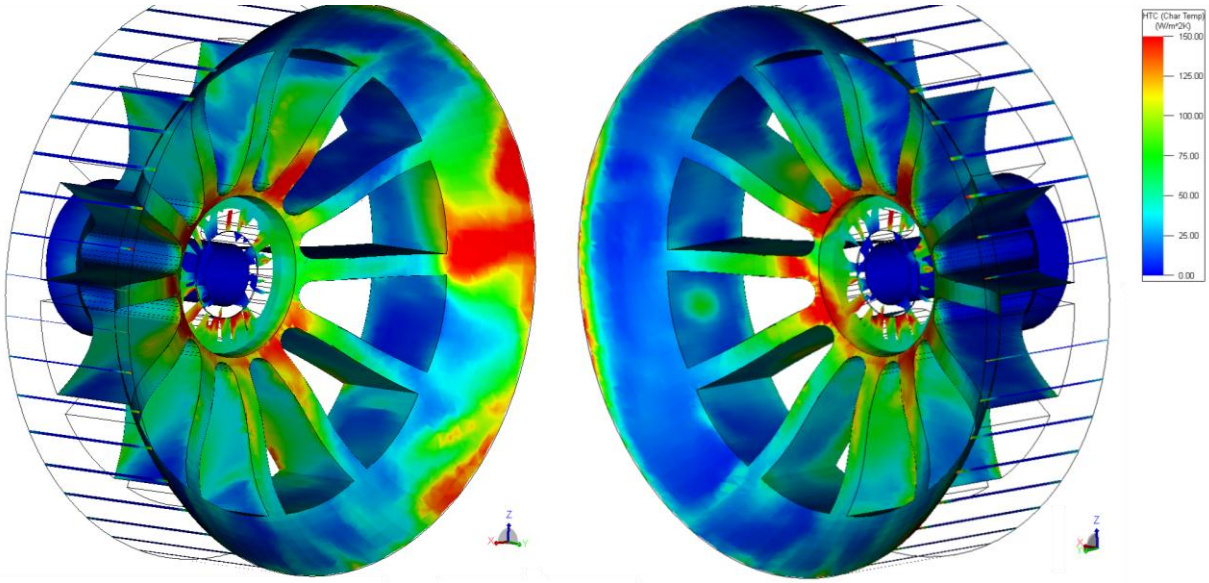

Figure 74: Wheel rim HTC surface image for the stationary assembly with V_{AIR} =25m/ (disc, tyre and upright hidden).

4.3.2. Sliding Mesh

Using the sliding mesh (SM) methodology component geometry within a bounded region is physically rotated, a development from the moving reference frame (MRF) methodology in which a velocity is imposed through the application of rotational fluid forces within a bounded region.

Integrated surface results in Figure 75 outlines that the introduction of rotation resulted in different flow structures for the disc and tyre, contrary to the stationary case, where the two components experienced similar steady flow structures, resulting in comparable trends of HTC throughout the simulation time frame. The variation in HTC due to rotation was not as evident for internal results to the same degree as the external results, with the average HTC over the tyre surfaces was 95W/m^{2}K, 17W/m^{2}K higher than that of the stationary case, while that of the disc was 14W/m^{2}K, similar to the stationary case, 16W/m^{2}K. The range of average surface HTC values experienced by the disc in the rotational case, 1.4W/m^{2}K, comparable to that of the stationary case, 1.17W/m^{2}K. Analysis of mismatched tyre surface and flow velocities supports these findings, which showed that the rotation of the tyre had less of an effect on the overall convective heat transfer of the disc than the flow velocity.

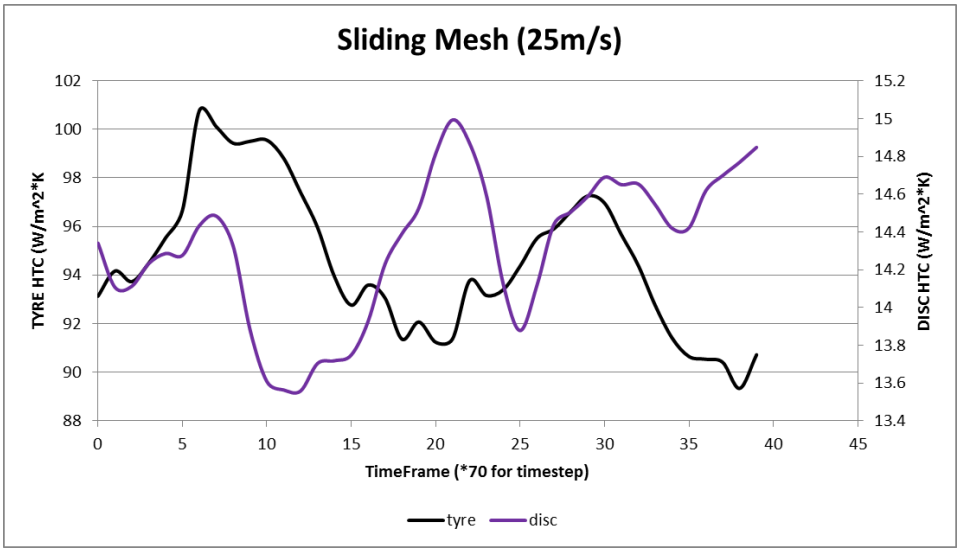

Figure 75: Sliding mesh simulation time averaged HTC for tyre and disc component surfaces.

Results of average HTC from the surface integrated data allowed the Nusselt number to be calculated at 25m/s using the respective diameters of each component (D_{TYRE}=0.31m, D_{DISC}=0.14m). The CFD results (Figure 76) show an increase of 24% at the sidewall, while the disc results are 33% lower than those in the wind tunnel. The difference can be attributed to the measurement technique used in CFD integrating every surface of the tyre or disc, as opposed to the wind tunnel, which logged only the outboard sidewall and a disc vane.

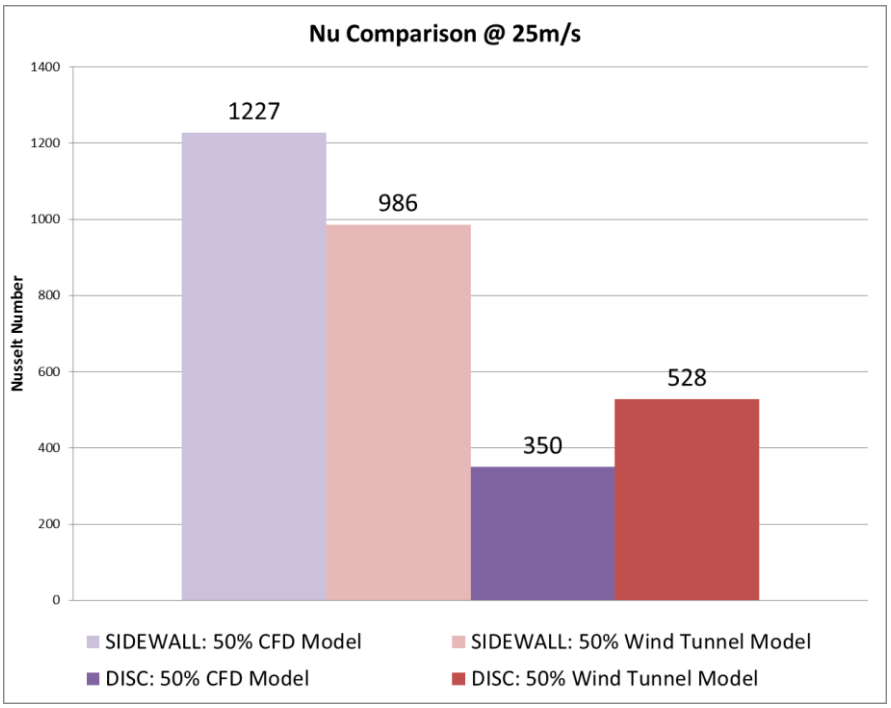

Figure 76: Nusselt number correlation to wind tunnel results for tyre sidewall and disc at 25m/s.

The separation point for the stationary simulation was found to occur at 235deg CCW of the stagnation point. For the rotational simulation using sliding mesh boundaries, the separation point occurred at 265deg (Figure 77), which agrees with the findings of Knowles (2005), Mears (2004) and Stapleford and Carr (1971), whereby

cylindrical rotation is found to advance flow separation compared to the stationary case. Separation is advanced compared to the stationary wheel due to the rotation of the tyre introducing momentum within the boundary layer. Comparable to the results determined in the sliding mesh simulation, Fackrell (1974) and Mears both found separation for a rotating wheel to occur at 280deg CCW, while Knowles reported 270deg CCW. These results, however, were recorded experimentally. Both Mears and Knowles reported CFD separation to be slightly delayed compared to experimental results; Mears, 245deg compared to 280deg, and Knowles, 265deg compared to 270deg.

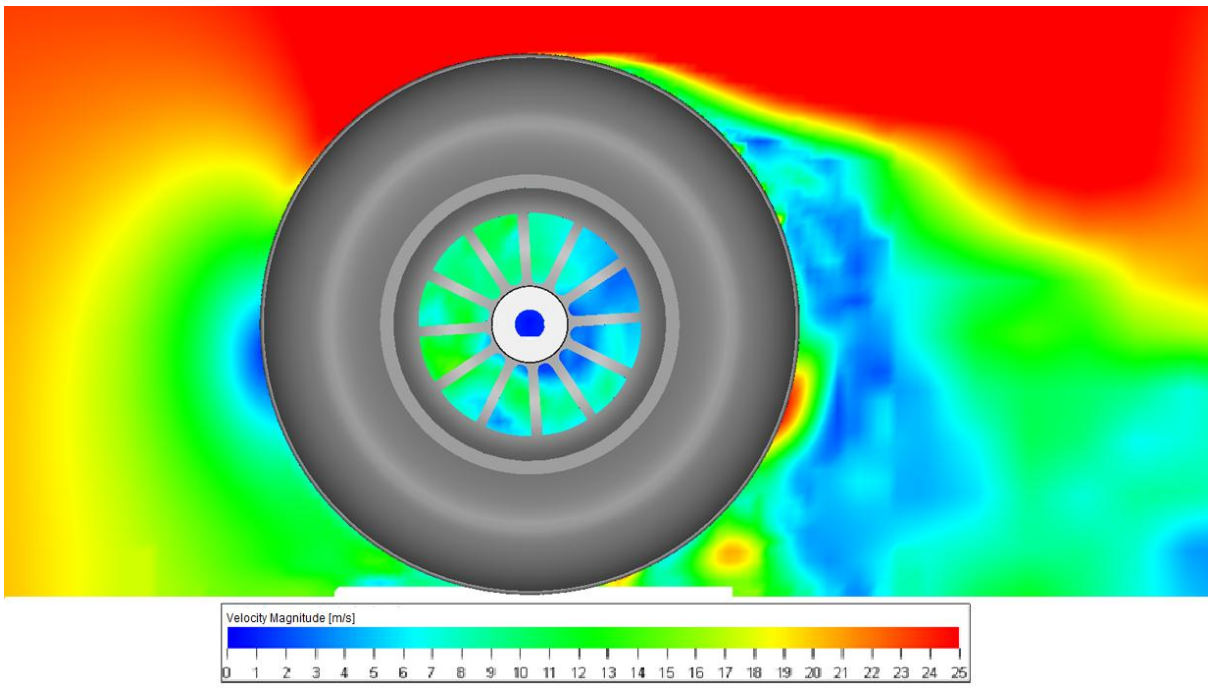

Figure 77: Velocity magnitude cross-sectional image plane for sliding mesh simulation (25m/s).

The range of separation point values from the computational results and the findings of Fackrell, Mears and Knowles, presents itself between 245-280deg. The level of correlation is satisfactory enough to assume the simulation behaved in an acceptable manner, given the marginal variation of setup parameters, such as Re, between the sourced results. The principle of separation advancement due to rotation is noted, and the effect of separation location with respect to heat transfer is highlighted as an important relationship, given the variation of rearward flow structure outlined by several researchers, particularly Kato et al. (2009), to show significant increase in HTC.

Tyre sidewall HTC surface contours extracted (Figure 78) outline a region of low HTC at the bottom rear quadrant of the tyre; the same result was found in the stationary configuration. The rearward flow structure is known to be influenced by the presence of the ground plane. Flow around a rotating cylinder with no boundary restrictions, is found to supress vortex development and have a prominent influence on the near wall flow field (Stojkovic et al., 2002). Similarly, flow around a stationary wheel in ground contact is also found to supress regular vortex shedding (Bearman et al., 1988).

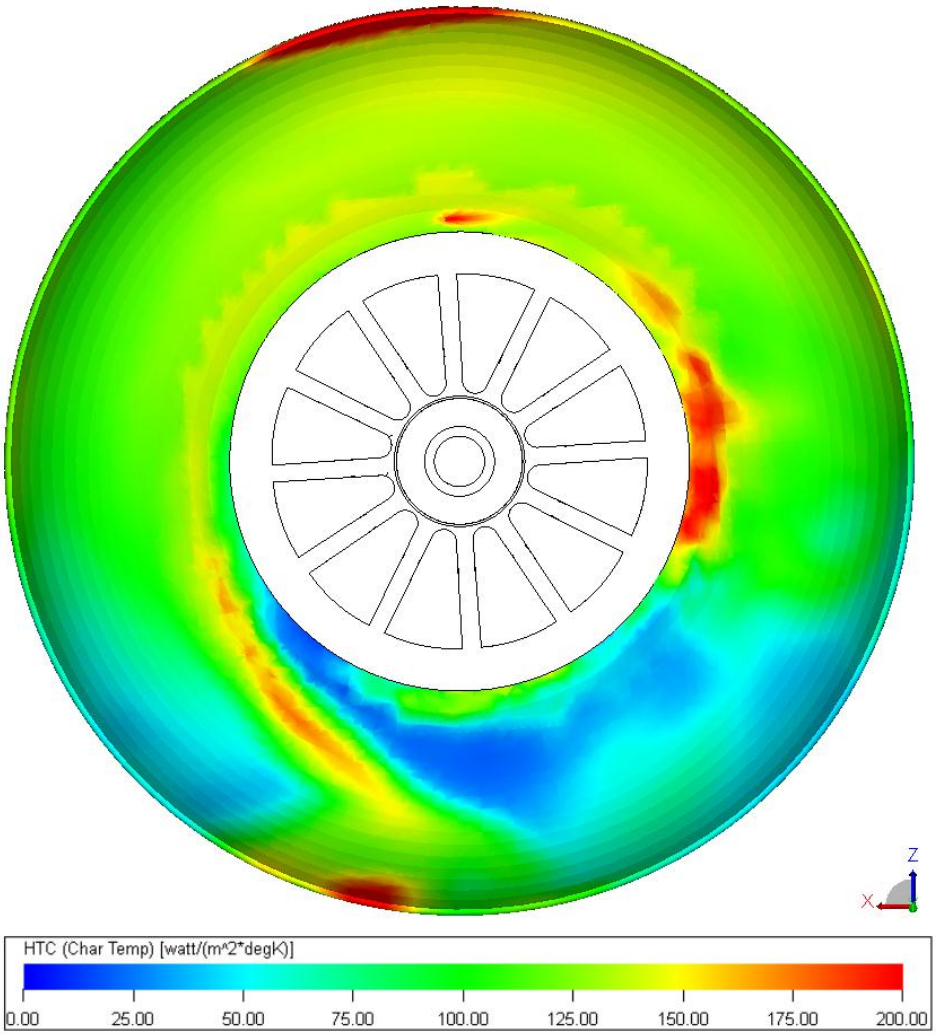

Figure 78: Sidewall HTC at 25m/s – sliding mesh CFD results.

As with the stationary case, the inboard side of the disc, which was exposed directly to oncoming flow directed through the scoop inlet, experienced the highest level of heat transfer (Figure 79). The introduction of rotation increased the heat transfer in all areas of the disc, with trends from the stationary case remaining; front heat transfer higher than rear, and upper approximately equal to lower. The effects due to the introduction of rotation can best be visualised using Figure 80, which shows a direct comparison of through-hub scoop inlet streamlines for the stationary and rotating (sliding mesh) cases.

The most distinct variation between the two cases is that the rotating tyre caused a recirculation of flow toward the rear of the internal geometry. The flow on the inboard side of the disc also experienced a suction effect, with flow travelling along the surface of the disc as it bends around to the outboard side of the disc.

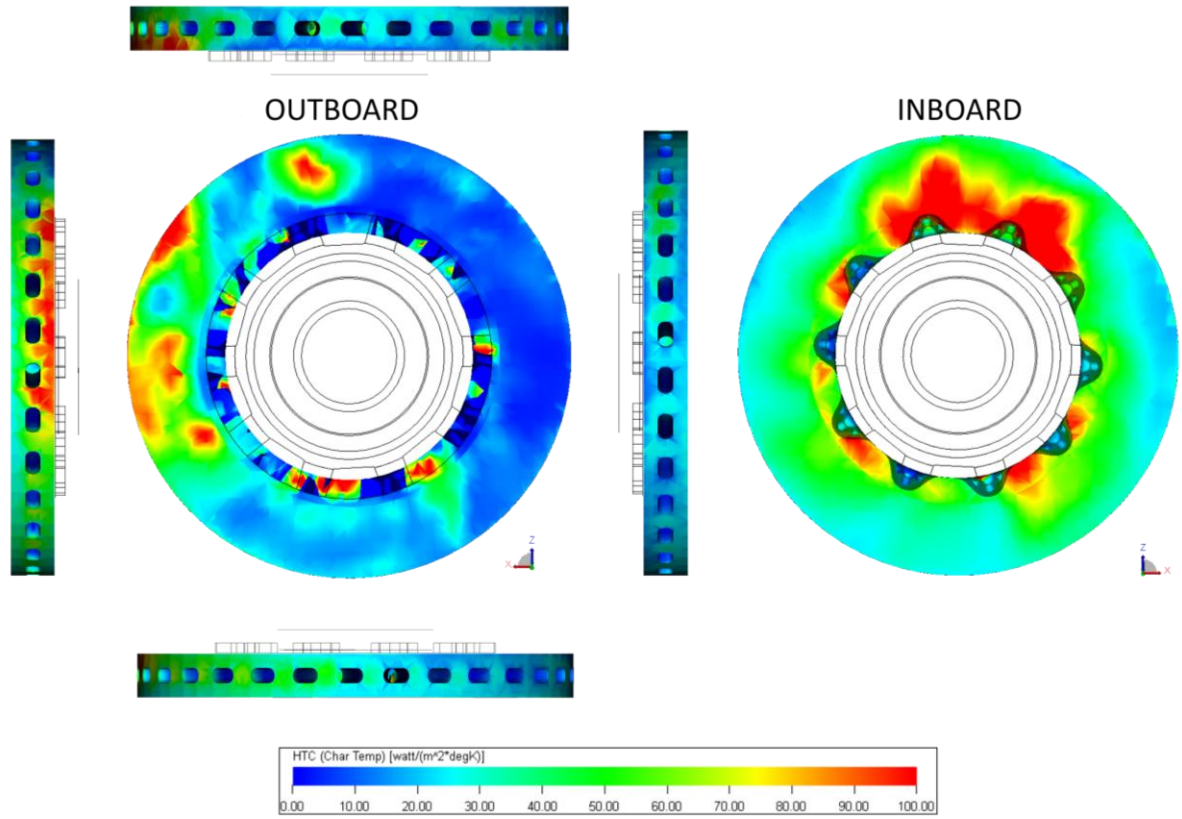

Figure 79: Visual overview of disc HTC using sliding mesh functionality at 25m/s (tyre, upright and wheel rim hidden).

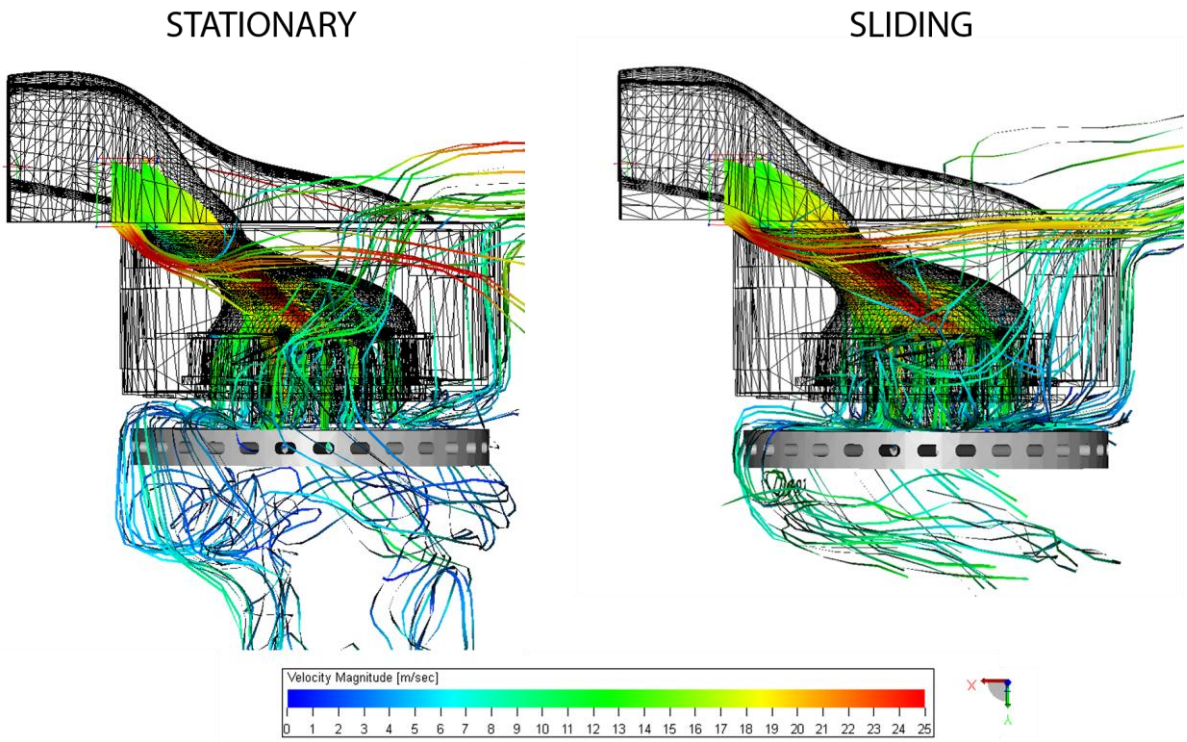

Figure 80: Comparison of scoop inlet internal flow streamlines for stationary and sliding mesh configurations at 25m/s (tyre and wheel rim hidden).

The HTC results for the spokes (Figure 81) show areas of a wide range of heat transfer occurring, with the downstream side of the rim experiencing higher HTC's than the upstream side. Such results indicate the heat transfer at the spokes was affected by flow in the surrounding areas,

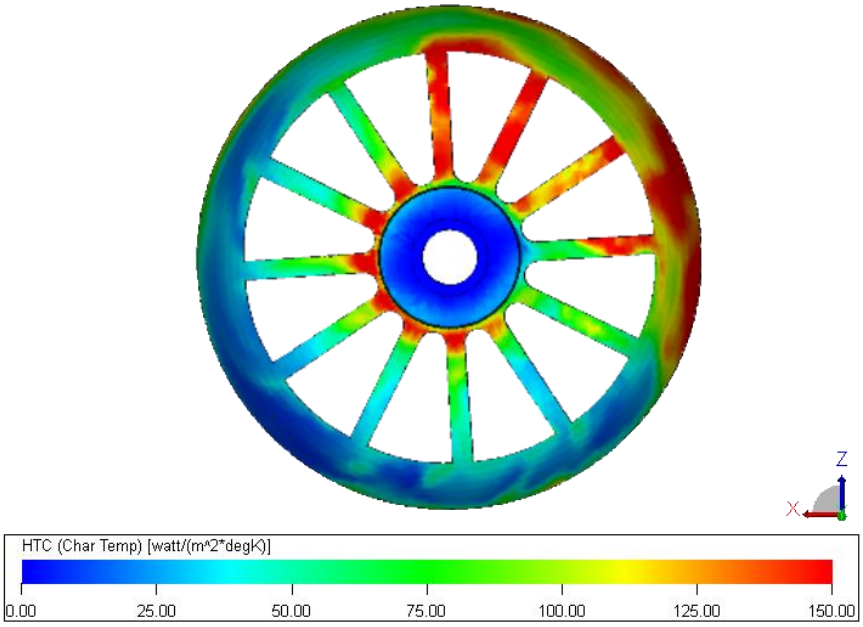

Figure 81: Sliding mesh surface air velocity vs. HTC for spoke region at 25m/s (disc, tyre and upright hidden).

On the inner spoke surfaces, the leading side of the spokes experienced the most heat transfer, as found in the wind tunnel results. The region in which the highest heat transfer was experienced was, with respect to angular position, in the region of separation of the tyre.

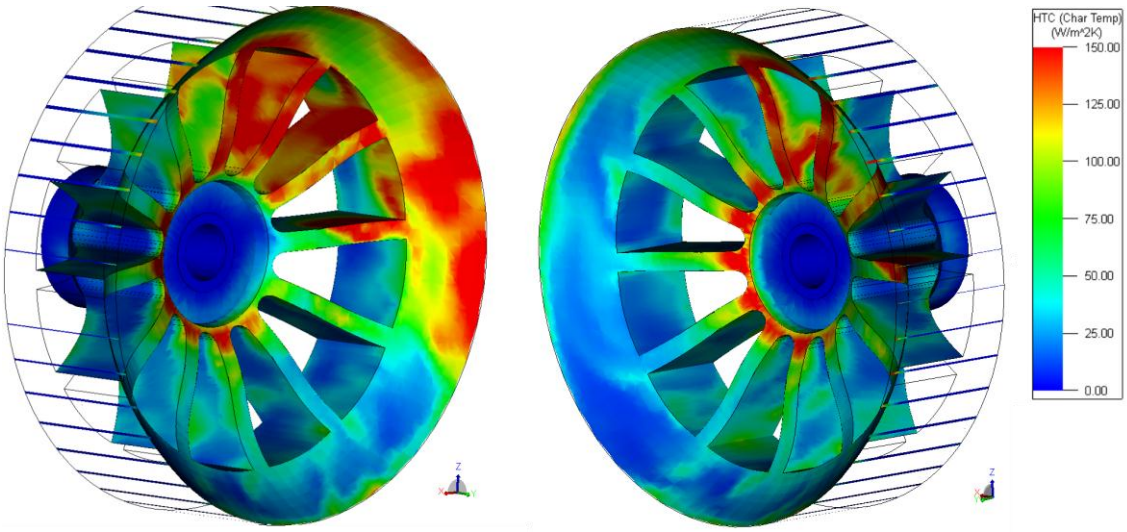

Figure 82: Spoke HTC at 25m/s - Leading and trailing view (tyre rotation around y-axis in positive x-direction) (disc, tyre and upright Hidden)

4.3.3. Moving Reference Frame

Another meshing capability of the Exa PowerFlow software is the Moving Reference Frame (MRF). Unlike the more recently developed Sliding Mesh, the MRF has no physical rotation, instead applying a velocity boundary to component walls located within an assigned rotating reference frame, within which, rotational fluid forces are applied (Gaylard, et al., 2010). The MRF methodology was used to determine the impact of using a simpler methodology on the HTC results. It has been found, from an aerodynamic perspective, that the effect of utilising a rotating wall improves the local pressure distribution accuracy, which affects the flow rate and airflow direction through and around the wheel (Kandasamy, et al., 2012), as such, results were expected to vary from those generated by the sliding mesh.

From the integrated surface results (Figure 83), it is evident that the entire system, internal and external, experienced similar flow structures toward the final 90deg of rotation; the disc at time-step 27 showed the same behaviour as the tyre, with a phase shift of 3 time-steps; equivalent to 27deg rotation. The effect of flow on the exposed tyre compared to that of the internal disc is that the tyre showed a lower level of heat transfer, which may be attributed to the generation of the boundary layer. In turbulent flow, the boundary layer thickens, which results in increased skin friction. High skin friction is a characteristic that delays flow detachment, thus resulting in higher levels of heat transfer. This is the mechanism behind turbulent boundary layers resulting in higher heat transfer and sustaining adverse pressure gradients to delay separation, but is also used as a means of reducing drag – as is the case with dimpling on golf balls. This is perhaps the mechanism behind dimpled wheel rims.

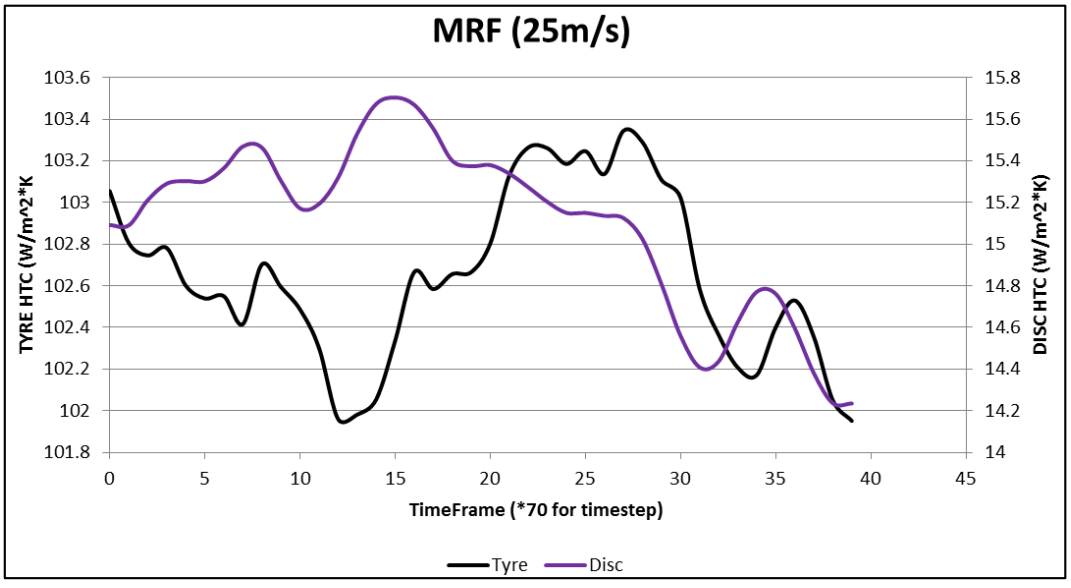

Figure 83: Integrated values of average surface HTC for the disc and tyre employing MRF.

It should be noted that the MRF boundary condition was described as the application of rotational forces to the fluid within a bounded region, however, with no physical rotation. The bounded region, the reference frame, was defined in Figure 35, and is fundamental to the developed flow structure in the MRF condition.

Rotational forces are applied only within the reference frame, leaving external flow to circulate as in the stationary case. This affects the flow distribution, with dispersion patterns varying from reality given the boundary of rotational flow which is evident in 4 key areas when comparing against the Sliding Mesh (Figure 84 and Figure 85): oncoming flow (1), rearward flow structure (2), separation point (3) and the sidewall passing flow. The interaction on either side of the reference frame results in frontal recirculation, and widespread longitudinal dispersion of flow.

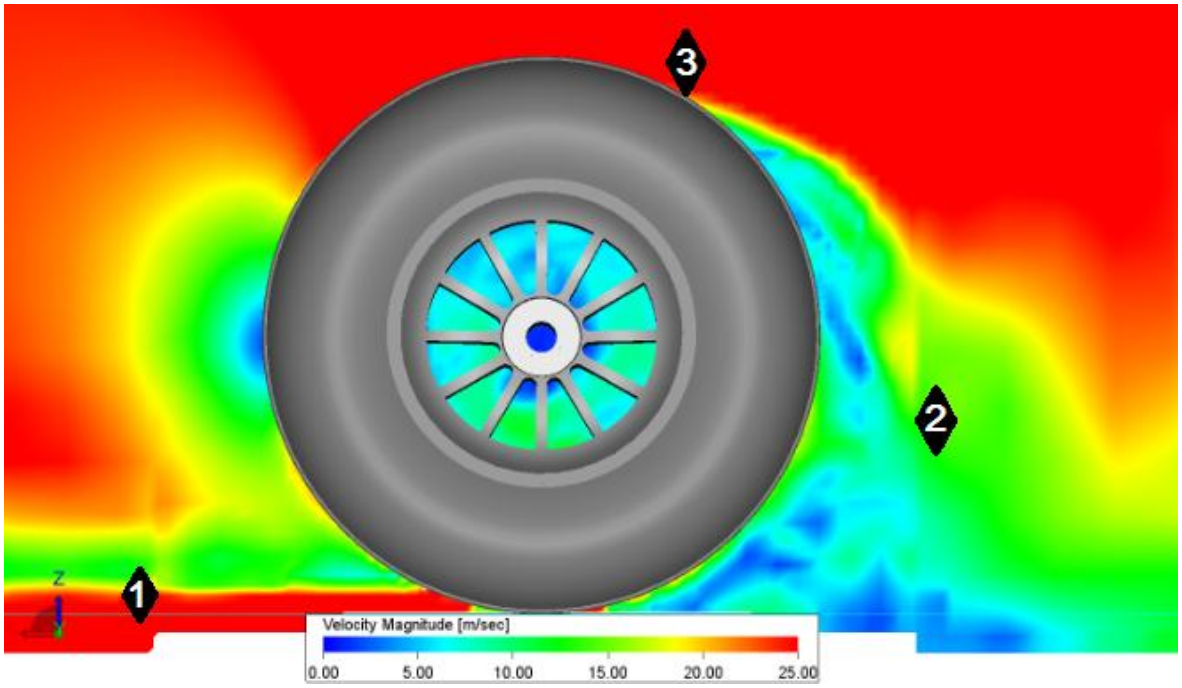

Figure 84: Velocity Plane for MRF Rotational Boundary at 25m/s (1) oncoming flow at free stream velocity (2) wake velocity (3) separation point is delayed using MRF compared to SM.

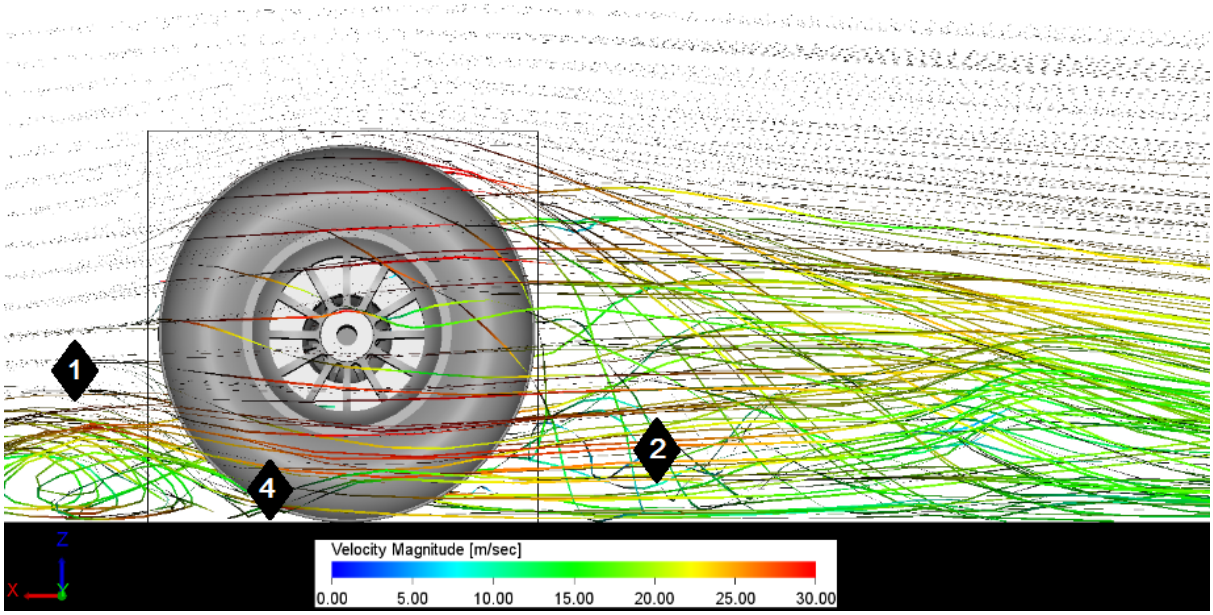

Figure 85: Velocity streamlines for MRF rotational boundary at 25m/s.

The separation point occurs further downstream (245deg CCW from SP) than in the sliding mesh simulation (265deg CCW from SP), representative of the stationary case (235deg CCW from SP). The inconformity of the separation point with rotational flow theory is likely a result of the boundary layer variation in and out of the reference frame region; the separation being a main influence on the rearward flow.

A characteristic of the sidewall HTC results (Figure 86) that stands out relative to the sliding mesh boundary condition is the much lower heat transfer prevalent for approximately a quarter of the tyre's rotation. This is a result of the oncoming flow outlined in Figure 85, with high vorticity upstream of the tyre, rather than downstream. Using sliding mesh a low level of heat transfer existed toward the rear bottom quadrant of the tyre where the flow was turbulent. Since the MRF method applies rotational forces to the fluid within the bounded region, perhaps the method is limited in this respect. The reference frame was used to bind the tyre, disc and spokes, but the areas within and surrounding the tyre remained outside the referenced region. Given it is these areas adjacent to the rotating components that will affect the flow around the tyre, it is necessary to investigate how far away from the bounded rotating wall the reference frame must be positioned for accurate results; this is important given the flow near the rotating wall is affected due to its rotation. The effect was seen with the delayed separation point, resembling that of the stationary case. This suggests there exists a discrepancy between the interaction of fluid and solid for 'imposed rotation' and physical rotation. The HTC was found to be moderate across the tyre's surface (Figure 86); the accuracy of which is questionable given the results from the wind tunnel showed a more regionally banded surface image.

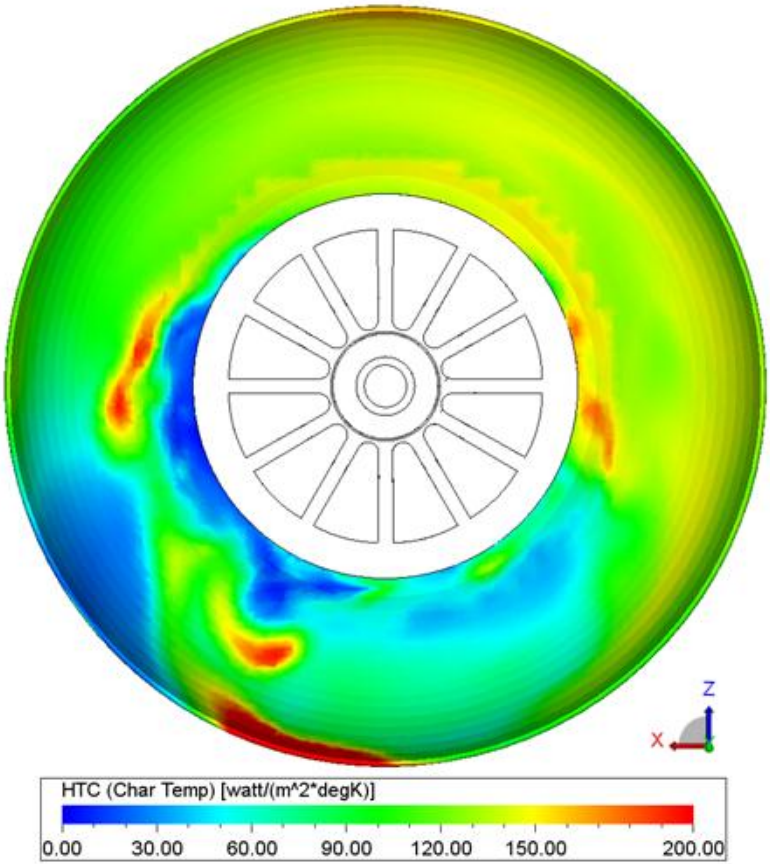

Figure 86: Surface image of HTC for MRF simulation at 25m/s.

With regard to the spokes, as with the sliding mesh, both leading and trailing spoke surfaces experienced the greatest heat transfer at the top half of the wheel rim geometry. In general, there was a moderate average heat transfer across the spokes, with the areas at the maximum range of heat transfer located on edges and the centre of the spoke surface flat. The leading and trailing spoke surfaces show lower HTC's than the sliding results as there is stagnation on the leading spoke surface in the realistically rotating sliding mesh simulation. The MRF methodology does not show this effect as it is not physically rotating, as is reflected in the results. There also existed a rearward bias, though to no concernable degree; a likely result of flow recirculation given the axis of rotation.

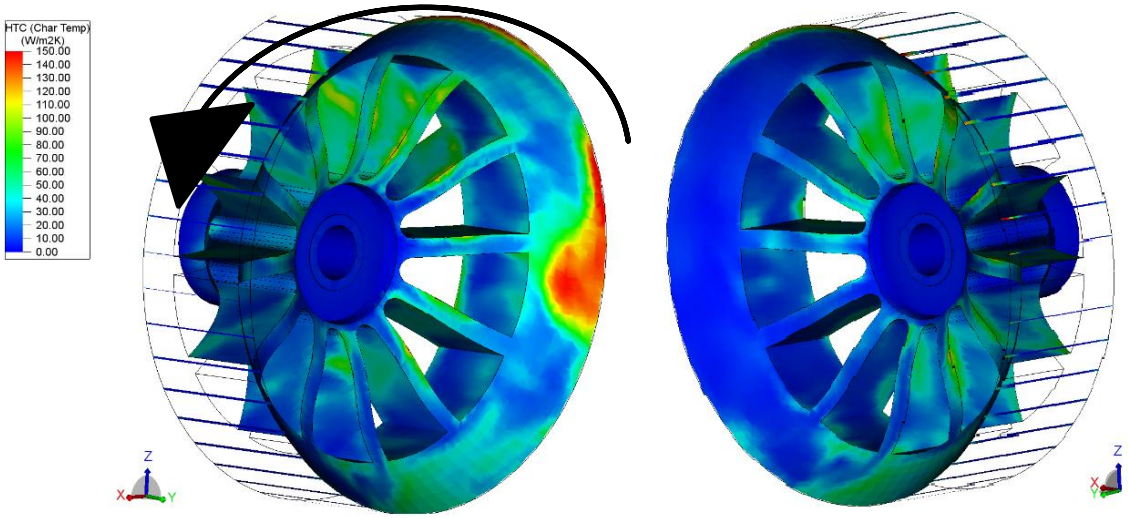

Figure 87: HTC surface Image for Spoke region at 25m/s MRF (disc, tyre and upright hidden).

Streamlines of flow velocity in Figure 85 support the HTC analysis, showing a high degree of unsteady and circulating flow. This should generate a higher degree of heat transfer, however the results are consistently in the moderate region of the HTC scale throughout the period of rotation. The rotation of the fluid after passing internal componentry such as the disc, has caused it to slow to 30-40% of the free-stream velocity. At this speed, the degree of heat transfer capability reduces. In the wind tunnel experiments, it was deduced that when analysing heat transfer along the tyre sidewall, the effect of tyre rotation becomes negligible, instead the heat transfer is characterised by the airflow speed; where the stationary tyre with a 25m/s air flow showed almost equal results to the matched tyre and air flow speed of 25m/s. Internally, this does not seem to be the case; the high degree of turbulence is a result of both the tyre's rotation and the free-stream velocity.

The disc experienced a low degree of heat transfer on the outboard side, while the inboard side, exposed to the oncoming flow from the scoop, showed a much greater range of HTC (Figure 88). The streamline trace in Figure 89 indicates a high degree of internal flow recirculation on the outboard side of the disc, more so than that occurring for the sliding mesh results. Gaylard et al.'s (2010) description of MRF outlined that within the defined region, rotational fluid forces are applied. The method of MRF seems to produce a higher degree of recirculated flow, perhaps an indication of improved accuracy for disc related results, an area that needs to be considered further in Section 0.

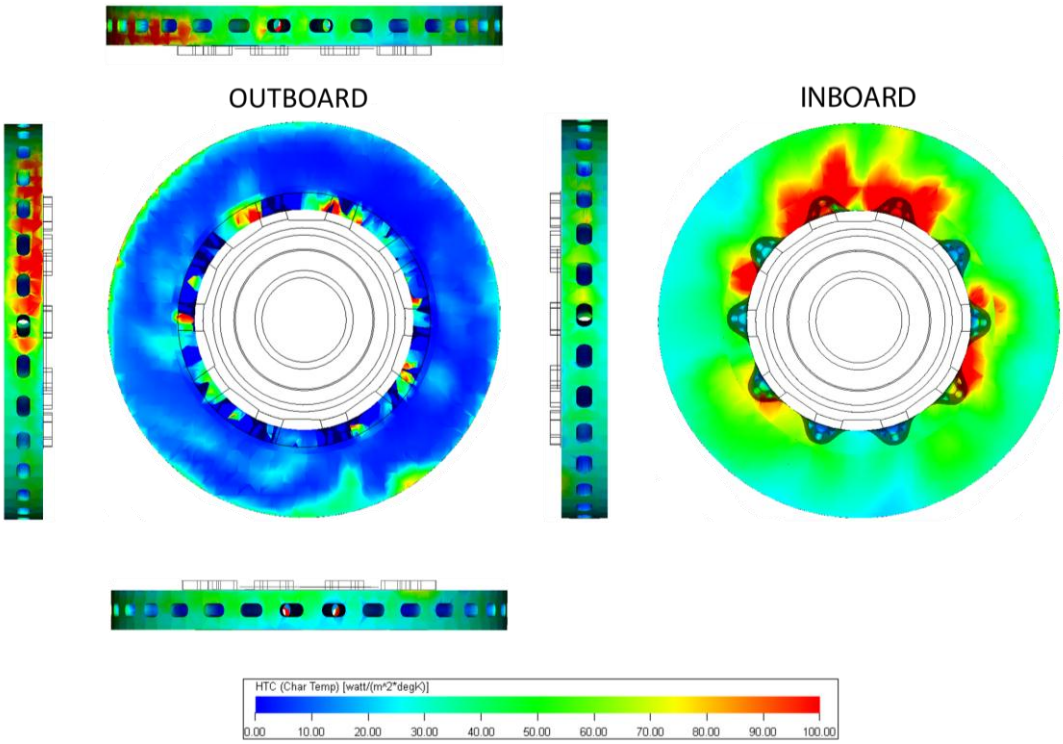

Figure 88: HTC surface images for disc using MRF at 25m/s.

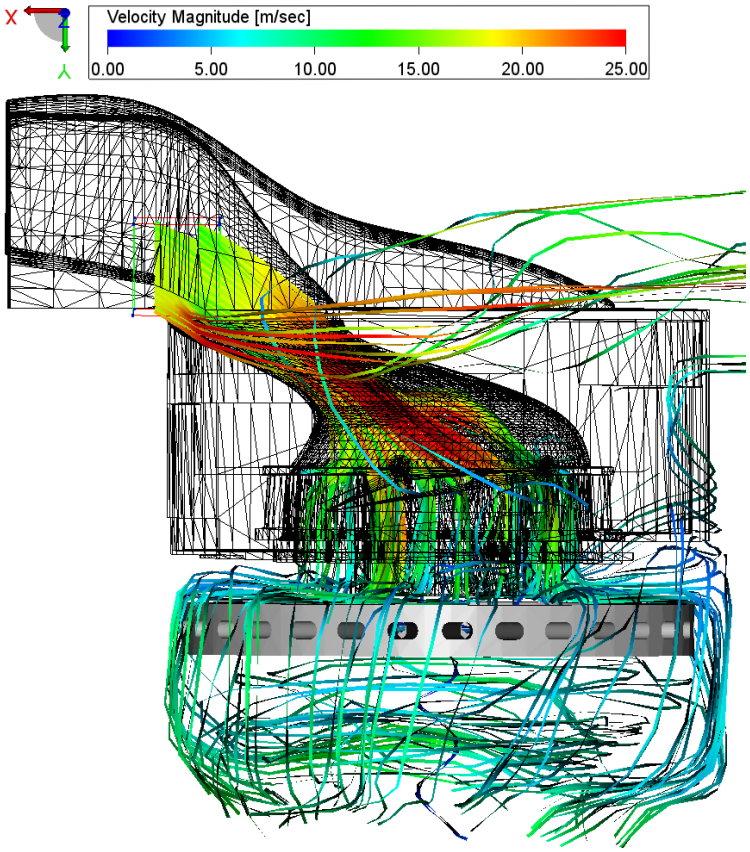

Figure 89: MRF internal velocity streamlines at 25m/s (tyre and wheel rim hidden).

4.3.4. 100% Scale Model Sliding Mesh Simulation

PowerFlow allows for the scaling of imported CAD geometry, a function that was utilised to create a full scale model of the wheel assembly in order to determine the effect of scaling geometry on HTC results. By maintaining simulation parameters from the original configuration, scaling only the geometry, is fundamentally changing the Reynolds number.

Integrated results (Figure 90) show the disc experienced significant generation in HTC, with results at the end of the timeframe range on a rise, beginning the next rotation at an accumulated HTC; external (sidewall) results show a more consistent flow than the internal results (disc), with data returning to a level approximate to that at timeframe 0.

The average HTC for the tyre was approximately 125W/m^{2}K, while that of the disc was 30W/m^{2}K. The sidewall experienced a greater range of HTC's throughout the simulation, 13W/m^{2}K, compared to that of the disc, 3.7W/m^{2}K. Comparison to the original sliding mesh simulation utilising the 50% scaled model geometry (Figure 91) shows the overall effect of scaling the geometry on the magnitude of HTC. The disc incurred an increase of 114% from the original 50% scale model, while the tyre showed less of a variation, increasing by 32%.

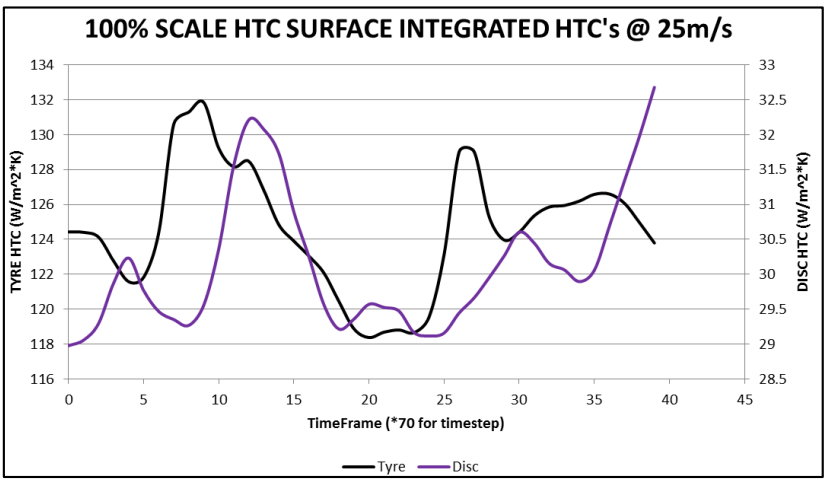

Figure 90: Integrated surface HTC results for 100% scale simulation using sliding mesh methodology.

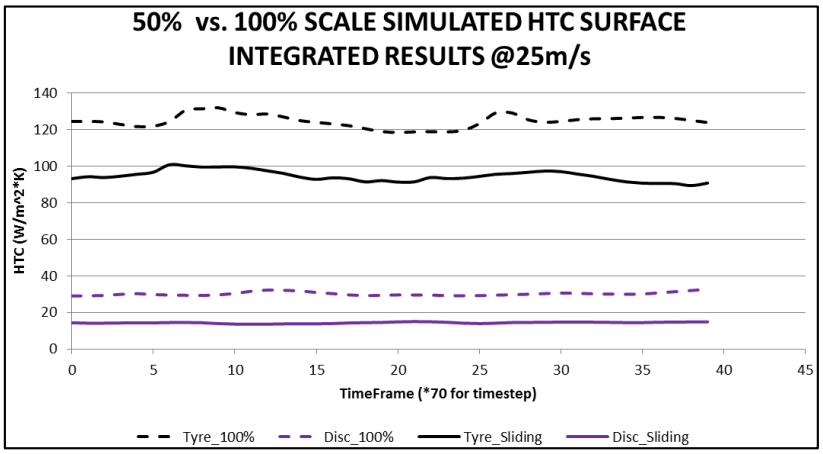

Figure 91: Comparison of integrated surface HTC results for 50% and 100% scale simulations.

Stagnation occurs just below the centreline (Figure 92), a characteristic of a rotating cylinder in flow, and in proximity of a ground plane. Separation occurs close to that of the original simulation's separation point (265deg CCW of SP). Approximately 270deg CCW of the SP, shedding of low velocity flow occurs, inferring that after the flow stagnates on the frontal surface, the velocity boundary layer thickens until gradually separating. No other simulation has shown a transitional low speed flow on the tyre surface, rather they have indicated free-stream flow velocity until the point of separation. The streamlines in Figure 93, support the previous statements with regard to the separation point occurring at the top of the tyre. There also exists a high degree of flow recirculation at the rear of the tyre; characteristic of increasing the Re through scaling.

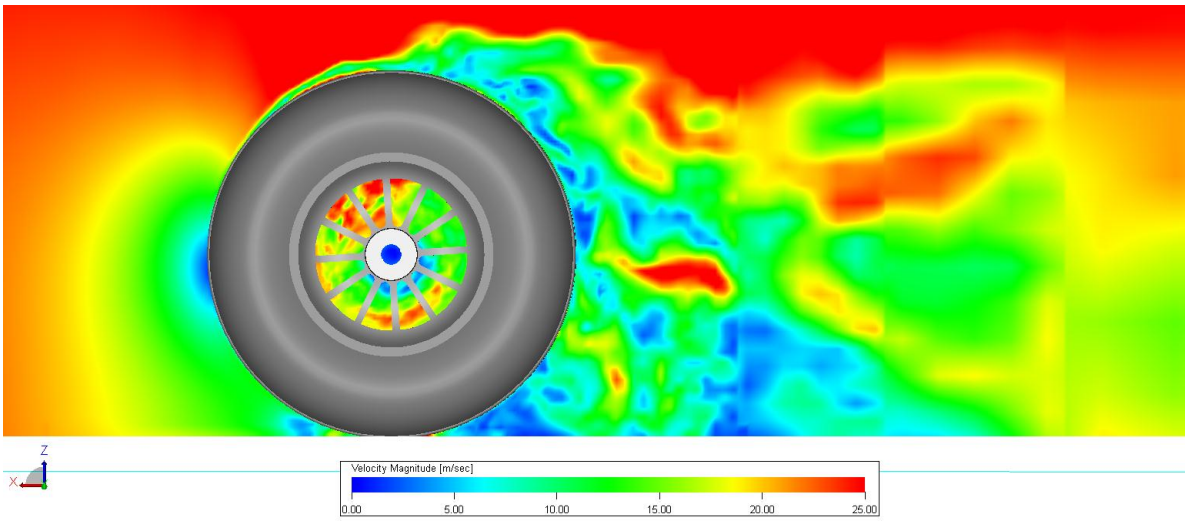

Figure 92: Velocity plane for 100% scale tyre separation point identification (270deg CCW).

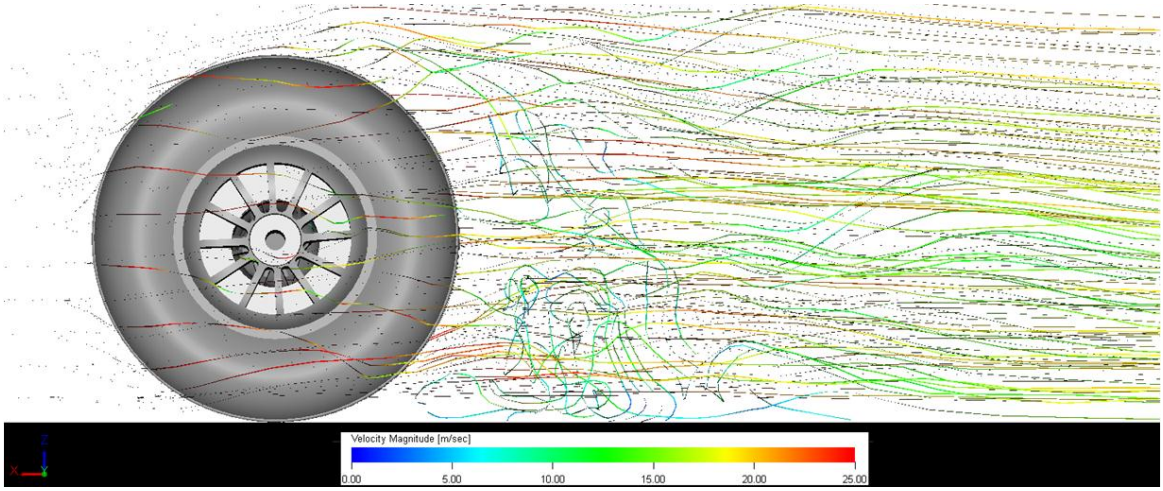

Figure 93: Velocity streamlines for 100% scale assembly.

Sidewall heat transfer surface contours show the top of the tyre, particularly on the OD edges, experiencing the highest level of heat transfer. Given the velocity plane indicated complex flow over the tyre, the level of unsteady flow must have introduced variations to the flow field that are not seen within the original, 50% scale simulations. Simulated results showed a high level of flow spillage out of the inboard side of the wheel rim (Figure 95); recirculating disturbed air into the flow stream will change the characteristics of the heat transfer, particularly with flow mixing of various velocities.

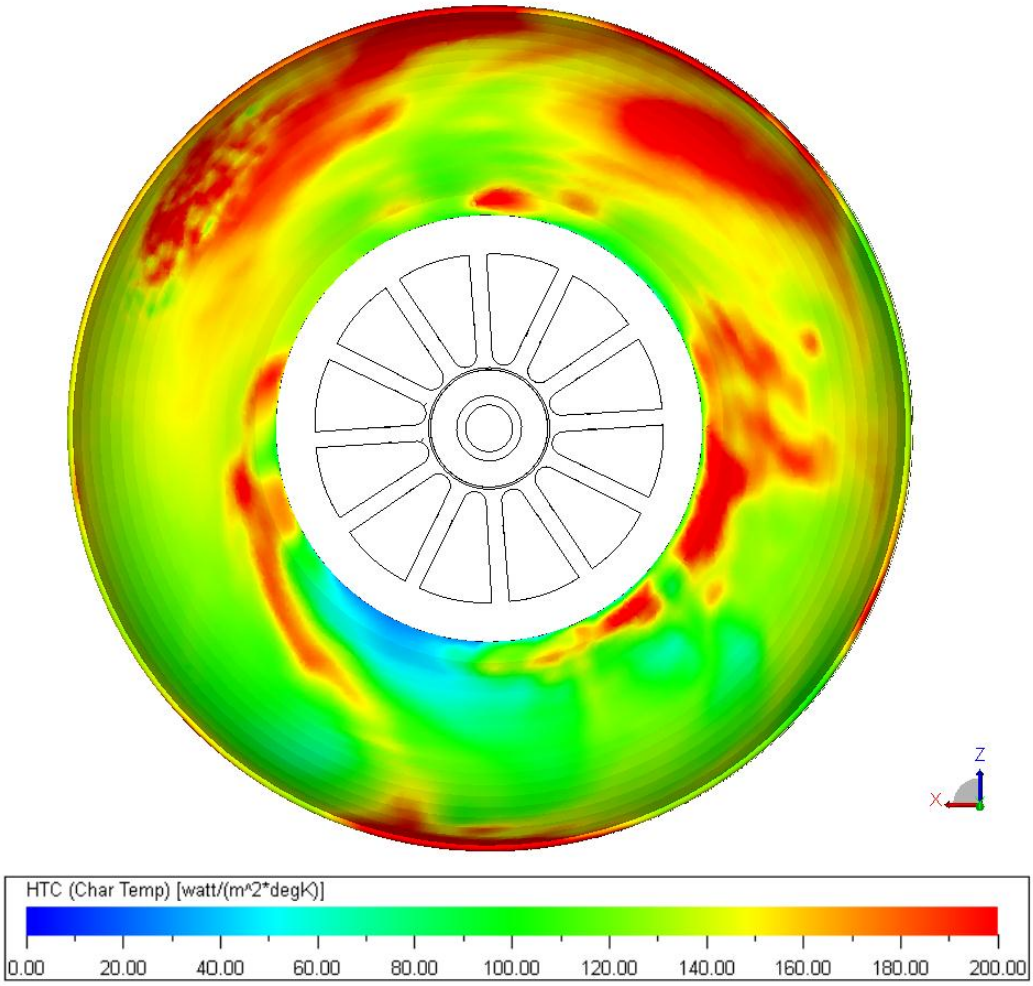

Figure 94: Sidewall HTC surface contours for 100% scale tyre using sliding mesh methodology.

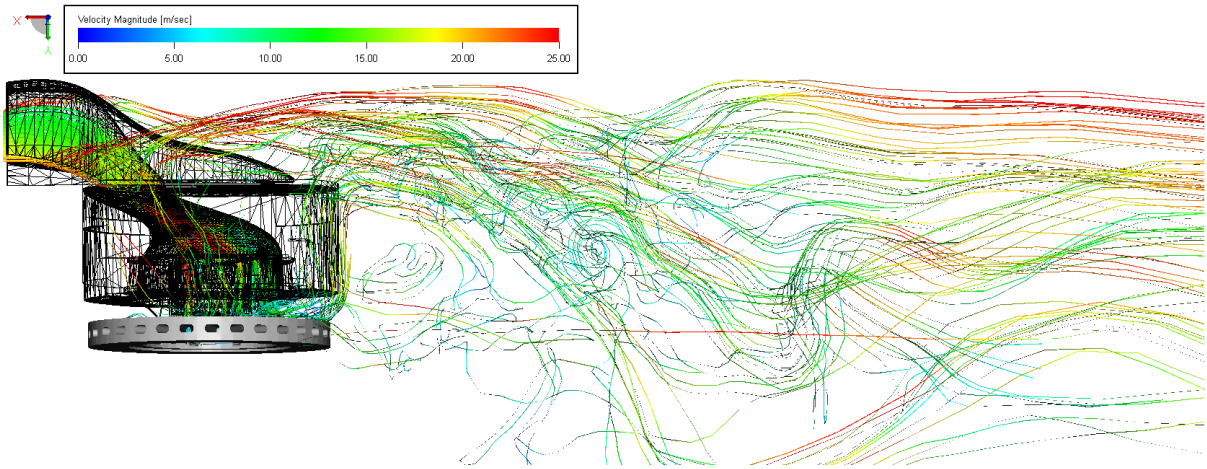

Figure 95: Velocity streamlines for flow through Inlet scoop at 25m/s for 100% scale model (tyre and wheel rim hidden).

In conjunction with Figure 95, the HTC surface images for the disc (Figure 96) show the inboard side's greatest HTC to occur on the bottom edge where the spillage occurred. Flow was restricted through the internals after passing through the scoop, with the LHS of the internal geometry lacking visual evidence of flow. As with the previous methodologies, the full scale model experienced a higher degree of heat transfer on the inboard side of the disc as a result of the introduction of flow from the Inlet scoop on the inboard side.

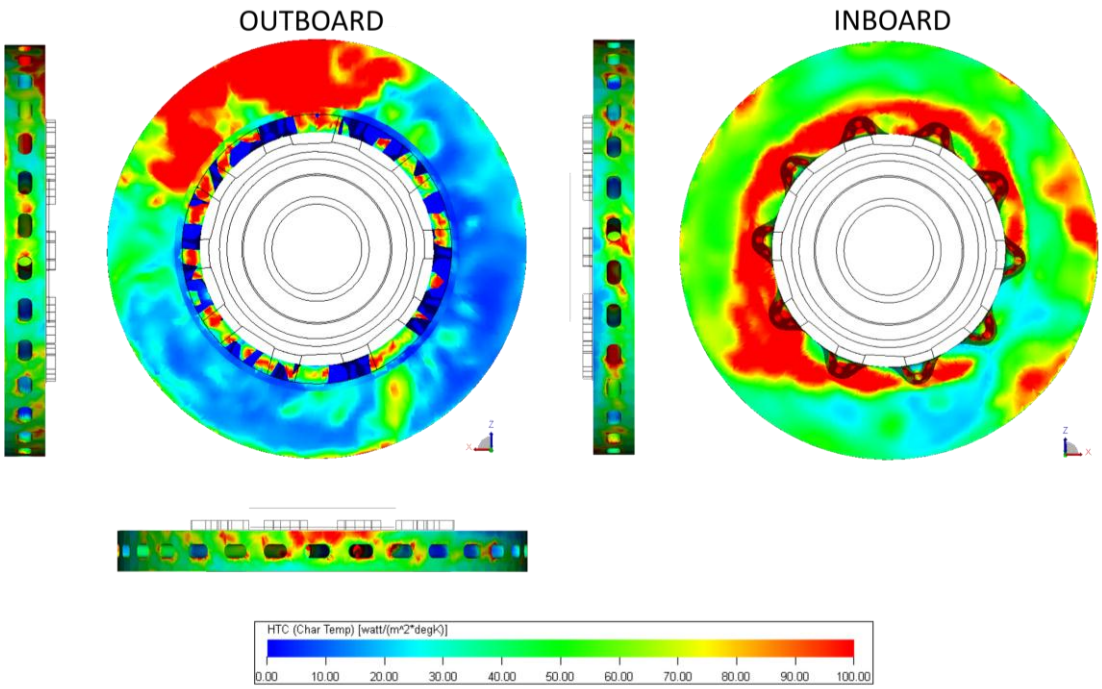

Figure 96: HTC surface contours for disc at all orientations - 100% scale at 25m/s using sliding mesh.

The spoke region experiences a range of values (Figure 97), with the greatest heat transfer occurring in the upper rearward region on the leading spokes. Considering the central extrusion was occupied by the connector shaft, one can compare the rim internal sidewall HTC to that of the central extrusion as blocked versus unblocked. Evidently the through flow from the oncoming air directed by the scoop is responsible for a proportion of the heat transfer.

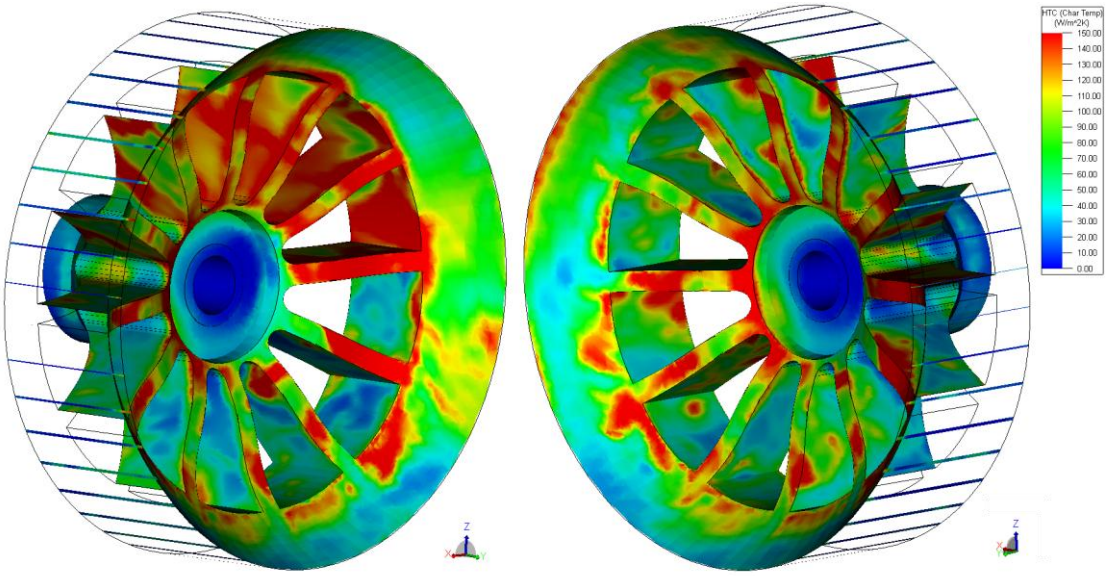

Figure 97: Left and right angled views for leading and trailing spoke HTC analysis on 100% scale wheel rim (disc, tyre and upright hidden).

The effect of utilising geometry scaling within the CFD simulations on the HTC results and flow characteristics was determine by increasing the model geometry scale from 50% (original model) to full scale (100%), and as a result, increasing the Reynolds number. The sliding mesh methodology was utilised as its physical rotation of components produces a more accurate system configuration. Increasing the geometry scale increased the HTC of magnitude in all areas as a result of the increased Reynolds number. Though magnitudes varied, the areas of high and low HTC showed similarities, however, neither scale was able to produce HTC surface contours representative of the patterns experienced in the wind tunnel results.

The HTC results were found to be affected more than the flow characteristics, with the average surface HTC of the tyre found to increase 32% from the original model, while the disc incurred an increase of 114%. The increase in HTC can be attributed to the increased Reynolds number. Comparatively, the areas of low and high HTC showed areas of commonality, such as the high HTC on the downstream side of the wheel rim. The inboard side of the disc maintained a higher degree of heat transfer compared to the outboard side, and the leading spoke showed higher HTC than the trailing, as in the original model.
The Stagnation point was unaffected, however, the velocity plane presented a more complex velocity profile above the tyre's surface than the original model. The separation point, however, occurred around the same position as the original model (270deg compared to original 265deg). The downstream flow showed more disturbances than the original model, characteristic of the increased Reynolds number.

5.0. Discussion

The following section aims to draw associations from the literature and results explored in the preceding chapters, outlining the key findings from the results set.

The comparison of error in both experimental systems is drawn upon to determine the effect upon the disc HTC results incurred by varying the method of flow application. Further experimental discussion surrounds the effect of varying upright geometry, particularly the influence of the scoop inlet flow, on the disc HTC. Comparison of the two rotating simulation methodologies is used to explore the influence of the different flow characteristics on the HTC results, and the effect on HTC by increasing geometry scale in the CFD is explored. The derivation of Nusselt number equations from experimental and CFD results is discussed, outlining areas of correlation, and presenting model fits to capture the range of possible heat transfer.

5.1. Measurement Accuracy between Experimental Configurations

Error levels were assessed based on the convective heat transfer coefficient of the disc under theoretical no-flow conditions. The magnitude of error in the rig, 14W/m^{2}K, was greater than that in the wind tunnel, 2W/m^{2}K. The range of heat transfer variation for the rig experiment was at least six times that of the wind tunnel; due to the variation of relationship between average HTC and velocity for the two setups (Figure 98). The rig shows average HTC to have an almost linear relationship with velocity, while the wind tunnel shows a peak HTC which then falls again at 17m/s.

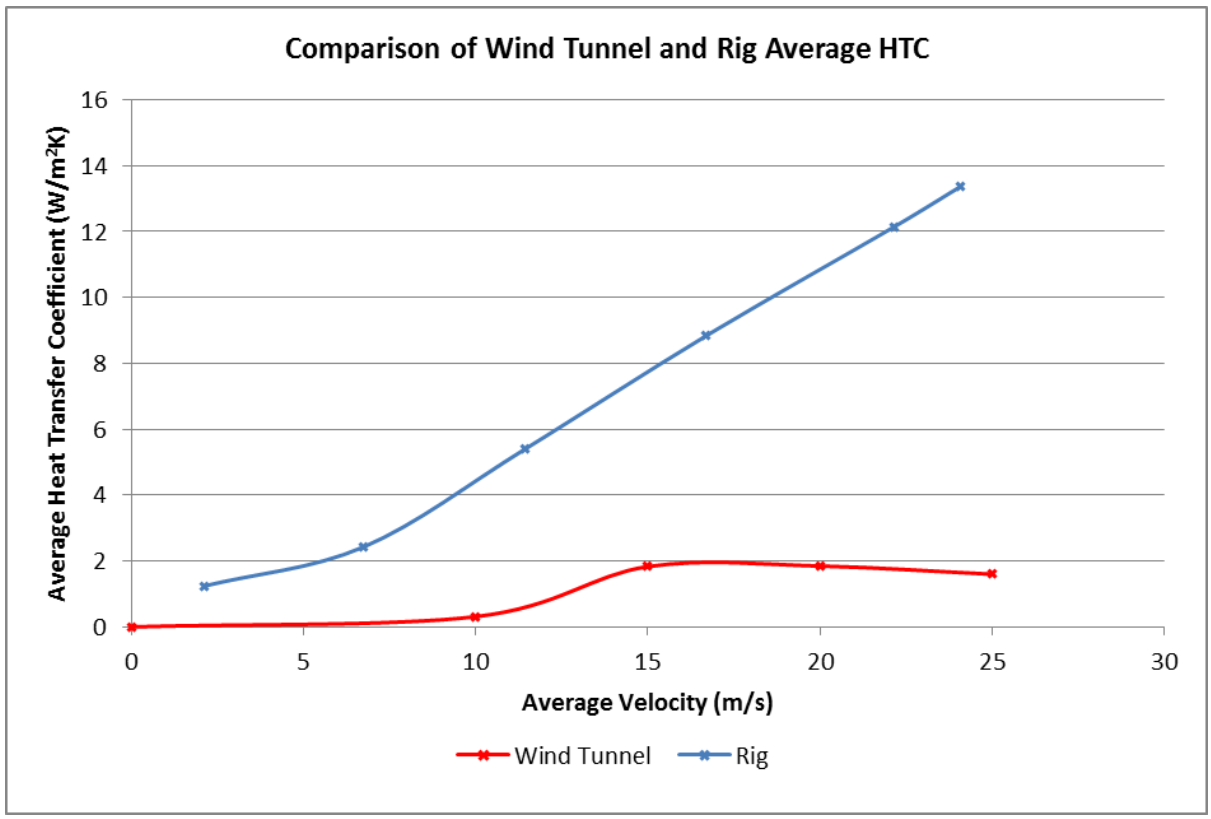

Figure 98: Comparison of hot film error between rig and wind tunnel tests.

Comparing the two experimental configurations, the main variations are those of the wiring arrangements, the method of airflow application, use of different CTA's, and the introduction of a ground plane, however the error measurements conducted with the system sealed would not have been affected by the ground plane. The wiring arrangement for the rig test involved the excess wire, which remained so as not to reduce the possibility of future application in other experiments, to be evenly distributed in opposing directions around the circumference of the tyre before passing through the slip ring and to the CTA. For the WT, the wiring was more involved, with a greater length of wiring required to pass over the sting arm assembly. The wiring was attached to the wheel rim and passed through the hollow support shaft before passing through the slip ring. Both arrangements utilised twisted pairs in order to provide some degree of shielding. The wind tunnel setup utilised a mostly linear arrangement of the wiring, and so the influence of wiring arrangement in the rig setup on the HTC error can be attributed to the circumferential arrangement of wires.
Each experiment utilised a different CTA, with that of the wind tunnel capable of measuring two simultaneous channels. Although bridge resistance variation was compensated through consideration in the calculation of convective HTC, there is most likely more error within the analogue system (rig).

In order to determine whether varying the application of flow application affects the HTC of the disc, and indeed whether the rig produces accurate results when compared to the wind tunnel, the two systems must be compared at equivalent velocity.
The mass flow was the same for both scenarios, given the correlation with results to Minto's (2011) Hub Flow Number theorem, defined as the volumetric flux ratio between the scoop and the free-stream velocity. By applying Minto's relationship to the experimental system, the equivalent velocity at the scoop inlet plane was found to be approximately equal to that of the free-stream, with a resulting velocity ratio of 1.0029.
At 25m/s, the time averaged HTC of the disc on the rig was 91W/m^{2}K, while that in the wind tunnel was 102W/m^{2}K. Given the difference between the two results is less than the maximum error found in the error band test (14W/m^{2}K), it can be concluded that the method of flow application does not vary the disc HTC, and that the rig was able to provide comparable internal HTC results relative to the wind tunnel.

5.2. Effect of Geometry

5.2.1. Internal Disc Shield

The brake cooling test rig was run at two test configurations; with and without the shield, which partially covered the outer diameter of the disc.
Results for the shielded and open systems indicate an equal level of heat transfer between the two configurations for the lower velocities, with introduction of an approximate 3W/m^{2}K variation at a free-stream velocity of 20 and 25m/s. Despite the use of the shield introducing a reduction in HTC for both speeds, the magnitude of variation was not, in the case of this experiment, high enough to be regarded as significant. Given the sealed disc error was found to reach a maximum of 14W/m^{2}K at 25m/s on the rig, the 3W/m^{2}K variation may be merely a portion of error in the system.

5.2.2. Brake Scoop Inlet

Another geometrical aspect that affects the internal flow, and therefore the heat transfer experienced at the disc, is the inlet scoop. A wind tunnel configuration was run with a blocked scoop, utilising multiple layering of heavy duty tape, to determine the degree of heat transfer occurring as a result of the scoop flow. The open scoop showed average heat transfer results at least 10x larger than the blocked scoop configuration, confirming that the cooling due to the scoop inlet flow was the predominant influence on heat transfer. As with the shielded case, the level of error determined within the system must be considered; 2W/m^{2}K maximum error in the wind tunnel system, implying that with a blocked scoop, the disc will only experience cooling above 10m/s.

Comparison of the blocked and open configurations allows identification of scoop inlet flow as the primary source of convective heat transfer, however, the blocked scoop results indicate that the rotational fluid forces generated due to the centrifugal flow, were responsible for an approximate upper limit of 10% of the convective heat transfer at the disc.

5.3. Stationary vs. Rotating – Wind Tunnel and Simulated Comparisons

Many studies preceding this work have outlined aerodynamic/flow variations for stationary and rotating components, with the main findings involving the advancement of separation caused as a result of cylindrical rotation (Knowles, 2005). Cylindrical rotation has also been found to suppress vortex development (Stojkovic, et al., 2002), while wake-breathing/jetting effects have also been observed; affecting the wake (Mears, 2004). Both stationary and rotating configurations were tested in the wind tunnel and using CFD. The precise location of the HTC was extracted from the wind tunnel test, while data on the whole surfaces were extracted from CFD, using surface integration, to gain the best understanding of the simulated flow to complement experimental findings.

Simulated results of HTC were much lower than those in the wind tunnel test. The simulated results showed the inboard disc face experienced a much higher degree of heat transfer given its position directly in the path of oncoming flow from the scoop; this flow was directed through disc extrusions on the inboard side for flow through disc vanes. The ambiguity in utilising the surface integration method is highlighted in Figure 99, where the difference between stationary and rotating simulations is approximately 1W/m^{2}K, whereas wind tunnel results show a difference of over 45W/m^{2}K between stationary and rotating configurations. The simulated disc HTC results outline a fairly steady heat transfer throughout a rotational cycle, a consequence of the inclusion of both inboard and outboard surfaces; the high inboard HTC balanced by the low outboard HTC.

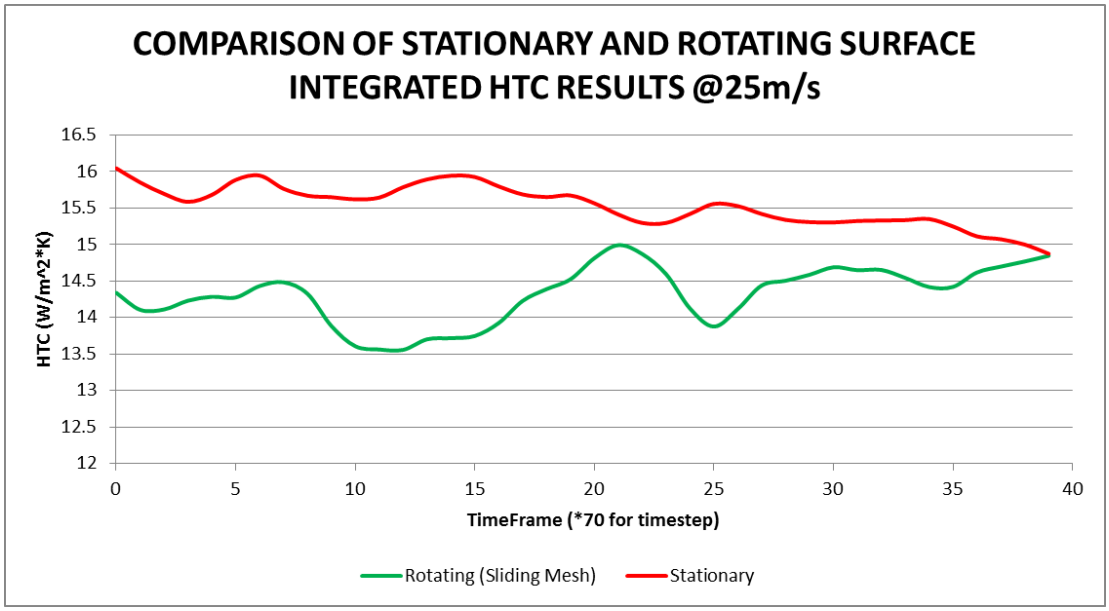

Figure 99: Comparison of disc surface integrated HTC results for a stationary and rotating simulation at 25m/s.

Accuracy of the wind tunnel results was proven with results of average HTC for the reference disc maintaining results within a narrow band of variation for nine test runs, with results showing clear and consistent trends. Furthermore, there was no distinct trend between HTC and hot film location between different sidewall positions (i.e. error after each increment of movement), suggesting that the film did not incur any circuit damage during its movement. Results for the disc lay within the expected error (determined to be +/- 2W/m^{2}K).

Polar result traces indicated that the highest level of heat transfer occurred at the top half of the disc, with variation from the bottom half for each speed approximately +4 W/m^{2}K @10m/s, +8 W/m^{2}K @15m/s, +10 W/m^{2}K @20m/s and +10 W/m^{2}K @25m/s. This is in agreement with the HTC surface image of the simulated results, where the highest degree of heat transfer on the inboard side of the disc occurred in the same region; indicative of the highest rate of flow. This supports the conclusion that the heat transfer in the simulated disc vane would be higher than the average component HTC returned by integrated results. Results for the spokes, however, showed better correlation than for other areas of the geometry, with both wind tunnel and CFD results indicating that the leading surface of the spoke experienced a greater level of convective heat transfer than the trailing surface; as the leading surface cut through the air the oncoming flow was stagnated.

Stationary simulation results show the inner sidewall surface of the rim, between the spokes, experiences the lowest levels of heat transfer of the component, together with the frontal face of the wheel rim outer surface, while rotational results show a significant HTC increase (Figure 100). The stationary tyre allows the free-stream flow to travel past the sidewall and wheel rim, picking up the flow spillage from the wheel rim and carrying it further downstream, potentially the reason for higher HTC toward the rear of the rim.

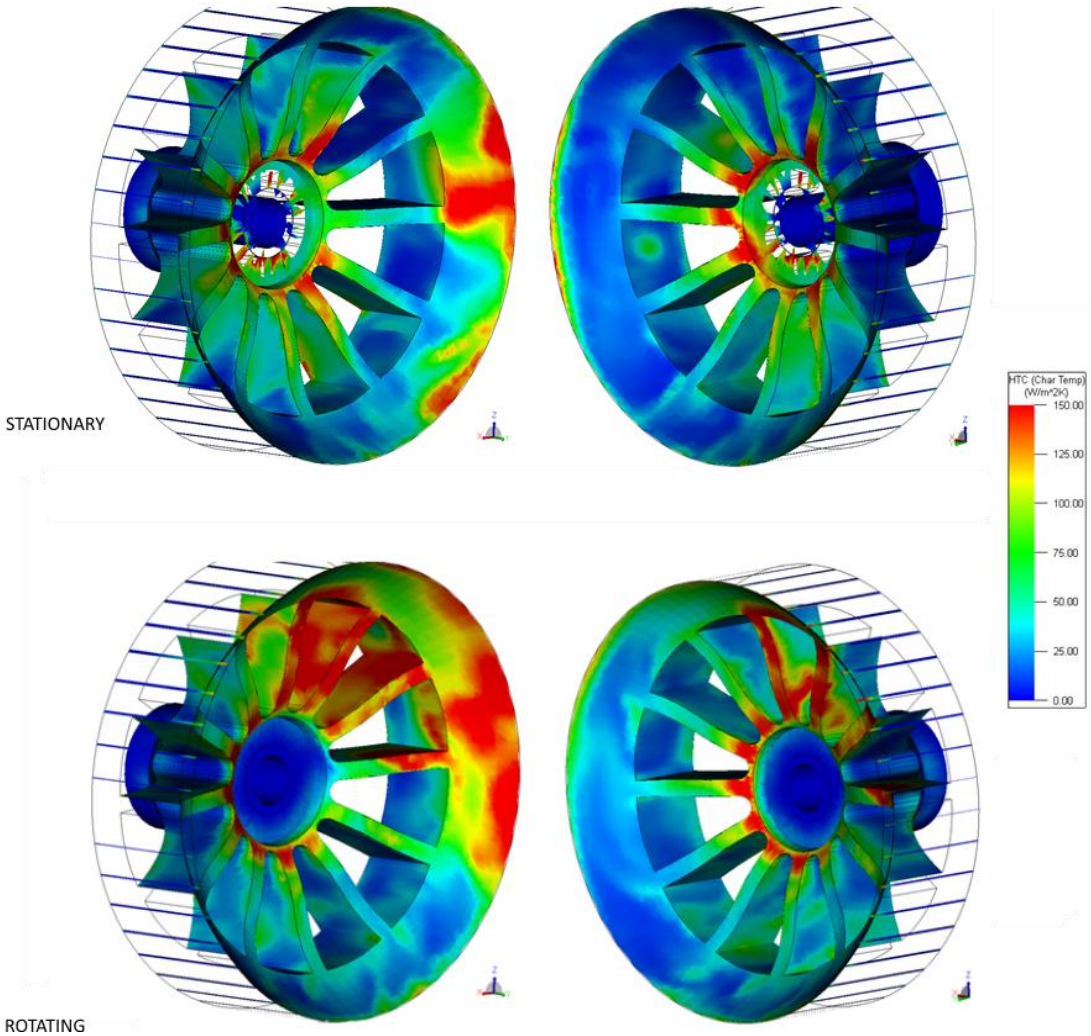

Figure 100: HTC surface image comparison for stationary and rotating simulations at 25m/s.

The sidewall heat transfer experienced in the wind tunnel displayed complex patterns with relation to speed and position, while the simulation provided little scope for investigation, with a near constant heat transfer across the sidewall.

For the simulated results, the lower rear quadrant experienced a lower velocity as a result of recirculated turbulent flow in that region. The same phenomenon was experienced on the stationary tyre, though to a lesser degree, suggesting rotation induces a lower velocity behind the wheel. There was an otherwise average heat transfer for the rotating simulation of approximately 100W/m^{2}K (at 25m/s) across the surface of the sidewall. Contrarily, a more complex set of results were produced in the wind tunnel, providing insight into the dependence on geometry as well as position and velocity.

The stationary experiment presented results across the tyre sidewall at approximately 3.5±0.5W/m^{2}K, however one set of data lay outside the bounds of consensus. Position 2, the inner most position to the wheel rim, presented an average HTC of 7W/m^{2}K. Given the sensors proximity to the wheel rim, results suggest the turbulence from the spoke region caused some additional localised heat transfer.

It was deduced from the observed trends in HTC from the wind tunnel, that the positions upstream and downstream of the highest point on the tyre sidewall profile experienced different boundary layer states.

Moving away from the centrally located high point (both toward ID and toward OD), the heat transfer increased. Just as the spokes underwent a transitional flow between 10-15m/s, so too did the tyre, with the centre point taking on characteristics of the inner most positions when in rearward flow, and the outer most positions when in free-stream flow.

5.4. Comparison of Rotating Simulations

The variation in flow structure upstream and around the tyre affects the location of the separation point between the two simulation methods (Figure 101). The accuracy of the chosen rotational simulation method is important to capture the correct flow structures, with rotating structures causing flow recirculation. The velocity of the rearward flow will partially affect the level of subsidiary heat transfer occurring from its recirculation. The sliding mesh imposes a more realistic rotation of components within the simulation, while the MRF methodology applies rotational forces to the fluid bounded within the reference frame. This was noted in the MRF simulation, which showed a degree of recirculation at the front of the tyre, indicating stationary wall like blockage; unlike the jetting phenomena identified by Mears (2004), which can only be induced with wheel rotation, such as that occurring from the sliding mesh.

In terms of sidewall HTC, both rotational methods show generally similar average HTC across the sidewall (Sliding mesh = 95W/m2K and MRF = 103W/m^{2}K), with noticeable variation at the front of the MRF tyre; concordant with the results from the streamline traces. Both methods show a peak of HTC just before the separation point; using the MRF delays separation. Neither methodology produced a HTC map with the relations found in the WT i.e. a central low-point of HTC which increases toward the OD and ID.

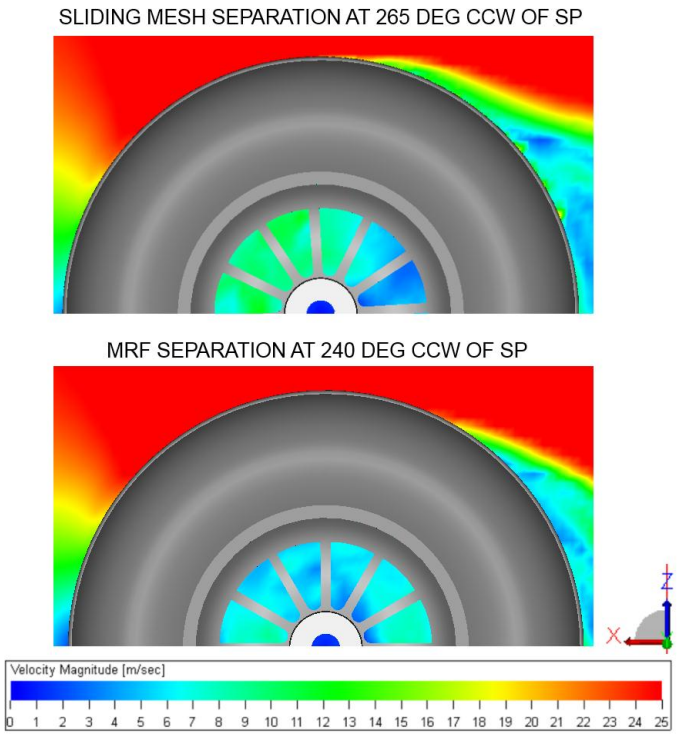

Figure 101: Comparison of separation point in SM and MRF simulation methodologies.

Internally (Figure 102), the MRF showed a more realistic representation of flow recirculation than the sliding mesh, with more flow recirculation occurring at the outboard face of the disc, and a more even distribution of flow around the periphery of the disc rather than the frontal flow only in the sliding mesh. The generation of the reference frame is also an element of introduced error. Exa PowerFlow allows for generation using a co-ordinate point cloud, or methods such as offsets from surfaces. Complete accuracy is limited given the upright needs be excluded as it is a stationary component, leaving the internal area outside the reference frame. Concerns arise as to the behaviour of flow within this region as there should be induced flow disturbances as a result of the rotating wheel rim, however, the MRF methodology is defined as applying rotational fluid forces to those within the bounds of the reference frame; understanding of the software's ability to create a relation between the two areas of flow is required to assess its capability.

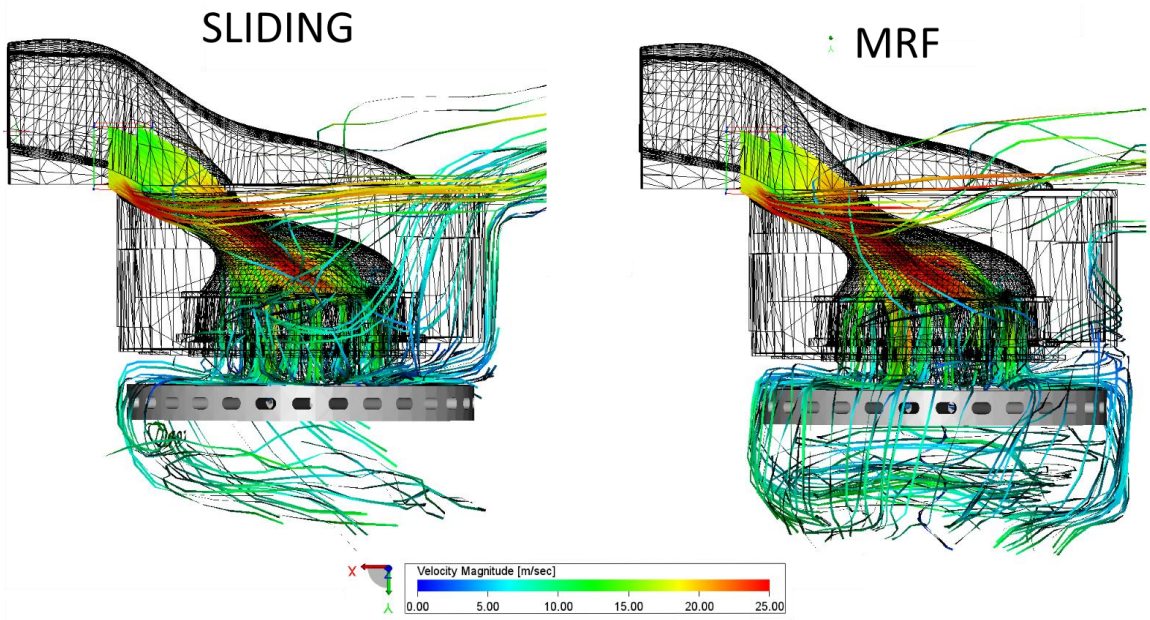

Figure 102: Comparison of SM and MRF internal streamlines at 25m/s.

5.5. Nusselt Number Analysis

Data recorded for the disc in the wind tunnel was found to fit well with the derived Nusselt number equation, and correlated with previous findings in the reviewed literature of the Reynolds number exponent, m. Comparison with the CFD results (Figure 103), reveals that the CFD produces lower heat transfer for a given Reynolds number than the experimental data. The difference in results can be attributed to the use of different integration areas between measurement techniques, with the CFD expected to show lower heat transfer as it considered results in areas of lower heat transfer (outboard side). This may also have affected the slope of the CFD heat transfer curve compared to the experimental result.

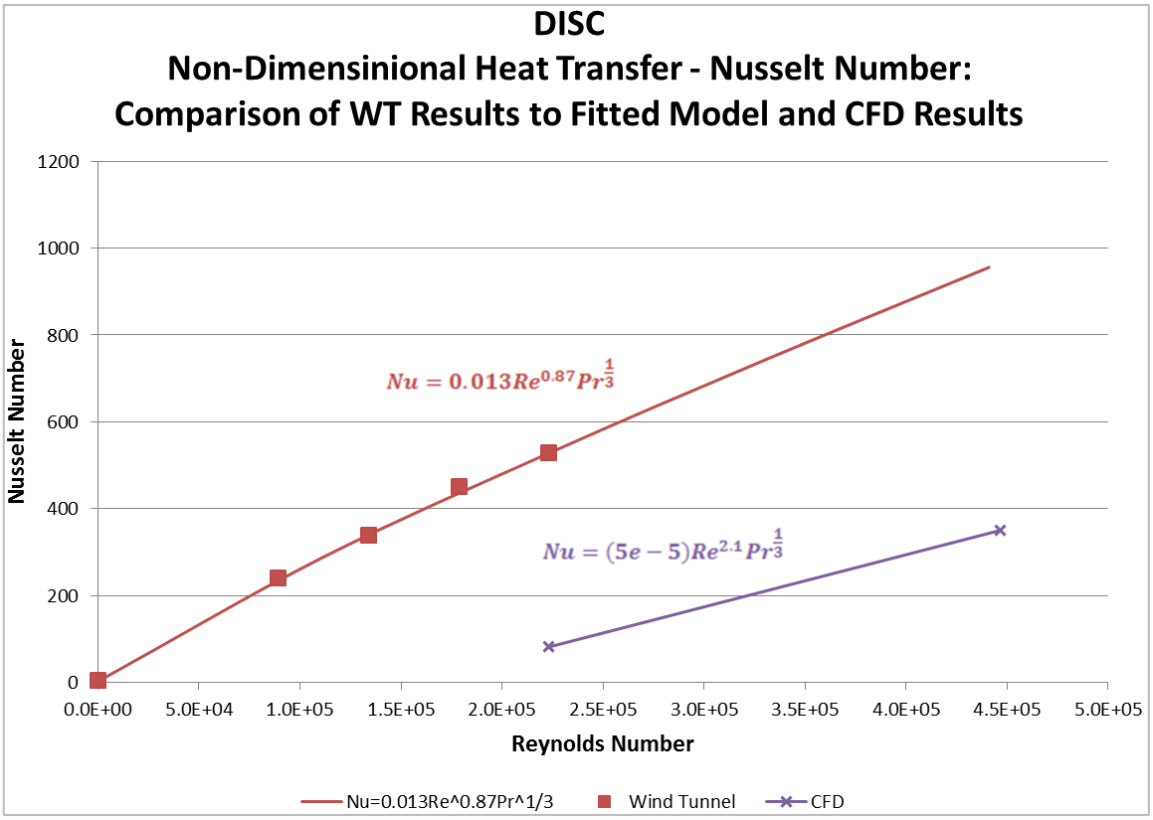

Figure 103: Nusselt number comparison for wind tunnel and CFD data.

The sidewall experimental results presented an underestimate of the Reynolds number exponent, m, while the CFD showed an overestimate (Figure 104). Results at Reynolds number 4.04E+05 (25m/s), show good correlation between CFD and experimental Nusselt number, after which point, experimental data points were not collected at higher Reynolds numbers. The Reynolds number exponent has been recorded in literature to an approximate value of 0.8 up to Reynolds numbers of 400,000. The Model Fit equation presents an extended trend line for the wind tunnel Results, while the CFD trace outlines the trend for the CFD results. In order to balance the over and underestimated 'm' values, a Combined Model Fit was determined as a negotiation between the two measurements, outlining the range that results can be expected to fall within. The increasing difference between experimental and CFD results after 25m/s may be attributed to the occurrence of a transitional phase along the sidewall that was not seen within the 0-25m/s data range in the wind tunnel. Nusselt number values from the original model (50% scale) experimental and CFD were used to determine the equivalent 100% scale HTC's at the disc (Figure 105) and tyre sidewall (Figure 106). The same model fit methods were applied to distinguish the range of possible values.

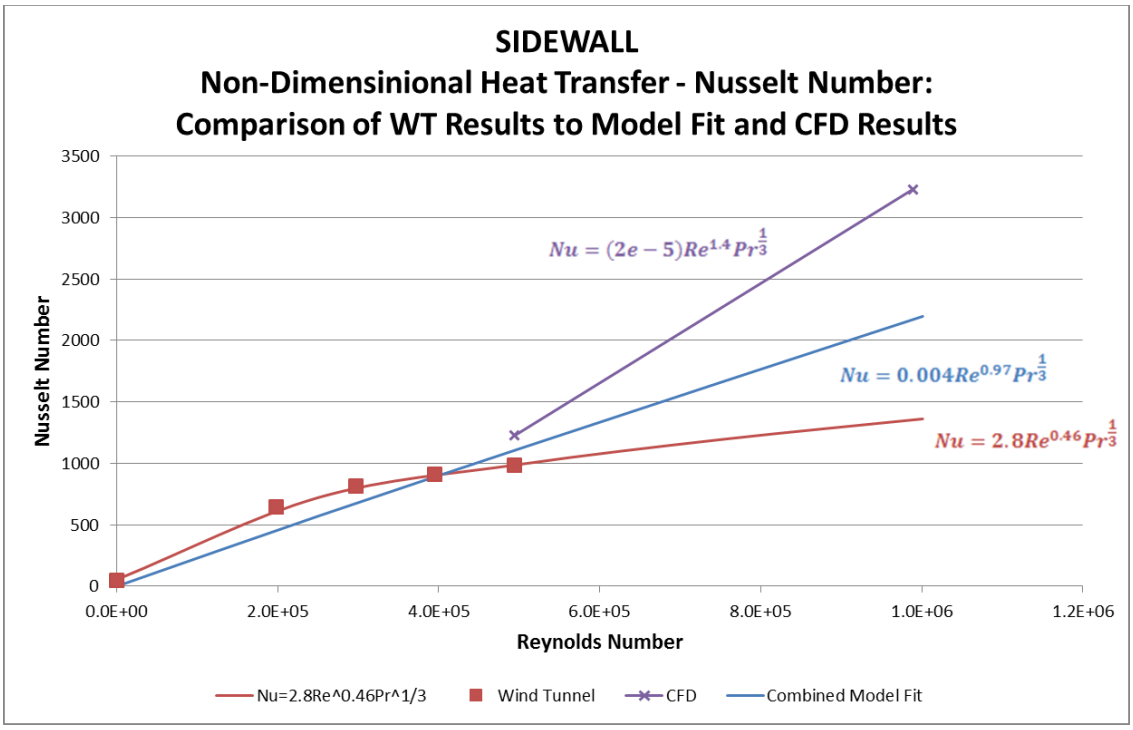

Figure 104: Nusselt number comparison for experimental, computational and model fit equations.

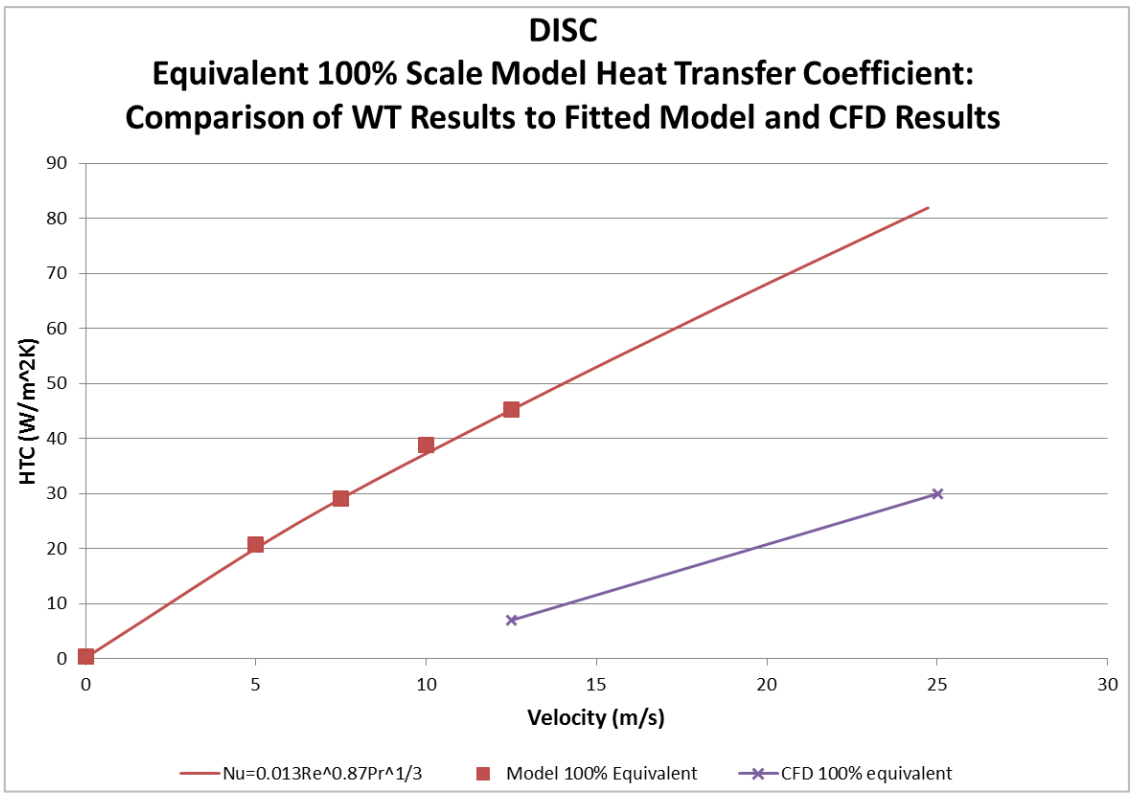

Figure 105: Equivalent 100% model HTC's for the disc.

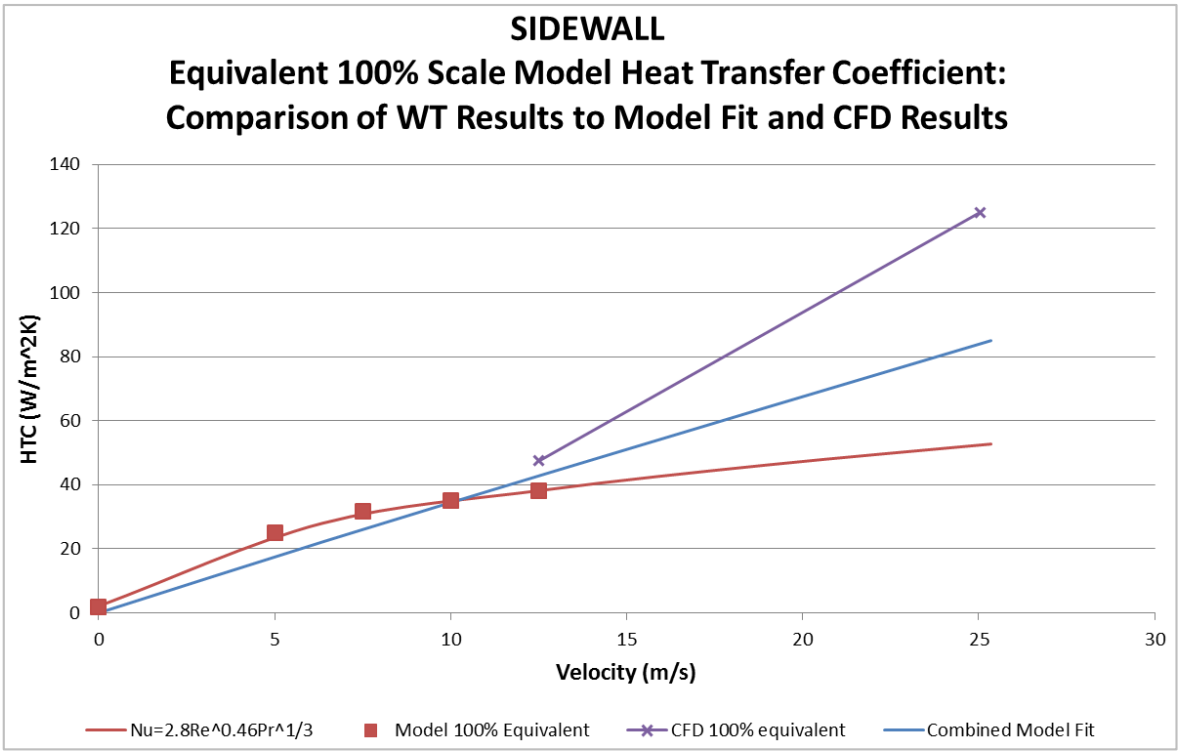

Figure 106: Equivalent 100% Model HTC's for the tyre sidewall.

5.6. Full Scale Simulation

Scaling the model from experimental component size to a full scale (100%) model while maintaining original simulation parameters, results in much higher heat transfer. Comparison of surface integrated results for the original and 100% scaled model revealed a 31% increase in average HTC at the sidewall for the full scale model, while the disc underwent an increase of 110%; increase in HTC occurred as a result of the larger Reynolds number from increasing the geometry scale.

6.0. Conclusions

The work presented has investigated the mechanisms of heat transfer in a wheel assembly, identifying the effects of wheel rotation and of the implementation of various geometries within the assembly on heat transfer. The primary mechanism of interest was the convective heat transfer, which was investigated using techniques including wind tunnel testing, rig testing and CFD simulations in order to compare capabilities of various methodologies in determining the HTC at the disc and tyre sidewall. The literature review introduced the effects of cylindrical rotation and ground planes upon the flow structure, and identified the effect of the variation of the separation point and boundary layer development; factors that affect the of potential cooling capability within a flow. The Nusselt number equations were derived for experimental and CFD data, which provided confidence of the wind tunnel accuracy.

In order to complement the experimental and simulated tests, the experimental apparatus was created in CAD geometry both to aid with the design and commissioning of experimental fixtures to carry out hot film measurements on a brake cooling test rig and in the wind tunnel, and to carry out CFD simulations. Results of HTC from the wind tunnel were processed into a geometrically related positional heat transfer map of the tyre sidewall.

6.1. Assessment of Systematic Error

Hot-film sensor sensitivity to flow is of high fidelity, a facet of the experimental procedure which proved beneficial for determining system level error in both experimental setups.

The systematic error was considered by removing external flow conditions from the disc sensor, allowing the determination of the level of HTC while at theoretical zero-flow condition. The wind tunnel results were accurate to within 2W/m^{2}K, while measurement of error on the bench-top rig, using a different CTA, was recorded up to 14W/m^{2}K. Given the difference between the time averaged HTC of the disc on the rig and wind tunnel was less than the maximum error found in the Error Band Test (14W/m^{2}K), concluding that the rig was able to provide comparable internal HTC results relative to the wind tunnel despite the difference in external flow application methodology.

6.2. Geometry Variations

Two geometry variations were tested for their effects on internal cooling variations; upright shield on/off and Inlet scoop blocked/unblocked. The shield partially covered the outer diameter of the disc, while the inlet scoop was blocked using tape to determine the level of cooling due solely to the rotation of the disc. Application of the upright shield on the rig test had no implication at the lower end of the speed range, and introduced a small reduction in HTC, 3W/m^{2}K, at higher speeds of 20m/s and 25m/s; a difference within the rig measurement error range of 14W/m^{2}K.

The wind tunnel tests with open and blocked scoop showed that a difference occurred at speeds above 10m/s. The open scoop average HTC was ten times greater than that of the blocked scoop scenario, confirming the Inlet scoop flow as the main source of internal cooling.

6.3. Rotating Simulation Methodologies

Two variations of rotational simulation were explored within the simulated results; physically rotating components using the sliding mesh approach, versus an implied rotation using the moving reference frame (MRF) method.

While the sliding mesh imposes a more realistic rotation of components within the simulation, the need for a rotating reference frame by the MRF approach raises concerns about flow property continuity across its boundary, and to its inability to follow the geometric contours of the body. The MRF simulation showed a degree of recirculation at the front of the tyre, indicating stationary like conditions that differ from the jetting phenomena identified in the literature as characteristic of rotating wheels. In general, the airflow was unstructured for the MRF, while the sliding mesh showed appropriate rearward vortex generation and streamlined flow over and around the tyre.

The HTC for both simulation methods generally agreed across the tyre sidewall, with some variation introduced from the incorrect upstream flow in the MRF simulation. Positionally, both simulations showed peak HTC just before the separation point, but using MRF the separation point is delayed.

6.4. Wind Tunnel vs. CFD

The correlation exercise between wind tunnel and CFD indicated that the CFD software produced lower HTC's, with the magnitude of the difference varying depending on the precise location within the wheel assembly. A study of the effect of wheel rotation on disc HTC showed a difference between stationary and rotating simulations to be approximately 1W/m^{2}K (Figure 102) while the wind tunnel results produced a much greater difference in HTC of over 45W/m^{2}K between the stationary and rotating tests.

Internally, the CFD was able to predict the positional pattern of HTC across the surface to some degree, with both rotational methods indicating the highest level of heat transfer occurred around the top half of the disc on the inboard side. Both methods also showed the leading Spoke surface experienced a greater level of heat transfer compared to that of the trailing.

The sidewall heat transfer experienced in the wind tunnel displayed a complex pattern with relation to speed and position, while the simulation provided little scope for investigation, with a near constant heat transfer across the sidewall. As a consequence of this lack of accuracy, conclusions on tyre sidewall HTC were solely based on experimental results from the wind tunnel.

The flow either side of the highest geometric point on the tyre sidewall profile experienced different boundary layer states, and increased in HTC with increased distance from the high point. Furthermore, heat transfer increased for a shorter period of the tyre's rotation the closer to the ID the measurements were taken.

Increasing the scale of the simulation model from 50% to full size (100%), like 50% simulations, showed no correlation to the complex patterns experienced in the wind tunnel. Evidently, the scaling factor within the CFD software shows no significant benefit with respect to correlation, but with a decrease in efficiency in the form of increased simulation run times. However, without a set of 100% scale experimental data, it is difficult to draw firm conclusions.

The derivation of Nusselt number equations proved wind tunnel HTC results at the disc to be accurate, with correlation in Reynolds number exponent to literature. The values presented for the sidewall, however, were found to fall between a range bounded by the wind tunnel and CFD results. As such, a combination of both model fits was created, which saw more reasonable figures of 'm' and C, and can be used in further investigations of heat transfer.

References

Albukrek, C., Doddegowda, P., Ivaldi, A., Amodeo, J. et al., *Unsteady Flow Analysis of a Formula Type Open Wheel Race Car in Cornering*, SAE Technical Paper 2006-01-3661, 2006, doi:10.4271/2006-01-3661.

Assaad, M. et al., 2008. *Thin-Film Heat Flux Sensor for Measuring the Film Coefficient of Rubber Components of a Rolling Tire*. Tire Science and Technology, 36(4), pp. 275-289.

Bearman, P., De Beer, D., Hamidy, E., Harvey, J., 1988. *The Effect of a Moving Floor on Wind-Tunnel Simulation of Road Vehicles*, SAE Technical Paper 880245, 1988, doi:10.4271/880245.

Bejan, A., 2013. *Convective Heat Transfer.* 4th ed. New Jersey: John Wiley & Sons, Inc..

Belhocine, A. & Bouchetara, M., 2012. *Simulation of Fully Coupled Thermomechanical Analysis of disc brake Rotor*. WSEAS: Transactions on Applied and Theoretical Mechanics, 7(3).

Belvins, R., 1990. *Flow Induced Vibration*. 2nd ed. New York: Van Nostrand Reinhold Co..

Bergman, T. & Lavine, A., 2011. *Introduction To Heat Transfer.* 6th ed. New Jersey: John Wiley & Sons, Inc..

Beringer, C. W., Kwon, Y. D. & Prevorsek, D. C., 1987. *Sensitivity of Temperature Rise in a Rolling Tire to the Viscoelastic Properties of the Tire Components*. Tire Science and Technology, 15(2), pp. pp123-133.

Browne, A. & Wickliffe, L., 1980. *Parametric Study of Convective Heat Transfer at the Tire Surface*. Tire Science Technology, 8(3-4), pp. 37-67.

Cengel, Y., Turner, R. & Cimbala, J., 2008. *Fundamentals of Thermal-Fluid Sciences.* 3rd ed. New York: McGraw-Hill.

Clark, S., 1976. *Temperature Rise Times in Pneumatic Tires*. Tire Science and Technology, 4(3), pp. 181-189.

Dantec Dynamics, 2013. *Miscellaneous Probes.* Available: http://www.dantecdynamics.com/products-and-services/miscellaneous-probes#glue-on-film. Last accessed 10th October 2014.

Duncan, B., Senthooran, S., Hendriana, D., Sivakumar, P. et al., *Multi-disciplinary Aerodynamics Analysis for Vehicles: Application of External Flow Simulations to Aerodynamics, Aeroacoustics and Thermal Management of a Pickup Truck*, SAE Technical Paper 2007-01-0100, 2007, doi:10.4271/2007-01-0100.

Fackrell, J., 1974. *The Aerodynamics of an Isolated Wheel Rotating in Contact with the Ground*, London: Imperial College London

Gaylard, A., Lynch, D., Amodeo, J. & Amunugama, R., 2010. *The Simulation of brake Dust Desposition*. Grove, MIRA.

Gomez-Osorio, M. et al., 2013. A Formulation for the Flow Rate of a Fluid Passing Through an Orifice Plate from the First Law of Thermodynamics. *Flow Measurement and Instrumentation,* Volume 33, pp. 197-201.

Jancirani, J., Chandrasekaran, S., and Tamilporai, P., *Virtual Heat Transfer Analysis of the Automotive disc brakes*, SAE Technical Paper 2003-28-0022, 2003, doi:10.4271/2003-28-0022.

Jarosinski, W., *Experimental Study of Heat Transfer from the Heated Rib-Roughed Wall to a Steady or Pulsating Flow*, SAE Technical Paper 2001-01-1249, 2001, doi:10.4271/2001-01-1249.

Kandasamy, S., Duncan, B., Gau, H., Maroy, F. et al., *Aerodynamic Performance Assessment of BMW Validation Models using Computational Fluid Dynamics*, SAE Technical Paper 2012-01-0297, 2012, doi:10.4271/2012-01-0297.

Kandasamy, S., Lounsberry, T., Gleason, M., Sbeih, K. et al., *The Effects of Detailed Tire Geometry on Automobile Aerodynamics - a CFD Correlation Study in Static Conditions*, *SAE Int. J. Passeng. Cars – Mech. Syst.* 2(1):849-860, 2009, doi:10.4271/2009-01-0777.

Kato, K., Yamaguchi, M., Miyazono, T. & Tsuruta, M., 2009. *Enhancement of Tire Durability by Considering Air Flow Field*. Tire Science and Technology, 37(2), pp. 103-121.

Katz, J., 1947. *Race Car Aerodynamics*. Cambridge, MA, USA: R.Bentley.

Knowles, R., 2005. *Monoposto Racecar Wheel Aerodynamics: Investigation of Near-Wake Structure & Support-Sting Interference*, Cranfield: Cranfield University.

Kurganov, V., 2011. Heat transfer coefficient, s.l.: Thermopedia.

Laurantzon, F., Tillmark, N. & Henrik, P., 2010. *What does the hot-wire measure?*, Stockholm, Stockholm Royal Institute of Technology KTH

Lei, C., Cheng, L. & Kavanagh, K., 1999. *Re-examination of the effect of a plane boundary on force and vortex shedding of a circular cylinder*. Journal of wind Engineering and Industrial Aerodynamics.

Lietz, R., Mallick, S., Kandasamy, S., and Chen, H., *Exterior Airflow Simulations Using a Lattice Boltzmann Approach*, SAE Technical Paper 2002-01-0596, 2002, doi:10.4271/2002-01-0596.

Lopez, C. & Tirovic, M., 2012. *Maximising Heat Dissipation from Ventilated Wheel-Hub-Mounted Railway brake discs.* Cranfield, IMechE.

Lundstrom, H., Sandber, M. & Mosfegh, B., 2007. *Temperature Dependence of Convective Heat Transfer from Fine Wires in Air: A Comprehensive Experimental Investigation with Application to Temperature Compensation in Hot-Wire Anemometry*. Experimental Thermal and Fluid Science, Volume 32, pp. 649-657.

Mears, A. P., 2004. *The aerodynamic characteristics of an exposed racing car wheel*, Durham theses, Durham University. Available at Durham E-Theses Online: http://etheses.dur.ac.uk/3124/

Minto, J., Sprot, A., Sims-Williams, D., and Dominy, R., *Aerodynamic Investigation on the Effect of Varying Through-Hub Flow on a Formula One Front Wheel Assembly*, *SAE Int. J. Passeng. Cars – Mech. Syst.* 4(1):929-944, 2011, doi:10.4271/2011-01-1431.

Mukutmoni, D., Han, J., Alejbegovic, A., Colibert, L. et al., *Numerical Simulation of Transient Thermal Convection of Heated Plate*, SAE Technical Paper 2010-01-0550, 2010, doi:10.4271/2010-01-0550.

Nemati, H., Farhadi, M. S. K., Fattahi, E., 2011. Multi-Relaxation-Time Lattice Boltzman Model for Uniform Shear Flow Over a Rotating Circulat Cylinder. Thermal Science, XV(3), pp.859-878.
Ng, J., 2013. The Measurement of Brake Cooling Using Hot-Film Sensors, Durham: Durham University.

Nutwell, B. and Ramsay, T., *Modeling the Cooling Characteristics of a Disk brake on an Inertia Dynamometer, Using Combined Fluid Flow and Thermal Simulation*, SAE Technical Paper 2009-01-0861, 2009, doi:10.4271/2009-01-0861.

Palmer, E., Mishra, R. & Fieldhouse, J., 2009. *An Optimization Study of a Multiple-row Pin-vented brake disc to Promote brake Cooling Using Computational Fluid Dynamics*. Journal of Automobile Engineering, 223(7), pp. 865-875.

Rae, W. and Skinner, G., *Measurements of Air Flow Velocity Distributions Inside a Rolling Pneumatic Tire*, SAE Technical Paper 840066, 1984, doi:10.4271/840066.

Ratamero, L. and Ferreira, R., *Wheel Cover Affected by the Heat Generated in the brake System*, SAE Technical Paper 2010-36-0380, 2010, doi:10.4271/2010-36-0380.

Sakamoto, H., 2004. *Heat Convection and Design of brake discs*. Journal of Rail and Rapid Transit, 218(3), pp. 203-212.

Scarborough, C., 2010. Tyre *Testing Sensors – What was seen in Abu Dhabi.* [Online] Available at: http://scarbsf1.com/blog1/2010/12/02/tyre-testing-sensors-what-was-seen-in-abu-dhabi/ [Accessed 22 January 2014].

Shekhter, Y., 2011. *Hot-Wire and hot film Anemometers,* s.l.: Thermopedia.

Sims-Williams, D. and Dominy, R., *The Design of an Open-Jet wind tunnel for Model Testing*, SAE Technical Paper 2002-01-3340, 2002, doi:10.4271/2002-01-3340.

Siqueira, C. and Fragoso, H., *Numerical Simulation of the Flow in Wheel Systems*, SAE Technical Paper 2003-01-3600, 2003, doi:10.4271/2003-01-3600.

Siroux, M., Harmand, S. & Desmet, B., 2001. *Experimental Study Using Infrared Thermography on the Convective Heat Transfer of a TGV brake disc in the Actual Environment*. SPIE: Thermosense XXIII, Volume 4360, pp. 712-719.

Song, T., Lee, J., and Yu, H., *Rolling Resistance of Tires - An Analysis of Heat Generation*, SAE Technical Paper 980255, 1998, doi:10.4271/980255.

Sprot, A. J., 2013. *Open-Wheel Aerodynamics: Effects of tyre Deformation and Internal Flow*, Durham theses, Durham University. Available at Durham E-Theses Online: http://etheses.dur.ac.uk/7292/

Stapleford, W.R., Carr, G. W., *Aerodynamic Noise in Road Vehicles, Part I: The Relatinoship Between Aerodynamic Noise and the Nature of Airflow*, MIRA, Report No. 1971/2

Stojkovic, D., Breuer, M. & Durst, F., 2002. *Effect of High Rotation Rates on the Laminar Flow around a Circular Cylinder*. Phys. Fluids, 14(9), pp. 303-334.

Sumer, M. & Fredsoe, J., 2006. *Hydrodynamics Around Cylindrical Structures*, Singapore: World Scientific.

Thornhill, D., Stewart, A., Cuningham, G., Troxler, P. et al., *Experimental Investigation into the Temperature and Heat Transfer Distribution around Air-Cooled Cylinders*, SAE Technical Paper 2006-32-0039, 2006, doi:10.4271/2006-32-0039.

Webster, J., 2000. *The Measurement, Instrumentation, and Sensors Handbook.* 1st ed. Florida: CRC Press LLC.

Woschni, G., *A Universally Applicable Equation for the Instantaneous heat transfer coefficient in the Internal Combustion Engine*, SAE Technical Paper 670931, 1967, doi:10.4271/670931.

Yamaguchi, M., Tsuruta, M., and Kato, K., *Experimental and CFD Analysis of Tire Cooling sidewall*, *SAE Int. J. Passeng. Cars - Mech. Syst.* 1(1):1-8, 2009, doi:10.4271/2008-01-0148.

Yavari, B., Tworzydlo, W. & Bass, J., 1993. *A Thermomechanical Model to Predict the Temperature Distribution of Steady State Rolling Tires*. Tire Science Technology, 21(3), pp. 163-178.

Yokota, K., Higuchi, E., and Kitagawa, M., *Estimation of Tire Temperature Distribution and Rolling Resistance under Running Conditions Including Environmental Factors*, SAE Technical Paper 2012-01-0796, 2012, doi:10.4271/2012-01-0796.

Appendices

Appendix 1: CTA Bridge Resistance Calculations

Wind tunnel CTA: FlowPoint

$$\frac{V_{probe}}{V_{output}} = \frac{R_{hot} + R_{cable}}{R_{bridge} + R_{hot} + R_{cable}}$$

$$\frac{0.393}{0.629} = \frac{16.6826 + 0.04}{R_{bridge} + 16.6826 + 0.04}$$

$$= \frac{16.7226}{R_{bridge} + 16.7226}$$

$$let\ x = \frac{0.393}{0.629}$$

$$x.R_{bridge} + 16.7226x = 16.7226$$

$$R_{bridge} = \frac{16.7226 - \left(16.7226 * \left(\frac{0.393}{0.629}\right)\right)}{\frac{0.393}{0.629}}$$

$$= 10.04\Omega$$

Brake cooling test rig CTA: DISA55M10

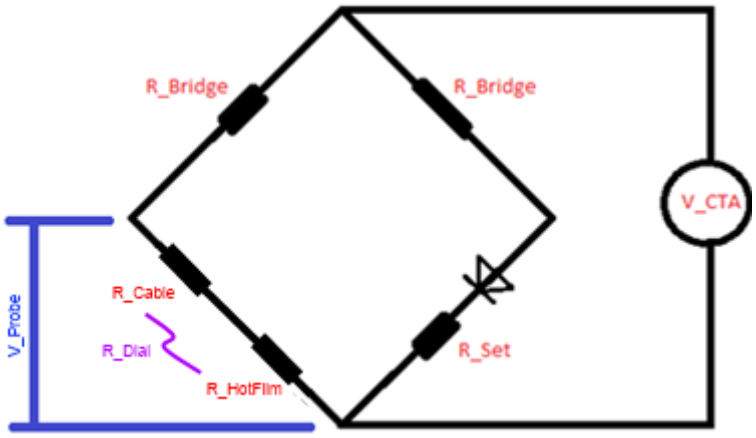

$$R_{bridge} = \frac{R_{dial} - \left(R_{dial} * \left(\frac{V_{probe}}{V_{output}}\right)\right)}{\left(\frac{V_{probe}}{V_{output}}\right)}$$

$$= \frac{16.423 - \left(16.423 * \left(\frac{0.361}{1.43}\right)\right)}{\left(\frac{0.361}{1.453}\right)}$$

$$49.68\Omega$$

Appendix 2: Calculation of Rotational Period

$$Tyre\ Diameter = 0.31\ m$$
$$Tyre\ Velocity = 25\ \frac{m}{s}$$
$$Tyre\ Angular\ Velocity = 161.29\ \frac{rad}{sec}$$
$$= 9241.23629\ \frac{deg}{sec}$$

$$1\ Timestep(TS) = 1.426 * 10^{-5}\ sec$$
$$1\ Simulation = 7700\ timesteps$$
$$Start\ of\ Data\ Recording\ at\ TS = 4900$$

$$1\ Simulation = 7700 - 4900\ TS$$
$$= 2800TS$$

$$Realtime\ Simulation\ Time = 0.039928\ sec$$
$$2800TS = 0.039928sec$$
$$Since:$$
$$Speed = \frac{Distance}{Time}$$
$$theta = 9241.23629\ \left(\frac{deg}{\text{sec}}\right) * 0.039928\ (\text{sec})$$
$$theta = 368deg$$

$$For\ 5\ rotations:$$
$$theta = 1800\ deg$$
$$For\ 1\ rotation:$$
$$360 = 9241.23628x$$
$$x = 0.03895583\ sec$$

$$1TS = 1.426 * 10^{-5}\ sec$$
$$xTS = \frac{0.03895583}{1.426 * 10^{-5}}$$
$$= 2732TS$$

$$Simulation\ results\ start\ at\ 4900TS, so:$$
$$TS = (2731.82539 + 4900) * 5TS$$
$$= 18560\ for\ 5\ rotations$$

Appendix 3: Hot Film Sensor Data Sheet (Dantec Dynamics, 2013)

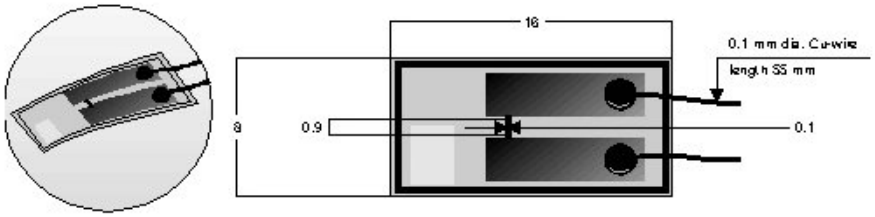

Technical Data for Glue-on Film Sensors	
Thickness of quartz coating	0.5 µm
Medium	Air
Sensor material	Nickel
Sensor dimensions	0.9 x 0.1 mm
Sensor resistance R20 (approx.)	15 W
Temperature coefficient of resistance (TCR) a 20 (approx.)	0.40%/°C
Max. sensor temperature	200°C
Max. ambient temperature	120°C

Appendix 4: Pressure Tap Spacing (British Standards, 2003)

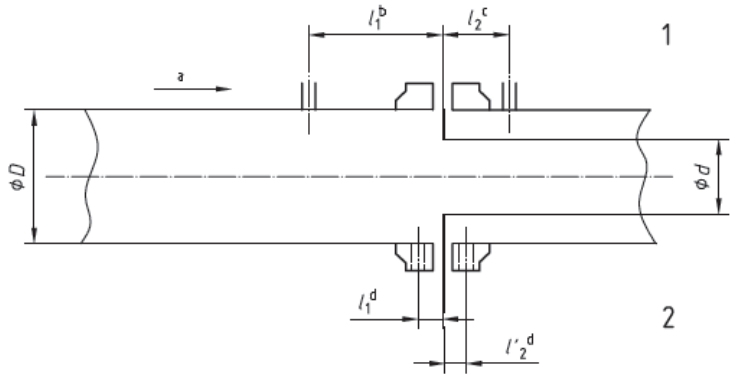

Key

1 D and $D/2$ pressure tappings

2 flange tappings

a Direction of flow.

b $l_1 = D \pm 0{,}1D$

c $l_2 = 0{,}5D \pm 0{,}02D$ for $\beta \leqslant 0{,}6$
$0{,}5D \pm 0{,}01D$ for $\beta > 0{,}6$

d $l_1 = l'_2 = (25{,}4 \pm 0{,}5)$ mm for $\beta > 0{,}6$ and $D < 150$ mm
$(25{,}4 \pm 1)$ mm for $\beta \leqslant 0{,}6$
$(25{,}4 \pm 1)$ mm for $\beta > 0{,}6$ and 150 mm $\leqslant D \leqslant$ 1 000 mm

Appendix 5: Orifice Plate Discharge Coefficient for D and D/2 Tappings where D > 71.12mm (British Standards, 2003)

Diameter ratio	Discharge coefficient, C, for Re_D equal to											
β	5×10^3	1×10^4	2×10^4	3×10^4	5×10^4	7×10^4	1×10^5	3×10^5	1×10^6	1×10^7	1×10^8	∞
0,10	0,600 3	0,598 7	0,597 7	0,597 3	0,596 9	0,596 7	0,596 6	0,596 3	0,596 2	0,596 1	0,596 1	0,596 0
0,12	0,601 0	0,599 1	0,597 9	0,597 5	0,597 1	0,596 9	0,596 7	0,596 4	0,596 2	0,596 1	0,596 1	0,596 1
0,14	0,601 6	0,599 5	0,598 2	0,597 7	0,597 2	0,597 0	0,596 8	0,596 5	0,596 3	0,596 2	0,596 1	0,596 1
0,16	0,602 3	0,600 0	0,598 5	0,598 0	0,597 4	0,597 2	0,597 0	0,596 6	0,596 4	0,596 2	0,596 2	0,596 2
0,18	0,602 9	0,600 4	0,598 9	0,598 2	0,597 7	0,597 4	0,597 1	0,596 7	0,596 5	0,596 3	0,596 3	0,596 3
0,20	0,603 7	0,600 9	0,599 2	0,598 5	0,597 9	0,597 6	0,597 4	0,596 9	0,596 6	0,596 4	0,596 4	0,596 4
0,22	0,604 4	0,601 5	0,599 6	0,598 9	0,598 2	0,597 9	0,597 6	0,597 1	0,596 8	0,596 6	0,596 5	0,596 5
0,24	0,605 3	0,602 1	0,600 1	0,599 3	0,598 5	0,598 2	0,597 9	0,597 3	0,597 0	0,596 7	0,596 7	0,596 6
0,26	0,606 2	0,602 7	0,600 6	0,599 7	0,598 9	0,598 5	0,598 2	0,597 5	0,597 2	0,596 9	0,596 9	0,596 8
0,28	0,607 2	0,603 4	0,601 1	0,600 2	0,599 3	0,598 9	0,598 5	0,597 8	0,597 5	0,597 2	0,597 1	0,597 0
0,30	0,608 2	0,604 2	0,601 7	0,600 7	0,599 8	0,599 3	0,598 9	0,598 2	0,597 8	0,597 4	0,597 3	0,597 3
0,32	0,609 4	0,605 1	0,602 4	0,601 3	0,600 3	0,599 8	0,599 4	0,598 6	0,598 1	0,597 7	0,597 6	0,597 5
0,34	0,610 7	0,606 0	0,603 1	0,602 0	0,600 9	0,600 4	0,599 9	0,599 0	0,598 5	0,598 1	0,597 9	0,597 8
0,36	0,612 1	0,607 1	0,604 0	0,602 7	0,601 6	0,601 0	0,600 5	0,599 5	0,598 9	0,598 4	0,598 3	0,598 1
0,38	0,613 7	0,608 2	0,604 9	0,603 5	0,602 3	0,601 6	0,601 1	0,600 0	0,599 4	0,598 8	0,598 6	0,598 5
0,40	0,615 3	0,609 5	0,605 9	0,604 4	0,603 1	0,602 4	0,601 8	0,600 6	0,599 9	0,599 3	0,599 1	0,598 9
0,42	0,617 2	0,610 9	0,607 0	0,605 4	0,603 9	0,603 2	0,602 5	0,601 2	0,600 5	0,599 8	0,599 5	0,599 3
0,44	0,619 2	0,612 4	0,608 2	0,606 5	0,604 9	0,604 1	0,603 4	0,601 9	0,601 1	0,600 3	0,600 0	0,599 7
0,46	0,621 4	0,614 0	0,609 4	0,607 6	0,605 9	0,605 0	0,604 2	0,602 7	0,601 7	0,600 8	0,600 5	0,600 2
0,48	0,623 8	0,615 7	0,610 8	0,608 8	0,607 0	0,606 0	0,605 2	0,603 5	0,602 4	0,601 4	0,601 0	0,600 6
0,50	0,626 4	0,617 6	0,612 3	0,610 1	0,608 1	0,607 1	0,606 2	0,604 3	0,603 1	0,602 0	0,601 6	0,601 1
0,51	0,627 8	0,618 6	0,613 1	0,610 8	0,608 7	0,607 6	0,606 7	0,604 7	0,603 5	0,602 3	0,601 9	0,601 4
0,52	0,629 2	0,619 7	0,613 9	0,611 5	0,609 3	0,608 2	0,607 2	0,605 2	0,603 9	0,602 7	0,602 1	0,601 6
0,53	0,630 7	0,620 7	0,614 7	0,612 3	0,610 0	0,608 8	0,607 8	0,605 6	0,604 3	0,603 0	0,602 4	0,601 9
0,54	0,632 2	0,621 8	0,615 5	0,613 0	0,610 6	0,609 4	0,608 3	0,606 1	0,604 7	0,603 3	0,602 7	0,602 1

Appendix 6: Orifice Plate Expansion Factor (British Standards, 2003)

Diameter ratio		Expansibility [expansion] factor, ε, for p_2/p_1 equal to							
β	β^4	0,98	0,96	0,94	0,92	0,90	0,85	0,80	0,75
for κ = 1,2									
0,100 0	0,000 1	0,994 1	0,988 3	0,982 4	0,976 4	0,970 5	0,955 5	0,940 4	0,925 2
0,562 3	0,100 0	0,993 6	0,987 1	0,980 6	0,974 1	0,967 6	0,951 1	0,934 5	0,917 7
0,668 7	0,200 0	0,992 7	0,985 3	0,977 9	0,970 5	0,963 1	0,944 3	0,925 4	0,906 3
0,740 1	0,300 0	0,991 5	0,982 9	0,974 3	0,965 7	0,957 0	0,935 2	0,913 2	0,891 0
0,750 0	0,316 4	0,991 2	0,982 4	0,973 6	0,964 8	0,955 9	0,933 5	0,910 9	0,888 1
for κ = 1,3									
0,100 0	0,000 1	0,994 6	0,989 1	0,983 7	0,978 2	0,972 7	0,958 7	0,944 6	0,930 3
0,562 3	0,100 0	0,994 0	0,988 1	0,982 1	0,976 0	0,970 0	0,954 7	0,939 1	0,923 4
0,668 7	0,200 0	0,993 2	0,986 4	0,979 6	0,972 7	0,965 8	0,948 4	0,930 7	0,912 8
0,740 1	0,300 0	0,992 1	0,984 2	0,976 2	0,968 2	0,960 2	0,939 9	0,919 3	0,898 5
0,750 0	0,316 4	0,991 9	0,983 8	0,975 6	0,967 4	0,959 1	0,938 3	0,917 2	0,895 8
for κ = 1,4									
0,100 0	0,000 1	0,995 0	0,989 9	0,984 8	0,979 7	0,974 6	0,961 5	0,948 3	0,934 8
0,562 3	0,100 0	0,994 5	0,988 9	0,983 3	0,977 7	0,972 0	0,957 7	0,943 1	0,928 3
0,668 7	0,200 0	0,993 7	0,987 4	0,981 0	0,974 6	0,968 1	0,951 8	0,935 3	0,918 4
0,740 1	0,300 0	0,992 7	0,985 3	0,977 9	0,970 4	0,962 9	0,943 9	0,924 6	0,905 0
0,750 0	0,316 4	0,992 5	0,984 9	0,977 3	0,969 6	0,961 9	0,942 4	0,922 6	0,902 5
for κ = 1,66									
0,100 0	0,000 1	0,995 8	0,991 5	0,987 2	0,982 8	0,978 4	0,967 3	0,955 8	0,944 1
0,562 3	0,100 0	0,995 3	0,990 6	0,985 9	0,981 1	0,976 3	0,964 0	0,951 5	0,938 6
0,668 7	0,200 0	0,994 7	0,989 3	0,983 9	0,978 5	0,973 0	0,959 0	0,944 7	0,930 1
0,740 1	0,300 0	0,993 8	0,987 6	0,981 3	0,974 9	0,968 5	0,952 3	0,935 7	0,918 6
0,750 0	0,316 4	0,993 6	0,987 2	0,980 8	0,974 3	0,967 7	0,951 0	0,934 0	0,916 4
NOTE This table is given for convenience. The values given are not intended for precise interpolation. Extrapolation is not permitted.									

Appendix 7: Cp Calculations for Bench Test Data

$$Re_D = value\ from\ Appendix\ 6$$

$$C = value\ from\ Appendix\ 6$$

$$\varepsilon = value\ from\ Appendix\ 6$$

$$Vel_D = \frac{Re_D \mu}{OD_D \rho} \qquad \frac{m}{s}$$

$$P_{DYN_D} = \frac{1}{2}\rho v^2 \qquad \frac{kg}{m.s^2}$$

$$P_{DYN\_MEAS\_1} = \frac{P_{DYN_D}(1-\beta^4)}{(\beta^4.c^2.\varepsilon^2)} \qquad \frac{kg}{m.s^2}$$

$$CP_{DYN\_MEAS\_1} = \frac{P_{DYN_{MEAS}}}{P_{DYN_D}}$$

Quasi-Velocity

$$Q(v) = \sqrt{\frac{2P_{DYN_{MEAS}}}{\rho}} \qquad \frac{kg}{m.s^2}$$

$$and: \beta = diameter\ ratio$$

$$c = coefficient\ of\ discharge\ from\ BS\ standard\ tables$$

$$\varepsilon = expansion\ factor$$

$$Q\left(\frac{Re}{m}\right) = \frac{Q(v) * \rho}{\mu}$$

Calculated Coefficient of Pressure

$$CP_{DYN_{MEAS_{CALC}}} = \frac{P_{DYN_{MEAS_1}}}{P_{DYN_{D_2}}}$$

Dynamic Pressure at Diameter 'D2'

$$P_{DYN_{D2}} = P_{DYN_d}.\beta^4$$

Dynamic Pressure at Diameter 'd'

$$P_{DYN_d} = \frac{C^2.\varepsilon^2.P_{DYN_{MEAS_1}}}{1-\beta^4}$$

Pressure Loss

$$\Delta\varpi = \frac{\sqrt{1-\beta^4(1-C^2)} - C\beta^2}{\sqrt{1-\beta^4(1-C^2)} + C\beta^2}\Delta p$$

Pressure Loss co-efficient

$$\mathrm{K} = \frac{\Delta\omega}{0.5 * \rho * Q(v)^2}$$

Measured Coefficient of Pressure

$$Cp_{MEAS} = -K$$

Appendix 8: Wind Tunnel Test Mounting Frame – Various Component Drawings

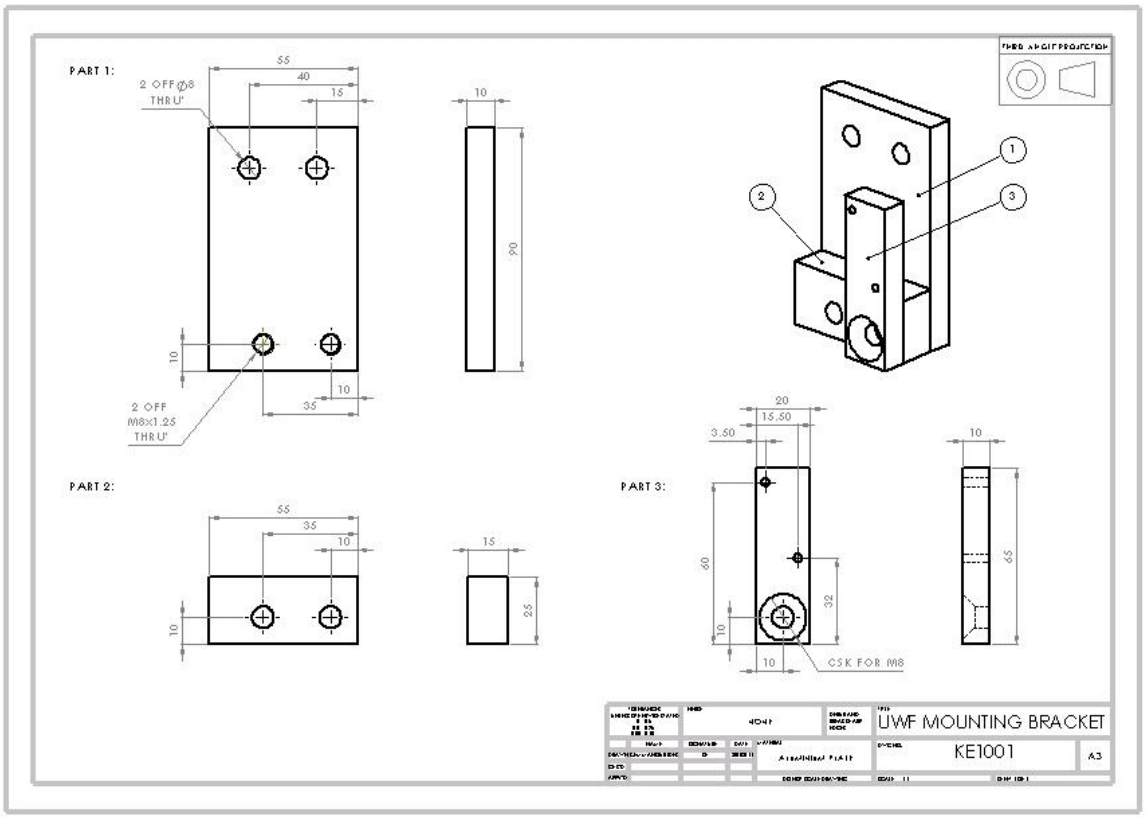

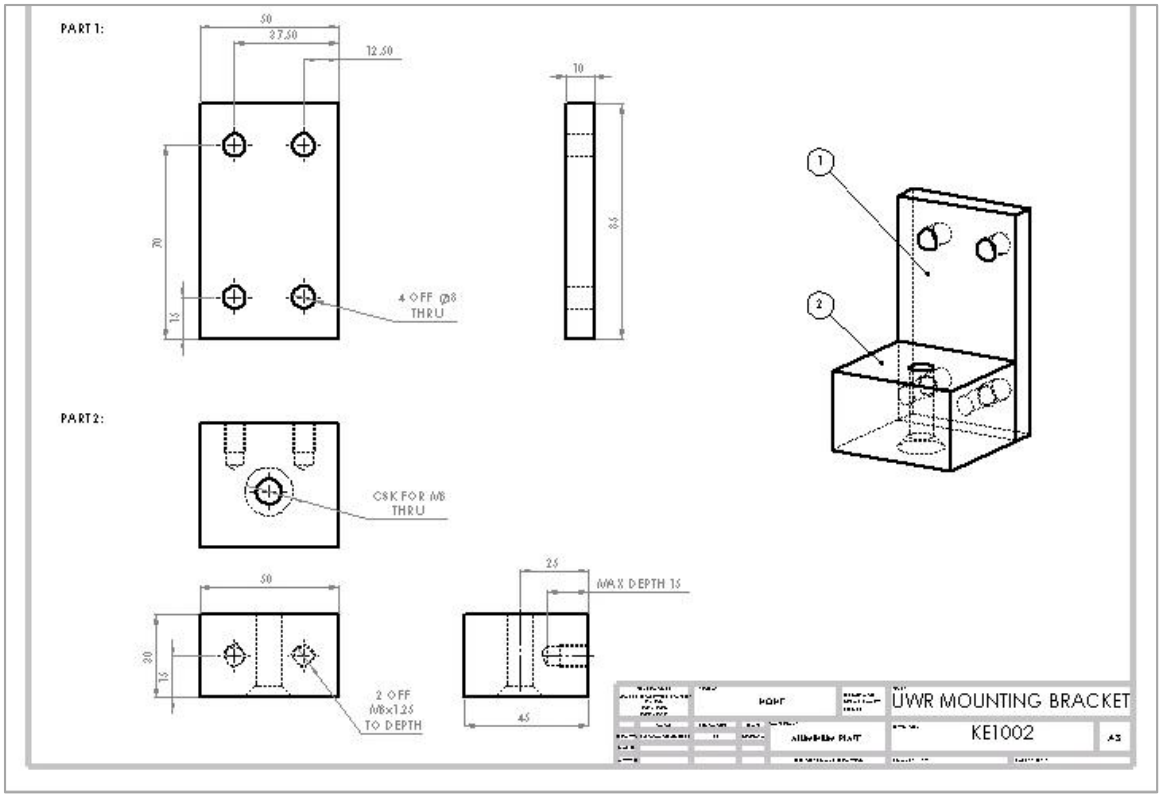

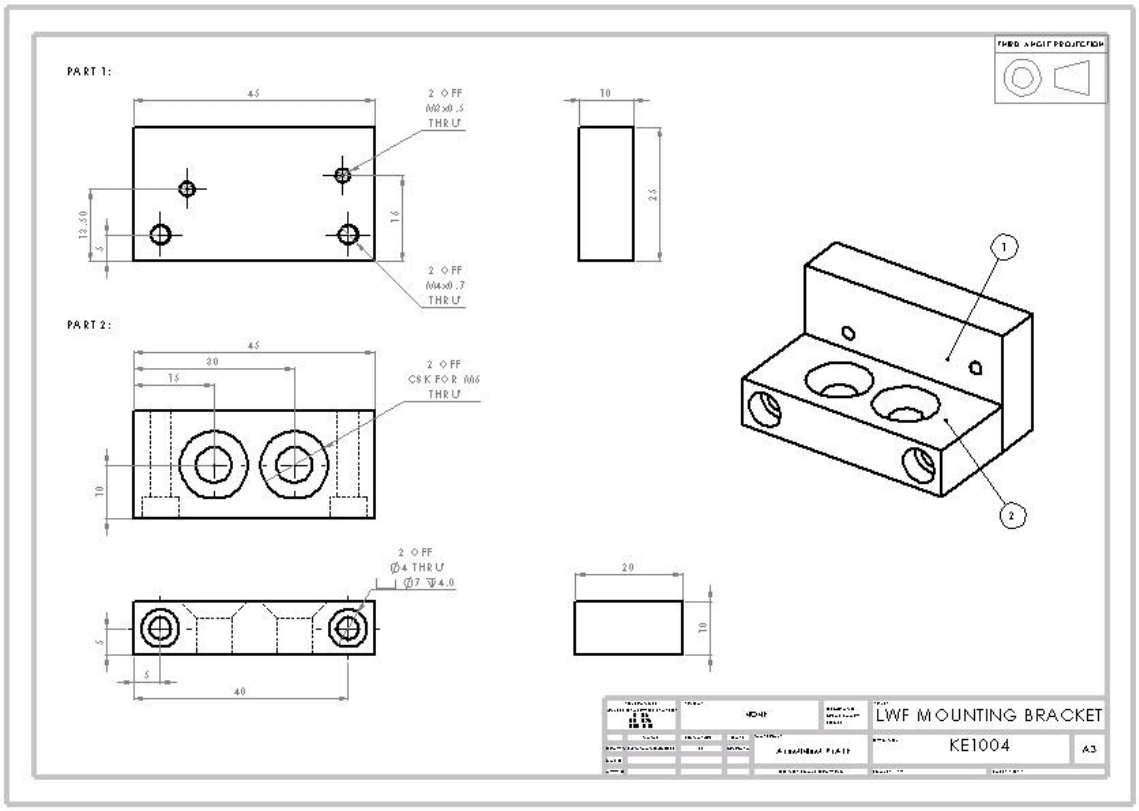
PART 1:
45
2 ◇FF
M2x0.5
THRU
10
25
12.50
5
16
2 ◇FF
M4x0.7
THRU
PART 2:
45
20
15
2 ◇FF
CSK FOR M6
THRU
10
2 ◇FF
Ø4 THRU
⌴ Ø7 ▽4.0
5
5
40
20
10
1
2
THIRD ANGLE PROJECTION
NONE
ALUMINIUM PLATE
LWF MOUNTING BRACKET
KE1004
A3

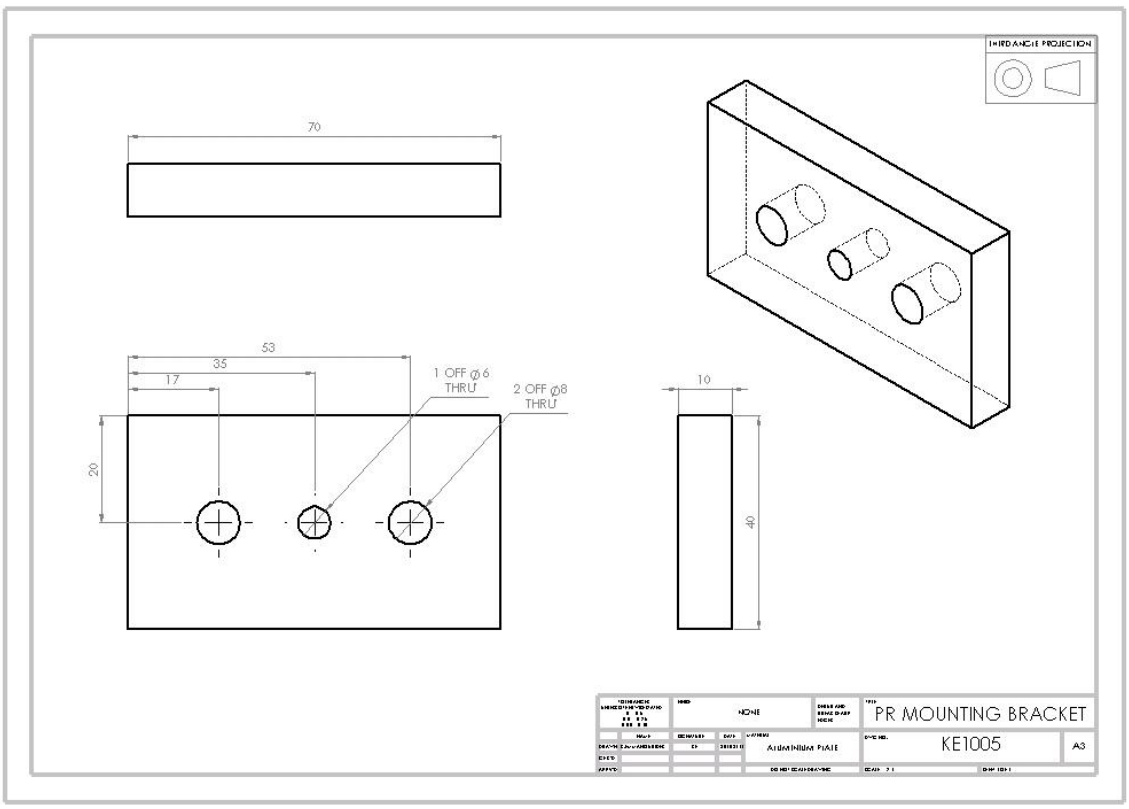
70
53
35
17
1 OFF Ø6
THRU
2 OFF Ø8
THRU
20
10
40
THIRD ANGLE PROJECTION
NONE
ALUMINIUM PLATE
PR MOUNTING BRACKET
KE1005
A3

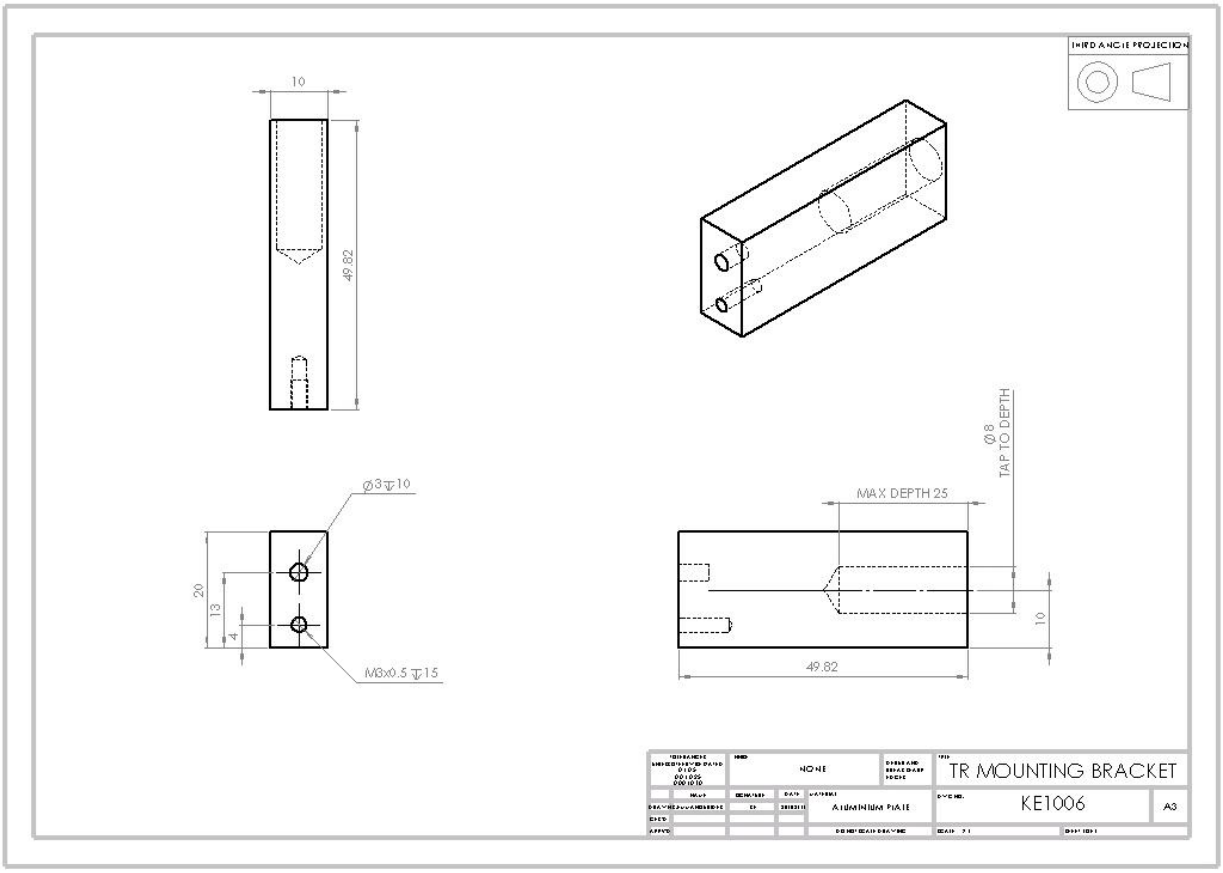
THIRD ANGLE PROJECTION
10
49.82
Ø3↧10
20
13
4
M3x0.5↧15
Ø8
TAP TO DEPTH
MAX DEPTH 25
10
49.82
NONE
TR MOUNTING BRACKET
ALUMINIUM PLATE
KE1006
A3

Appendix 9: Wind Tunnel Sidewall HTC Graphs

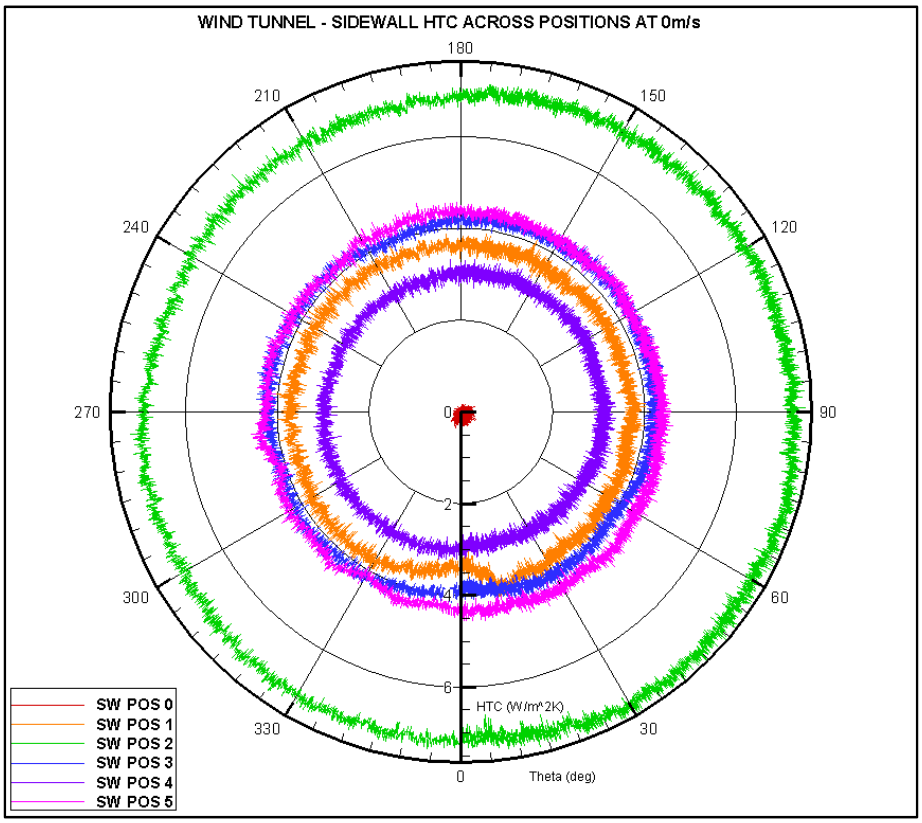

Sidewall HTC for All Positions at 0m/s

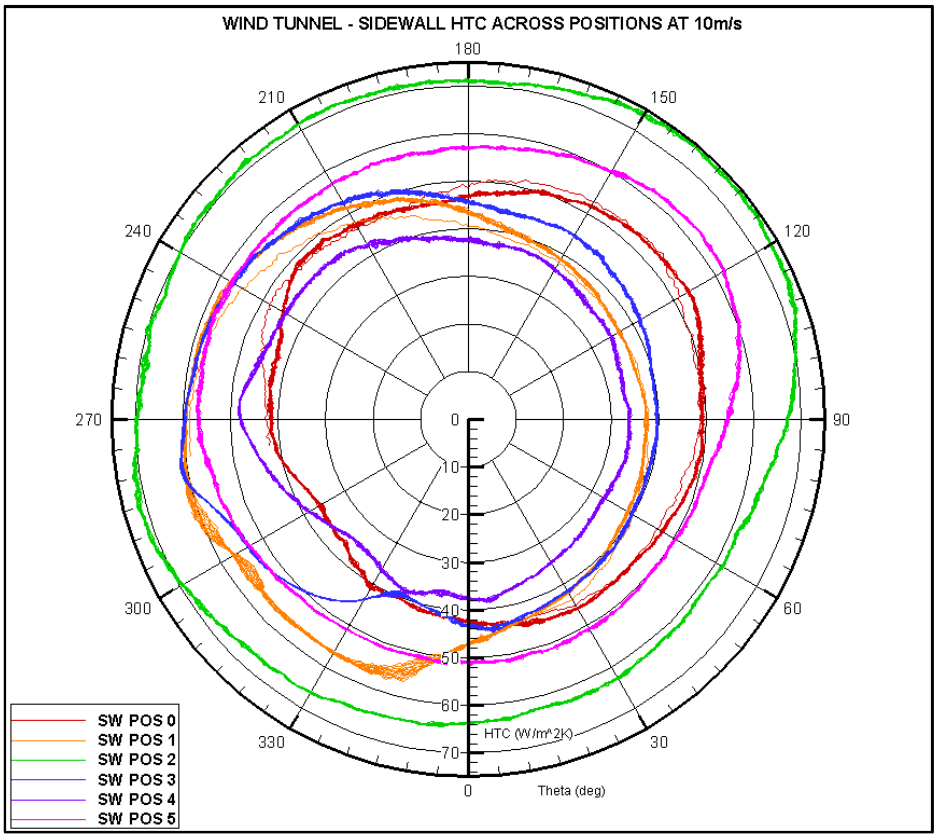

Sidewall HTC for All Positions at 10m/s

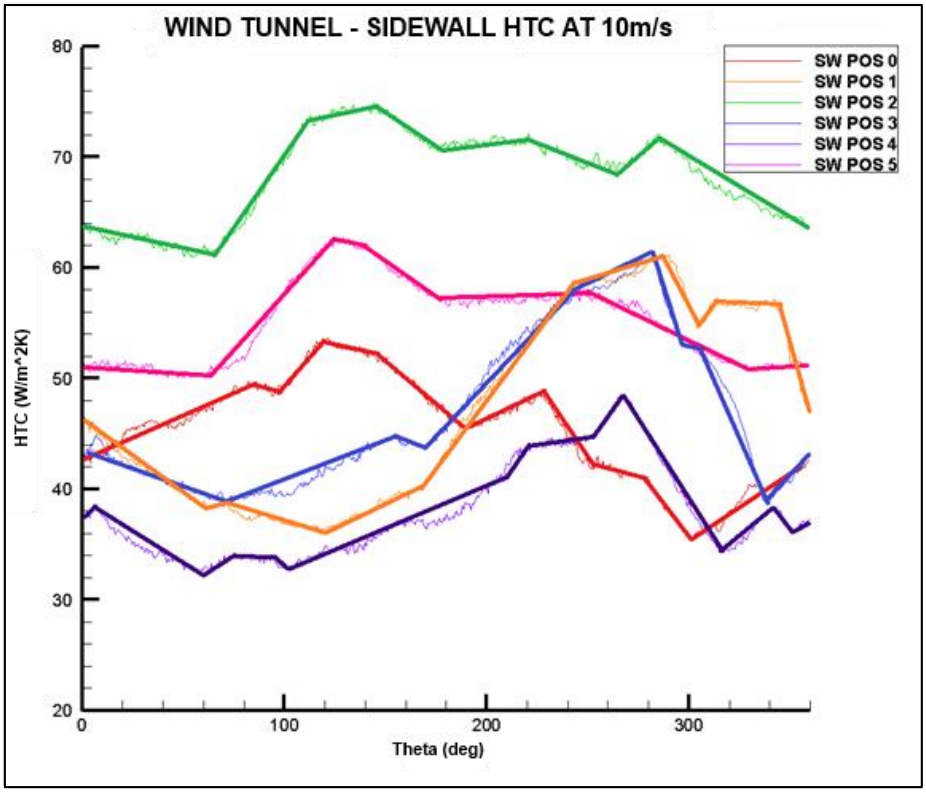

Sidewall HTC at 10m/s – Modified to Outline Positional Trends

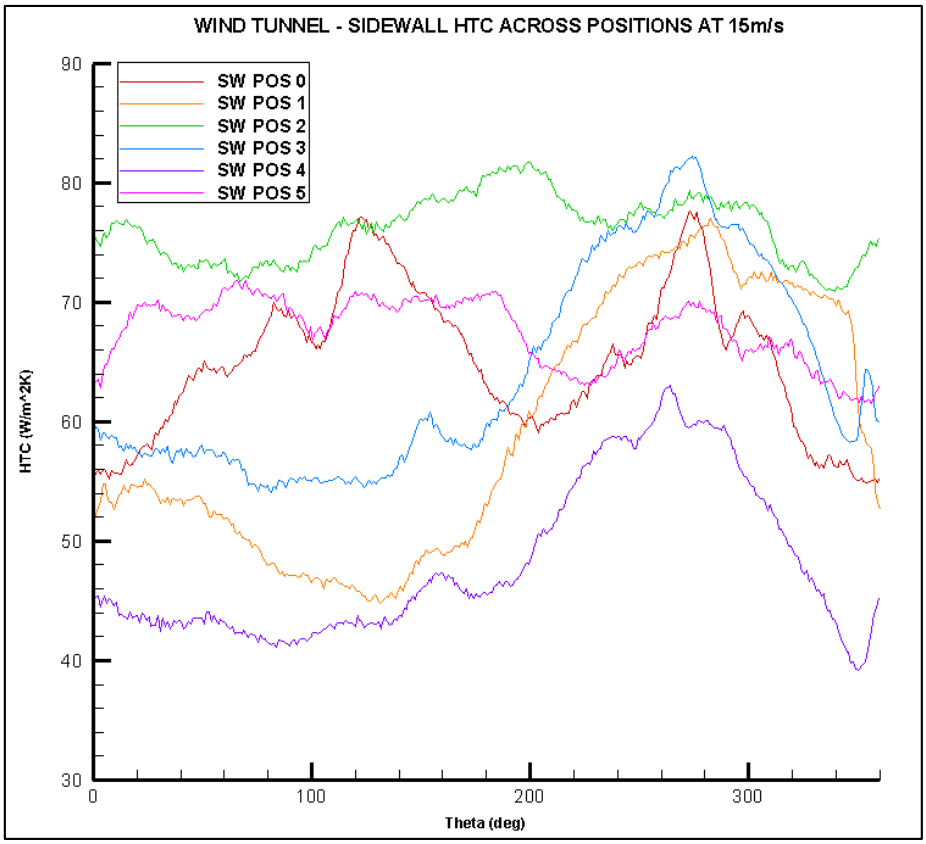

Sidewall HTC for All Positions at 15m/s